5-2021

Spectroscopic properties of ferroic superlattices

Shiyu Fan
sfan1@vols.utk.edu

Recommended Citation

Fan, Shiyu, "Spectroscopic properties of ferroic superlattices. " PhD diss., University of Tennessee, 2021.
https://trace.tennessee.edu/utk_graddiss/6702

To the Graduate Council:

I am submitting herewith a dissertation written by Shiyu Fan entitled "Spectroscopic properties of ferroic superlattices." I have examined the final electronic copy of this dissertation for form and content and recommend that it be accepted in partial fulfillment of the requirements for the degree of Doctor of Philosophy, with a major in Physics.

Janice Musfeldt, Major Professor

We have read this dissertation and recommend its acceptance:

Haidong Zhou, Norman Mannella, Steven Johnston

Accepted for the Council:

Dixie L. Thompson

Vice Provost and Dean of the Graduate School

(Original signatures are on file with official student records.)

Spectroscopic properties of ferroic superlattices

A Dissertation Presented for the
Doctor of Philosophy
Degree
The University of Tennessee, Knoxville

Shiyu Fan
May 2021

Acknowledgments

First and foremost I wish to thank my advisor, Professor Janice L. Musfeldt, for bring me to the amazing spectroscopy world. Your enthusiasm, professional attitude and broad knowledge inspire and push me to try my best to be a strong scientist. You have been a big influence on both my personal and professional development.

I am grateful to Professors Haidong Zhou, Norman Mannella, Steven Johnston for serving on my committee, as well as for all of their interest, help, and advice.

I wish to acknowledge all the members of our research group: Amal al-Wahish, Judy Cherian, Brian Holinsworth, Ken O'Neal, Amanda Clune, Kendall Hughey, Nathan Harms, Kevin Smith, Sabine Neal, Avery Blockmon, Kiman Park, and Brandon Chapman for their help, encouragement, and collaboration. I am grateful to all the faculty and staff of the Physics Department who shared their knowledge with me and helped in a variety of ways during my graduate program.

I would like to thank Jason Haraldsen, Sang-Wook Cheong, Stephen A. McGill, Hena Das, Alejandro F. Rébola, Julia A. Mundy, Charles Brooks, Megan Holtz, Ramamoorthy Ramesh, Darrell G. Schlom, David A. Muller, Craig J. Fennie, and Adam A. Aczel, for their collaboration and inspiring conversations during these years. Without these brilliant scientists giving their effort and input, the work would not have been half of what it became.

Finally, I wish to thank my parents, family, and friends for always believing in and supporting me. I could not have finished my degree without your help, patience, and understanding. I will also thank my fiancee Chenchen Sun and my cat Luna for accompanying with me, help me release the pressure in the graduate school.

Abstract

The interplay between charge, structure, magnetism, and orbitals leads to rich physics and exotic cross-coupling in multifunctional materials. Superlattices provide a superb platform to study the complex interactions between different degrees of freedom. In this dissertation, I present a spectroscopic investigation of natural and engineered superlattices including Fe_xTaS_2 and $(LuFeO_3)_m/(LuFe_2O_4)_1$ under external stimuli of temperature and magnetic field as well as chemical substitution. Studying the phase transitions, symmetry-breaking, and complex interface interactions from a microscopic viewpoint enhances fundamental understanding of coupling mechanism between different order parameters and the exciting properties.

In Fe_xTaS_2, we use optical spectroscopies to analyze the electronic properties. Strikingly, Fe intercalation dramatically changes the metallic character, revealing two separate free carrier responses in the Fe monolayer and TaS_2 slabs, respectively. Signatures of chirality are deeply embedded in the electronic structures. These include a transition of electron density pattern from triangular to Kagome to honeycomb, a hole → electron pocket crossover at the K-point, and low energy excitations between spin split bands that cross the Fermi surface. These findings advance the understanding of intercalation and symmetry-breaking on the fundamental excitations in metallic chalcogenides, while at the same time, raise important questions about how the embedded metal monolayer affects vibrational properties due to the free-carrier response screened the infrared-active phonons.

To address these issues, we extended this work using Raman scattering spectroscopy to reveal the vibrational properties. We particular focus on the coherent excitations in the Fe monolayer. The results reveal both in- and out-of-plane vibrational excitations at low frequencies in the intercalated Fe monolayer. Extending the measurements to other intercalated chalcogenides such as $Cr_{1/3}NbS_2$ and $RbFe(SO_4)_2$ reveals structural-property relations, which confirms the intercalated monolayer excitations are general and intrinsic. Furthermore, the intercalated monolayer excitations have a trend that depend upon the metal-metal distance, the size of the van der Waals gap, and the metal-to-chalcogenide slab mass ratio. A model for how mass ratio affects the frequencies of the monolayer excitations is developed as well, which excellently fits to our experimental trend. These findings suggest that external stimuli such as pressure and strain may be able to tune these intercalated monolayer excitations.

In the $(LuFeO_3)_m/(LuFe_2O_4)_1$ multiferroic superlattices (m = 3, 7, and 9), we combined optical spectroscopy, magnetic circular dichroism, and first-principle calculations to uncover the origin of high temperature magnetism and charge-ordering states in a site-specific manner. Analysis of the dichroic spectra reveals optical hysteresis loops for different Fe sites. The site-specific coercivity vs. temperature curves are extracted from the optical hysteresis, which demonstrates that bulk magnetism derives principally from the $LuFe_2O_4$ layers. Magnetism emanating from the $LuFe_2O_4$ layer becomes more robust as the (3, 1) → (7, 1) → (9, 1) series progresses - a trend that correlates with increasing Lu-layer distortion. To understand this relationship more deeply, we extract the spectral signature of the interface for the $(LuFeO_3)_m/(LuFe_2O_4)_1$ series (m = 3, 7 and 9). While the overall contribution of spin-down channel excitations is persistent over the sequence, enhanced Lu-layer distortion at the interface increases the contribution of the $Fe^{2+} \rightarrow Fe^{3+}$ charge-transfer excitation in the spin-up channel. This amplifies $LuFe_2O_4$ layer magnetization and pinpoints the role of Fe^{2+}. Key to this discovery is the ability of magneto-optical spectroscopy to provide direct, microscopic, site-specific information about interface magnetism in a two-dimensional material with multiple magnetic centres. Comparison of the theoretically predicted magnetic circular dichroism with the experimental spectrum also establishes the non-polar self-doped structure as the precise charge-ordering arrangement within the $LuFe_2O_4$ layer of the (3, 1) superlattice, thus resolving controversy regarding the many different isoenergetic charge states. In addition to introducing a remarkably powerful and versatile spectroscopic decomposition technique for revealing microscopic spin and charge character at the interface of a multiferroic superlattice with many different iron centres in a site-selective manner, this work provides a pathway to link bulk and interface properties in other engineered materials.

Table of Contents

List of Tables

List of Figures

Chapter 1

Introduction: Superlattice architectures lead to new functionalities

A superlattice is a periodic structure with repeating atomically thin layers of two or more materials along a certain crystalline direction. They attract broad research interest because the nature of combining two distinct components can lead to new types of functional materials. In addition, complex interactions at the interface present unique opportunities for the discovery of entirely new quantum phenomena. There are two general types of superlattices: natural occuring and engineered superlattices [Fig. 1.1]. In this work, I have been interested in both.

1.1 Natural occuring and engineered superlattices

Natural occuring superlattices are based on periodicity in a material's own crystal structure. They are known as homologous phase compounds, and can usually be obtained by chemical substitution. Intercalated transition metal dichalcogenides

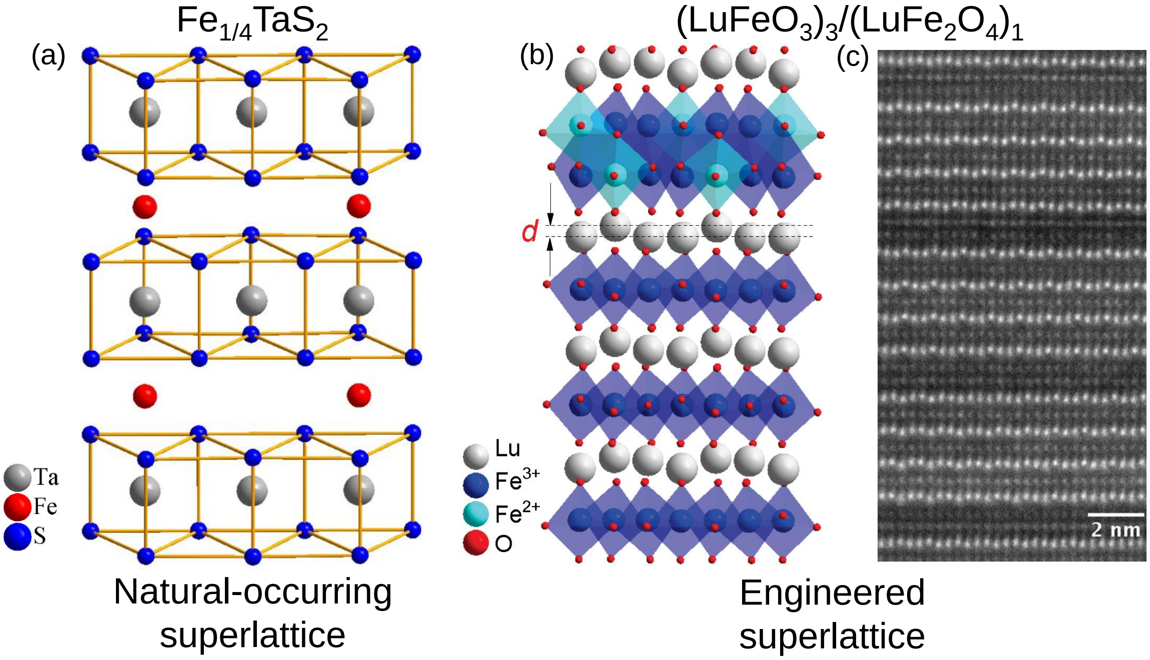

Figure 1.1: (a) Crystal structure of the natural occuring superlattice $Fe_{1/4}TaS_2$. The Fe intercalation at the van der Waals gap results in a $2a \times 2a$ superstructure. (b) Unit cell of the engineered superlattice $(LuFeO_3)_3/(LuFe_2O_4)_1$, grown on $(ZrO_2)_{0.905}(Y_2O_3)_{0.095}$ substrates using molecular-beam epitaxy [1]. (c) STEM image of the $(LuFeO_3)_3/(LuFe_2O_4)_1$ superlattice, viewed along the $[1\bar{1}0]$ zone axis. Atomic number contrast shows the bright, heavy lutetium atomic rows layered with the less bright iron atomic rows.

such as Fe_xTaS_2 and Cr_xNbS_2 are typical natural occuring superlattices. Within this family of materials, the 3d transition metal elements are intercalated in the van der Waals gap betweem two neighbouring layers of TX_2, forming the weakly bonded atomically thin monolayer [Fig. 1.1 (a)]. Superstructures are formed after intercalation, which profoundly modifies physical properties.

Engineered superlattices are artificially created by alternating the growth of ultra-thin films of different materials on a proper substrate [Fig. 1.1 (b,c)]. Each layer in the superlattice is atomically thin, which is why heteroepitaxy is sometimes said to form "interface materials". Two typical methods for synthesis engineered superlattices are pulsed laser deposition and molecular-beam epitaxy. They are mostly used for the growth of complex oxides with the precise control of their composition, thickness, and structures [2]. Lattice mismatch between the substrate and the growing film has significant effects on epitaxy, which can induce structural defects between the film-substrate interface, affect the growth morphology of the film in both 3D island and 2D layer growth modes, and influence the epitaxial orientation of the grown film by affecting the heterogeneous nucleation process [3]. These effects are due to the interfacial energy which is related to the strength of bonding at the interface as well as to the degree of lattice mismatch [3].

1.2 Interface-induced properties in Fe_xTaS_2 and $(LuFeO_3)_m$/ $(LuFe_2O_4)_n$

For both natural occuring and engineered superlattices, the interface is the key factor that can lead to exotic physical properties [1, 4, 5]. For example, domain walls can be formed at the interface [6, 7], which can localize charges and modulate phonon modes [7–9]. Helical magnetic order is observed in $Cr_{1/3}NbS_2$ due to the interlayer

Dzyaloshinskii-Moriya interactions [10, 11]. Lattice distortions can take place at the interface region due to the increasing lattice strain, which can dramatically boost magnetic transition temperature [1, 4]. In this work, we selected two different systems, with which to study the interface properties. One family of materials is the natural occuring superlattices $\mathrm{Fe}_x\mathrm{TaS}_2$ ($x = 1/4$ and $1/3$), and the other system involves a series of engineered multiferroic superlattices $(\mathrm{LuFeO}_3)_m/(\mathrm{LuFe}_2\mathrm{O}_4)_n$. We use the former as platforms for exploring the electronic signatures of chirality, phonon properties of the intercalated metal monolayer, and the latter to probe interface magnetism in a site-specific manner.

$\mathrm{Fe}_x\mathrm{TaS}_2$ is a material within the metal-intercalated transition metal dichalcogenides family. This system attracts broad interest because of fascinating domain and domain wall patterns, as well as large magnetoresistivities and switching behavior [6, 12, 13]. The materials are based upon 2H-TaS_2 and have a set of stable, well-ordered intercalation plateaus at $x = 1/4$ and $1/3$ [6]. The $x = 1/4$ compound yields a $2a \times 2a$ superstructure with a centrosymmetric space group $P6_3/mmc$. For $x = 1/3$, the Fe intercalation pattern is different and leads to a $\sqrt{3}a \times \sqrt{3}a$ superstructure with a non-centrosymmetric and chiral space group $P6_322$ [6]. Figure 1.2 displays the domain and domain wall patterns in $\mathrm{Fe}_x\mathrm{TaS}_2$ ($x = 1/4$ and $1/3$). In $\mathrm{Fe}_{1/4}\mathrm{TaS}_2$, it reveals the Z_4 type domain patterns with antiphase boundaries. While in $\mathrm{Fe}_{1/3}\mathrm{TaS}_2$, the domain patterns change to $\mathrm{Z}_2 \times \mathrm{Z}_3$ type, and the domain boundaries become antiphase and chiral, forming the structural Z_6 vortices [14]. That these domain topologies are rarely observed in other intercalated compounds such as $\mathrm{Cr}_{1/3}\mathrm{NbS}_2$ and $\mathrm{Fe}_{1/3}\mathrm{NbS}_2$ makes the $\mathrm{Fe}_x\mathrm{TaS}_2$ an interesting system to study.

It has been determined that the domain topology in $\mathrm{Fe}_x\mathrm{TaS}_2$ has a significant effect on the magnetic properties [6]. Figure 1.2 (c) displays magnetic hysteresis curves at 4 K. The inset shows the extracted coercivities as a function of Fe concentration.

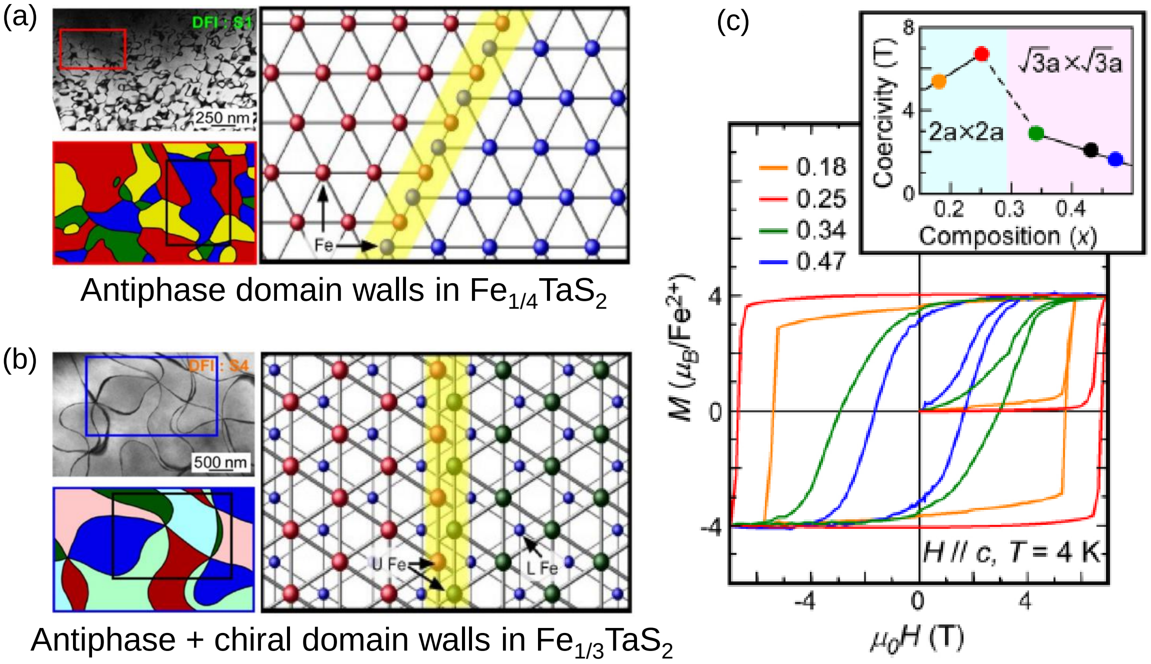

Antiphase domain walls in $Fe_{1/4}TaS_2$

Antiphase + chiral domain walls in $Fe_{1/3}TaS_2$

Figure 1.2: (a,b) Domain and domain wall patterns in $Fe_{1/4}TaS_2$ and $Fe_{1/3}TaS_2$, respectively. (c) Magnetic hysteresis curves of $x = 0.18$, 0.25, 0.34, and 0.47. These curves were measured at 4 K in magnetic fields along the c axis. Note that $x = 0.18$ and 0.25 show the $2a \times 2a$-type superstructure, whereas $x = 0.34$ and 0.47 exhibit the $\sqrt{3}a \times \sqrt{3}a$-type one. The inset shows the magnetic coercivity as a function of Fe composition [6].

The hysteresis of $Fe_{1/4}TaS_2$ with the Z_4 type domains exhibits sharp switching of magnetization with large coercivities. On the other hand, the hysteresis of $Fe_{1/3}TaS_2$ with $Z_2 \times Z_3$ domains show relatively broad switching of magnetization with small coercivity. The distinct magnetic behaviors are associated with different degrees of pinning of domain walls [6].

The unique and exotic domain and domain wall patterns in $Fe_{1/3}TaS_2$ are due to its structural chirality. Other than those structural domain patterns, chirality can also induce complex magnetic ordering in the intercalated transition metal chalcogenides. Another such example is $Cr_{1/3}NbS_2$, where the chiral helical magnetic ordering forms below 131 K [10, 11]. However, there are very few studies about how chirality affects electronic properties. The difficulty is due to the bulk measurement techniques such as magnetization and electronic transport only reveal an average response but not the insight of interplay between structures, charge, spin, and orbit for a particular site. Particularly for the Fe_xTaS_2 system, the insight of how symmetry-breaking affects electronic structures, lattice excitations, charge densities, and spin-lattice coupling are highly under explored. Revealing those properties are important to advance the fundamental understanding of the interlayer interactions and interface properties in the entire family of intercalated transition metal dichalcogenides.

Another interesting system in this study is the engineered multiferroic superlattices $(LuFeO_3)_m/(LuFe_2O_4)_n$. This series of materials displays high magnetic transition temperature and fully coupled ferroelectric ferrimagnetism at the same time, which rarely coexist. This family of materials consists of two end members. One end member h-$LuFeO_3$ is a polar, improper ferroelectric below 1020 K, and it orders antiferromagnetically at 147 K in a pattern in which symmetry allows a slight canting of the spins - giving rise to weak ferromagnetism [16–19]. The other end member

$LuFe_2O_4$ is an antiferroelectric with a complex phase diagram, exemplified by a series of charge ordering transitions above room temperature, a 240 K ferrimagnetic ordering temperature, and a structural transition near 170 K [20–24]. In certain members of the $(LuFeO_3)_m/(LuFe_2O_4)_n$ series ($m = 9$ and $n = 1$), ferroelectric ferrimagnetism emerges with ordering temperatures up to 281 K [1]. Such a superlattice has a higher magnetic ordering temperature than either of its end members due to interface effects [1], generating families of room temperature multiferroics [Fig. 1.3]. The high temperature multiferroicity is closely related to the Lu-layer distortion at the $LuFeO_3$-$LuFe_2O_4$ interface [Fig. 1.3] [1]. This Lu-layer distortion raises as the superlattice periodicity becomes larger due to the increasing lattice strain. The Lu-layer distortion also affects the bulk magnetization and coercivities in the superlattices.

There are a number of questions that emerge from this prior work [1]. For example, the pathway by which the rumpling in the $LuFeO_3$ layer (Lu-layer distortion that causes broken inversion symmetry) couples to the magnetism in the $LuFe_2O_4$ layer is not established [15]. The origin of high temperature magnetism is not clear. The microscopic nature of these interface effects is highly under-explored. The electronic ground state is not determined due to multiple nearly degenerate charge-ordered states induced from the interfacial lattice distortion. One of the challenge to understanding the inner workings of these complex magnetoelectric multiferroics is the multitude of distinct Fe centres and their associated environments due to the extraordinary complexity from combining multiple components in a single unit. Since macroscopic techniques characterize average responses rather than the role of individual iron centres, a site-specific analysis of spin and charge is required to resolve the interplay between the interfacial lattice distortion and magnetism of each Fe site.

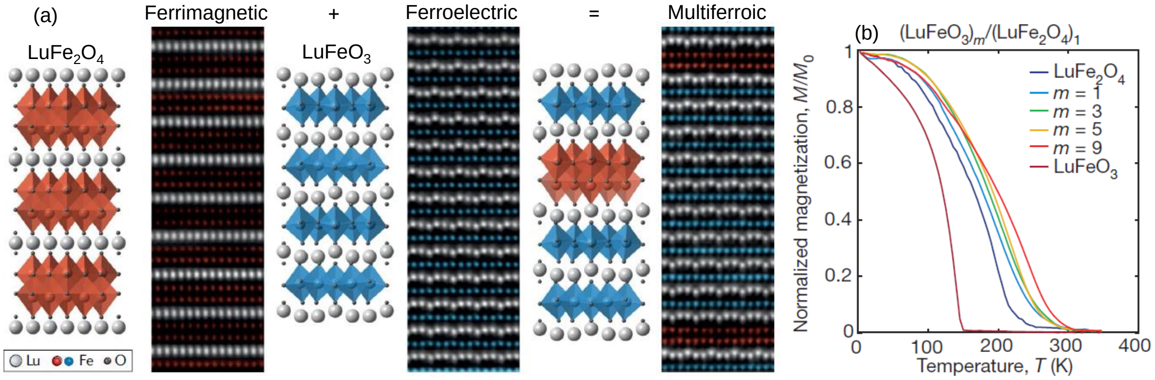

Figure 1.3: (a) crystal structures and STEM images of $LuFe_2O_4$ (left), $LuFeO_3$ (middle), and $(LuFeO_3)_m/(LuFe_2O_4)_n$ superlattices (right), respectively [15]. (b) Magnetization vs temperature for different superlattices [1].

1.3 Spectroscopy reveals properties in a site-specific manner

Spectroscopy provides a site-specific technique to understand the fundamental excitations of spin, charge, lattice as well as their interplay. Measurements in different energy regions can probe many different types of elementary excitations, as shown in Fig. 1.4. Two fundamental excitations of interest to my work include phonons and electronic excitations.

In the low frequency range, infrared spectroscopy can be employed to detect magnetic excitations, magnons, low lying electronic excitations, free-carrier response and vibrational modes (phonons) [Fig. 1.4], which play a major role in many material properties including thermal and electrical conductivities [25]. Phonons with odd symmtries can be detected by this technique. Strong infrared-active phonons are usually observed in semiconductors and insulators. However, for metalllic compounds, infrared-active phonons are screened by the low energy free-carrier response. In this case, Raman scattering spectroscopy is also used to compliment infrared techniques. Phonons that are Raman-active are the even symmetry modes. Combined with lattice dynamics calculations and a group theory analysis, phonon symmetries and their displacement pattern can be revealed to understand local structure environment and lattice distortion.

Phonons can also couple to the magnetism, which is called spin-lattice coupling. When lattice interacts with light and vibrates, some of the vibrational modes can change the bonding length and angle between metal and ligands, which modifies exchange interactions between metal centers. Magnetic materials usually display phase transitions when varying temperatures and magnetic field. During the transition, magnetic moments are reoriented, including spin flop, canting, or aligning

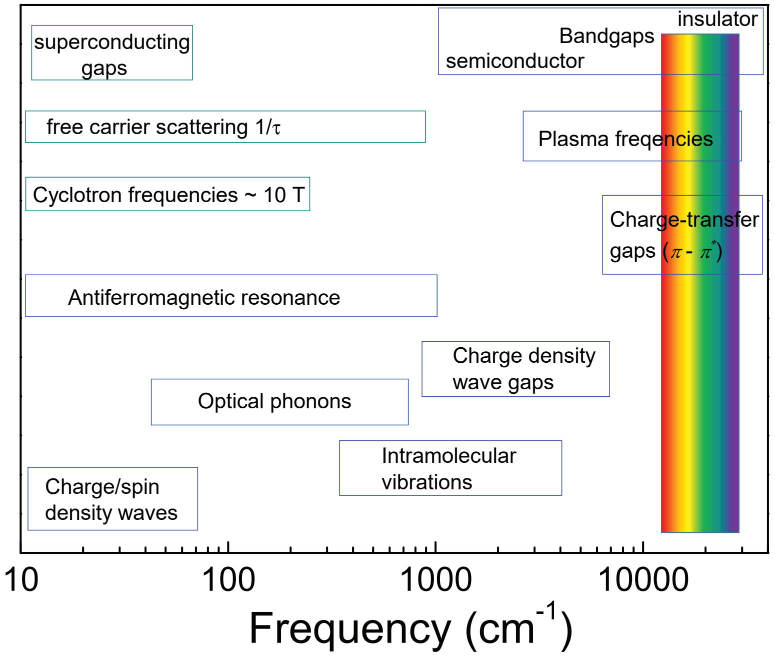

Figure 1.4: Chart showing optical processes in solids, with an indication of the frequencies where these processes typically may be studied [26].

towards the fully polarized magnetic state [27–29]. The reorientation of magnetic moments sometimes accompanied with a local lattice distortion, which can break symmetries and result in a splitting or a frequency shift of a particular phonon mode [28]. In this case, we use spectroscopy under variable temperatures or magnetic fields to explore the spin-phonon coupling effect. By tracking the phonon frequency vs. temperature or magnetic field, we can extract the spin-phonon coupling constant through the Boltzmann sigmoid model [29–31].

In the higher frequency region, optical spectroscopy is performed to explore the on-site d to d and interband charge transfer excitations [Fig. 1.4]. The on-site d to d excitations usually reside in the energy range below the charge transfer gap. They are due to crystal field splitting, and a Tanabe-Sugano diagram predicts where on-site d-to-d excitations should manifest, depending on the crystal field symmetry around the metal ion. Charge transfer excitations determine the band gap of materials. First-principles calculations (when they are correctly calculated) including density of states and band structures provide insight into the electronic structure of a material. Comparison of the theory and experimental spectra can provide accurate assignments of electronic excitations in a site-specific manner and even reveal more complex phenomenon such as charge-ordering.

Magnetic circular dichroism is another spectroscopic technique, which focuses on revealing magneto-optical properties of materials in a site-specific manner. We do this work in visible optics range. The dichroic intensity is linearly proportional to the magnetization, which is also correlated to the joint density of states and even to specific bands [32, 33]. The dichroic response (change in $\alpha(E)$) is also correlated to the first-derivative of the linear absorption spectra, which provides a pathway to link magnetism with various electronic excitations.

In this work, I focus on revealing the spectroscopic properties of natural occuring and engineered superlattices under external stimuli like temperature, magnetic field, and chemical substitution. The materials of interest include intercalated transition metal dichalcogenides Fe_xTaS_2 and $(LuFeO_3)_m/(LuFe_2O_4)_1$ multiferroic superlattices. For Fe_xTaS_2, I investigate the spectroscopic signatures of chirality and spin-lattice coupling induced from the Fe intercalation. In the $(LuFeO_3)_m/(LuFe_2O_4)_1$ multiferroic superlattices, our work focuses on uncovering the microscopic origin of high tempearture magnetism and charge-ordering in a site-specific manner. My detailed findings are summarized in Table 1.1.

1.4 Main findings in Fe_xTaS_2 and multiferroic superlattices $(LuFeO_3)_m/(LuFe_2O_4)_1$

1.4.1 Electronic properties of Fe_xTaS_2

Figure 1.5 summarizes our spectroscopic findings in Fe_xTaS_2. We observed two separate free-carrier responses in Fe monolayer and TaS_2 slabs, respectively [Fig. 1.5 (d)]. Examining the electron density patterns verifies the existence of the weak free-carrier response between two neighbouring Fe domains [Fig. 1.5 (b)]. At higher energies, the spectra reveal several localized electronic excitations [Fig. 1.5 (e)]. Compared to the $Fe_{1/4}TaS_2$, the spectrum of the $x = 1/3$ compound shows a clustered excitation because the Fe conduction bands move up in energy and become more dispersive. Signatures of chirlity in the $Fe_{1/3}TaS_2$ are deeply embedded in the electronic structures. These include charge-density patterns that progress from triangular ($x = 0$) to Kagomé ($x = 1/4$) to honeycomb ($x = 1/3$) [Fig. 1.5 (b)], a hole → electron pocket crossover at the K point, and low-energy excitations between spin split bands that cross the Fermi surface [Fig. 1.5 (f)]. These findings advance the understanding of symmetry-breaking in quasi two-dimensional systems and are useful for the

Table 1.1: Scientific problems and important findings in this dissertation

Model Compound	Scientific Problem	Our Findings
Fe_xTaS_2 ($x = 1/4$ and 1/3)	• Revealing how metallic characters change with the intercalation concentration (x) • Investigating the spectroscopic signatures of chirality in $Fe_{1/3}TaS_2$	• Two Drude responses in Fe and TaS_2 layers • Electron density pattern transits from triangular to Kagomé to honeycomb with increasing x • A hole to electron pocket crossover at the K-point when structure changes from centrosymmetric to non-centrosymmetric • Low energy excitations between spin split bands in the non-centrosymmetric compound
Fe_xTaS_2 ($x = 1/4$ and 1/3), $Cr_{1/3}NbS_2$, and $RbFe(SO_4)_2$	• Revealing phonons of the intercalated Fe monolayer and spin-lattice coupling • Revealing the structural-property relations between different intercalated chalcogenides	• In- and out-of-plane monolayer excitations are identified, which display structural-property relations. Their frequencies depend on in-plane metal-metal distance, size of the van der Waals gap, and the metal-to-chalcogenide slab mass ratio • A mass ratio model to describe thresholds of monolayer excitation frequencies
$(LuFeO_3)_m/(LuFe_2O_4)_1$ superlattices (m = 3, 7, 9)	• Revealing the magnetic response of each individual Fe center • Revealing the origin of the bulk magnetism and high magnetic T_C • Revealing the structrual-property relations • Uncovering the interfacial magnetism • Determine the charge-ordering states in the (3,1) superlattice	• Site-specific optical hysteresis loops are obtained • Bulk magnetism derives principally from the $LuFe_2O_4$ layer • Interface dichroic spectra are extracted • Enhance magnetism and T_C come from the increasing Fe^{2+} and Fe^{3+} density of states in the spin-up channel • A non-polar Fe bilayer charge-ordering state with asymmetric Lu-layer distortion are determined

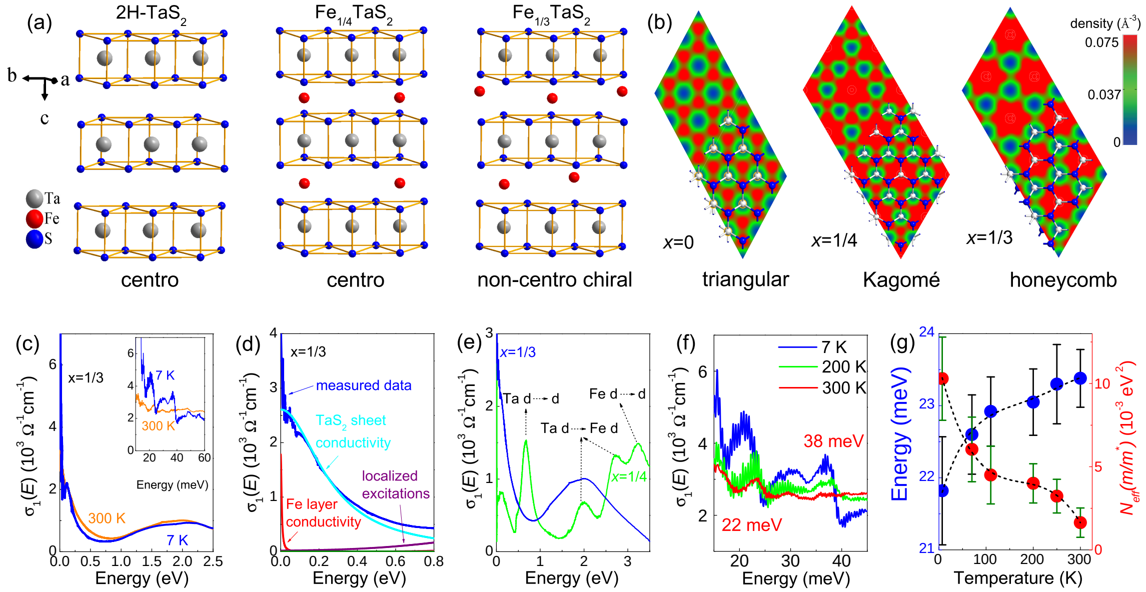

Figure 1.5: (a) Crystal structures of 2H-TaS$_2$, Fe$_{1/4}$TaS$_2$, and Fe$_{1/3}$TaS$_2$. (b) Electron density patterns of x = 0, 1/4 and 1/3 materials. (c) Optical conductivity of the Fe$_{1/3}$TaS$_2$ at 300 and 7 K. (d) Close-up view of using two Drude functions to fit the experimental spectra. (e) Optical conductivity of the x = 1/4 and 1/3 compounds. (f) Close-up view of the low energy electronic excitations. (g) Oscillator strength vs. temperature for the 22 and 38 meV modes.

development of low-symmetry multifunctional chalcogenides.

1.4.2 Phonon properties in Fe_xTaS_2 and their structural analogs

Figure 1.6 summarizes our Raman results. The Fe intercalation induces clear, strong, and coherent in- and out-of-plane intercalated monolayer excitations below 200 cm^{-1} [Fig. 1.6 (d)]. Those monolayer excitations are also observed in other intercalated transition metal dichalcogenides including $Cr_{1/3}NbS_2$ and $RbFe(SO_4)_2$ [Fig. 1.6 (d)], which indicates the intercalated metal monolayer excitations are intrinsic and gerneral. The frequencies of the metal monolayer excitations depend upon the metal-to-chalcogenide slab mass ratio [Fig. 1.6 (e)]. We developed a mass ratio model to provide a threshold frequency of the in- and out-of-plane monolayer excitations. Beyond this limit, interlayer interactions become comparable to intralayer interactions, the system behaves more like a standard multilayered material. The in- and out-of-plane excitations also reveal a strong spin-phonon coupling in the $Fe_{1/4}TaS_2$ material [Fig. 1.6 (f)]. These findings indicate the monolayer excitations are highly tunable by pressure or chemical substitution, which are potentially useful to design ultra low-frequency resonators.

1.4.3 Site-specific measurements of spin and charge in multiferroic superlattices $(LuFeO_3)_m/(LuFe_2O_4)_1$ (m = 3, 7, 9)

Figure 1.7 summarizes our spectroscopic findings in $(LuFeO_3)_m/(LuFe_2O_4)_1$. The dichroic spectra reveal several distinct Fe-related excitations at different energies [Fig. 1.7 (c)]. Fixed cuts at characteristic energies reveal optical hysteresis loops for distinct Fe sites [Fig. 1.7 (d)]. The extracted coercivity vs temperature Curves

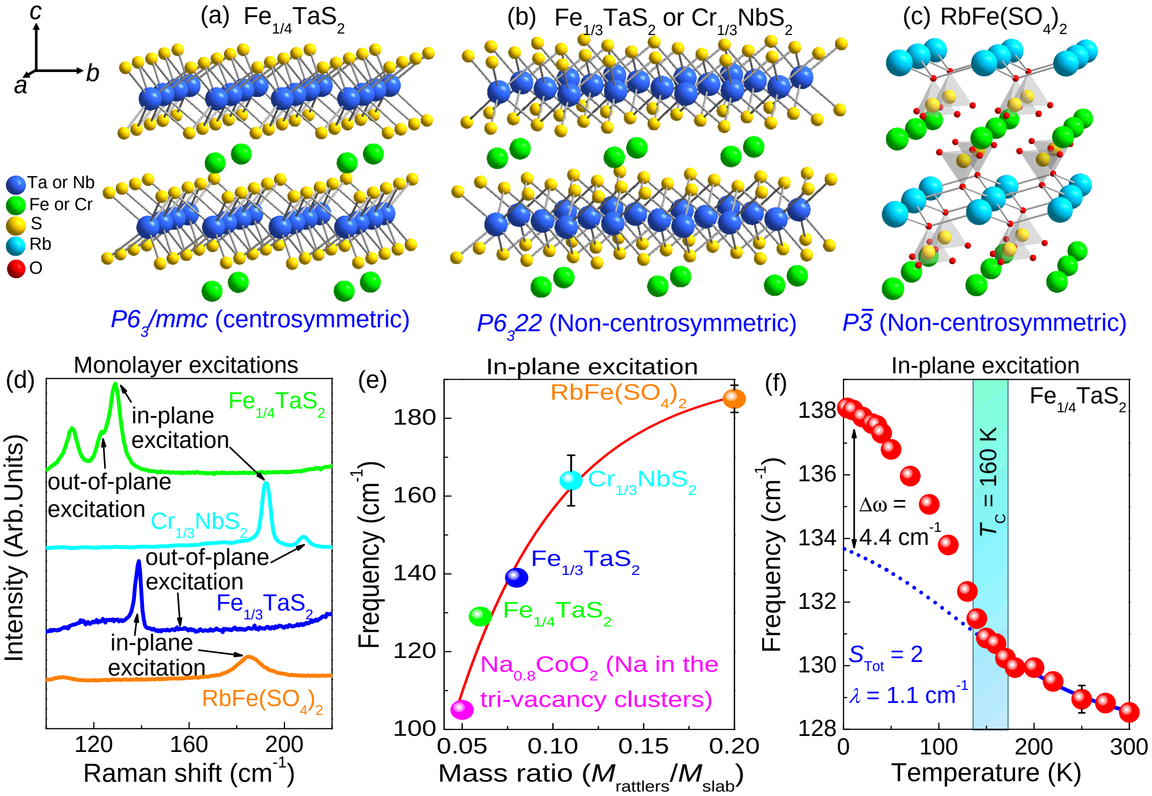

Figure 1.6: (a) Crystal structure of $Fe_{1/4}TaS_2$. (b) Crystal structure of $Fe_{1/3}TaS_2$ or $Cr_{1/3}NbS_2$ with a non-centrosymmetric space group. (c) Crystal structure of $RbFe(SO_4)_2$. (d) Intercalated monolayer excitations of different chalcogenides. (e) Frequency of the in-plane monolayer excitation vs. metal-to-chalcogenide slab mass ratio. (f) Frequency vs. temperature trend of the in-plane Fe monolayer excitation in the $Fe_{1/4}TaS_2$ material.

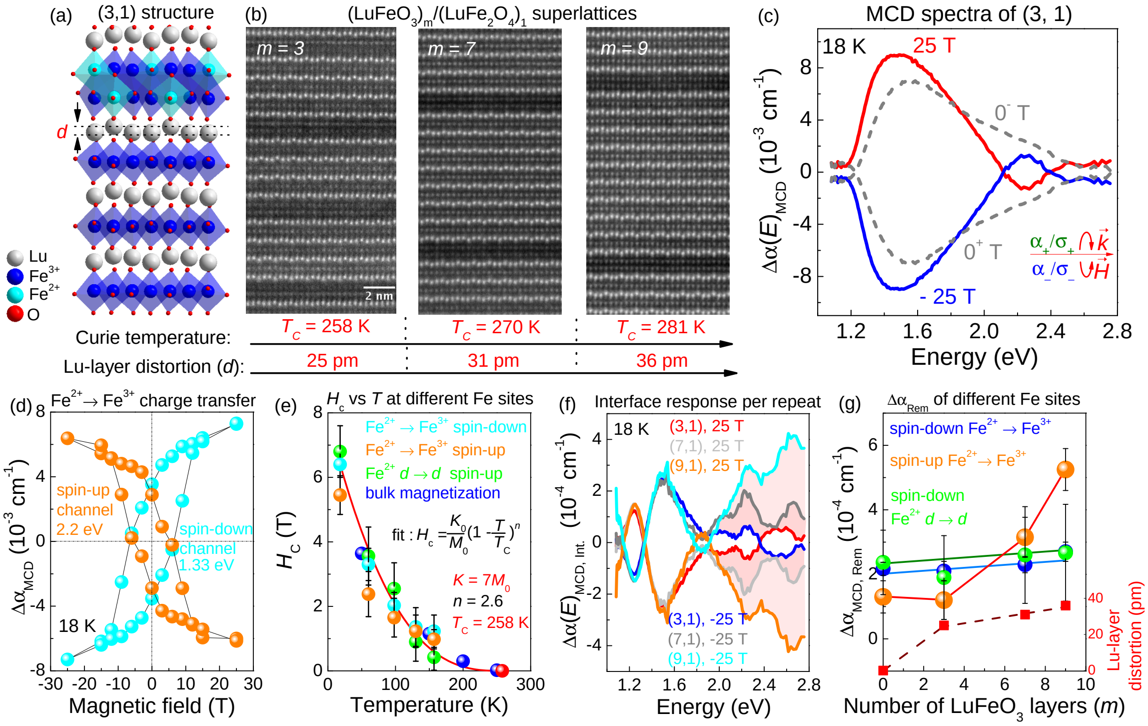

Figure 1.7: (a) Crystal structure of the (3, 1) superlattice. d represents the Lu-layer distortion. (b) STEM images of the (3, 1), (7, 1), and (9, 1) superlattices. Below displays the magnetic Curie temperatures and the amplitude of Lu-layer distortion for each superlattice. (c) Magnetic circular dichroism spectra of the (3, 1) superlattice at ± 25 T and 0 T. (d) Optical hysteresis loop of the spin-up and spin-down channel $Fe^{2+} \rightarrow Fe^{3+}$ charge transfer excitations. (e) Extracted coercivity vs temperature trend for all types of Fe-related excitations. (f) Extracted magnetic circular dichroic spectra of interfaces. (g) Remnant dichroic intensity as a function of superlattice periodicity (m) for different types of Fe-related excitations. The Lu-layer distortion vs m is also plotted to show the correlations.

indicate the bulk magnetism principally derives from the $LuFe_2O_4$ layer [Fig. 1.7 (e)]. We successfully extracted the interface spectra [Fig. 1.7 (f)]. The same energy cuts in the interface dichroic spectra reveal that the Lu-layer distortion at the $LuFeO_3$-$LuFe_2O_4$ interface selectively enhances the magnetization of the spin-up channel $Fe^{2+} \to Fe^{3+}$ charge transfer excitation [Fig. 1.7 (g)]. We also reveal a self-doped type charge ordering state in the (3,1) superlattice by comparing the theoretically calculated and experimental dichroic spectra. This charge ordering state contains asymmetric Lu-layer distortion and a non-polar Fe bilayers. These findings provide an insight of how interface rumpling couples to the magnetism in a local site, which advances the understanding of expanding the classes of multiferroics across a hetero-interface.

1.5 Outline

The remainder of the dissertation is organized as follows: Chapter 2 presents a literature survey of properties of multiferroics and transition metal dichalcogenides, as well as the other intercalated transition metal dichalcogenides systems. Chapter 3 discusses basics of infrared, Raman and optical spectroscopies, as well as magnetic circular dichroism. Theories of how light interacts with matter, sample preparation, and other experimental and theoretical techniques are introduced as well. Chapter 4 and 5 present our spectroscopic findings of Fe_xTaS_2, including both electronic and vibrational properties. Chapter 6 gives the details of how we perform a site specific measurement of spin and charge in high temperature multiferroic superlattices $(LuFeO_3)_m/(LuFe_2O_4)_1$. Chapter 7 summarizes my work.

Chapter 2

Literature survey

2.1 Multiferroic materials

Materials with ferroic order can display interesting physical properties because their order parameters can be switched by a conjugate field [35–37]. There are four primary ferroic terms: ferromagnetic, ferroelectric, ferroelastic and ferrotoroidic order. Figure 2.1 displays the schematic view of these primary ferroic orders. Ferromagnetic materials exhibit a spontaneous magnetization, the direction of which can be switched by the external magnetic field. The spontaneous magnetization is due to breaking of the time-reversal symmetry. Ferroelectricity displays a spontaneous polarization in the materials. Electric field can be applied to switch the polarization direction. Spatial inversion symmetry has to be broken for a ferroelectric material. Similarly, ferroelasticity corresponds to a spontaneous lattice strain. However, ferroelasticity does not require to break either time-reversal or spacial inversion symmetry. Ferrotoroidicity is more complex, it related to a spontaneous magnetic vortex, which can generate a "toroidal moment". In general, a toroidal - like moment is formed by N $\geq$ 2 spins per unit cell. It originates from two pairs of spins yielding oppositely oriented toroidal moments of different amplitude. A spontaneous uniform alignment

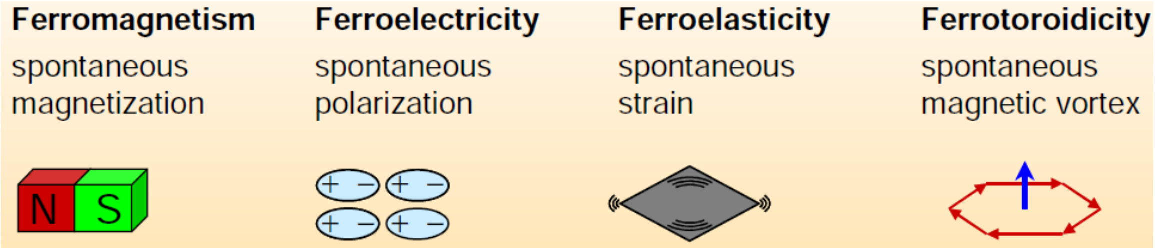

Figure 2.1: Schematic view of the four types of primary ferroic orders [37].

of toroidal moments is the basis of a ferrotoroidic state [38]. Ferrotorodicity requires breaking both spacial inversion and time reversal symmetry. The symmetry requirement for all types of ferroic orders are summarized in Table 2.1.

Multiferroic materials are defined by simultaneously exhibiting two or more ferroic, ferrioic or antiferroic ordering parameters. They attract broad interest to researchers because of the cross-coupling between different ferroic orders, which has a great potential for the device applications. In this chapter, we particularly focus on the magneto-electric multiferroic materials, which is a specific type of materials that combine ferroelectricity and magnetic behaviors.

2.1.1 Cross-coupling in multiferroics

The most interesting phenomenon in multiferroics is the cross-coupling between different ferroic order parameters. Figure 2.2 displays a schematic view of using various external stimulus to control the phase in multiferroics. In a ferroic material, P, M, or σ are spontaneously formed to produce ferromagnetism, ferroelectricity, or ferroelasticity, respectively. In a multiferroic, the coexistence of at least two ferroic forms of ordering leads to additional interactions. For example, interactions between the ferroelectricity and magnetic ordering induce magnetoelectric effect, which means the electric polarization can be switched by magnetic fields, or the induction of magnetization by an electric field. The interaction between lattice strain and electric dipole moment leads to piezoelectricity. As a result, multiferroics may lead to faster, smaller, more energy-efficient data-storage technologies.

The most important type of multiferroics is magnetoelectric materials. These materials attract broad research interest because of their huge potential for making new device architectures. Although multiferroic materials can display both ferroelectricity and magnetism in a single phase, they are not always coupled because

Table 2.1: Spatial-inversion and time-reversal symmetry in ferroics

Ferroic orders	Spatial-inversion symmetry ?	Time-reversal symmetry ?
Ferromagnetism	Yes	No
Ferroelectricity	No	Yes
Ferroelasticity	Yes	Yes
Ferrotoroidicity	No	No

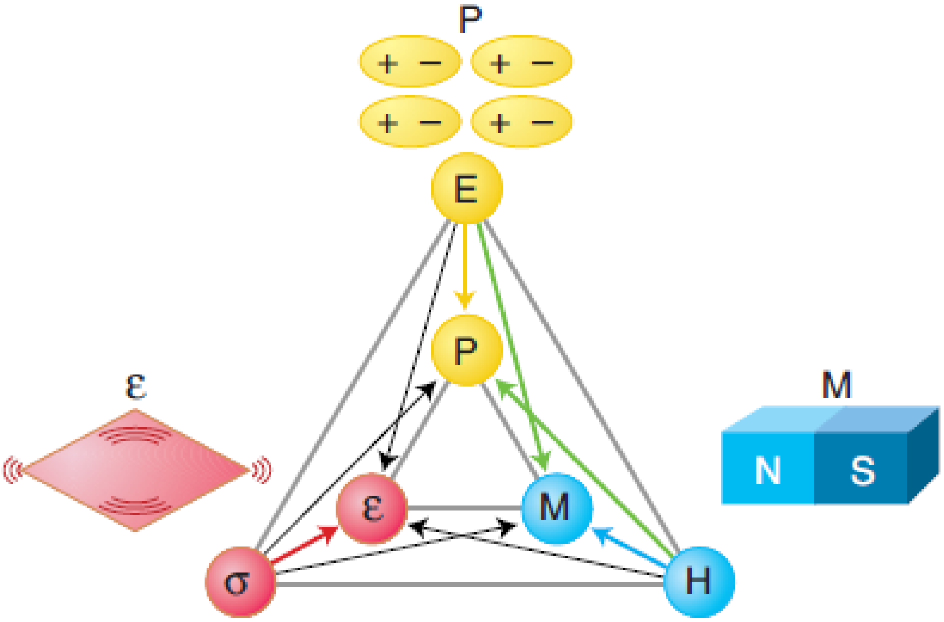

Figure 2.2: A schematic diagram shows how magnetic field H, electric field E, and stress σ control the magnetization M, electric polarization P, and lattice strain ϵ, respectively. The cross coupling between different ferroic orders leads to an electric field controlled magnetization and a magnetic field controlled electric polarization (green arrows). Figure is taken from Ref 39.

of the contradiction of the mechanism between ferroelectricity and magnetism [40–42]. As a result, the magnetoelectric coupling is the most interesting effect in multiferroics.

From the mathematical perspective, the free energy of a system can be described by Landau's expression:

$$F(E,H) = F_0 - P_i^s E_i - M_i^s H_i - \frac{1}{2}\epsilon_0 \chi_{ij}^e E_i E_j - \frac{1}{2}\mu_0 \chi_{ij}^v H_i H_j - \alpha_{ij} E_i H_j - \cdots \quad (2.1)$$

where, P_i^s = - $\frac{\partial F}{\partial E_i}$, M_i^s = - $\frac{\partial F}{\partial H_i}$, and $\alpha_{ij} = \frac{\partial P_i}{\partial H_j} = \frac{\partial M_i}{\partial E_j}$, P_i and M_i are the static electric polarization and magnetization, and α_{ij} is the linear magneto-electric coupling coefficient.

2.1.2 Magnetoelectric multiferroics

Magnetoelectric materials are very rare in nature. The reason is that the existence of both ferroelectricity and ferromagnetism is, in itself, a contradiction (typically, ferroelectricity and magnetism are mutually exclusive) [40–42]. One simple reason is that ferroelectic materials are typically insulators to maintain a sustainable electric polarization, whereas ferromagnetic materials are usually metals. However, this is not the case for materials with ferrimagnetic or antiferromagnetic ordering, which are typically insulators. The more in depth reason is the so called ferroelectric "d^0" rule [42]. Ferroelectric materials must undergo a phase transition to eliminate the center of symmetry. In conventional ferroelectric materials, the polarization arises when nonmagnetic cations shift away from the center of their surrounding anions. This uneven displacement, or noncentrosymmetry, between positive and negative charges is what gives rise to an electric dipole moment. Magnetic cations, however, tend to sit exactly at the center of the surrounding anions, in centrosymmetric positions, such that no dipole moment forms. This can be understood by the occupancy of *d* orbitals. The non-magnetic cation has empty *d* shells (d^0-orbital). Energy of the covalent or ionic bonding is much larger than the Coulomb interaction in the non-magnetic cation, this generates an electric dipole moment that leads to a polarization. As a result, the non-magnetic cation tends to move off-center to favor the ferroelectricity. In contrast, in magnetic materials, the magnetic cation requires a partially occupied *d* orbital, the Coulomb repulsion between electrons is larger than the bonding energy, which prohibits the ions to move out of center. This contradiction explains why magnetic ferroelectric is so rare in nature. The ferroelectric d^0 rule can be broken if details of chemistry or structure create an asymmetric potential with a double potential well in spite of the *d* occupation of the magnetic cation [42], however, synthesis the magnetoelectric multiferroics with this type are not easy. This mechanistic picture is developed for ABO_3 perovskites.

Multiferroics can be classified as two different types according to whether the ferroelectric and the magnetic transition temperatures are the same or not. Type I multiferroics corresponds to materials with different transition temperatures. The most famous example is $BiFeO_3$ [43, 44]. This material has the perovskite structure where Bi occupies the non-magnetic A-site and Fe occupies the B-site. The A-site cation moves off-center, breaking the inversion symmetry and brings ferroelectricity; the Fe atoms display antiferromagnetic ordering below the magnetic Curie temperature. The material is categorized as a proper ferroelectric (Type I), because the ferroelectricity is not caused by the magnetic ordering. As a result, the ferroelectric and magnetic transition temperatures are different. The disadvantage of Type I multiferroics is that the magnetoelectric coupling is weak due to the different machanism of ferroelectricity and magnetic ordering. Type II multiferroics displays the same transition temperature for ferroelectricity and magnetic ordering. They are categorized as the improper ferroelectrics as the magnetic ordering breaks the inversion symmetry and induces electric polarization. Type II multiferroics exhibits large magnetoelectric coupling, however, the transition temperature is usually not high enough. One famous example of the Type II multiferroics is $TbMnO_3$ [45]. Clearly, the most challenging work in the field of multiferroics is to systhesis materials that can combine large magnetoelectric coupling and high transition temperatures.

2.1.3 Mechanisms supporting multiferroicity

The mechanisms that support multiferroicity are quite complicated. Ferroelectricity can be driven by four typical mechanisms: electronic lone pairs, geometric effects, charge-ordering and magnetism. In the first three cases, the magnetic and ferroelectric orders are not strongly coupled, and occur independently. The multiferroics with these three mechanisms are denoted as Type I. For the last case, the ferroelectric and magnetic transitions emerge jointly and are strongly coupled. This mechanism supports for the type II multiferroics.

Lone-pair mechanism: Lone-pair mechanism is first proved in the most famous single-phase multiferroic $BiFeO_3$ [37, 46]. Lone-pair ferroelectricity is based on the spatial asymmetry created by anisotropic distribution of unbounded valence electrons around the host ion (Fig. 2.3a). In $BiFeO_3$, the large electric polarization is driven from a pair of Bi^{3+} valence electron, in the 6*s* orbital, which is not involved in the *sp* hybridization. This lone-pair electron create a local dipole moment that induces polarization of of 100 μCcm^2 below the ferroelectric Curie temperature ($T_C = 1103$ K) [47]. Fe 3*d* electrons contribute to the antiferromagnetism in the system with $T_N = 643$ K [48]. Among the lone-pair systems, $BiFeO_3$ is the only room-temperature single-phase multiferroic material [37]. Magnetoelectric coupling is observed in this

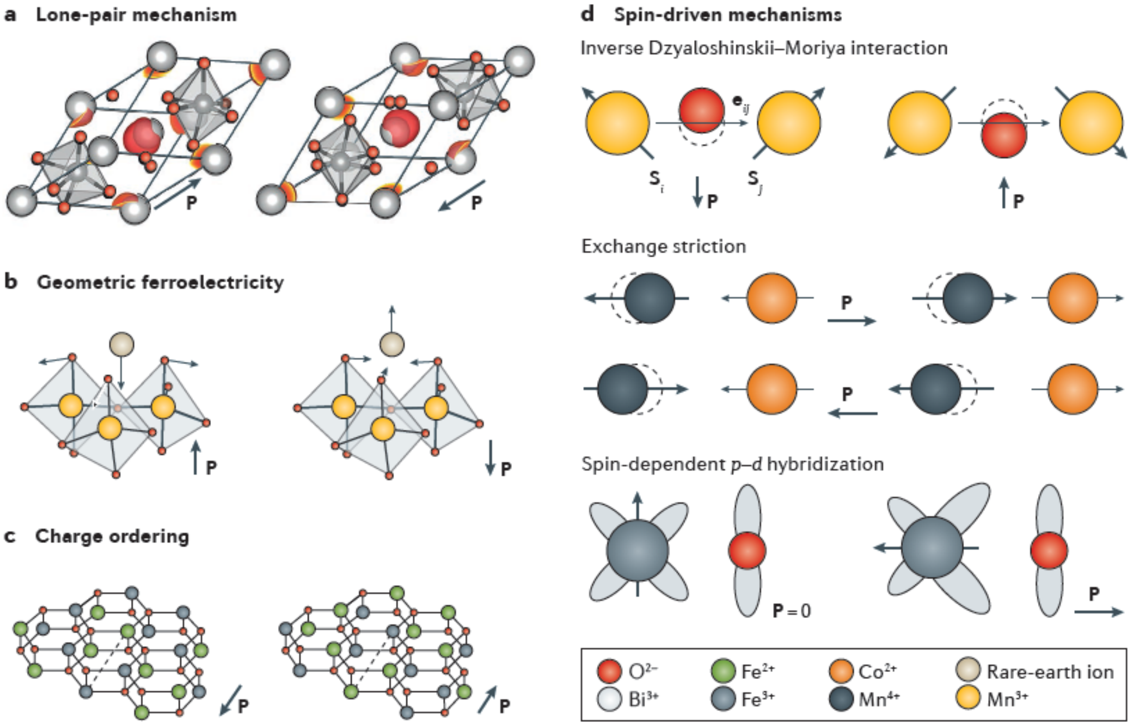

Figure 2.3: **a**, Lone-pair ferroelectricity in $BiFeO_3$. The isosurface (red) of the electron localization function illustrates the lone-pair. **b**, A tilt and deformation of MnO_5 bipyramids induces geometric ferroelectricity in h-$RMnO_3$. **c**, Charge ordering in $LuFe_2O_3$ creates alternating layers with Fe^{2+} / Fe^{3+} ratios of 2:1 and 1:2. This can create a spontaneous polarization between the two layers. **d**, Mechanisms for spin-induced ferroelectricity [37, 49]. Figure is taken from Ref 37.

material, however, the coupling strength is not strong due to the different origins of ferroelectricity and magnetism.

Geometric ferroelectricity: Geometric ferroelectricity is caused by space-filling effects. Geometric constraints can cause structural instabilities in materials. If such steric effects, rather than bond chemistry, lead to ionic shifts that result in the formation of a polar state, the term geometric ferroelectricity can be used [37]. In geometric multiferroics, the small non-magnetic cation (in the A-site) allows for a rotation or tilt of the polyhedra centered with the B-site cation, which often accompanies with the shift of the A-site cation that generates the polarization. Since the rotation or tilting of the polyhedra can induce a canted magnetism, this mechanism offers a coupling between polarization and magnetism.

Depending on whether the spontaneous polarization is the primary order parameter or as a secondary consequence from a lattice distortion, ferroelectric materials can be identified as a proper or improper type, respectively. One example of proper ferroelectrics is $BaMF_4$ (M = Mn, Fe, Co, or Ni). The ferroelectricity of this family of materials originate from the softening of a single polar phonon mode, which involves both rotational motions of the fluorine octahedra and polar displacements of the Ba cations [50]. Since the distortion is polar in nature, this family of materials represent a confirmed example of the proper geometric ferroelectrics. One famous example of improper ferroelectrics is hexagonal phase rare-earth manganites $RMnO_3$, in which the ferroelectricity comes from a coupling between unstable zone-boundary mode with a stable zone-center mode [51]. Figure 2.3b illustrates this mechanism. Since the ferroelectricity is not directly caused by a polar distortion, this material is a typical improper ferroelectric. The h-$LuFeO_3$ thin film in this dissertation is the improper multiferroic, due to this mechanism.

The magnetoelectric coupling of the geometric ferroelectrics are usually larger than that from the lone-pair mechanism due to the structural distortion can cause a canted magnetism in the system. However, for improper ferroelectrics, it is challenging to switch the polarization by electric field because the electric field is not a conjugate field for polyhedral rotations. As a result, understanding the fundamental mechanism of polarization switching in such improper ferroelectrics is a key next step, alongside the development of improved proper geometric ferroelectrics [46].

Charge-ordering: Charge-ordering is another mechanism to support ferroelectricity. Valence electrons can be distributed non-uniformly around their host ions in the crystal lattice to form a periodic superstructure [37]. The most famous material with the charge-ordering mechanism is $LuFe_2O_4$. This material has the Fe double layers with alternatively ordered Fe^{2+} and Fe^{3+} sites [Fig. 2.3] [34]. The unequal distribution of charge inside the Fe bilayers induces an internal electric polarization. Although there are some studies questioned about the ferroelectricity in $LuFe_2O_4$ [20, 242], a charming development in charge-ordered multiferroics is the establishment of a polar charge-ordered state below 100 K in the first technologically relevant magnet, ferrimagnetic magnetite, Fe_3O_4 [46, 52]. For now, charge order-driven multiferroicity essentially remains at the stage of an interesting concept.

Spin-driven mechanisms: The magnetic ordering can also break the spatial inversion symmetry of the lattice and induce the ferroelectric polarization. The interaction of spins and charges may transfer the non-centrosymmetry from the magnetic to the electric lattice, driving the formation of a polar state [37]. Since the ferroelectricity is a secondary effect from the magnetic ordering, multiferroics with this mechanism is improper ferroelectrics. There are three main types of the spin-driven mechanisms.

The first type of mechanism is called inverse Dzyaloshinskii-Moriya (DM) interaction. The term DM interaction describes an antisymmetric exchange between two magnetic ions through a third ion, which breaks the inversion symmetry with respect to the two magnetic ions and causes a canting of the collinear spins through the spin-orbit interaction [53]. The inverse DM interaction is the exact opposite effect, where the canted spin structure drives a non-centrosymmetry displacement of charges by minimize the lattice energy. This can cause the electric polarization. Multiferroics with this type of mechanism was first found in Cr_2BeO_4 and $TbMnO_3$ [45, 54].

Other than the inverse DM interaction, exchange striction is another type of the spin-driven mechanism. This type of mechanism describes the symmetric exchange for a collinear spin structure. The collinear magnetic ordering can cause an acentric displacement of charges by optimizing the spin product $\mathbf{S}_i \cdot \mathbf{S}_j$, which induces a ferroelectric polarization [Fig. 2.3d] [55]. Since this interaction is much stronger than the DM interaction, the electric polarization induced by this mechanism is usually an order of magnitude larger than that originates from the inverse DM interaction. One of the example is o-$TbMnO_3$, where the polarization amplitude dramatically increases during the magnetic transition from a canted mangetic state to a collinear antiferromagnetic state under pressure [56].

The third type of the spin-driven mechanism is through the spin-dependent $p - d$ hybridization [37, 49, 57, 58]. Other than the inverse DM interaction and exchange striction, which describe the electric polarization induced from the spin-spin correlation, this mechanism only corresponds to the single spin. The spin-dependent p–d hybridization mechanism is based on the fact that the locally polar bond e_{il} connecting the spin site i and the ligand site l can be modulated by the spin-direction dependent hybridization arising from the spin-orbit coupling [49]. The polarization is proportional to $(\mathbf{S}_i \cdot \hat{e}_{il})^2 \hat{\mathrm{e}}_{il}$, where $\hat{\mathrm{e}}_{il}$ is the unit vector that connects the transition metal and ligands. Some examples of this mechanism include $Ba_2CoGe_2O_7$ [57] and $CuMnO_2$ (M = Fe or Cr) [58].

Overall, the spin-driven multiferroics usually display small polarization because the ferroelectricity is a secondary effect, in this case, materials with this mechanism are usually Type II multiferroics. On the other hand, the magnetoelectric coupling in the spin-driven multiferroics are strong, which leads to potential device applications. However, the main challenge that prevents the development in this direction is the low magnetic transition temperatures.

2.1.4 Heterostructure multiferroics

Figure 2.4 summarizes multiferroics with different types of mechanisms. For application purposes, the dream is to make multiferroics that can display strong magnetoelectric coupling and high transition temperatures at the same time. It is extremely challenging to combine those two factors into the conventional single-phase multiferroics because of the contradiction between the mechanism of ferroelectricity and magnetism. A new direction is to make composite multiferroics by artificially combining a non-magnetic ferroelectric (such as $BaTiO_3$) and a non-ferroelectric magnet (such as $CoFe_2O_4$). This attracts a lot of research attention recently. The $(LuFeO_3)_m/(LuFe_2O_4)_n$ superlattices in this work belongs to this composite multiferroics family.

Oxide thin films can be grown layer by layer with atomic scale precision, thus much more accurately and controllably than bulk crystals. The idea is to grow materials with certain properties by applying heteroepitaxy growth on a proper substrate. In particular, the effects of strain and interfaces in thin-film architectures are important because they can influence the ferroelectric and magnetic properties profoundly. The interfaces between different phases can either transfer the interaction between the constituents of the system or have an active role in determining the properties of the material [37].

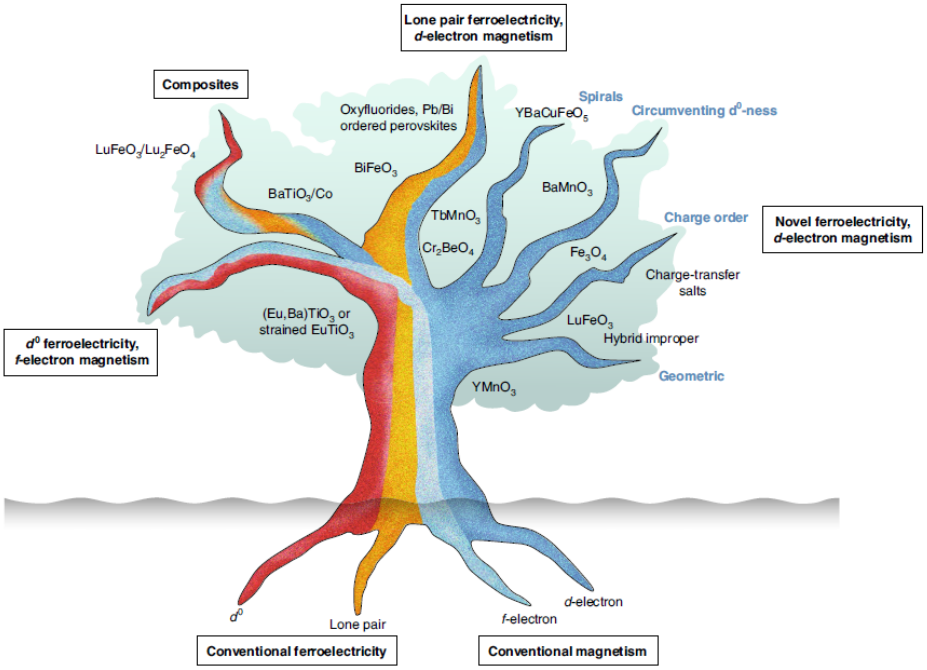

Figure 2.4: Multiferroicity, arising from the combined interplay of magnetic and ferroelectric mechanisms, can result from several different sources. Here, we outline different combinations of these 'root' mechanisms and how they are responsible for different types of multiferroic materials. This visualization shows the combinations of magnetic and ferroelectric mechanisms that occur in existing multiferroics, and also suggests less explored options that may prove fruitful in the future. Figure is taken from Ref 46.

Epitaxial strain: Heteroepitaxy growth usually accompanies with large epitaxial strains due to the lattice mismatch between the film and its substrate. Controlling the epitaxial strain is useful to moderate the properties of thin films and induce phase transitions. For example, strain was used to demonstrate the correlation between ferroelectric and magnetic spiral order in $BiFeO_3$ thin films [59]. Strain can also induce the ferroic orders in non-ferroic compounds. For example, polar order and ferromagnetism are induced in $SrTiO_3$ [60] and $LuMnO_3$ [61] films, respectively. Furthermore, strain can be used to couple ferroelectric domains to ferromagnetic domains across an interface through magnetostrictive and magnetoelectric coupling [Fig. 2.5] [37, 62, 63]. A typical example with this effect is in the CoFe–$BaTiO_3$ superlattice, where the anisotropy and ordering temperature of interfacial magnetism can be controlled by electric fields [64].

Interface enhanced functionality: In heterostructure multiferroics, studying the interface is very important to understand the origin of multiferroicity. In composite multiferroics, the interface between two components usually displays low local symmetry, confinement effects, strain gradients, domain walls and chemical anisotropy [Fig. 2.6] [37]. Typical examples of multiferroicity induced by the interface interaction is found in the $BaTiO_3$ thin film [65]. The interface can break the spatial inversion symmetry and induce ferroelectricity [1], however, it does not break the time-reversal symmetry. In this case, understanding how interface affects the magnetic properties is the key to develop new strongly coupled multiferroics. In this work, we performed a magnetic circular dichroism measurement on room temperature multiferroic $(LuFeO_3)_m/(LuFe_2O_4)_n$ superlattices to resolve the interface magnetism.

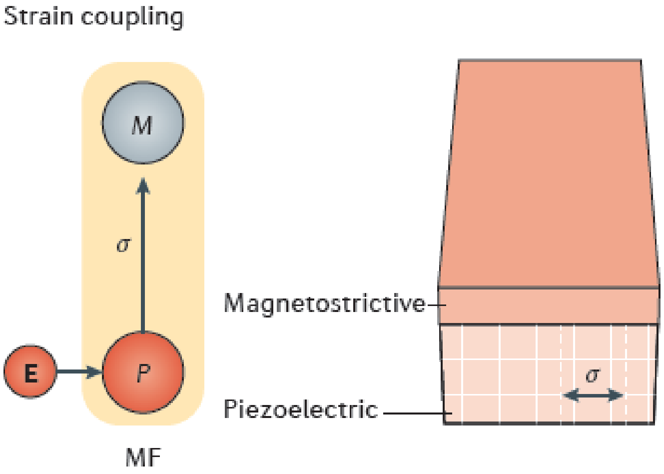

Figure 2.5: the magnetoelectric coupling between a piezoelectric and magnetostrictive constituent is established via strain σ [37].

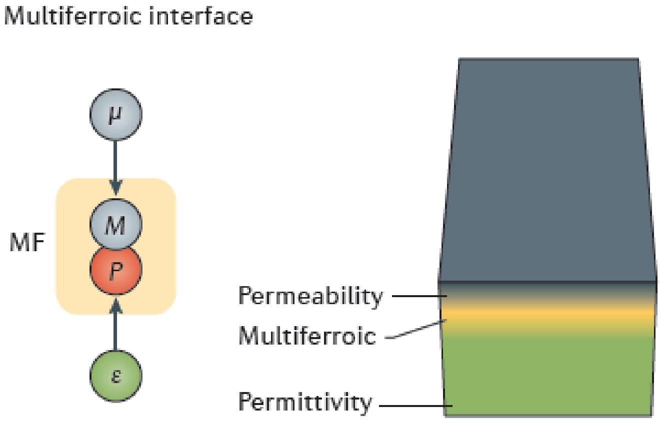

Figure 2.6: In 2D confined multiferroics, only the interface between two material phases is multiferroic. In this figure, these phases are the permittivity, , and permeability, , states of different compounds, and multiferroicity emerges as an interface effect. Figure is taken from Ref 37.

2.1.5 Domain and domain walls

Domains are regions with a uniform orientation of the relevant order parameter (polarization or magnetization in multiferroics). A typical ferroic material consists of multiple domains. Between two neighbouring domains, the interface region with the lower symmetry is called domain walls. They denote the region across which the order parameter reorients between adjacent domains. The width of domain walls are usually on the order of tens of nanometers.

Domains and domain walls are crucial for the control of many material properties, such as coercivity and resistance [37]. Since bulk multiferroics consist of many domains, understanding the magnetoelectric coupling between an individual magnetic domain and a ferroelectric domain is important. This gives us a microscopic approach to understand the cross-coupling in multiferroics. Scanning-probe and electron-microscopy techniques pushed the resolution of domain imaging to nanoscale, which makes it possible to study domain walls. At the walls, spin or charge dynamics can be quite different compared to the domains, the famous example is the observation of electrical conductivity at the ferroelectric domain walls in $BiFeO_3$, while all nearby domains are insulating [66–68]. This finding opened an entirely new avenue of research into novel functionalities at multiferroic domain walls motivated by the prospect of metallic transport through nanoscale channels that can be electrically written, erased and moved [69, 70].

Besides the electronic properties of the domain walls, new techniques have been developed recently to study the phonon behavior at the domain walls. Traditional phonon-probe techniques such as far-field infrared spectroscopy only provides an average response and unable to address the nano-scale heterogeneities of domain walls due to its poor spatial resolution. Recently, scientists successfully combined atomic force microscopy and near-field infrared spectroscopy to detect the local phonon behavior at the domain walls in $Ca_3Ti_2O_7$ [8]. This allows for a microscopic analysis of how centain vibrational mode changes with the rotation of structural order parameters [Fig. 2.7].

2.2 Intercalated transition metal dichcogenides

2.2.1 Transition metal dichalcogenides

Two-dimensional materials attracts broad research interest because of their fascinating physical properties and potential applications in the semiconductor industry. The first two-dimensional material that was obtained is graphene [71], which is a well known 2D material which displays unprecedented electronic, mechanical, thermal, and optical properties. Transition metal dichcogenides is another important type of materials in the two-dimensional material's family. The chemical formula is of the form MX_2, where M stands for a transition metal (such as Mo, W, Ta, Nb) and X represents a chalcogen element, such as S, Te, or Se. Compare to graphene, transition metal dichalcogenides consist of more than one element, which makes their lattice dynamics more complicated. These group of materials display interesting electronic and optical properties, and they are also very sensitive to external stimulus such as strain, pressure or temperature. Furthermore, the physical properties in transition metal dichalcogenides are layer dependent, involving a transition from an indirect gap for multi-layer samples to a direct gap for single-layer samples [72–76], pointing out the important role of interlayer hopping of carriers in these compounds. The most used method to obtain monolayer transition metal dichalcogenides and graphene is by mechanical exfoliation [Fig. 2.8].

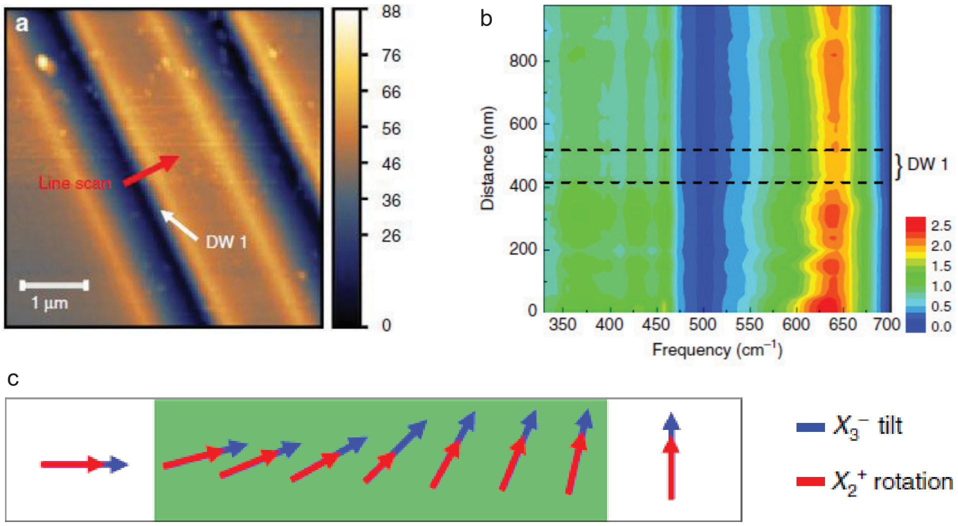

Figure 2.7: a. Atomic force microscopic (AFM) images of the crystal surfaces showing the two ferroelastic domain walls of interest. b. Contour plots of the near-field amplitude normalized to a gold reference across the ferroelastic domain wall. c. Order parameter space. The order parameters for the X_3^- octahedral tilt and X_2^+ octahedral rotation are shown with blue and red arrows, respectively. Figure is from Ref 8.

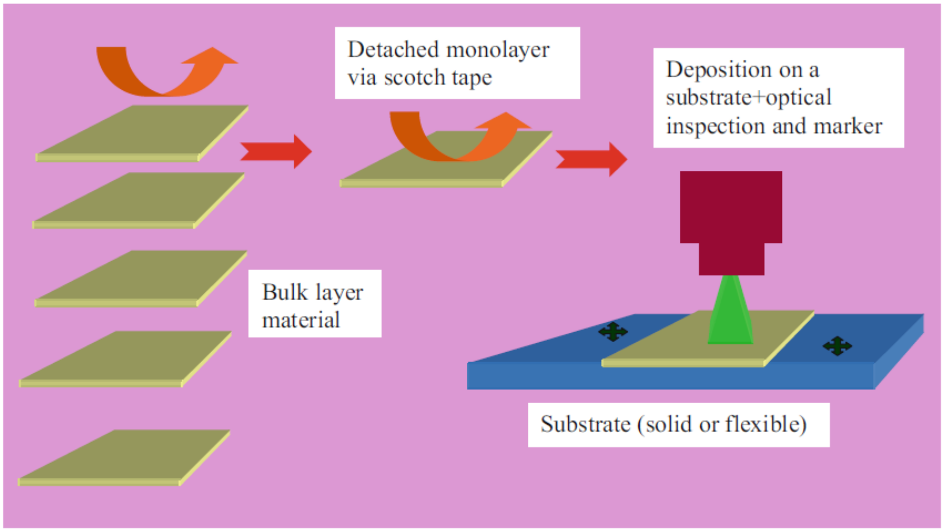

Figure 2.8: Schematic diagram that shows the mechanical exfoliation method to obtain two-dimensional materials [77].

2.2.1.1 Crystal structures of transition metal dichalcogenides

Transition metal dichcogenides have many polytypes, the three typical structures are 1T, 2H, and 3R, where T represents trigonal, H means hexagonal, and R stands for rhombohedral. The number 1, 2, 3 refers to the number of layers in an unit cell. Figure 2.9 displays the difference between those three structural phases. For the 2H and 3R phases, the transition metal occupies the center of the trigonal prism formed by six chalcogen atoms. The upper triangle is the mirror image of the bottom triangle in each prism. The transition metal center can also has an octahedra environment, where the bottom triangle is the inversion of the top triangle in an unit cell. This structure configuration represents for the 1T phase. The electronic and optical properties are very different between the trigonal prismatic symmetry and octahedral coordination of metal atoms. For example, strong charge density waves are observed in the 1T-TaS_2 system, while in the 2H phase, the charge density wave has been dramatically suppressed [78, 79]. For monolayer MoS_2, the 2H phase is semiconducting while 1T phase is metallic [80, 81].

Figure 2.10 displays the schematic of the in-plane two-dimensional Brillouin zone of MX_2. The Γ, M, and K are three high symmetry points. The six Q points correspond to the minimum of the conduction band for multi-layer samples. The electronic properties at the different symmetry points are closely related to the specific crystal structures, which we will discuss in later sections.

The MX_2 group of materials usually display a large crystal anisotropy. In the MX_2 slabs, the atoms are strongly bonded; Between the layers, the slabs are weakly bonded by the van der Waals force. This gives a possibility to intercalate transition metal centers into the van der Waals gap, which will form different superstructures depending on the doping concentration. The intercalation boosts the dimensionalty and dramatically changes the physical properties. We will talk about this effect in

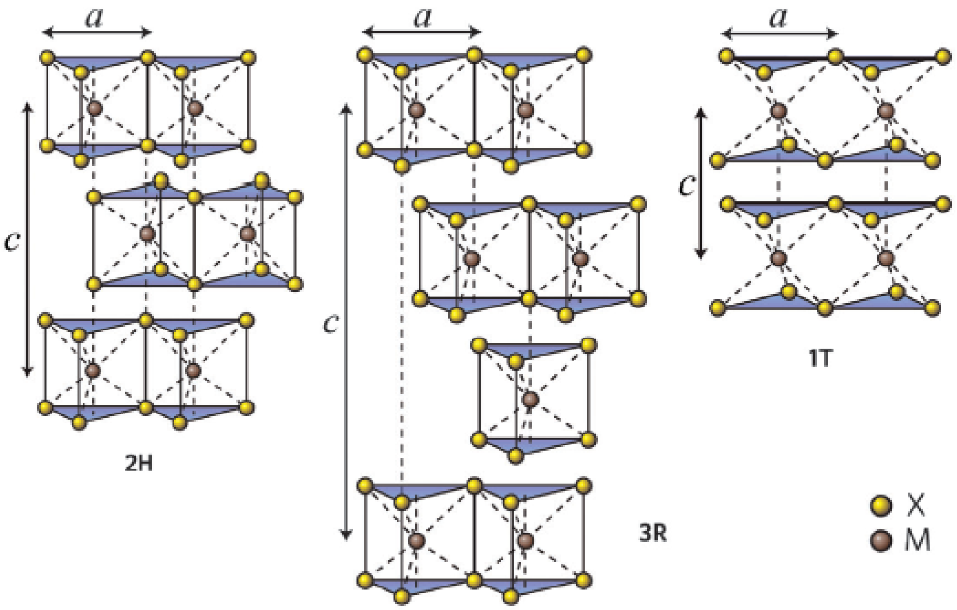

Figure 2.9: Schematic view of the 2H, 3R, and 1T phases in transition metal dichalcogenides. a and c represent the lattice constants [82, 83].

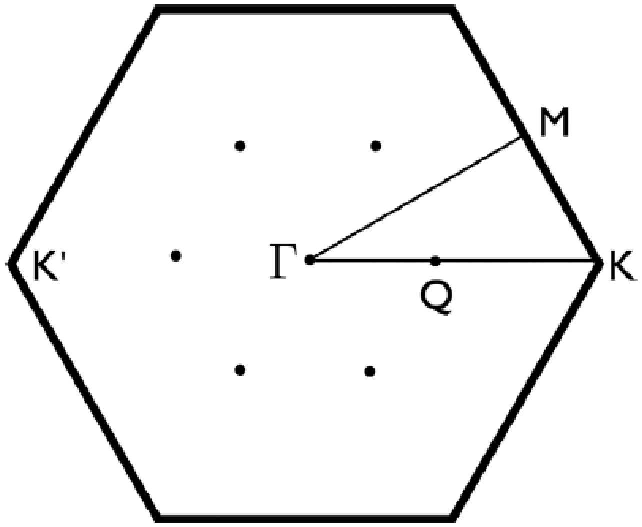

Figure 2.10: Two-dimensional Brillouin zone of MX_2. The high-symmetry points $\Gamma =$ (0,0), $M = \frac{4\pi}{3a}$ $(0,\frac{\sqrt{3}}{2})$ and $K = \frac{4\pi}{3a}$ (1,0) are shown. The Q points (which are not high symmetry points) indicate the position of the conduction band edge in multi-layer samples. Figure is taken from ref 84.

detail in later sections.

2.2.1.2 Electronic properties of transition metal dichalcogenides

Based on the electronic properties, transition metal dichalcogenides (TMDs) can be classified as two groups: metallic or semiconducting TMDs. Metallic TMDs (such as TaS_2) display interesting coexistence of charge density waves and superconducting phase at low temperatures, which originates from strong electron-phonon coupling [85]. Semiconducting TMDs (such as MoS_2), exhibit layer-dependent band gaps, which can be tuned by external strain field [86]. In this subsection, we will introduce the electronic, transport, and vibrational properties of these two classes of TMDs. The work in this dissertation mainly focuses on the metallic transition metal dichalcogenides.

Metallic tranisition metal dichalcogenides Metallic TMDs such as TaS_2, NbS_2, $TaSe_2$ and $NbSe_2$ are an important branch in the transition metal dichalcogenides family. In their electronic structures, the Fermi level is always crossing a band with *d*-orbital character, implying that the electrons move mostly in the chalcogenide slabs [87]. The density of states at the Fermi level is usually quite high. The most interesting physics in the metallic transition metal dichalcogenides is the coexistence of charge density waves (CDW) and the superconducting phase at low temperatures. One ideal platform to study the charge density wave transitions is TaS_2 [78,79,88,89].

TaS_2 has two stable phases: 1T and 2H. The electronic structure of these two phases are very distinct. The former is a semiconductor at room temperature, which displays several different charge density waves transitions that depend on both temperature and sample thickness. The latter is a metal with the charge density wave transition at 78 K and the superconducting transition at 1 K [79, 89]. Figure 2.11 displays different charge density wave states in 1T-TaS_2. The crystal structure is

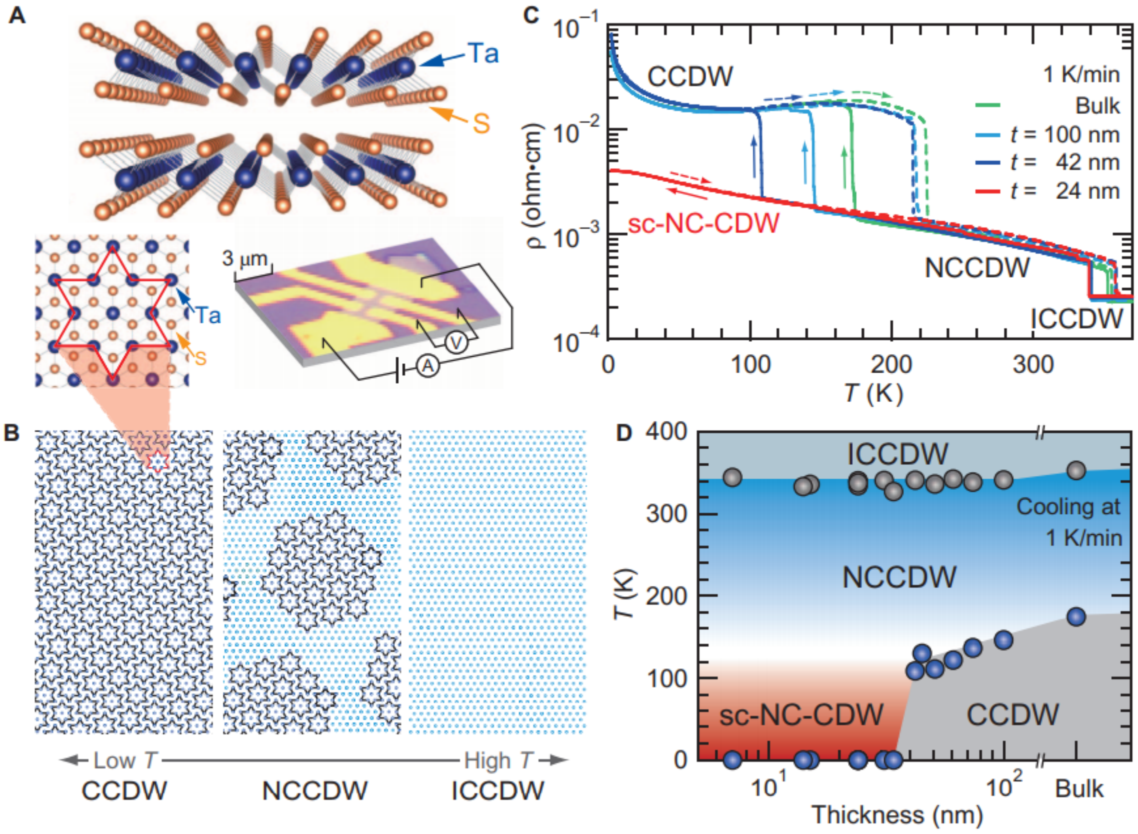

Figure 2.11: (A) The side and top view of the crystal structure of 1T-TaS$_2$. Also shown is the optical microscope image of a typical nano-thick crystal device. (B) Schematic pictures of a Ta atom network in the CCDW (left), hexagonal NCCDW (middle), and ICCDW (right) phases. The dark blue circles represent the Ta atoms displaced from their undistorted lattice coordinates, forming the David-star clusters. (C) Temperature dependence of the resistivity for bulk and nano-thick crystals of 1T-TaS$_2$. The solid and broken lines represent the cooling and warming cycle, respectively. The notation sc-NCCDW represents supercooled NCCDW. (D) Temperature-thickness phase diagram of 1T-TaS$_2$ nano-thick crystals upon cooling at 1 K/min [88]. Figure is taken from ref 88.

hexagonal, where the planes of Ta atoms are surrounded by six S atoms in an octahedral arrangement. The top view of the crystal structure shows a star of David cluster, where 12 Ta atoms within the layer move toward a 13th central Ta atom [88]. Panel B displays a schematic view of the commensurate charge density wave state (CCDW), the nearly commensurate charge density wave state (NCCDW), and the incommensurate charge density wave state (ICCDW). These different CDW states affect the electronic conductivity profoundly. For the low temperature phase (CCDW), the strong charge density wave suppresses the free-carrier response and increases the resistance by opening a gap at the Fermi level. If the temperature is reduced further, 1T-TaS_2 can even transform into a Mott insulator or a superconductor depending on the applied external field [90–97]. For the NCCDW phase, the charge density wave forms domain structures, the electron conduction derives from the mobile carriers in domain boundaries or the discommensurate region. At higher temperatures, the NCCDW state transits to the incommensurate charge density wave state (ICCDW). In this state, the charge density wave is weak because of the small shift of the Ta atoms. Above 543 K, the charge density wave is gone and the system become fully metallic. As a result, the material experiences a metal-semiconductor-insulator transition due to the increasing lattice instability as temperature decreases, which makes this material very interesting.

Compared to the 1T-TaS_2, changes of the electronic properties due to charge density waves are more subtle in the 2H phase due to the incommensurate CDW state at low temperatures ($T_{CDW} \approx 78$ K). Figure 2.12a displays the resistivity as a function of temperature for 2H-TaS_2 and two Na doped samples. Other than an abrupt change of resistivity in 1T-TaS_2 [Fig. 2.11c], the changes here are more smooth and gradual. Figure 2.12b shows the optical conductivity spectra for 2H-TaS_2 above and below the charge density wave transition temperature. Overall, the

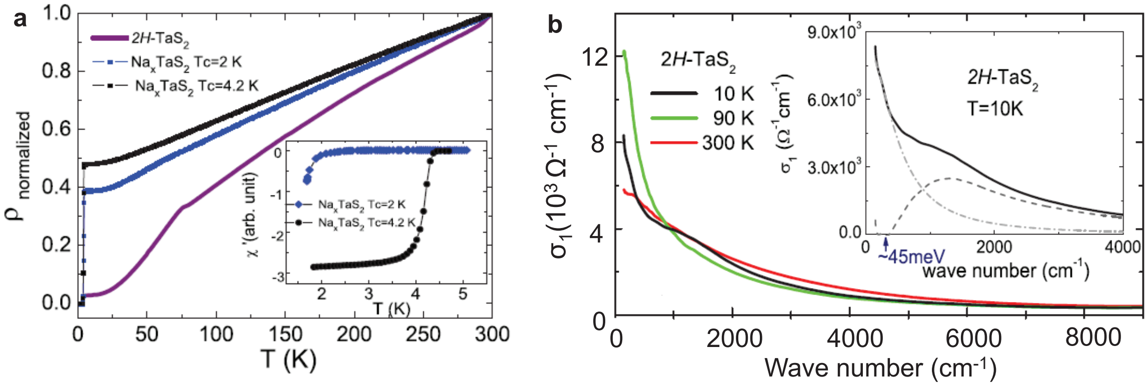

Figure 2.12: **a,** Temperature-dependent resistivity for 2H-TaS2 and two $\mathrm{Na}_x\mathrm{TaS}_2$ crystals. The values are normalized to respective values at 300 K. The inset shows the real part of ac susceptibility below 5 K, which identifies T_c for two $\mathrm{Na}_x\mathrm{TaS}_2$ crystals as 2 and 4.2 K, respectively [79]. **b,** The real part of optical conductivity of the 2H-TaS_2 at some select temperatures. The inset shows a close-up view. For 2H-TaS_2, the experiment data, a Drude fit, and the result of $\sigma_1(\omega)$ minus Drude fit are plotted by a black line, a gray dash dot line, and a dark gray dash line, respectively [79]. Figure is taking from Ref 79.

spectra are very similar. The difference is from a subtle peak in the mid-infrared region in the spectra at 10 K. The charge density wave gap is calculated around 45 meV from the analysis of this feature. These behaviors indicate the charge density wave does not dramatically change the electronic properties of 2H-TaS_2.

However, the charge density wave can have a relatively large influence on phonon properties in 2H-TaS_2. Figure 2.13 displays the Raman spectra, mode assignments, and the mode displacement patterns in bulk 2H-TaS_2. Clearly, a lot of new peaks emerge at low temperatures due to the symmetry-breaking induced by the charge density waves. Peaks below 110 cm^{-1} are assigned as amplitude modes caused by the charge density waves since they modulate the magnitude of the CDW rather than its phase [89,98,99]. Lack of inversion symmetry breaking in the incommensurate CDW state of bulk 2H-TaS_2 prevents the observation of phase modes by Raman scattering. The soften and broadening of the two amplitude modes when warming across T_{CDW} are the key signatures of the CDW state. Another important CDW mode is the two-phonon peak centered around 180 cm^{-1}. This peak is from second order scattering of acoustic and quasi-acoustic modes near the CDW wave vector $Q_{CDW} \approx \frac{2}{3}\,\Gamma M$ and is commonly observed in other Group V TMDs [100–104]. The fact that this mode persists even at the room temperature indicates there is a structural instability above the charge density wave transition temperature. As a result, short-range CDW state can exist at room temperature in 2H-TaS_2. One of the work in this dissertation is to study the vibratinoal response of the Fe_xTaS_2 system, in which the Fe is intercalated between the van der Waals gap in 2H-TaS_2. Identify the phonons related to the charge density wave is very useful to help assign the features in the intercalated compounds.

Semiconducting tranisition metal dichalcogenides: The other branch of the transition metal dichalcogenides is the semiconducting TMDs such as MoS_2,

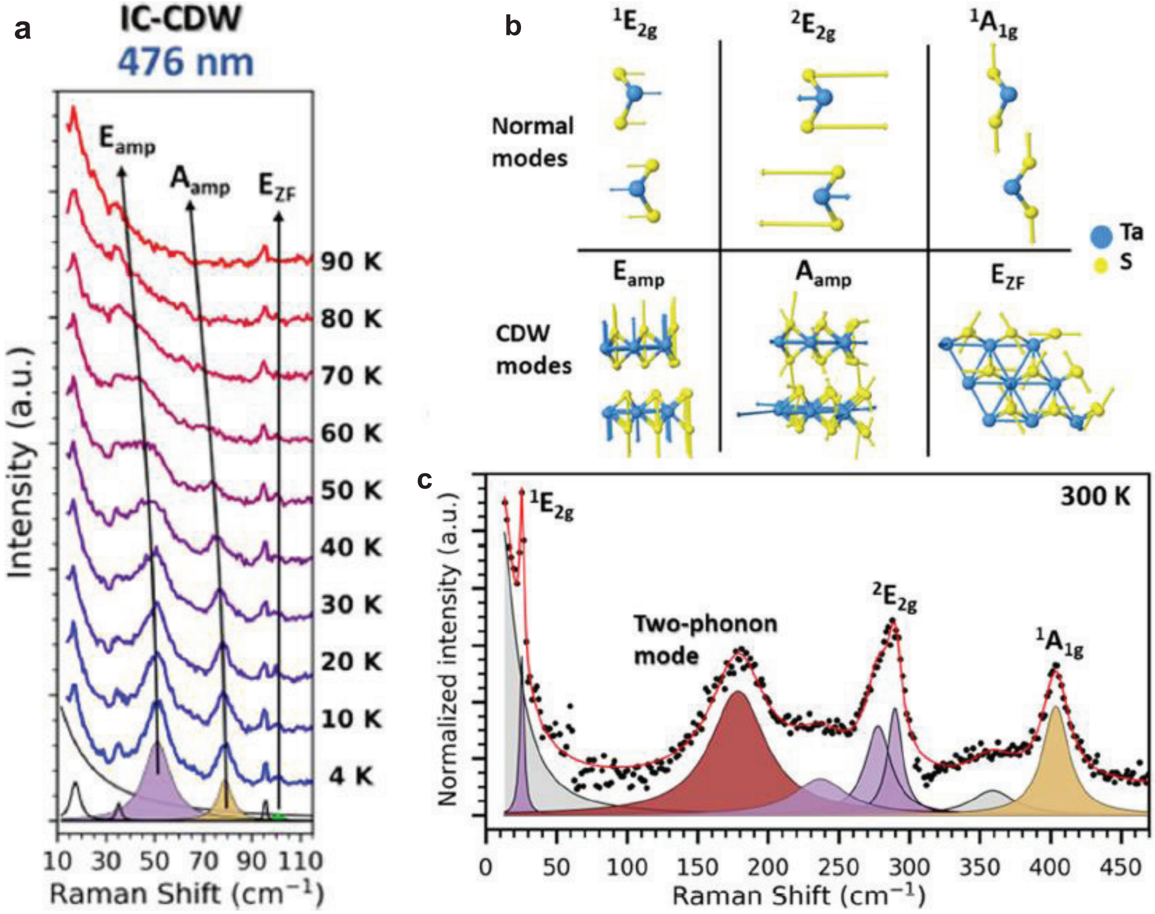

Figure 2.13: **a,** Variable temperature Raman spectra of the 2H-$\mathrm{TaS_2}$. The CDW modes E_{amp} and A_{amp} are indicated. The Lorentzian fit shown for the data at 4 K. **b,** Displacement pattern of the normal Raman modes and the CDW-related modes. **c,** Close-up view of the Raman spectra of bulk 2H-$\mathrm{TaS_2}$ with observed modes and their assignments. Figure is taking from Ref 89.

WS_2, $MoSe_2$, and WSe_2. These materials are interesting because they present a gap in the optical range of the energy spectrum that makes them candidates for device applications. A lot of experiments have demonstrated that the band structures of these materials are highly dependent on the layer thickness. The band gap for multilayer samples are indirect, whereas a direct band gap forms in the single layer samples. Furthermore, their electronic properties can be tuned by external stimulus including strain, pressure, and temperature, which makes those materials a potential for device applications. Table 2.2 summarizes the energy of band gaps in MoS_2, WS_2, $MoSe_2$, and WSe_2, from which we can see the gap energy is associated to the layer thickness.

Figure 2.14 displays the band structures for single layer, bilayer, and bulk MoS_2, $MoSe_2$, WS_2, and WSe_2 [84, 105]. Closely examine the band structures can reveal some important electronic properties in the semiconducting MX_2 family. First, the band structure of the monolayer samples are quite different compared to the bulk and bilayer samples in terms of the minimum of the conduction band and maximum of the valence band. All single layer compounds exhibit direct band gaps, with the gap lying at two inequivalent K and K′ points of the Brillouin zone [Fig. 2.10]. However, when the layer thickness increases, the minimum of the conduction band shift to the Q point, meanwhile, the maximum of the valence band shifts to the Γ point, at the center of the hexagonal Brillouin zone. This reveals that the band gaps for multilayer compounds are all indirect. Second, the band structures for all compounds reveal a large splitting of valence bands at the K point due to the spin-orbital interaction. Since the spin-orbital coupling is larger for heavier atoms, the splitting of WX_2 on the bottom channel of Fig. 2.14 is more obvious than the MoX_2 (top channel in Fig. 2.14). Specifically, the splitting energies of the MoX_2 and WX_2 are on the order of 150 meV and 400 meV, respectively. The spin-orbital coupling also results in a

Table 2.2: Band gap energies of some typical semiconducting transition metal dichalcogenides. All energies are expressed in the unit of eV [84, 105].

Materials	Monolayer	Bilayer	Bulk
MoS_2	1.72	1.71 - 1.2	1.71 - 0.79
$MoSe_2$	1.41	1.42 - 1.2	1.39 - 0.85
WS_2	1.66	1.66 - 1.34	1.64 - 0.92
WSe_2	1.44	1.44 - 1.3	1.41 - 0.91

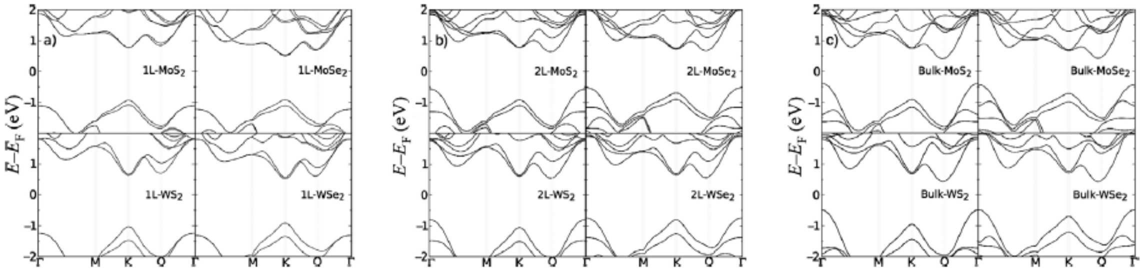

Figure 2.14: Band structure of single layer, (a), bilayer (b), and bulk (c) of MoS$_2$, MoSe$_2$, WS$_2$, and WSe$_2$ obtained from density functional theory calculations [84, 105]. Dashed vertical lines indicate the position of the Q point in the Brillouin zone [84, 105]. Figure is taken from ref 105.

splitting of bands at the K points in the conduction bands, which leads to a secondary minimum at the Q points.

Another interesting aspect is that the band gaps can be tuned by external stimulus including strain, pressure, and electric field. Figure 2.15 displays how band structures of MX_2 (M = Mo and W, X = S and Se) develop under applied biaxial strains. Under biaxial tensile strains, the X atom moves toward the M atom, which leads to a decrease in the X-M-X angle [106]. Clearly, both the maximum of the valence bands and the minimum of the conduction bands at the K points increase monotonically with the strength of the negative strains. As a result, the energy gap at K points becomes larger with the increasing negative strain strength. This trend is consistent for all semiconducting TMDs and does not depend on the transition metal elements. Another interesting behavior is that the maximum shifts from the K points to the Γ points when the strength of the positive strain increases, which changes the direct gap at K-K$'$ to an indirect gap from Γ to K$'$.

Pressure can also be applied to TMDs to tune the band gaps. Figure 2.16 shows an example of how band gaps change with pressure in MoS_2. In contrast to the applied strain field, the band gap energies change non-monotonically with the increasing pressure. For monolayer 2H-MoS_2, the band gap increases below 25 GPa and then decreases monotonically when pressure is greater than 30 GPa. At around 68 Gpa, the band gap fully closes and the material transit to a metallic state [107]. As the layer thickness increases, the critical pressure becomes much smaller. Panel (b) summarizes this behavior in a phase diagram. A metallic state is more easily reached in the bulk state because more interlayer interactions are present [107]. This phase diagram can be understood in terms of orbital hybridization between the Mo $d_{x^2y^2}$, d_{z^2} and S p_x, p_y, and p_z orbitals. The conduction and valence bands are composed by these orbitals. At relatively low pressure, the increasing pressure moves those

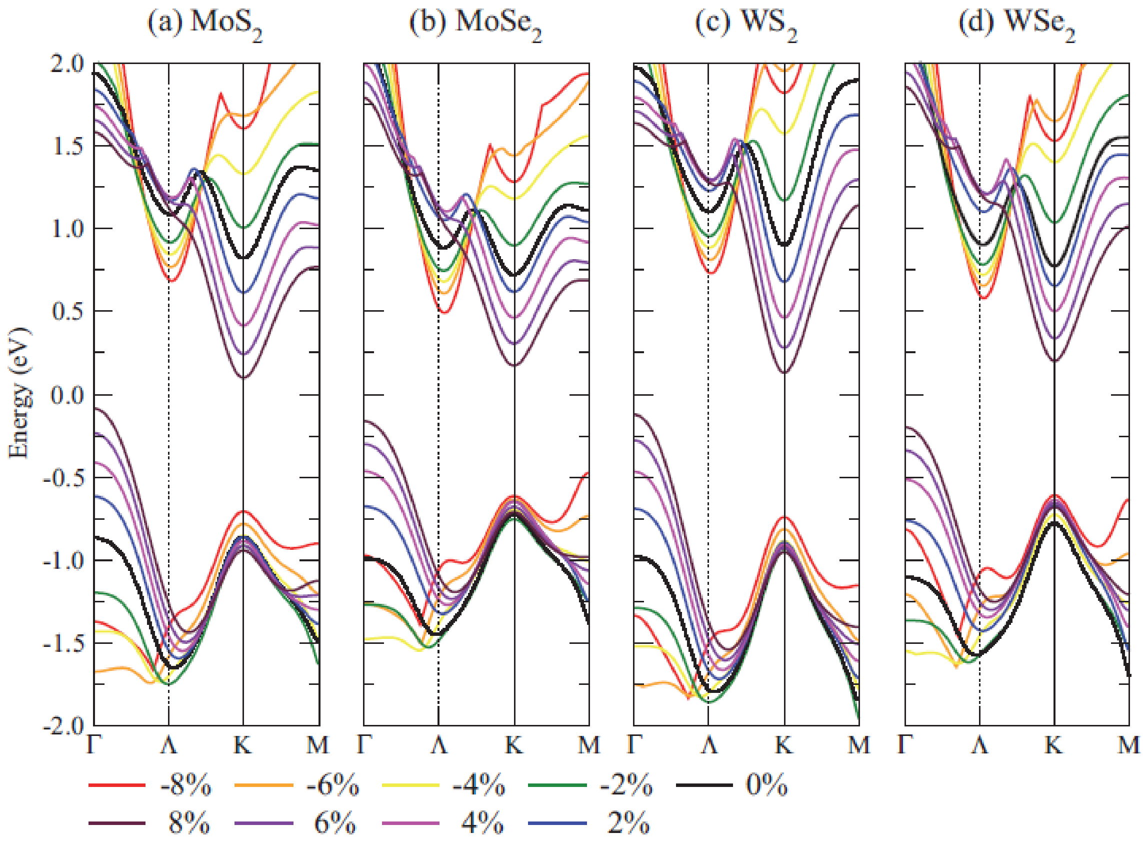

Figure 2.15: The change of highest valence band and lowest conduction band of (a) MoS$_2$ (b) MoSe$_2$ (c) WS$_2$ and (d) WSe$_2$ under compressive and tensile biaxial strains [106].

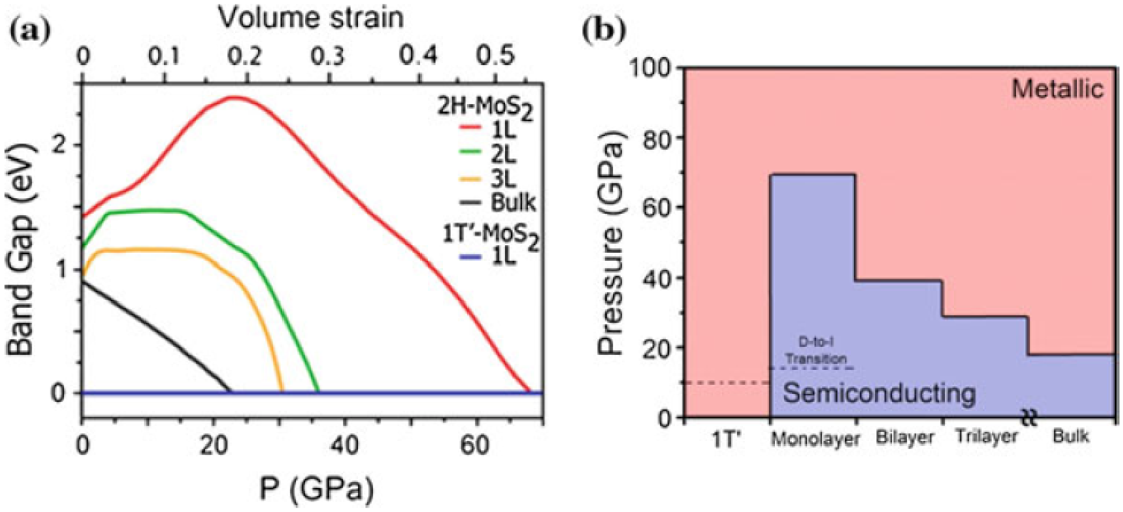

Figure 2.16: (a) Band gaps as a function of hydrostatic pressure for 2H-MoS$_2$ at different layer thicknesses. MoS$_2$ with the 1T' phase is added for comparison. (b) Pressure-layer thickness phase diagram for MoS$_2$. Figure is taking from Ref 107.

orbital away from the Fermi level, which increases the band gap energy. However, when the pressure is high, the out-of-plane compression becomes more dominant, the Mo d_{z^2} and p_z orbitals interact strongly with the S p orbitals, which leads to an orbital hybridization and decreases the energy gap. As the pressure continues to increase, the strong intra-plane hybridization will ultimately change the system to metallic [107]. This is consistent with the easier metallization behavior in the bulk MoS_2 material.

Finally, the band gaps can be also tuned by the electric field. Figure 2.17 (a) displays the band structure of MoS_2 under the external electric field. Clearly, the foundamental gap of MoS_2 decreases with the increasing electric field, and it fully closes when $E = 3$ V/nm [108]. Figure 2.17 (b) shows how band gaps respond to electric field for a series of MX_2 materials. The band gaps of all TMD semiconductors decreases monotonically with the increasing electric field. Interestingly, when the chalcogen elements change from S to Se to Te, the critical electric field decreases systemically. This is because the increasingly diffuse nature of the valence p_z orbitals in going from S to Te, the latter facilitating greater charge transfer from the chalcogen to Mo at the same level of electric field. The effect of changing the transition metal from Mo to W while retaining the chalcogen (S) was very weak [108, 109].

To summarize, the band gaps of the TMD semiconductors are highly tunable by external stimulus such as strain, pressure, and electric field. At the same time, by applying exfoliation, very thin films with atmoic scale thickness can be obtained. The monolayer TMDs exhibit very interesting and distinct electronic properties. All of these facts make the TMDs very useful in applications in making electronic devices. We will talk about some applications in the next section.

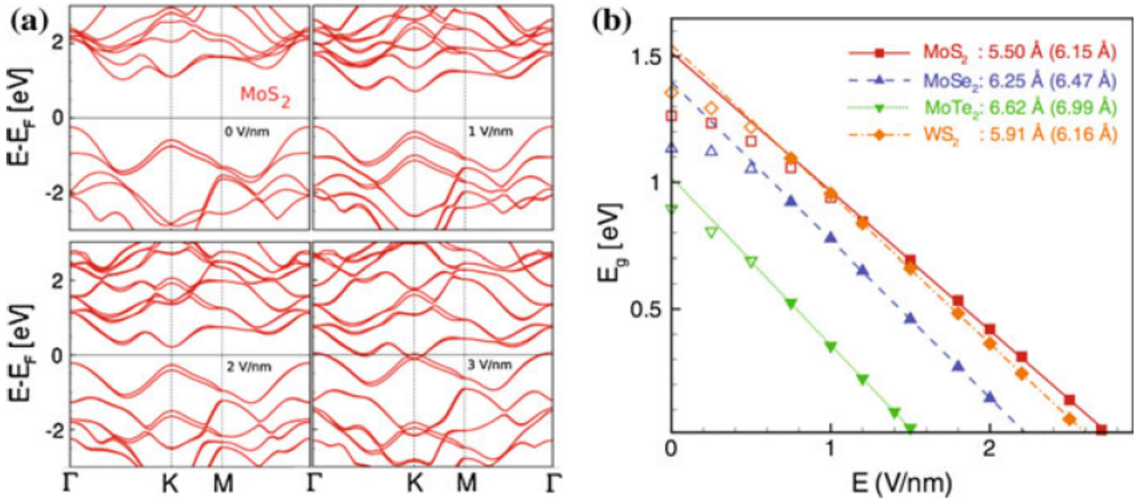

Figure 2.17: (a) Band structure of MoS_2 along ΓKMΓ direction in reciprocal space as a function of applied external electric field. (b) Band gap vs. applied electric field E for MoS_2, $MoSe_2$, $MoTe_2$, and WS_2. Figure is taking from Ref 109.

2.2.1.3 Devices based on transition metal dichalcogenides

One of the important applications by using transition metal dichalcogenides semiconductors is transistors. A transistor is a device composed of a semiconductor material with typically three terminals for connection to an external circuit [109]. Voltage can be applied to one pair of its terminals to control the current at another pair of terminals. This is the fundamental principle for an amplifier, in which one can use a small signal to produce a much stronger signal through the transistor. Alternatively, the transistor can be used to turn current ON or OFF in a circuit as an electrically controlled switch.

One of the typical type of modern transistors is the field-effect transistor (FET). A typical FET is composed into three main parts: source, gate, and drain. For a NPN-type transistor, the gate is a P-type semiconductor. The input current flows from the gate to source, and the output current flows from source to drain. The current amplitude in the gate associates to the free carrier densities (for NPN type the carrier is holes).

Figure 2.18 displays a typical type of FET transistors using MoS_2 as a gate material. In this device, 6.5 $\mathring{A}$ thick exfoliated MoS_2 layer served as the semiconducting channel. It was deposited on SiO_2 and covered by a 30 nm thick layer of HfO_2, which served as the top-gate dielectric. A mobility of at least 200 cm^2 V^{-1} s^{-1} was obtained. The transistor exhibited a current on/off ratio exceeding 108 at room temperature [110]. Besides the very high on/off ratio, the device exhibited off-state currents smaller than 100 fA (25 fA/μm) [109, 110]. The high degree of electrostatic control is also reflected by the subthreshold slope $S = (d(logI_{ds})/dV_{tg})^{-1}$, which was as low as 74 mV/dec [109].

The encapsulation of MoS_2 using insulating HfO_2 was crucial to achieve high mobility. A complementary approach to achieve high mobility consists in vacuum

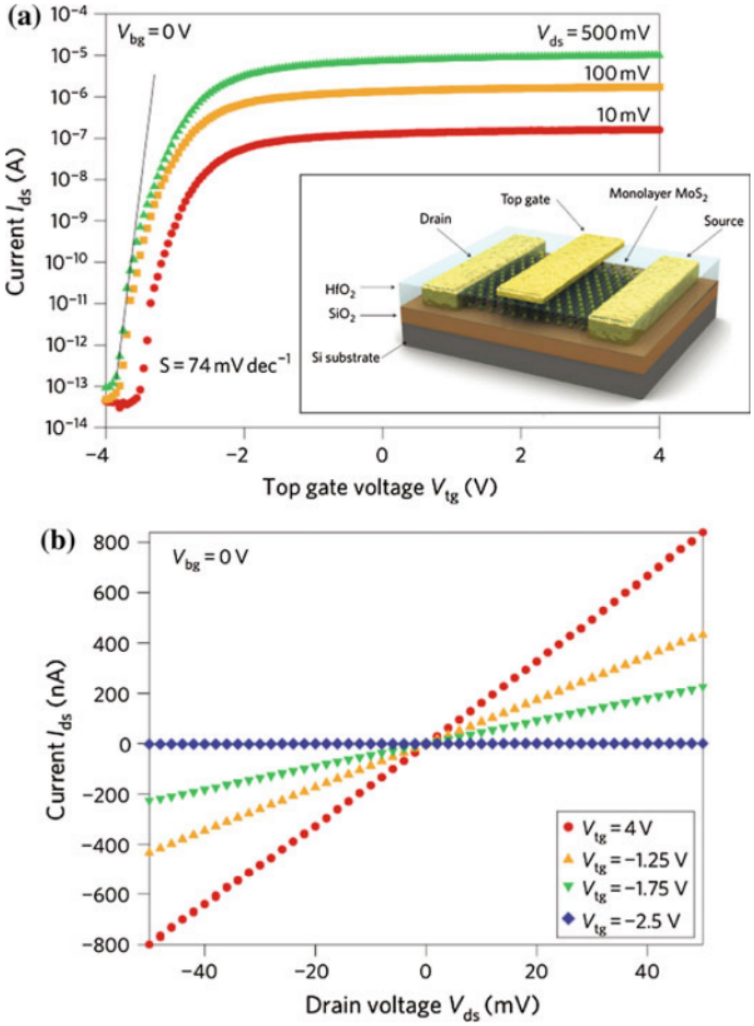

Figure 2.18: (a) I_{ds} vs. V_{tg} curves recorded for a bias voltage ranging from 10 to 500 mV. Measurements were performed at room temperature with the back gate grounded. Inset Three-dimensional schematic view of one of the transistors. (b) I_{ds} vs. V_{ds} curves recorded for different values of V_{tg} [110]. Figure is taking from Ref 109.

annealing to remove adsorbates. Using this approach, intrinsic (field-effect) mobility as high as 1000 $\mathrm{cm}^2\ \mathrm{V}^{-1}\mathrm{s}^{-1}$ was obtained at low temperature in both monolayers and bilayers [109, 111]. Intrinsic mobility and conductivity of single-layer MoS_2 in single and dual-gated geometry was also studied in ref 112. It was found that at charge carrier densities n_{2D} below $\approx 10^{13}\ \mathrm{cm}^{-2}$, the MoS_2 single-layer exhibits decreasing conductance as the temperature is decreased [109]. For n_{2D} larger than $10^{13}\ \mathrm{cm}^{-2}$, the conductance increased with decreasing temperature, which is the hallmark of a metal-insulator transition [109].

2.2.2 Intercalation leads to new functionalities

Metal centers can be intercalated into the multilayered transition metal dichalcogenides, forming different superstructure patterns depending upon the concentration. When incorporated in this manner, the intercalated elements forms metal monolayers within the van der waals gap, which supports high temperature magnetic ordering [10, 13, 113], novel metallicity that is distinct from that of the parent compound [79, 114], and superconductivity [115]. Intercalated metal monolayers are also responsible for the development of different types of domain walls in layered chalcogenides [6]. It is well-established that the 3d transition metals occupy octahedral sites between the trigonal prismatic tansition metal dichalcogenides layer for the 2H- polytype. Moreover, the intercalated TMDs (M_xTX_2, where M = intercalated elements, T = Nb or Ta, X = S or Se) are ordered on $\sqrt{3}a \times \sqrt{3}a$ or $2a \times 2a$ superlattices for $x = 1/3$ and $1/4$, respectively. The former sports a non-centrosymmetric and chiral space group $P6_322$ [Fig. 2.19(a)] and the latter gives a centrosymmetric space group $P6_3/mmc$ [6, 116–118]. They are the only stoichiometric compounds that attract our interest here.

The intercalation can dramatically change the magnetic properties of the parent

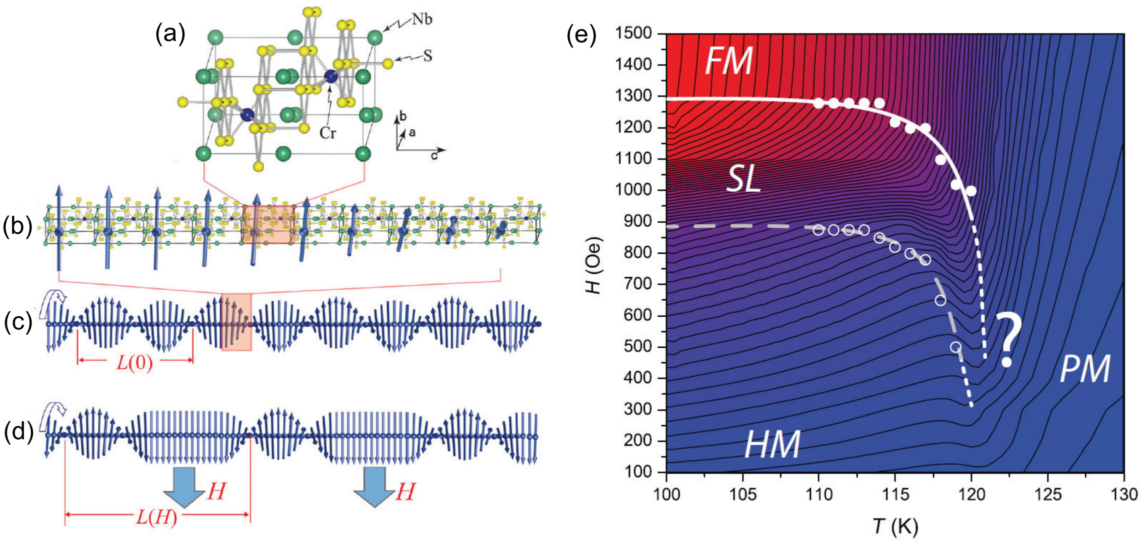

Figure 2.19: (a) Crystal structure of $Cr_{1/3}NbS_2$. The Cr atom is intercalated between the van der Waals gap of two NbS_2 prisms, resulting in a non-centrosymmetric and chiral space group $P6_322$ [10]. (b) Ground state left-handed chiral helimagnetic structure along c axis [10]. (c) Whole structure of the left-handed chiral helimagnetic state [10]. (d) Magnetic structure of the chiral soliton lattice state [10]. (e) Phase-diagram of $Cr_{1/3}NbS_2$ [11].

compound. One example is the chiral helimagnet $Cr_{1/3}NbS_2$. This material attracts a lot of attention because of the helical magnetic phase along the *c*-axis below 131 K [10, 11]. Figure 2.19 (b-d) displays the schematic view of the different magnetic phases in $Cr_{1/3}NbS_2$. At low temperatures, the material exhibits long-range helical magnetic order along the chiral axis *c*. The origin of this magnetic phase is due to the competition between Dzyaloshinskii–Moriya interaction between localized neighboring spins $\mathbf{S}_1$ and $\mathbf{S}_2$ along the crystallographic *c*-axis and the isotropic ferromagnetic (FM) coupling in the *ab*-plane [10, 11]. Figure 2.19 (e) displays the temperature-magnetic phase diagram of $Cr_{1/3}NbS_2$. Below 131 K, the sample transitions from a paramagnetic phase to other magnetic phases that depend on the amplitude of the magnetic field. At low field amplitude, the material displays purely helical magnetic phase. When one gradually increases the strength of the magnetic field perpendicular to the helical axis, more moments are aligned in the *ab*-plane, inducing a chiral magnetic solition lattice phase [Fig. 2.19 (d)]. Continue to increase the magnetic field strength perpendicular to the chiral axis eventually results in a fully-polarized ferromagnetic phase. The saturation field is around 1300 Oe. These types of magnetic ordering are important for the applications in spintronics.

The magnetic ordering in $Cr_{1/3}NbS_2$ also modifies its transport and electronic properties profoundly [11]. Figure 2.20 (a) displays the measured resistivity as a function of temperature in $Cr_{1/3}NbS_2$. Clearly, a sharp slope change is observed at the chiral helical magnetic transition temperature 131 K. This feature is magnified in the inset derivative plot. This is due to reduction in the spin disorder scattering in the magnetic phase [11]. Figure 2.20 (b) shows the magnetoresistance measure at 2 K as a function of magnetic field. The change in magnetoresistance around 1 kOe is quite sharp and coincides with the solition lattice phase indicated by magnetization measurements. As the applied magnetic field begins to align the moment toward its

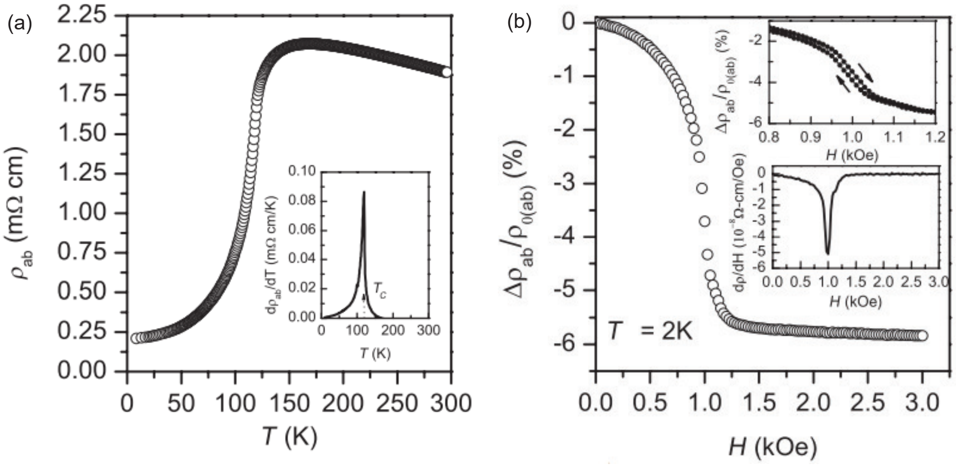

Figure 2.20: (a) Electrical resistivity of $Cr_{1/3}NbS_2$ as a function of temperature measured in the *ab*-plane. Inset shows the temperature derivative of the resistivity [11]. (b) Magnetoresistance measured at T = 2 K. The upper inset shows the change in slope in the magnetoresistance in the vicinity of the field where the metamagnetic transition is observed in the magnetization measurements. The lower inset shows the derivative of the resistivity with respect of the field. The sharp change occurs at 1 kOe [11]. Figure is taken from Ref. 11.

direction, spin disorder scattering decreases thereby reduce the electric resistivity. When the magnetic field fully polarizes the spins, there is no further change observed at higher fields.

The band structures are also deeply influenced by the magnetic ordering. Figure 2.21 (a,b) displays the calculated band structure of $Cr_{1/3}NbS_2$ for the non-magnetic and magnetic state, respectively. In the non-magnetic phase, there are several bands crossing the Fermi level, and in addition flat bands virtually abutting the Fermi level from M to K and H to M. Those crossing bands lead to a high density of states at the Fermi level [Fig. 2.21 bottom panel]. When moving to the magnetic phase, there are less bands in the Fermi level. At the same time, they become more dispersive. The density of states at the Fermi level is dramatically reduced, indicating a substantial loss of spectral weight around E_F.

Intercalation can also induce superconductivity. Figure 2.22 shows a phase diagram in Cu_xTiSe_2. As the intercalation concentration increases, the charge density wave is suppressed. The transition from a CDW state to a superconducting state takes place when $x \geq 0.04$. The superconducting transition temperature is highest when $x = 0.08$, followed by a decrease of T_c before the chemical phase boundary is reached at $x = 0.11$. There is a small boundary composition region ($0.04 \leq x \leq 0.06$), where superconductivity and CDW behaviour seem to coexist. The origin of this coexisting is complex. One possiblity is that the Cu doping results in a tendency towards increasing the dimensionality of the Fermi surface, destabilizing the CDW and allowing for correlations to build in a third dimension, tipping the balance in favour of superconductivity [115]. The other possibility is that the change in electron count on Cu doping [115]. In any case, the intercalation is the key to the superconducting phase.

In this work, we will focus on studying the spectroscopic properties of the

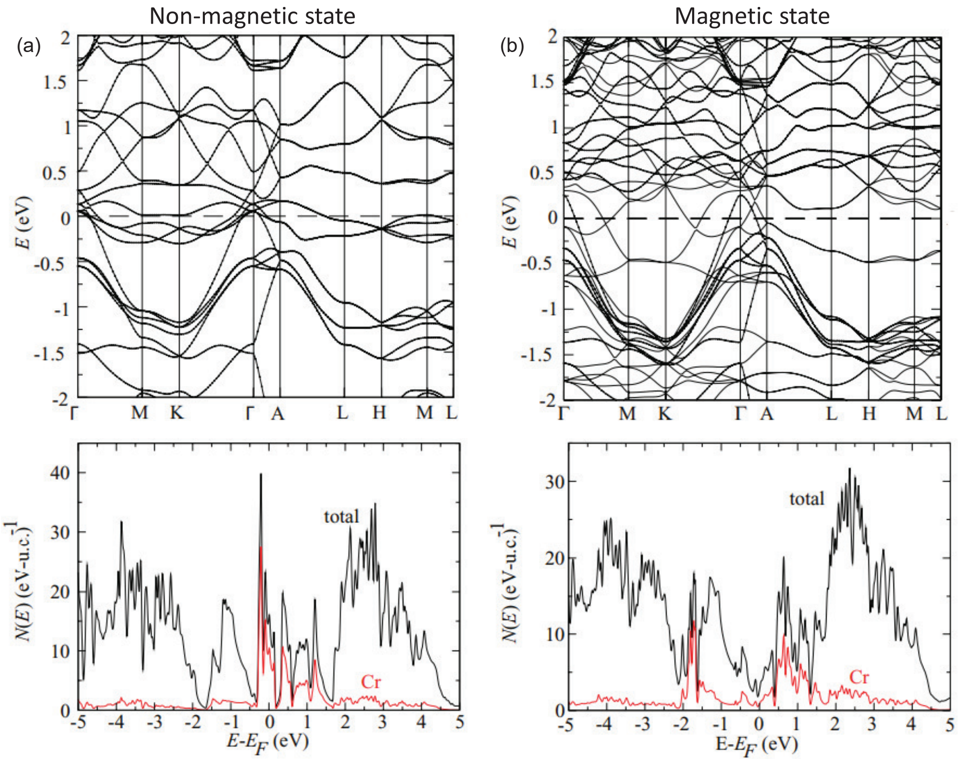

Figure 2.21: (a) The calculated band structure and density of states of $Cr_{1/3}NbS_2$ in the nonmagnetic state. (b) Ground state left-handed chiral helimagnetic structure along c axis [11]. (b) The calculated band structure and density of states of $Cr_{1/3}NbS_2$ in the magnetic state [11]. Figure is taken from Ref. 11.

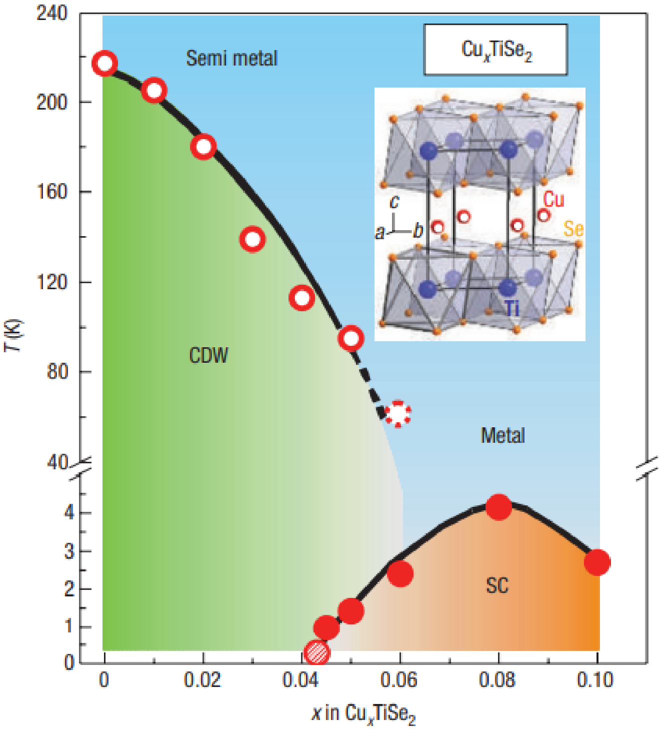

Figure 2.22: Phase diagram of Cu$_x$TiSe$_2$. Open circles represent the charge density wave transition temperature, and the filled circles correspond to the superconducting transition temperature. The shaded circle at $x = 0.04$ indicates that the transition temperature is just below our minimum available temperature, and the dashed circle at $x = 0.06$ marks the barely visible CDW transition at $x = 0.06$. Inset: Crystal structure of Cu$_x$TiSe$_2$ [115].

intercalated transition metal dichalcogenides Fe_xTaS_2, with $x = 1/3$ and 1/4. The detailed discussions are in chapters 4 and 5.

2.3 Materials of interest

2.3.1 Intercalated transition metal dichalcogenides: Fe_xTaS_2 ($x = 0$, 1/4, and 1/3)

Research on engineered superlattice materials has blossomed in recent years due to the discovery of unexpected properties deriving from interface effects [1, 119–121]. Naturally occurring superlattices like intercalated oxides and chalcogenides are of contemporary interest as well. Examples include the chiral helimagnets $Cr_{1/3}NbS_2$ and $[Pb_2BiS_3][AuTe_2]$, superconducting Pd-intercalated $IrTe_2$, and interlayer I-doped $BiOIO_3$ nanoplates [10, 11, 122–124]. The Fe_xTaS_2 system attracts our attention because of its interesting magnetic properties and fascinating domain wall patterns due to stacking effect of the Fe intercalated monolayers [6, 126, 127]. This system is based upon 2H-TaS_2 [79, 128] and has a set of stable, well-ordered intercalation plateaus at x=1/4 and 1/3 [6]. Figure 2.23 (a-c) displays the crystal structures of Fe_xTaS_2 with $x = 0$, 1/4, and 1/3, respectively [114]. The Fe is intercalated in the van der Waals gap between two neighbouring TaS_2 slabs, forming a single metal monolayer. For $x = 1/4$ compound, the Fe atoms stack identically along the c-axis (AA-type), supporting a centrosymmetric space group $P6_3/mmc$ [6]. When the intercalation concentration increases to 1/3, the Fe layers alternatively stack along the c-axis (AB-type), which breaks the inversion symmetry and results in a non-centrosymmetric and chiral space group $P6_322$ [6]. The symmetry-breaking effect profoundly modified the electron density pattern in these materials. As the Fe concentration increases, the projected charge density patterns in the Fe plane transit

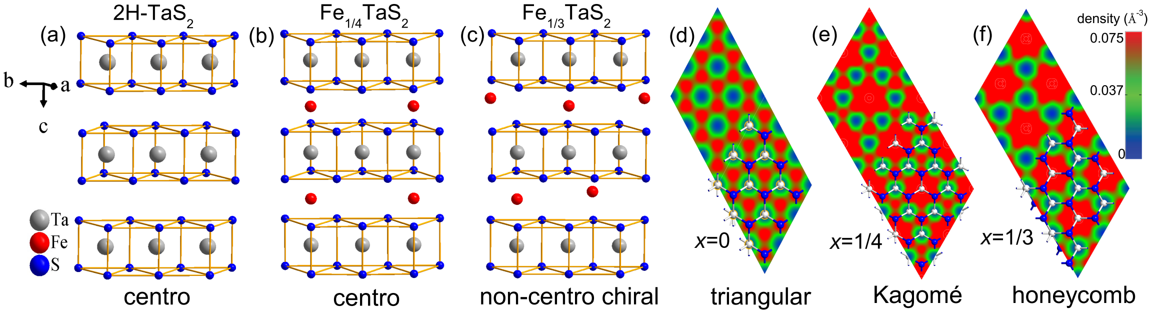

Figure 2.23: (a) Crystal structure of 2H-TaS$_2$ in the centrosymmetric $P6_3/mmc$ space group [125]. Ta^{4+} is at the center of a prism formed by six S^{2-} centers. (b) Fe$_{1/4}$TaS$_2$ also belongs to the $P6_3/mmc$ space group [6]. Each Fe center is octahedrally coordinated by six S^{2-} atoms. Stacking along c is AA type, yielding an expanded $2a \times 2a$ superlattice. (c) The structure of Fe$_{1/3}$TaS$_2$ is non-centrosymmetric and chiral (space group $P6_322$) [6]. Stacking along c is alternating (AB) type, yielding a $\sqrt{3}a \times \sqrt{3}a$ superlattice. (d, e, f) Projected charge density in the Fe plane for 2H-TaS$_2$, Fe$_{1/4}$TaS$_2$, and Fe$_{1/3}$TaS$_2$.

from triangular ($x = 0$) to Kagomé ($x = 1/4$) to honeycomb ($x = 1/3$) [114]. More detailed discussions about this is in Chapter 4.

One of the most interesting phenomenon in this set of materials is the domain and domain wall patterns that are depending on the intercalation concentration at room temperature. Figure 2.24 displays the domain and domain wall patterns of Fe_xTaS_2 ($x = 1/4$ and $1/3$). The antiphase boundaries, separating neighboring antiphase domains, are clearly visible as dark line contrasts in superlattice dark-field images in both cases. The domain patterns are quite different for the $x = 1/4$ and $x = 1/3$ cases, which can be understood by using the color theory. For the $x = 1/4$ case, the domain pattern is Z_4 (red, blue, yellow, and green)-colorable, and these Z_4 colors correspond to the AA-, BB-, CC-, and DD-type $2a \times 2a$ superstructures, respectively. The domain pattern in the $x = 1/3$ compound is much more complicated. First, there are six domain edges (domain walls) always merge into a vortex point. Furthermore, each domain is always surrounded by an even number of vertices, thus forming a so-called "even-gon" [6]. To map this domain pattern, the standard one-step proper coloring can be extended to that of two-step (tensorial) proper coloring. The first-step is to classify the six domains as light and dark colors, where dark domains are not touching bright domains with the same color through edges, and vice versa. For example, the dark red domain and the pink domain are not connecting through their edges. For the second step, the dark and light domains can be further painted with three colors (In Fig 2.24(b), they are red, blue and green). We call the domain type with these configurations as the $Z_2 \times Z_3$ domain patterns. The Z_3 corresponds to three types of $\sqrt{3}a \times \sqrt{3}a$ superstructure antiphase domains, that is, AB-, BC-, and CA-type antiphase domains. The Z_2 is associated with chiral domains without centrosymmetry [6]. In this case, the domain wall type in the $x = 1/4$ is purely antiphase. However, in the $x = 1/3$ compound, the domain wall is antiphase and

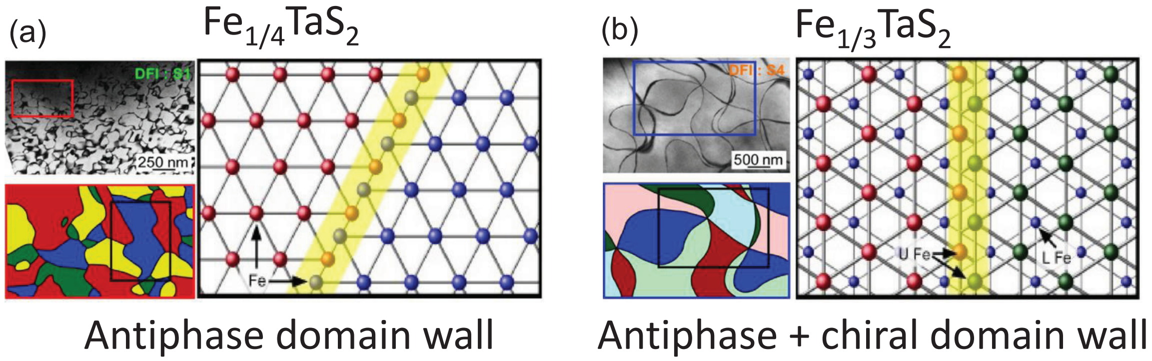

Figure 2.24: (a) Dark-field image, schematic view of domains, and local structure antiphase domain walls in $Fe_{1/4}TaS_2$. (b) Dark-field image, schematic view of domains, and local structure of antiphase + chiral domain walls in $Fe_{1/3}TaS_2$ [6].

chiral simultaneously.

It has been turned out that the domain topologies has a strong influence on the magnetic properties of $\mathrm{Fe}_x\mathrm{TaS}_2$. Figure 2.25 d displays the magnetic hysteresis ($M(H)$) curves at 4 K with the magnetic field along the c-direction, and magnetic coercivity, extracted from $M(H)$ curves, vs x in $\mathrm{Fe}_x\mathrm{TaS}_2$. It clearly shows that for the low concentration samples ($x = 0.18$ and 0.25), the coercivity is very large. Since in both $x = 0.18$ and 0.25 samples, there are large density of Z_4 type domains with small domain size, there seems indicate that high-density antiphase boundaries associated with Z_4 domains are probably associated with a strong pinning effect of magnetic domain walls and lead to an avalanche-like depinning of magnetic domain walls in the presence of high external magnetic fields [13,129]. On the other hand, for large Fe concentration samples with large domain size and $\mathrm{Z}_2 \times \mathrm{Z}_3$ domain patterns, the magnetization exhibits a broad switching with small coercivity. This indicates large $\mathrm{Z}_2 \times \mathrm{Z}_3$ domains with a small number of antiphase/chiral domain boundaries accompany weak pinning of magnetic domain walls and a small coercivity field [6].

The magnetotransport properties of $\mathrm{Fe}_x\mathrm{TaS}_2$ are determined to be strongly dependent on the intercalation concentration x. $\mathrm{Fe}_x\mathrm{TaS}_2$ has a ferromagnetic ground state for x = 0.23 - 0.4 with the magnetic easy axis along the c-axis [12,128]. When x is great than 0.4, the system becomes more antiferromagnetic [6]. Figure 2.26 displays the magnetoresistance measurement for $\mathrm{Fe}_x\mathrm{TaS}_2$ at different concentrations. The value of magnetoresistance is very sensitive to the concentration x, and the trend is non-monotonic. When x changes from 0.249 to 0.264, the magnetoresistance increases dramatically. The maximum vaule is observed at $x = 0.28$. Further experiments indicates the magneoresistance increase even more when $x = 0.297$ [12]. Above $x = 0.297$, the magnetoresistance begins to drop, and when $x = 0.348$, the magneoresistance drops to the similar magnitude as $x = 0.231$. The large variation

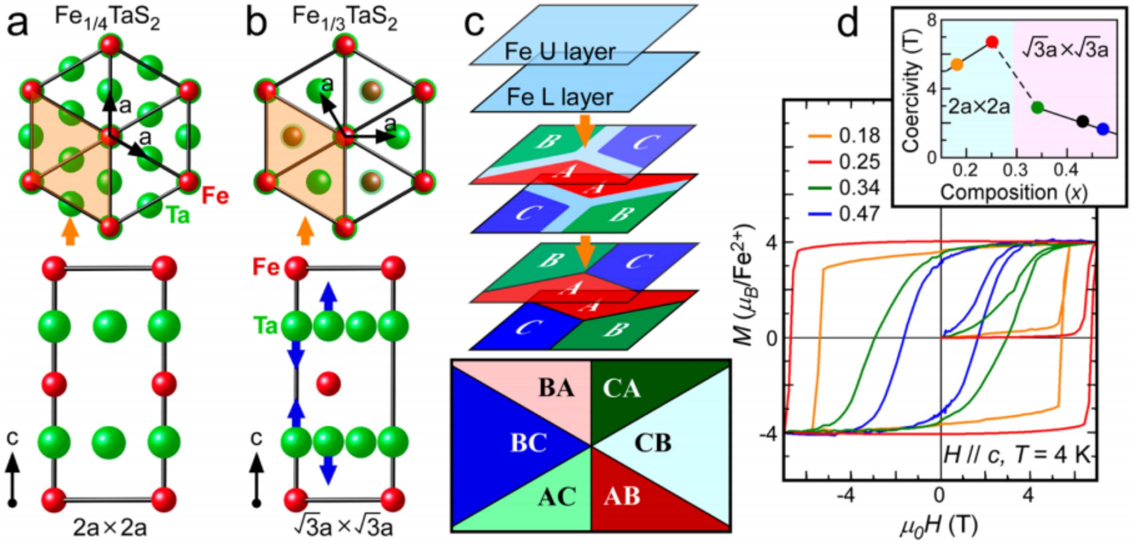

Figure 2.25: Domain evolution and magnetic properties in Fe_xTaS_2. (a,b) The top-view and side-view schematics of the crystallographic structures of $Fe_{1/4}TaS_2$ and $Fe_{1/3}TaS_2$, respectively. Only Fe (red) and Ta (green) ions are depicted. The side-view schematics correspond to the portions indicated in orange in the top-view schematics. The arrows depict the displacement of Ta ions along the c-axis. (c) Schematics of the evolution of a $Z_2 \times Z_3$ domain during the disorderorder transition of Fe ions. (d) Magnetic hysteresis curves of $x = 0.18$, 0.25, 0.34, and 0.47. These curves were measured at 4 K in magnetic fields along the c-axis. Note that $x = 0.18$ and 0.25 show the $2a \times 2a$-type superstructure, whereas $x = 0.34$ and 0.47 exhibit the $\sqrt{3}a \times \sqrt{3}a$ type one. The inset shows the magnetic coercivity as a function of Fe composition. Figure is taken from Ref. 6.

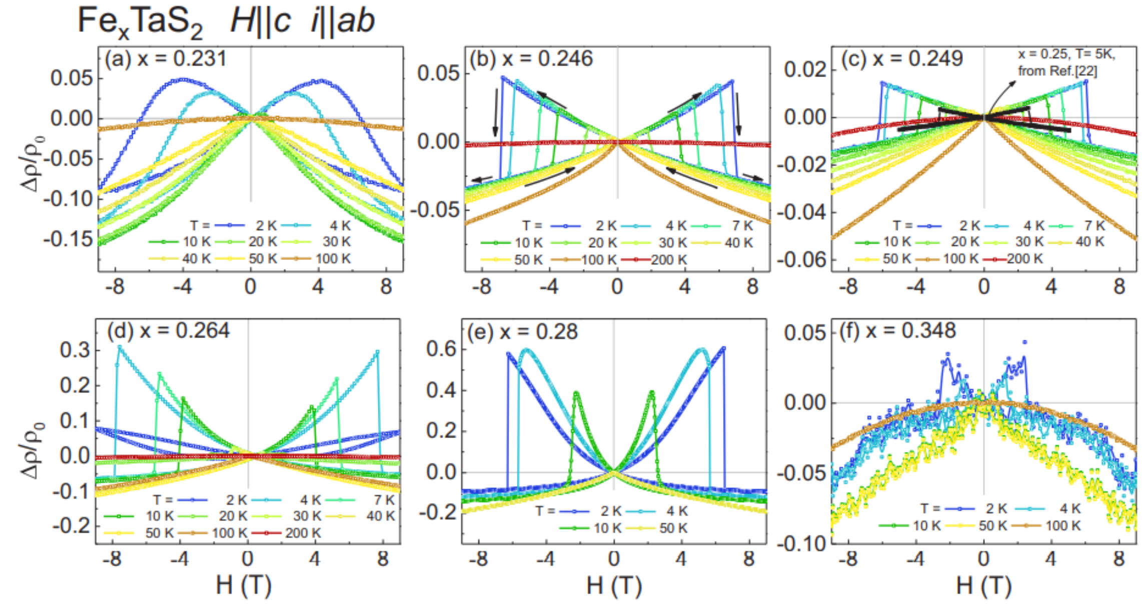

Figure 2.26: Magnetoresistance of Fe$_x$TaS$_2$ at (a) $x = 0.231$, (b) 0.246, (c) 0.249, (d) 0.264, (e) 0.280, and (f) 0.348. Arrows in (b) indicate the field sweep direction [12].

of the magnetoresistance is due to the magnetic disorder scattering, which originates from the misalignment of the magnetic moments. The misalignment is attributed to crystallographic defects, such as vacancies due to the deviation from the commensurate Fe concentrations (1/4 or 1/3), the antiphase boundaries [6] or both [12].

Considering all of these interesting properties, in this work, we perform spectroscopic measurements to understand the symmetry-breaking and spin-lattice coupling from a microscopic point of view. Details of the work is introduced in Chapters 4 and 5.

2.3.2 Engineered superlattices: $(\mathrm{LuFeO_3})_m/(\mathrm{LuFe_2O_4})_n$ (m = 3, 7, 9; n = 1)

The dream of a ferroelectric ferromagnet that is fully coupled at room temperature is the grand challenge of multiferroics and magnetoelectrics. Heteroepitaxy enlarges the design space to achieve this difficult but important goal, and examples abound of superlattices and interfaces at which exotic properties emerge [130–148]. Superlattices of the form $(\mathrm{LuFeO_3})_m/(\mathrm{LuFe_2O_4})_n$ that sport ferroelectric ferrimagnetism are prominent examples [1]. The layer indices run from 0 to 9 and for simplicity are denoted (m, n). One end member h-$\mathrm{LuFeO_3}$ is a polar, improper ferroelectric below 1020 K, and it orders antiferromagnetically at 147 K in a pattern in which symmetry allows a slight canting of the spins - giving rise to weak ferromagnetism [16–19]. The other end member $\mathrm{LuFe_2O_4}$ is an antiferroelectric with a complex phase diagram, exemplified by a series of charge ordering transitions above room temperature, a 240 K ferrimagnetic ordering temperature, and a structural transition near 170 K [20–24, 149].

Figure 2.27 displays the crystal structures of two end-members and the high-angle annular dark field scanning transmission electron microscopy (STEM) images of the

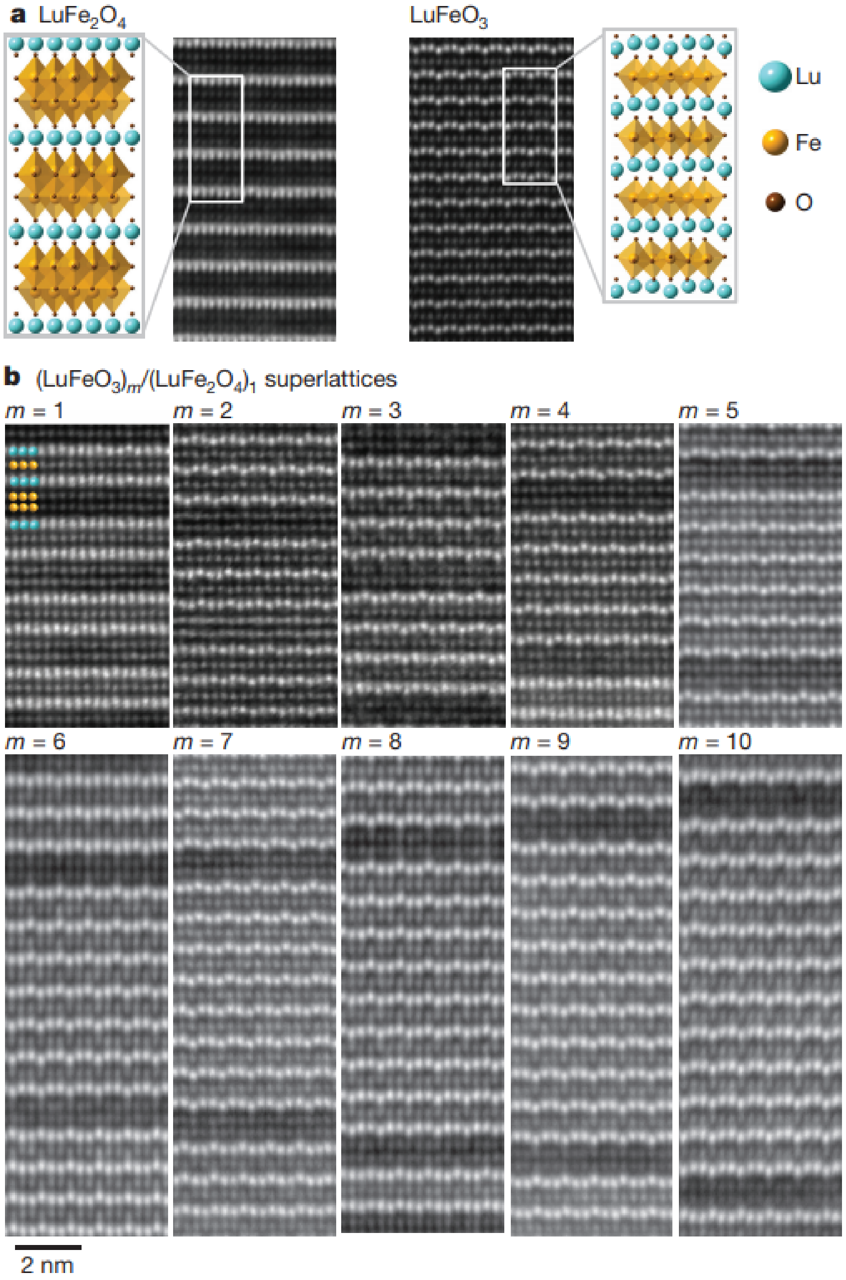

Figure 2.27: **a**, End-members LuFe$_2$O$_4$ (left) and LuFeO$_3$ (right). **b**, (LuFeO$_3$)$_m$/(LuFe$_2$O$_4$)$_1$ superlattice series for $1 \leq m \leq 10$. Samples are imaged along the LuFeO$_3$ $P6_3cm$ [100] zone axis. LuFe$_2$O$_4$ is imaged down the equivalent zone axis, which, owing to the primitive unit cell of LuFe$_2$O$_4$, is the [120] zone axis. Schematics of the LuFe$_2$O$_4$ and LuFeO$_3$ crystal structures are shown in a with lutetium (Lu), iron (Fe) and oxygen (O) in turquoise, yellow and brown, respectively. Figure is taken from Ref. 1

$(LuFeO_3)_m/(LuFe_2O_4)_n$ superlattices. The characteristic "up-up-down" pattern of the lutetium atoms in $LuFeO_3$, which is also present in the hexagonal manganites [150], is evident and reflects the polar nature of the h-$LuFeO_3$ film. This "up-up-down" pattern of the Lu-layer displacement is also observed in the $LuFeO_3$ layers in superlattices. The other end member $LuFe_2O_4$, however, does not show any Lu-layer displacement. Interestingly, in the $m \geq 2$ superlattices, the Lu-layer in the $LuFe_2O_4$ - $LuFeO_3$ interface becomes distorted and displays some displacements. This is due to the increasing lattice strain originates from the lattice mismatch between the two components [1]. This Lu-layer displacement at the interface monotonically increases when the superlattice periodicity and has a significant influences on the magnetism and ferroelectricity.

Figure 2.28a displays the magnetization as a function of temperature in the $(LuFeO_3)_m/(LuFe_2O_4)_n$ superlattices. Strikingly, the magnetic Curie temperatures increase with the number of $LuFeO_3$ layers (m). Ferrimagnetic T_C in superlattices is higher than any of the end members. For the (9,1) case, it reaches to 281 K, which is very close to the room temperature. This result is very important because this is the first observation of the room temperature multiferroics with simultaneously ferrimagnetism and ferroelectricity. Conventional single phase multiferroics such as $BiFeO_3$ is also a room temperature multiferroic, however, the magnetization is weak because of the antiferromagnetism in the system. In this case, the magnetoelectric coupling strength is small in $BiFeO_3$. Type II multiferroics such as $TbMnO_3$ can display the stonger magnetoelectric coupling, however, the magnetic transition temperature is really low.

Figure 2.28b shows the magnetization curves for the (9,1) superlattice. A large coercivity around 5 T at low temperature is observed, which indicates a robust magnetism in the system. The hysteric behavior persists at 300 K, which indicates

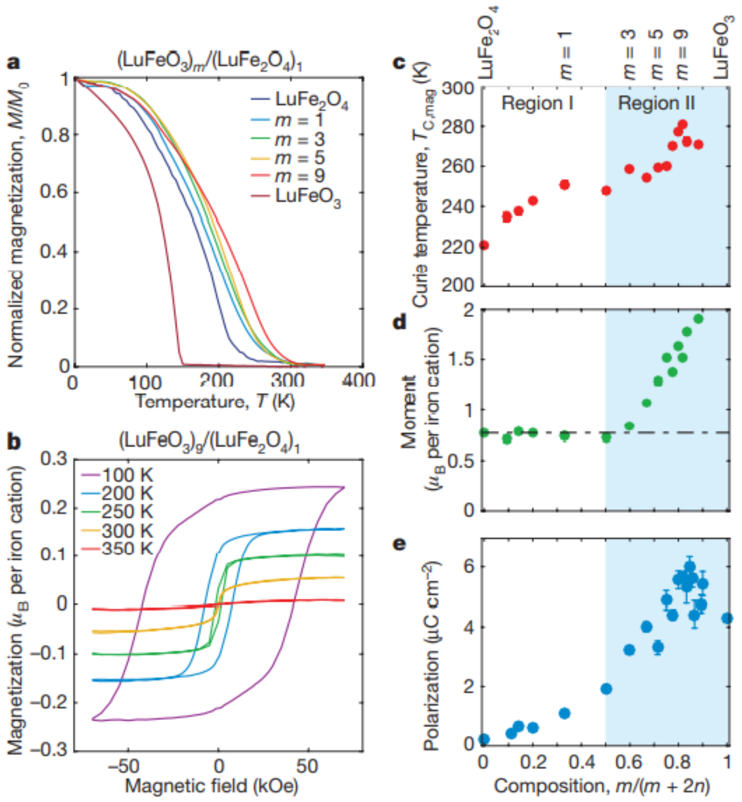

Figure 2.28: **a**, M–T curves for a series of $(LuFeO_3)_m/(LuFe_2O_4)_1$ superlattices cooled in a 1-kOe field. **b**, Loops of the magnetization as a function of the magnetic field for the $(LuFeO_3)_9/(LuFe_2O_4)_1$ superlattice, at various temperatures. **c**, The ferromagnetic Curie temperatures $T_{C,mag}$ extracted from the M–T curves (some of which are shown in a) plotted as a function of the fraction of iron ions that sit in the $LuFeO_3$ layers, $m/(m+2n)$. Regions I and II show data for the $(LuFeO_3)_1/(LuFe_2O_4)_n$ and $(LuFeO_3)_m/(LuFe_2O_4)_1$ series, respectively. The Curie temperature reaches a maximum of 281K for the $(LuFeO_3)_9/(LuFe_2O_4)_1$ compound. **d**, The total moment per iron cation in $LuFe_2O_4$ at 50K assuming the moment of $LuFeO_3$ remains constant. The measured moment of end-member $LuFe_2O_4$ is displayed as a horizontal line for reference. **e**, Average polarization from HAADF-STEM for superlattice layering plotted as a function of composition. Ferroelectric distortions are observed for the $(LuFeO_3)_m/(LuFe_2O_4)_1$ superlattices with $m \geq 2$ $(m/(m+2n) \geq 0.5)$. Figure is taken from Ref. 1.

there is some short-range ferromagnetism above the magnetic transition temperature.

Figure 2.28c,d shows the Curie temperature and the saturation magnetic moment as a function of $LuFeO_3$ layer number. Both Curie temperature and magnetic moments increases monotonically with m. This has been determined to be associated with the stronger Lu-layer distortion at the interface [1], however, the mechanism of how the Lu-layer distortion influences the magnetization is not very clear. In this dissertation, we proposed a spectroscopic method to investigate the microscopic origin of this high temperature magnetism.

Figure 2.28e displays the polarization as a function of m. The polarization is extracted from the STEM images through the Lu-layer distortion amplitude. It clearly shows that the electric polarization increases with m, which proves the superlattices are ferroelectric. The temperature dependence of the ferroelectric order in the $(LuFeO_3)_m/(LuFe_2O_4)_1$ superlattices was further probed using variable-temperature X-ray linear dichroism (XLD). Fittings to a universal order parameter suggest ferroelectric transitions at about 550 K and 500 K for the $m = 3$ and $m = 5$ samples, respectively. The dichroic signal for the $m = 9$ sample persists beyond the measurement range, suggesting a higher-temperature ferroelectric transition [1]. Figure 2.29 displays the local ferroelectric switching in (9,1) superlattice by using the piezoresponse force microscopy (PFM). A $(LuFeO_3)_9/(LuFe_2O_4)_1$ film was electrically poled at 300 K to construct distinct “up” and “down” c-oriented polar domains as shown in Fig. 2.29a. The resulting magnetic order was then imaged at 200 K and 320 K using X-ray magnetic circular dichroic photoemission electron microscopy (XMCD PEEM) on the Fe L_3 edge [1]. As shown in the ratio images in Fig. 4b, c, the magnetic ordering directly correlates with the electrically poled domain structure, demonstrating magnetoelectric coupling between ferroelectricity and magnetism [1].

Another important problem in this family of materials is to determine the correct

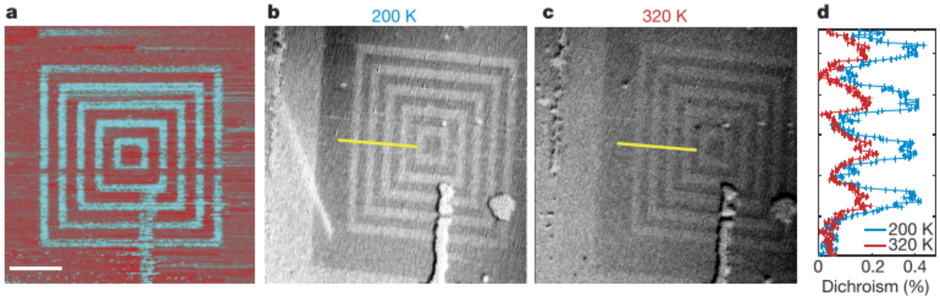

Figure 2.29: **a,** Out-of-plane piezoresponse force microscopy (PFM) image at 300K of the domain structure following electrical poling using a d.c. bias applied to the proximal tip. The “up” and “down” *c*-oriented domains appear in turquoise and red, respectively. Scale bar, 3 m. **b, c,** X-ray magnetic circular dichroism (XMCD) PEEM ratio images from the Fe L_3 edge acquired at 200 K (b) and 320 K (c). The correlation between the electrical poling and magnetic imaging demonstrates electric-field control of ferrimagnetism at 200 K. **d,** Comparison of the dichroic signals along the yellow lines in **b** and **c**. Figure is taken from ref. 1

charge-ordering states in the superlattices. It is well known that there are degenerate charge-ordering states in the $LuFe_2O_4$ end member [34, 242]. The charge-ordering in the Fe-bilayers are the key to determine ferroelectricity in this system. Prior studies reveal an antiferroelectric charge-ordering state in the bulk $LuFe_2O_4$ [242]. The charge ordering in the superlattices are much more complicated due to the Lu-layer distortion at the interface. Figure 2.30 displays three possible charge-ordering states in the $(LuFeO_3)_m/(LuFe_2O_4)_n$ superlattices. These three charge-ordered states are nearly degenerate [1]. For the single domain type, all the Lu-layer distortion is along the same direction, with the "up-up-down" pattern along the *c*-axis. This result in a ferroelectric state where all the polarization are pointing to the upper c direction. In the Fe bilayers in the $LuFe_2O_4$ site, the upper Fe layer has the ratio of 1:2 between the Fe^{2+} and Fe^{3+} centers, whereas the bottom Fe layer shows the 2:1 charge ratio. This state supports for polar Fe double layer. Cases are more complicated in the doped-type charge-ordering pattern. In this state, there is a spontaneous electron transfer from the Fe^{2+} site in the Fe bilayer to the Fe^{3+} site in the middle Fe layer in the $LuFeO_3$ layers. This reverses the Lu distortion at the interface and flips the polarization direction. In this case, the tail-to-tail and head-to-head ferroelectric domain walls are formed in the non-polar $LuFe_2O_4$ layer. The undoped-states is in between those two states. Determining the correct charge-ordering states in the superlattices are essential because it determines the magnetic ground state in the superlattices. In this dissertation, we combine the magnetic circular dichroism and the first-principle calculations to resolve this issue. Details of this work is described in Chapter 6.

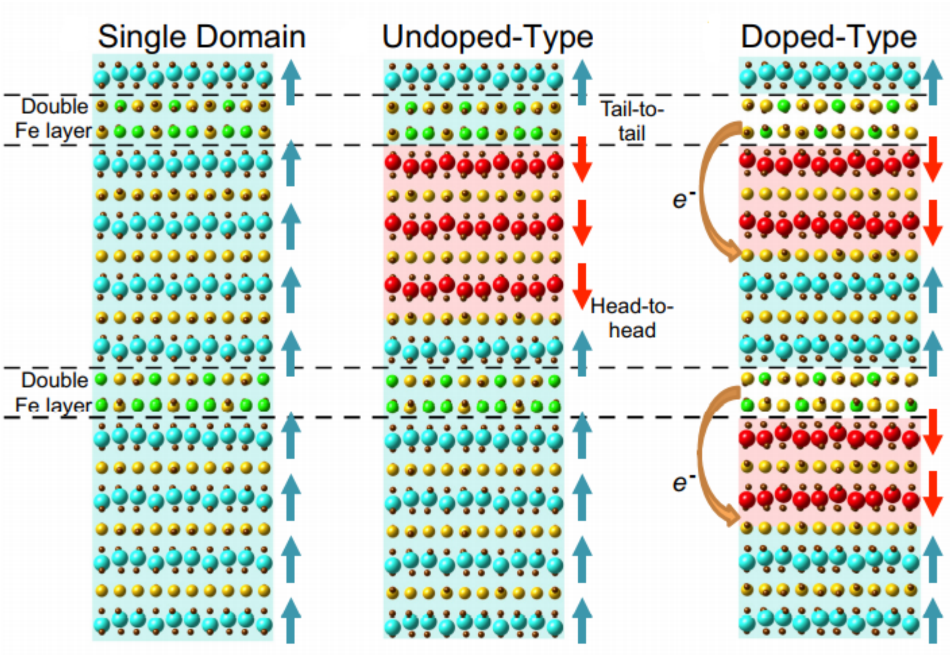

Figure 2.30: Different charge-ordering states in the $(\mathrm{LuFeO_3})_m/(\mathrm{LuFe_2O_4})_n$ superlattices. Figure is taken from Ref. 1.

Chapter 3

Spectroscopic Methods

3.1 Spectroscopy of materials

This chapter describes the theory of light-matter interaction and experimental setup of some spectroscopic techniques including infrared, Raman, optical spectroscopy and magnetic circular dichroism. Spectroscopic methods under different external stimulus such as variable temperatures and high magnetic field are introduced as well. At the end of this chapter, we explain the detailed procedure of sample growth, spectroscopic measurements, data analysis, and complementary first-principles calculations on intercalated transition metal dichalcogenides and engineered high-temperature multiferroic superlattices.

3.1.1 Fundamentals of absorption spectroscopy

One of the most common spectroscopic techniques is absorption spectroscopy. It measures the absorption of electromagnetic radiation as a function of wavelength or frequency. Usually, we use infrared, visible or ultraviolet light as a radiation source. Quantum mechanically, particles in the matter will absorb the energy of photons, which leads an electronic excitation to higher energy levels (Fig. 3.1).

Light fields will act to couple quantum states of the matter, and provide a time-dependent perturbation to the potential of the Hamiltonian:

$$\hat{H(t)} = \hat{H}_0 + \hat{V(t)}. \tag{3.1}$$

Here, $\hat{H}_0$ is the unperturbed Hamiltonian and $\hat{V(t)}$ defines the time dependence of the interaction between the system and external (perturbing) field(s). The interaction operator introduces time-dependence into the Hamiltonian.

When the frequency of the light matches the energy difference of the two quantum states, the light may be absorbed or emitted, as shown in Fig. 3.1. For instance, the transition rate created by one-photon from initial state to final state $|i\rangle$ is, in accordance with Fermi's golden rule, proportional to the transition moment squared of the invoking operator [151–154], as shown by the following:

$$P_{ij}(\omega) = \frac{\pi}{2\hbar^2}|M|^2\delta(\omega - \omega_{ij}). \tag{3.2}$$

Here, ω is the frequency of the optical field, $\hbar\omega_{ij} = E_j$ - E_i, $M = \langle i|\hat{\mu}|j\rangle$ is the transition moment integral, $\langle i|$ and $|j\rangle$ correspond to the initial and final state, respectively. $\hat{\mu}$ is the dipole moment operator (for the infrared and optical spectroscopy). This dipole moment is a function of r and can be expanded as a Taylor series about the equilibrium position $r = r_e$. The magnitude of M gives the intensity of the absorption response. For infrared and optical spectroscopy, the intensity is proportional to the square of the change in the dipole moment:

$$I \propto |M|^2 \propto |\frac{d\mu}{dr}|^2_{r_e}. \tag{3.3}$$

Therefore, Eqn 3.3 describes the selection rule for the infrared and optical

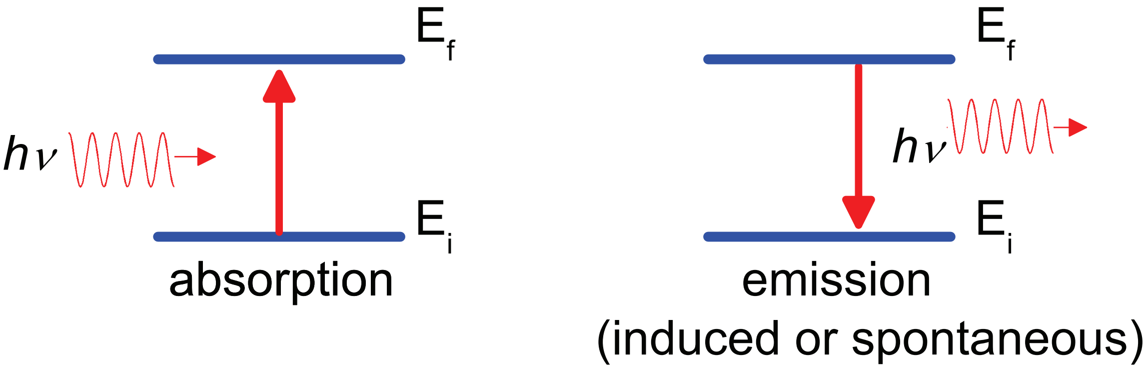

Figure 3.1: Schematic view of the light-induced electronic excitation and emission.

spectroscopy: if the moment integral is equal to zero, the transition is not allowed. If it is not equal to zero, then the transition is allowed.

Spectroscopy of solids differs from that of a molecule. It is far more complex due to the periodic arrangement of atoms/ions/molecules in a solid state. We study different properties of materials by using certain frequency range of light. Figure 3.2 displays a chart that identifies some of the excitations that govern the material's physics and indicates the part of the spectrum where they might be expected to appear. In this dissertation, we mainly focus on studying phonons, free-carrier responses, and interband electronic excitations of materials.

A Phonon is a collective lattice vibration in solids. In a 3D crystalline material with N number of atoms per unit cell, lattice vibrations are described in terms of 3N branches for the phonon dispersion curves. The latter contains three acoustic branches and 3N - 3 optical branches (Fig. 3.3). Infrared spectroscopy probes excitations at the center of the first Brillouin Zone ($k = 0$), while their dispersion is usually explored by inelastic neutron scattering techniques. Acoustic phonons includes one longitudinal mode and two transverse modes. The former are waves that occur due to in phase displacement of atoms present in the lattice of the crystal. The latter is a moving wave where atom oscillations are perpendicular to the direction of the wave or path of propagation. Acoustic phonons travel with sound velocity and converges to zero at the center of the Brillouin zone. Optical phonons are "internal vibrations" of atoms which exhibit non-zero frequency at the center of the Brillouin Zone. They are of interest to spectroscopists. Since infrared spectroscopy probes the dipole moment change inside materials, the displacement motion of the infrared active phonon has to be asymmetric.

Besides phonons, some low energy electronic excitations can also take place in the far infrared region. For metallic materials, electrons at the Fermi level are easily

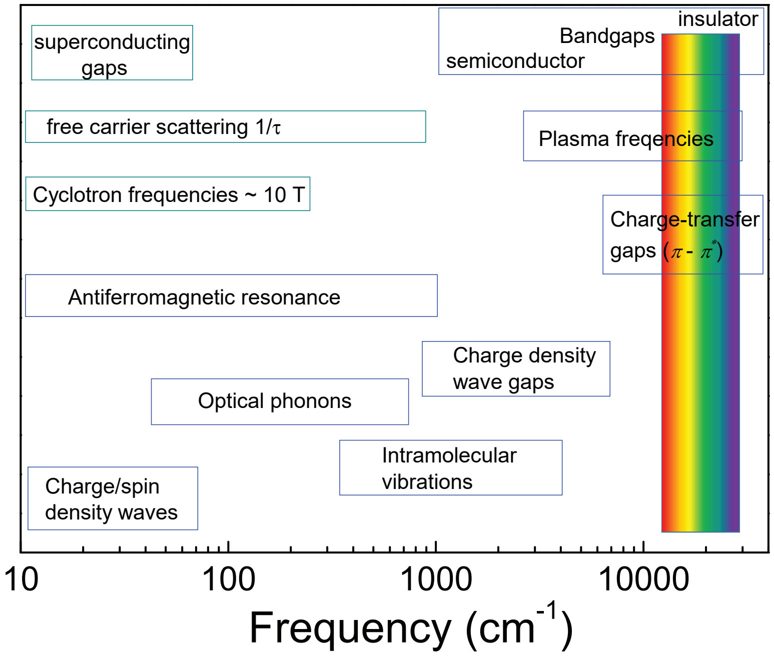

Figure 3.2: Chart showing optical processes in solids, with an indication of the frequencies where these processes typically may be studied [26].

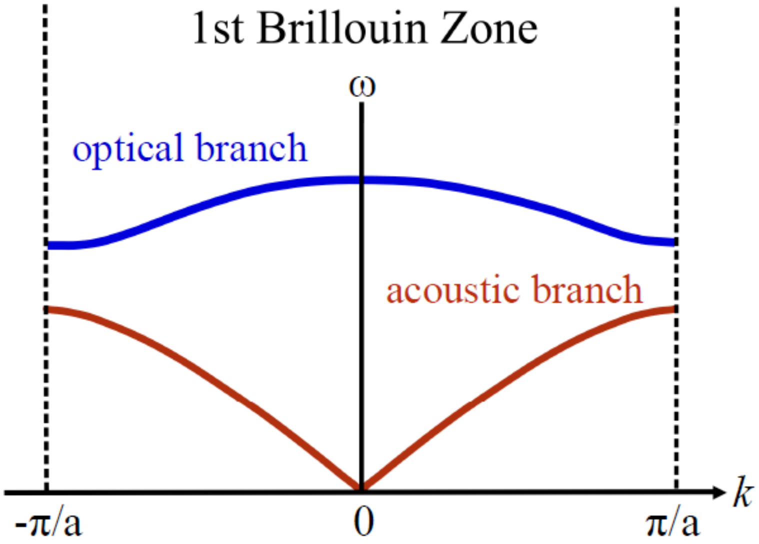

Figure 3.3: Phonon dispersion curves for the simple linear diatomic chain (-A-B-A-B-type), with optical and acoustic branches [155].

excited, which causes a strong free carrier response (a Drude peak) at very low energies. In this case, infrared active phonons are usually screened. For semiconductors and insulators, phonons are strong and usually easy to identify in the spectra. However, some of the materials have electronic excitations or magnons at low energies, which can mix with the phonons at the far infrared region. One way to separate them from phonons is to perform the oscillator strength sum rule analysis on the variable temperature spectra. The oscillator strength of a pure phonon peak is conserved with temperature, whereas that of a phonon peak mixed with electronic excitations or magnons is not conserved with temperature.

We use visible and ultraviolet light to study the electronic excitations at higher energies. These excitations are usually associated with the crystal field splitting or the band gap of materials. Tracking the energy of those type of excitations with temperature, pressure, or magnetic field can provide us a deep understanding of the electronic structures, phase transitions, and spin-charge coupling inside solids.

3.1.2 Theory of Raman spectroscopy

Raman spectroscopy is another important technique for exploring the vibrational properties of materials. The origin of the Raman signal is different from that of the infrared spectroscopy because Raman is based on the scattering of photons rather than on the absorption. The scattering process can be illustrated readily on the basis of classical physics. When a medium is subject to an electric field of strength E, it undergoes a distortion due to the opposite motion of electrons and nuclei governed by the Coulomb interactions. As a result, the applied field induces a dipole moment in the material:

$$\mu_{\mathbf{ind}} = \alpha \mathbf{E} = \alpha E_0 cos(2\pi\nu_0 t). \tag{3.4}$$

Here, α is the polarizability. If a molecule vibrates and modulates this induced dipole moment then the linear dependence of the polarizability on vibrational coordinate can be expressed as:

$$\alpha = \alpha_0 + \left.\frac{d\alpha}{dQ_i}\right|_{Q_i=0} Q_i^0 cos(2\pi\nu t). \tag{3.5}$$

Here Q is the vibrational coordinate, Q_i^0 is the vibrational amplitude, and α_0 and $d\alpha/dQ_i$ are evaluated the equilibrium position. Substituting the eqn 3.5 into eqn 3.4 one obtains:

$$\mu_{\mathbf{ind}} = \alpha_0 E_0 cos(2\pi\nu t) + \frac{1}{2}\left.\frac{d\alpha}{dQ_i}\right|_{Q_i=0} Q_i^0 E_0[cos2\pi(\nu_0+\nu)t + cos2\pi(\nu_0-\nu)t]. \tag{3.6}$$

The first term is responsible for the Rayleigh scattering at ν_0 while the second and third terms correspond to the inelastic Raman scattering, anti-Stokes (ν_0 + ν) and Stokes (ν_0 - ν), respectively. Thus, for the vibration to be Raman-active, the change in polarizability is required (i.e. $(d\alpha/dQ_i) \neq 0$). As in the case of infrared spectroscopy, the measured Raman intensity is proportional to the square of the change in the polarizability:

$$I \propto |\frac{d\alpha}{dQ_i}|^2. \tag{3.7}$$

When considering the quantum mechanics interpretation, light is considered as a collection of photons with different frequencies. Figure 3.4 displays the fundamental concept of the Raman spectroscopy. Rather than an absorption technique (infrared), Raman spectroscopy studies the scattering of photons. The incoming photon collides with crystal lattice, result in an energy and momentum transfer. Atoms in the crystal lattice absorb the photon energy after collision, being excited to a virtual energy

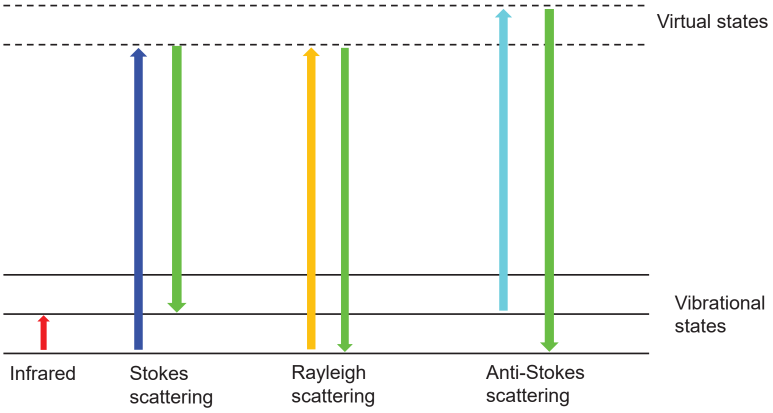

Figure 3.4: Schematic energy diagram which shows the process of Stokes, Rayleigh and Anti-Stokes scattering, as well as the concept of IR spectroscopy.

state. When this occurs, there are three different potential outcomes. First, the atoms can relax back down to the ground state and emit a photon of equal energy to that of the incident photon; this is an elastic process and is again referred to as Rayleigh scattering ($\nu_i = \nu_f$). Second, the atoms can relax to a real phonon state and emit a photon with less energy than the incident photon; this is called Stokes shifted Raman scattering ($\nu_i > \nu_f$). The third potential outcome is that the atoms are already in an excited vibrational state, is excited to a higher virtual state, and then relaxes back down to the ground state emitting a photon with more energy than the incident photon; this is called Anti-Stokes Raman scattering ($\nu_i < \nu_f$). Due to the fact that most atoms in the crystal lattice will be found in the ground state at room temperature, there is a much lower probability that a photon will be Anti-Stokes scattered. As a result, the intensity of the Anti-Stokes lines is much smaller than the Stokes scattering. In this work, most Raman measurements are performed considering only the Stokes shifted light.

3.1.3 Maxwell's equations and dielectric properties of materials

Since light has both electric and magnetic field vectors, the interaction between light and matter are well described by the Maxwell's equations. Spectroscopy provides a microscopic study of the electronic properties of materials, therefore, we only focus on the differential form of the Maxwell's equations (In SI units) [156]:

$$\nabla \cdot \mathbf{D} = \rho^{ext} \tag{3.8}$$

$$\nabla \cdot \mathbf{B} = 0 \tag{3.9}$$

$$\nabla \times \mathbf{E} = -\frac{\partial \mathbf{B}}{\partial t} \tag{3.10}$$

$$\nabla \times \mathbf{H} = \frac{\partial \mathbf{D}}{\partial t} + \mathbf{J}^{cond} + \mathbf{J}^{ext}, \tag{3.11}$$

where **E** and **H** are the electric and magnetic fields, **D** and **B** are the displacement field and magnetic induction, J^{cond} is current density arising from the motion of conduction electrons, and J^{ext} and ρ^{ext} are current and charge density induced by external force.

When electromagnetic waves interact with different media, their electric and magnetic field vector will induce the internal polarization or magnetization of the media, and cause the charge and spin re-distribution at the surface. For isotropic media, the linear relations between the internal polarization or magnetization and field vectors can be obtained as:

$$\mathbf{P} = \chi_e \mathbf{E} \tag{3.12}$$

$$\mathbf{M} = \chi_m \mathbf{H} \tag{3.13}$$

$$\mathbf{D} = \epsilon \mathbf{E} \tag{3.14}$$

$$\mathbf{B} = \mu \mathbf{H} \tag{3.15}$$

$$\mathbf{J}^{cond} = \sigma \mathbf{E}, \tag{3.16}$$

where **P** is polarization, **M** is magnetization, χ_e is the electric susceptibility, χ_m is the magnetic susceptibility, ϵ is the dielectric function, μ is the magnetic permeability, and σ is the conductivity. For anisotropic and inhomogeneous media, the susceptibility or conductivity will be a tensor.

Now we consider how light interaction with an isotropic media. Since our world is neutral, $\rho^{ext} = 0$. The dielectric constant ϵ is not depend on the spatial direction. Then we can simplify the Maxwell's equation and obtain the following equation:

$$\nabla^2 \mathbf{E} = \frac{\epsilon}{c^2} \frac{\partial^2 \mathbf{E}}{\partial t^2} \tag{3.17}$$

We only consider the electric field here because the energy provided by the electric field vector is much greater than by the magnetic field for an electromagnetic wave. This is a typical plane-wave equation, the solution of this equation should be in a complex form:

$$\mathbf{E} = \mathbf{E_0} e^{[i(\mathbf{k}\cdot\mathbf{r} - \omega t)]} \tag{3.18}$$

where $\mathbf{k}$ is the wave vector and ω is the angular frequency. Substituting equation 3.18 into equation 3.17 yields

$$k^2 = \frac{\omega^2}{c^2} \epsilon(\omega). \tag{3.19}$$

Now we introduce the frequency dependence of the dielectric constant ϵ because of the oscillation of electric field vector in a plane wave.

In this dissertation, a significant portion involves how circular polarized light interacts with materials. So we will also show how some corresponding relationship/extension in parallel to the classically defined methodology. When light shines on a material, either transmission, reflection, or absorption will happen. The total energy of the light is the summation of these three parts: $A + T + R = 1$, where A, T, and R refer to absorbance, transmittance, and reflectance coefficient. For a plane wave, the refraction coefficient will be in a complex form. The complex refractive index with unpolarized and circularly polarized light are:

$$N(\omega) = n(\omega) + i\kappa(\omega) \tag{3.20}$$

$$N_{\pm}(\omega) = n_{\pm}(\omega) + i\kappa_{\pm}(\omega), \tag{3.21}$$

Similarly, the dielectric functions are also complex:

$$\epsilon(\omega) = \epsilon_1(\omega) + i\epsilon_2(\omega) \tag{3.22}$$

$$\epsilon_{\pm}(\omega) = \epsilon_{1\pm}(\omega) + i\epsilon_{2\pm}(\omega), \tag{3.23}$$

Here, n and κ are the refractive index and the extinction coefficient, ϵ_1 and ϵ_2 are the real and imaginary part of complex dielectric function, and the ± represents the right- and left-circularly polarized (RCP/+ and LCP/-) light components.

The relation between $N(\omega)$ and $\epsilon(\omega)$ can be expressed by:

$$N(\omega) = \sqrt{\epsilon(\omega)}, \tag{3.24}$$

By combining equation 3.19 and equation 3.24, we can obtain the following relation:

$$k = \frac{\tilde{N}\omega}{c}. \tag{3.25}$$

Combining equation 3.20, 3.22, and 3.24, we can derive the following relations:

$$N^2 = n^2 - \kappa^2 + 2in\kappa = \epsilon = \epsilon_1 + i\epsilon_2. \tag{3.26}$$

Where we can easily see that

$$\epsilon_1 = n^2 - \kappa^2 \tag{3.27}$$

$$\epsilon_2 = 2n\kappa. \tag{3.28}$$

In turn, we can express n and κ as a function of ϵ_1 and ϵ_2:

$$n = \sqrt{(|\epsilon| + \epsilon_1)/2} \tag{3.29}$$

$$\kappa = \sqrt{(|\epsilon| - \epsilon_1)/2}, \tag{3.30}$$

where $|\epsilon| = \sqrt{(\epsilon_1)^2 + (\epsilon_2)^2}$.

From these equations, a lot of optical constants can be derived; here, we will focus on finding the absorption coefficient α and optical conductivity σ. Because when light hit a solid, the electromagnetic wave will be dampened with a decay length $c/\omega\kappa$. A new wave equation that includes a damping factor can be rewritten as:

$$E(x,t) = E_0 e^{i[(\tilde{N}\omega/c)x - \omega t]} = E_0 e^{-(2\pi\kappa/\lambda_\omega)x} e^{i(kx-\omega t)} \tag{3.31}$$

The expression $2\pi\kappa/\lambda_\omega$ describes the attenuation of the field and λ_ω is the light wavelength in vacuum. The first exponential factor describes the attenuation of wave amplitude with distance.

We consider the Poynting vector $\mathbf{S}$ of the electromagnetic wave. The time-averaged Poynting vector of an electromagnetic wave can be written as:

$$\mathbf{S} = \frac{1}{2}\mathbf{E} \times \mathbf{H} \tag{3.32}$$

Substitute the wave equations of both electric and magnetic field, and then take the real part of equation 3.32, we have:

$$\mathbf{S} = |\mathbf{E_0^2}|e^{\frac{-2x\omega\kappa}{c}} \tag{3.33}$$

The time-averaged Poynting vector is directly proportional to the intensity, which is also proportional to the square of amplitude of the electric field vector. As a result, by combining Beer's law, we have:

$$I(x) = EE^* = I_0 e^{-\alpha x}, \tag{3.34}$$

then a relationship between κ and α is found as

$$\alpha = \frac{2\omega\kappa}{c} = \frac{4\pi\kappa}{\lambda_\omega}. \tag{3.35}$$

Note that because $\epsilon_2 = 2n\kappa$, α can be related to the imaginary part of the dielectric function as:

$$\alpha = \frac{\omega\epsilon_2}{cn} \tag{3.36}$$

Adding the circular polarization to this equation, we obtain:

$$\alpha_\pm = \frac{\omega\epsilon_{2\pm}}{cn_\pm} \tag{3.37}$$

For a medium with finite conductivity, from the Maxwell's equations, we can calculate the relation between dielectric function and conductivity:

$$\epsilon(\omega) = 1 + \frac{i\sigma(\omega)}{\omega\epsilon_0} \tag{3.38}$$

$$\epsilon_\pm(\omega) = 1 + \frac{i\sigma_\pm(\omega)}{\omega\epsilon_0}, \tag{3.39}$$

Then, we can re-write the absorption coefficient as a function of conductivity as:

$$\alpha = \frac{\sigma_1}{n\epsilon_0 c} \tag{3.40}$$

$$\alpha_\pm = \frac{\sigma_{1\pm}}{n_\pm \epsilon_0 c}, \tag{3.41}$$

Where σ_1 is the real part of the conductivity. From this relation, we know that a material with low resistivity (high conductivity) has high absorption. Table 3.1 lists the relationships between the various response functions of $\epsilon(\omega)$, $\sigma(\omega)$, and $\tilde{N}(\omega)$. [156]

3.1.4 Beer - Lambert law

Despite the derivation of the absorption coefficient from the above mentioned method, we can also obtain the absorption coefficient from the measured transmittance spectra. Beer - Lambert law provides a more direct way to analyze the attenuation of the light for a sample thickness $d < \delta = \frac{c}{\omega\kappa}$, where δ is the penetration depth.

The Beer-Lambert law is a linear relationship between the absorbance and the concentration of the attenuating species (c), molar attenuation coefficient (ϵ) and optical path length (l) of a material:

$$A = \epsilon l c \tag{3.42}$$

Table 3.1: Relationships between the various response function $\epsilon(\omega)$, $\sigma(\omega)$, and $N(\omega)$

Dielectric constant $\epsilon(\omega)$	Conductivity $\sigma(\omega)$	Refractive index $N(\omega)$
$\epsilon = \epsilon_1 + i\epsilon_2$	$\epsilon_1 = 1 - \frac{4\pi\sigma_2}{\omega}$	$\epsilon_1 = n^2 - \kappa^2$
$\sigma_1 = \frac{\omega\epsilon_2}{4\pi}$	$\epsilon_2 = \frac{4\pi\sigma_1}{\omega}$	$\epsilon_2 = 2n\kappa$
$\sigma_2 = (1 - \epsilon_1)\frac{\omega}{4\pi}$	$\sigma = \sigma_1 + i\sigma_2$	$\sigma_1 = \frac{n\kappa\omega}{2\pi}$
$n = (\frac{1}{2}((\epsilon_1^2 + \epsilon_2^2)^{1/2} + \epsilon_1))^{1/2}$	$n = (\frac{1}{2}(((1 - \frac{4\pi\sigma_2}{\omega})^2 + (\frac{4\pi\sigma_1}{\omega})^2)^{1/2} + (1 - \frac{4\pi\sigma_2}{\omega})))^{1/2}$	$\sigma_2 = (1 - n^2 + \kappa^2)\frac{\omega}{4\pi}$
$\kappa = (\frac{1}{2}((\epsilon_1^2 + \epsilon_2^2)^{1/2} - \epsilon_1))^{1/2}$	$n = (\frac{1}{2}(((1 - \frac{4\pi\sigma_2}{\omega})^2 + (\frac{4\pi\sigma_1}{\omega})^2)^{1/2} - (1 - \frac{4\pi\sigma_2}{\omega})))^{1/2}$	$N = n + i\kappa$

For a sample with small reflectance, the intensity of the transmitted light is given by:

$$I = I_0 e^{-\alpha d} \tag{3.43}$$

with I and I_0 being the intensities of the transmitted and incident beams, respectively, d being the thickness, and α the absorption coefficient. We then can calculate the absorbance using the following two equations:

$$T = \frac{I}{I_0} \tag{3.44}$$

$$A = -\ln\frac{I}{I_0} = \alpha d. \tag{3.45}$$

Finally, the absorption coefficient $\alpha(\omega)$ is given by:

$$\alpha = -\frac{1}{d}\ln(T(\omega)), \tag{3.46}$$

giving the absorption coefficient α directly from sample thickness d and from transmittance as a function of frequency $(T(\omega))$. [157]

One important limitation of the Beer - Lambert law is the requirement of minimal or negligible reflectance. For a material with significant reflectance, the reflectance, optical constants can be derived from a combination of reflectance and transmittance spectra. A correction that includes the contribution of the reflectance is given as:

$$T = \frac{(1-R)^2 e^{-\alpha d}}{1 - R^2 e^{-2\alpha d}} \tag{3.47}$$

where R is the reflectance at the sample surface [158, 159]. The full connection is called Glover-Tinkham analysis [156, 160].

3.1.5 Polarized light and crystal anisotropy

Light is a transverse wave, the oscillation direction of the electric field wave vector **E** lies in the plane perpendicular to the light wave propagating direction [Fig. 3.5]. Polarized light is produced when the direction of E in the plane perpendicular to the direction of propagation is constrained in some fashion.

In general, the polarized light can be divided into three different types: linear, circular, and elliptical. The classification is based on the phase difference between E$_x$ and E$_y$. Let $E_x = E_{0x}\mathrm{e}^{[i(kz-\omega t)]}$, E$_y$ $= E_{0y}\mathrm{e}^{[i(kz-\omega t+\phi)]}$, where ϕ refers to the phase, the conditions for different polarized light is summarized in Table 3.2. As an example, figure 3.5 displays a diagrammatic representations of linearly and circularly polarized light as produced by an unpolarized light beam entering from the right and propagating through first a linear polarizer oriented at 45 degree and then a quarter wave plate with its fast axis oriented vertically. The linear polarizer transmits fully linearly polarized light, while the quarter wave plate delays the horizontal component of this light by 1/4 wave relative to the vertical component, producing left-handed circularly polarized light [161].

In anisotropic materials, their physical properties are directional dependent. The crystal symmetry is strongly associated with the electronic, vibrational, and magentic properties. When light interacts with an anisotropic crystal, the speed of light is dependent on the light polarization direction because of the different refraction index. In this case, the dielectric constant becomes a tensor, the relations between the electric displacement **D** and the electric field **E** can be written as:

$$\begin{aligned} D_x &= \epsilon_{xx}E_x + \epsilon_{xy}E_y + \epsilon_{xz}E_z \\ D_y &= \epsilon_{yx}E_x + \epsilon_{yy}E_y + \epsilon_{yz}E_z \\ D_z &= \epsilon_{zx}E_x + \epsilon_{zy}E_y + \epsilon_{zz}E_z \end{aligned} \tag{3.48}$$

The nine quantities ϵ_{xx}, ϵ_{yy},... constitute the dielectric tensor. The dielectric

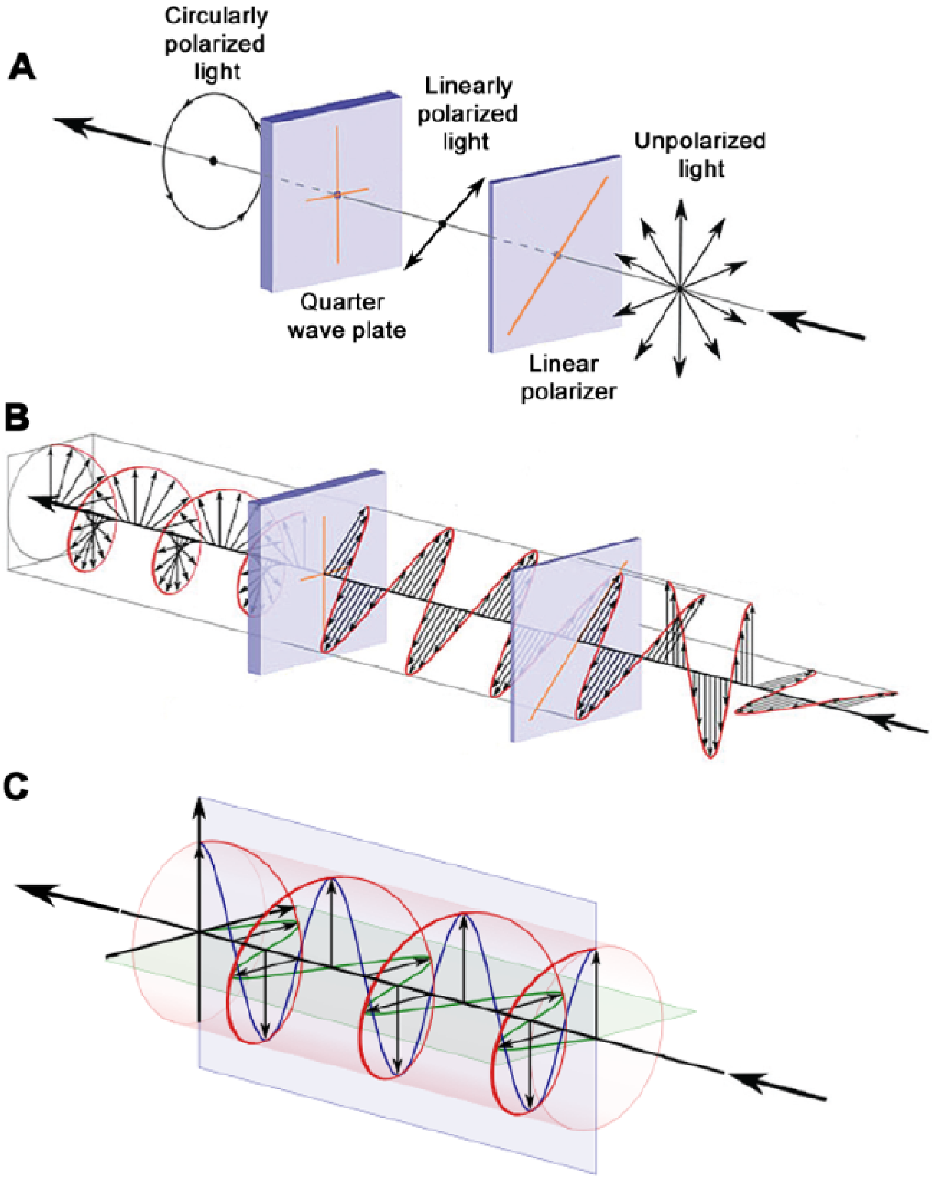

Figure 3.5: Schematic diagram of the representation of the unpolarized, linearly polarized, and circularly polarized light. Panels A and B illustrate two ways of portraying polarization (as axes or vectors). Panel C shows the successive peaks of the horizontal (green) and vertical (blue) components of the same circularly polarized wave, as well as the helical path traced by their resultant vectors (red) [161]. (Figure modified from Wikipedia.)

Table 3.2: Conditions for different polarized light

Phase difference $\Delta\phi$	Types of polarization
$\Delta\phi = n\pi$, $(n = 0, 1, 2...)$	linear polarization
$\Delta\phi$ = arbitrary but constant, (exclude $n\pi$ and $\frac{n\pi}{2}$)	elliptical polarization
$\Delta\phi = \frac{n\pi}{2}$, $(n = \pm\ 1, 3, 5)$	left or right circular polarization
ϕ, E_x, and E_y are randomly varying on a timescale that is much shorter than that needed for observation	unpolarized light

properties of an anisotropic material is thus depend on the light polarization direction.

3.1.6 Drude and Lorentz model

When materials interact with light, the electronic properties can usually be described by two models: the Drude model and the Lorentz model. The former quantitatively characterizes the free-carrier response of metallic materials, and the latter applies to the semiconductors and insulators.

The dielectric function of materials can be modeled by three parts:

$$\epsilon = \epsilon_{free} + \epsilon_{bound} + \epsilon_{\infty}, \tag{3.49}$$

where ϵ_{bound} is contributed from bound carriers and ϵ_{free} is the contribution from free electrons (or holes). For metallic compounds, at relatively low energies (below the plasma frequency), ϵ_{free} dominates the optical response and screen the contributions from ϵ_{bound} due to the large densities of the free-carriers. Above the plasma frequency, the energy is large enough to populate the bound carriers, where the interband excitations begin to dominate the optical response.

We will discuss the Drude model first. Figure 3.6 displays a schematic view of the charge distribution in a metallic crystal. Each metal ion consists of a nucleus and core electrons, which are immobile. Valence electrons are weakly bounded to the metal ions, generating the free-electron gas. Those electrons are highly delocalized and are also called conduction electrons.

There are four assumptions for the Drude model: (i) electron – electron, electron – metallic ion interactions between collisions are neglected. (ii) Drude only consider the collision between electrons and impenetrable ion cores, which is an instantaneous process. The scattering due to electron – electron collisions are neglected. (iii) An

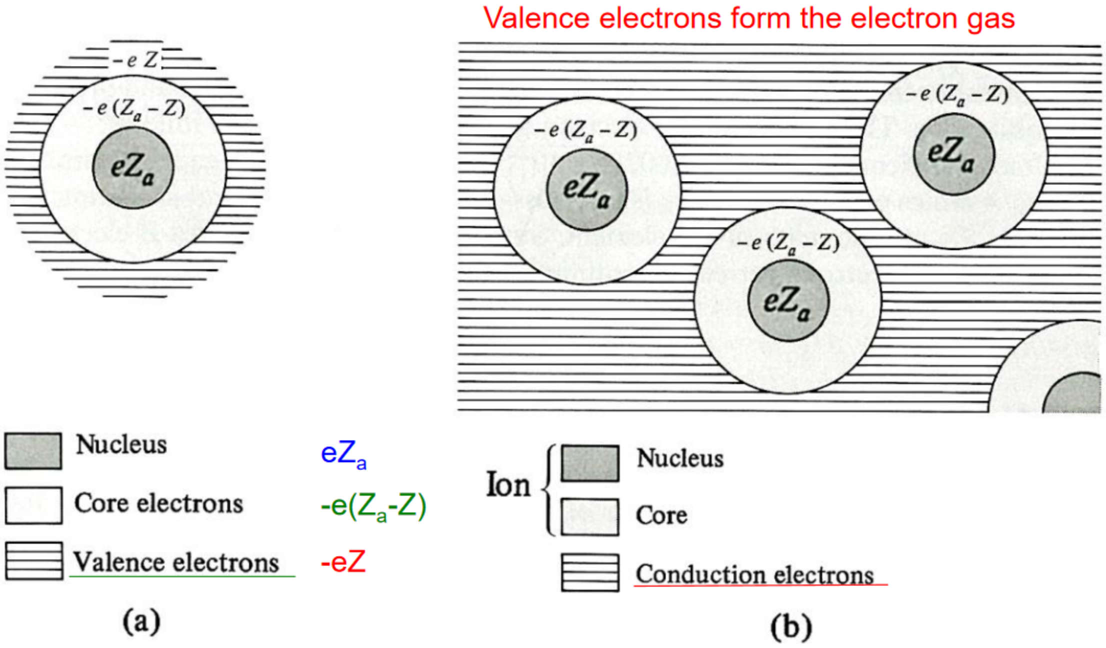

Figure 3.6: (a) The schematic view of the nucleus, core electrons, and valence electrons in an atom, the different amount of charges are indicated below [25]. (b) The schematic view of the charge distribution in a metal [25].

electron experiences a collision with a probability per unit time $1/\tau$, The probability to undergo a collision within a small time interval dt is dt/τ. Where τ is called relaxation time or mean free time, which means the average travel time for a random electron before its next collision. (iv) After each collision an electron emerges with a velocity that is randomly directed and with a speed appropriate to the local temperature.

Based on the above mentioned assumptions, the equation of motion of the Drude model can be written as:

$$m\frac{d^2r}{dt^2} + m\Gamma\frac{dr}{dt} = -eE_{loc} \tag{3.50}$$

where r is the displacement, m is the effective mass of the free-carriers (usually electrons), Γ is the damping constant, which is also equal to $1/\tau$, e is the electron charge, and E_{loc} is the local electric field acting on the electron.

Assuming the electric field acting on the conduction electron is homogeneous, combining equation 3.50 and the Maxwell's equations, we can derive the dielectric functions in the following:

$$\epsilon(\omega) = \epsilon_c - \frac{4\pi ne^2/m}{\omega^2 + i\omega/\tau} \tag{3.51}$$

where $\epsilon_c \approx 1$ when not considering the polarization of the ion core. Then the real and imaginary part of the dielectric function can be derived as:

$$\epsilon_1 = \epsilon_c - \frac{\omega_p^2}{\omega^2 + 1/\tau^2} \tag{3.52}$$

$$\epsilon_2 = \frac{\omega_p^2}{\omega\tau(\omega^2 + 1/\tau^2)} \tag{3.53}$$

where $\omega_p = \sqrt{\frac{4\pi ne^2}{m}}$ is called the plasma frequency.

Using the relations described in Table 3.1, we can obtain the expression of the optical conductivity:

$$\sigma_1 = \frac{ne^2\tau/m}{1+\omega^2\tau^2} = \frac{\sigma_{dc}}{1+\omega^2\tau^2} \tag{3.54}$$

$$\sigma_2 = \omega\tau\frac{ne^2\tau/m}{1+\omega^2\tau^2} = \omega\tau\frac{\sigma_{dc}}{1+\omega^2\tau^2} \tag{3.55}$$

where $\sigma_{dc} = \frac{ne^2\tau}{m}$ is the dc conductivity of the material.

The Lorentz model supposes that the bound electrons to the nucleus act similar to a harmonic oscillator, or a mass-spring system. The electrons react to an electromagnetic field via vibrating. The equation of motion now becomes:

$$m\frac{d^2r}{dt^2} + m\Gamma\frac{dr}{dt} + m\omega_0^2 r = -eE_{loc} \tag{3.56}$$

There is an additional term $m\omega_0^2 r$, which describe the binding energy between the bound electrons and the nucleus.

Figure 3.7 displayed a schematic model of how external electric field polarizes an insulating material. Compared to metals, the electric field will cause an internal polarization in the medium because of the separation between positive and negative charges inside the material in response to the external electric field. Now the total electric field is acting on an electron is:

$$\mathbf{E}_{loc} = \mathbf{E}_{ext} + \mathbf{E}_{neighbor} + \mathbf{E}_{int} \tag{3.57}$$

where, $\mathbf{E}_{ext}$ and $\mathbf{E}_{int}$ are the external and internal electric field, respectively. $\mathbf{E}_{neighbor}$ is electric field due to the neighboring dipoles. Thus, the total electric field is the

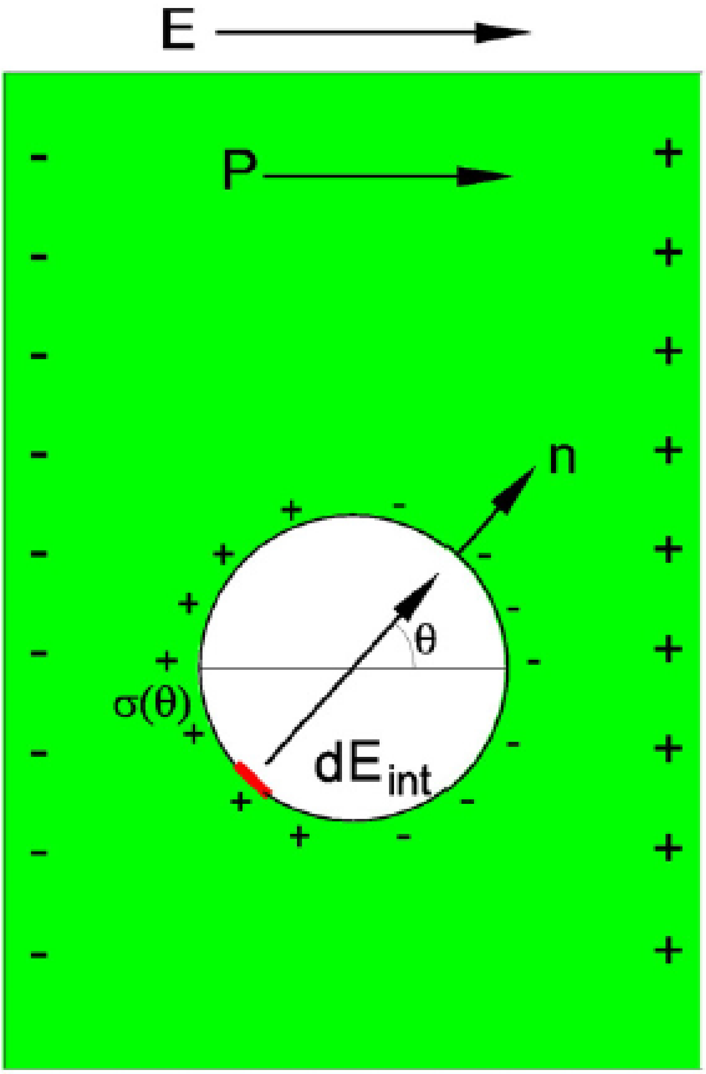

Figure 3.7: The schematic model to describe the electric polarization in an insulating material. The electric field, electric polarization, and charge distribution are depicted [26].

sum of all the fields.

The solution to equation 3.56 yields

$$r(\omega) = \frac{1}{m} \frac{-eE_{loc}}{(\omega_0^2 - \omega^2) + i\Gamma\omega}. \tag{3.58}$$

From this, the induced dipole moment μ is related to r through this equation:

$$\mu(\omega) = \frac{e^2 E_{loc}}{m[(\omega_0^2 - \omega^2) + i\Gamma\omega]}, \tag{3.59}$$

Since $\mu(\omega) = \alpha(\omega)E(\omega)$, the polarization per unit volume is given by

$$P(\omega) = N\alpha(\omega)E(\omega) = \epsilon_0 \chi(\omega)E(\omega). \tag{3.60}$$

The susceptibility $\chi(\omega)$, from the prior equation, is then

$$\chi(\omega) = \left(\frac{Ne^2}{\epsilon_0 m}\right) \frac{1}{\omega_0^2 - \omega^2 + i\Gamma\omega}, \tag{3.61}$$

where $(4\pi Ne^2/m)$ is the plasma frequency squared (ω_p^2). The dielectric function can then be written as

$$\epsilon(\omega) = 1 + \frac{\omega_p^2}{\omega_0^2 - \omega^2 + i\Gamma\omega}, \tag{3.62}$$

where ω_p equals

$$\omega_p = \sqrt{\frac{Ne^2}{\epsilon_0 m}}. \tag{3.63}$$

From this dielectric function, many optical parameters can be calculated, such as absorption $(\alpha(\omega))$, optical conductivity $(\sigma(\omega))$, refractive index $(n(\omega))$, and so on.

For this work, several instances call for the use of both the Drude and Lorentz models. These two models are extremely useful because we can use them to fit the experimental spectra to obtain the relaxation time, plasma frequency, dc conductivity, effective mass, and the carrier densities of different materials. By comparing the fit parameters for various doping concentrations, magnetic fields, or temperatures, trends can be observed. In this case, we are able to analyze how the material and specific excitations can be sensitive to different phase transitions.

3.1.7 Kramers-Kronig analysis and sum rules

There are many cases that materials do not transmit light. Therefore, reflectance measurements are needed. Kramers-Kronig analysis is a useful method to extract optical functions [156]. The reflectivity for normal incidence is given by r and the power reflectance is given by:

$$R(\omega) = rr^* = \frac{(n-1)^2+\kappa^2}{(n+1)^2+\kappa^2}. \tag{3.64}$$

The power reflectance $R(\omega)$ does not contain the phase information. The total reflectivity is given by:

$$r = \sqrt{R}e^{i\phi}, \tag{3.65}$$

The power reflectance and the phase-dispersion shift $\phi(\omega)$ are related by Kramers-Kronig transformation [156]:

$$\phi(\omega) = \frac{\omega}{\pi}\int_0^\infty \frac{lnR(\omega) - lnR(\omega^{'})}{\omega^{'2}-\omega^2} d\omega^{'}. \tag{3.66}$$

and combining equations 3.64, 3.66, and 3.65, n and k can be determined by $R(\omega)$ and $\phi(\omega)$ as

$$n(\omega) = \frac{1-R(\omega)}{1+R(\omega)-2\sqrt{R(\omega)}\cos\phi(\omega)} \tag{3.67}$$

$$\kappa(\omega) = \frac{2\sqrt{R(\omega)}\sin\phi(\omega)}{1+R(\omega)-2\sqrt{R(\omega)}\cos\phi(\omega)}. \tag{3.68}$$

From earlier identities and relationships, the real part of dielectric function and the real part of optical conductivity can be determined:

$$\epsilon_1 = n^2 - k^2 \tag{3.69}$$

$$\sigma_1 = \frac{\omega\epsilon_2}{4\pi} = \frac{\omega n k}{2\pi}. \tag{3.70}$$

All of these optical constants are frequency dependent. We can extract other optical constants such as $\alpha(\omega)$, $\tau(\omega)$ and so on. Notice that in Eq. 3.66, the integration is from zero to ∞. In reality, our optical measurements usually cover the frequency range from far-infrared to ultraviolet, proper extrapolations should be used for the low and high frequencies of the spectrum.

For the low-frequency extrapolation, there are four models can be used, depending on the properties of materials at hand. These models include: (i) a Hagen-Rubens formula, $(R(\omega) = 1-(2\omega/\pi\sigma_0)^{1/2})$, is used for a metallic materials. A constant dc conductivity extrapolation is used for insulators/semiconductors in the low frequency range. (ii) The two-fluid model: $(R(\omega) = 1-(2\omega/\pi\sigma_0)^2)$. (iii) Marginal Fermi Liquid model: $(R(\omega) = 1-(2\omega/\pi\sigma_0))$. (iv) Superconducting model: $(R(\omega) = 1-(2\omega/\pi\sigma_0)^4)$. Notice the only difference between those models are the power index of ω.

For the high frequency extrapolation, the equation is modeled as $R \sim \omega^{-x}$, where x varies from 0-4 and does not have to be an integer. The exact value of x can be determined by selecting the best match between the measured and calculated spectra when varying x.

Together with physical arguments about the behavior of the response in certain limits, the Kramers-Kronig relation can also be used to derive sum rules. That is

$$\int_0^\infty \omega' Im(-1/\epsilon(\omega'))d\omega' = 1/2\pi\omega_p^2, \tag{3.71}$$

where ω_p is the plasma frequency. A partial sum rule [156] is also useful in quantifying the change of absorption spectra

$$f \equiv \frac{2c}{N_e \pi \omega_p^2} \int_{\omega_1}^{\omega_2} n\alpha(\omega, B)\, \mathrm{d}\omega. \tag{3.72}$$

Here, f is the oscillator strength, N_e is the number of electrons per ion site, n is the refractive index, ω_p is the plasma frequency $\equiv\sqrt{\frac{e^2\rho}{m\epsilon_0}}$, e and m are the charge and mass of an electron, ϵ_0 is the vacuum dielectric constant, ρ is the density of magnetic ion sites, c is the speed of light, and ω_1 and ω_2 are the frequency limits of integration.

3.1.8 Magnetic circular dichroism

Magnetic circular dichroism (MCD) is a technique that measures the absorption difference between the left- and right- circularly polarized light under the external magnetic field. It is an magneto-optical effect, which describes a universal property of light absorption for all matter when placed in a magnetic field. The origin of the MCD signal is due to electromagnetic interaction of the external field with electronic charge within the sample. Compared to the natural circular dichorism cause by the difference of the speed of light between left- and right- circularly polarized light in a chiral molecule or crystal, MCD is an intrinsic effect for all materials. The MCD intensity can be expressed as:

$$\Delta\alpha = \alpha_- - \alpha_+ = \Delta\epsilon_M c l \mathbf{B} \tag{3.73}$$

Where $\Delta\alpha$ is the absorption difference between the left- and right- circularly polarized light, $\alpha_\pm$ represents the absorption coefficient of the left- or right- circularly polarized light, respectively. $\Delta\epsilon_M$ is the difference of the molar attenuation coefficient, c is the speed of light, l is the penetration depth, and $\mathbf{B}$ is the magnetic induction.

Magnetic circular dichroism originates from the Zeeman splitting:

$$H_{Zeeman} = -g\mu_B \mathbf{J} \cdot \mathbf{B} \tag{3.74}$$

Here, μ_B is the bohr magneton, $\mathbf{J}$ is the total electronic angular momentum, g is the Landé g-factor. The general form of the MCD intensity can be expressed as [162]:

$$I_{MCD} \sim [A(\frac{\partial f(E)}{\partial E}) + (B + \frac{C}{kT})f(E)] \tag{3.75}$$

where $f(E)$ is the linear absorption as a function of the photon energy. Notice in the Eqn 3.75, there are three terms A, B, and C. These terms have different origins. The A term describes the MCD signal from degenerate excited states. In contrast, the MCD C term originates from degenerate ground states. Since the population of electrons from the ground state depends on the thermal energy, this term is temperature-dependent. The origin of the B term relates to the mixed excited states. The physics of those terms can be better understood from the following energy diagram. Figure 3.8 displays the origin of the MCD A term as an example [162]. As shown in the figure, the ${}^1P_{1,0,-1}$ is a three-fold excited state. When applying the external magnetic field, this state splits to three different states due to the Zeeman splitting. The excitation energies induced by the left- and right- circularly polarized light is different when the external magnetic field is not zero. This is due to the

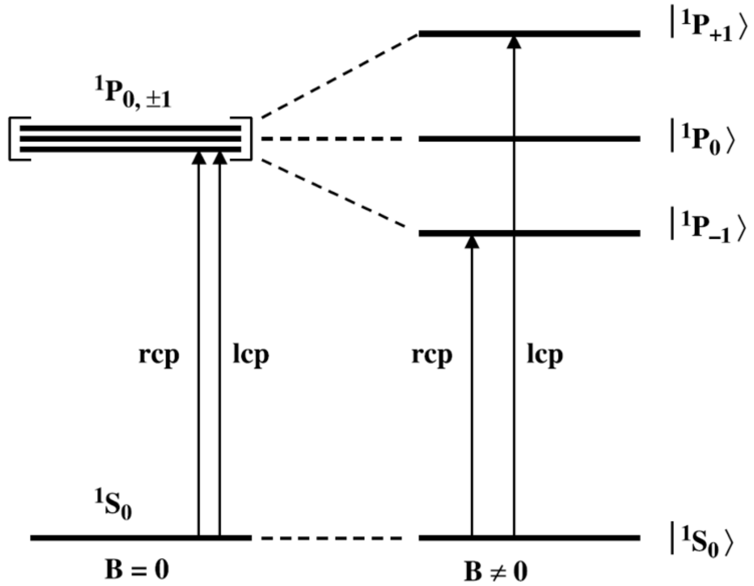

Figure 3.8: Energy levels for the atomic $s^2 \rightarrow sp$ transition. $^1S_0 \rightarrow {}^1P_{1,0,-1}$.

different selection rules for the left and right circularly polarized light ($\Delta m = +1$ for lcp; $\Delta m =$ -1 for rcp).

We can extend the understanding of the origin of MCD to solids. Figure 3.9 displays a schematic view of how band splits in a magnetic semicondutor. Since the angular momentum of the circularly polarized light can couple with the spin-angular momentum, the left and right circularly polarized light can probe the excitations in different spin channels. For a non-magnetic material (panel (a)), the excitation from the valence band to the conduction band has no spin-dependence, the corresponding MCD signal is zero in this case. For a magnetic semiconductor (panel (b)), the Zeeman interaction induces exchange splitting in the valence and conduction bands that depends upon the spin direction, forming a spin-polarized band structure which result in an absorption difference between the left and right circularly polarized light. The MCD signal is thus generated. Moreover, since the total magnetic moment in solids equals to the difference between the density of states in the spin-up and spin-down channel, the dichroic intensity is directly proportional to the magnetization in materials.

When the circular polarized light interacts with materials, it will probe the off-diagonal components of the dielectric tensor as [164]:

$$\epsilon = \begin{vmatrix} \epsilon_{xx} & i\epsilon_{xy} & 0 \\ -i\epsilon_{xy} & \epsilon_{yy} & 0 \\ 0 & 0 & \epsilon_{zz} \end{vmatrix} \approx n^2 \begin{vmatrix} 1 & iQm_z & 0 \\ -iQm_z & 1 & 0 \\ 0 & 0 & 1 \end{vmatrix}, \qquad \epsilon_{\pm} = \epsilon_{xx} \pm \epsilon_{xy}$$

Here, ± sign represents the left or right circular polarization, respectively. Notice in the dielectric tensor, the off-diagonal component is linearly proportional to the magnetic moment projected on the z-direction. This equation indicates the magnetic circular dichroism signal is directly proportional to the magnetization of materials.

The magnetic circular dichorism intensity can also be correlated to the joint

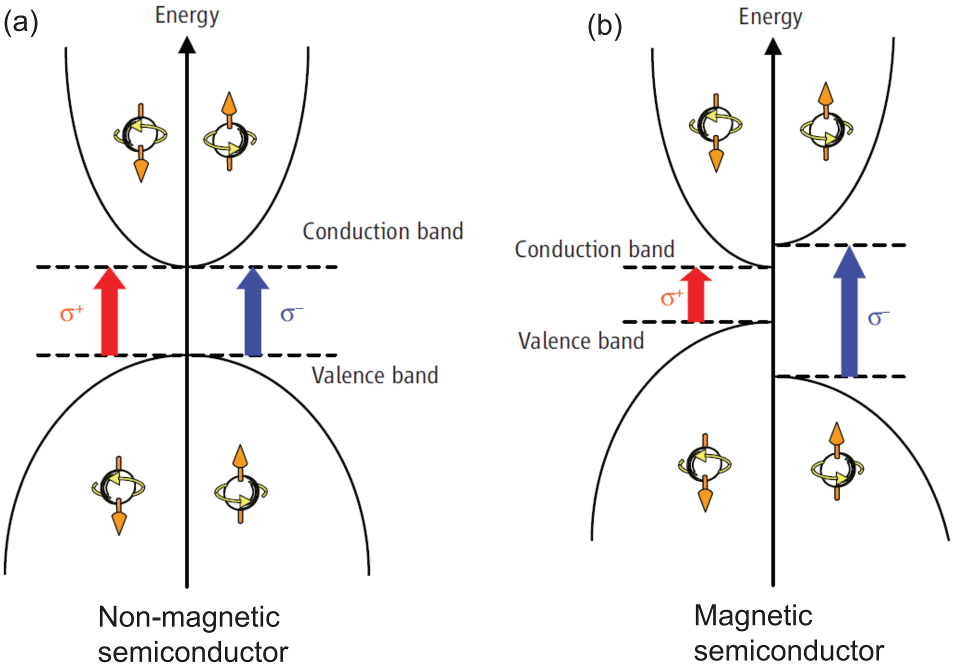

Figure 3.9: Schematic view of the density of states for (a) a non-magentic and (b) a magnetic semiconductor [163].

density of states and even to specific bands. These relationships are expressed as [32,33,165]:

$$\Delta\alpha(E)_{MCD} = \vec{\mu}_i \cdot \vec{k} = |\vec{\mu}_i||\vec{k}|\cos\theta \approx \frac{(\alpha_+(E) - \alpha_-(E))d}{2} \approx \frac{\Delta E}{2}\frac{1}{\alpha(E)}\frac{d\alpha(E)}{dE}. \tag{3.76}$$

Here, $\Delta\alpha(E)_{MCD}$ is the absorption difference between right and left circularly polarized light $(\alpha_+(E) - \alpha_-(E))$, $d\alpha(E)/dE$ is the energy derivative of the linear absorption spectrum, d is the sample thickness, ΔE is the peak-to-peak energy difference, $\vec{\mu}_i$ is the magnetic moment projected onto the light propagation direction $\vec{k}$, and θ is the angle between the magnetic moment and the light propogation. The moment is proportional to magnetic field. Equation 3.76 nicely highlights the first-derivative relationship between the linear absorption and magnetic circular dichroism. Any inflection point in the linear absorption spectra will be amplified in the dichroic response.

The dichroic response can be modeled using the calculated matrix elements of the optical conductivity tensor as [165,166]:

$$\Delta\alpha_{MCD} \approx \frac{d\omega}{2c}\Im(\overleftrightarrow{n}_+ - \overleftrightarrow{n}_-) \approx \frac{2\pi d}{c}\Im[\frac{\overleftrightarrow{\sigma}_{xy}}{(1 + \imath\frac{4\pi}{\omega}\overleftrightarrow{\sigma}_{xx})^{1/2}}]. \tag{3.77}$$

Here, $\overleftrightarrow{n}_\pm = (\overleftrightarrow{\epsilon}_{xx} \pm \overleftrightarrow{\epsilon}_{xy})^{1/2}$ is the refractive index of right or left circularly polarized light arising from the dielectric function ϵ, d is the sample thickness, and c is the speed of light. In this case, we can have a direct comparison between the calculated and measured magnetic circular dichroism spectra.

3.2 Spectrometers

The heart of spectroscopy is to study how materials interact with electromagnetic radiation. The electromagnetic radiation covers a wide energy range, from microwaves, terahertz, infrared, visible, to ultraviolet. Materials exhibit different physical properties in response to the variation of the incoming photon energy. For example, we can study the lattice vibrations and electronic excitations by using infrared light. Spectroscopy provides a microscopic understanding of how lattice, charge, and spin are coupled. In this work, the probing light of interest falls in the infrared through the ultraviolet region. Several different spectrometers were used in the analysis of each of the different regions. Each of these spectrometers overlap in their energy regions as to allow for merging and obtaining a full spectra, sweeping from 20-55,000 cm^{-1}. The following sections will lay out the spectrometers used, from lowest frequency to highest frequency.

3.2.1 Fourier transform infrared spectroscopy

One of the spectrometers in this work is the Fourier-transform infrared spectrometers. The goal of this technique is to obtain a continuous absorption spectrum of materials over a wide frequency range in the infrared region. The central part of the FTIR spectrometer is the interferometer, which is used to introduce an optical path difference between two beams of light and to produce an interference pattern. The interferometer allows to produce a unique type of signal that has all of the infrared frequencies “encoded” into it, which is a method for measuring all of the infrared frequencies simultaneously rather than individually.

Figure 3.10 displays a schematic view of a Michelson interferometer. The incident broadband infrared beam splits into two parts by a 50/50 beam splitter. Different types of beam splitters are chosen based on the frequency range of the light source.

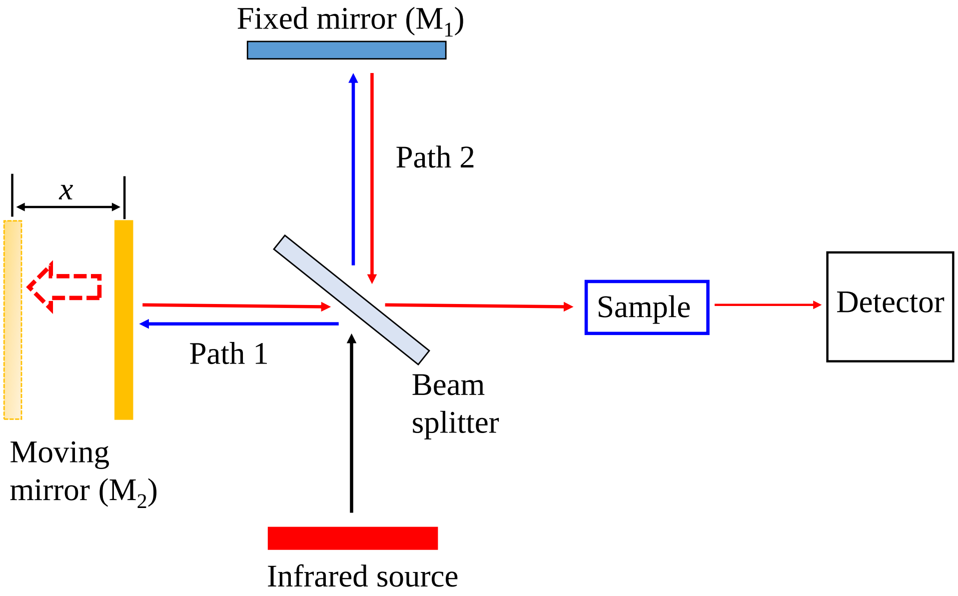

Figure 3.10: Schematic view of a Michelson interferometer in a Fourier transform infrared spectrometer setup.

One part of the beam is transmitted to a fixed mirror (M_1). The other part of the beam is reflected by the beam splitter and travels to a moving mirror (M_2). The returned beams reflected from the two mirrors (M_1 and M_2) are merged in the beam splitter. The recombined beam is then sent to the sample chamber. Signals are collected by the detector and then a computer will perform the Fourier transformation to the raw signal. The moving mirror periodically modifies the optical path difference between the two arms of the beam, generating constructive or destructive interference pattern. Therefore, the intensity is a function of the moving displacement x, known as an interferogram [167].

If M_2 travels at a constant velocity, the relation between the interferogram function $I(x)$ and the source intensity $B(\omega)$ is given by

$$I(x) = \frac{1}{2}\int_0^\infty B(\omega, x) cos 2\pi\omega d\omega, \tag{3.78}$$

where ω is the frequency in wavenumbers. $I(x)$ is the cosine Fourier transform of $B(\omega)$ and contains complete information about the spectrum [167]. This function describes the Fourier transformation of the raw signal, which converts the spatial displacement x to the frequency domain. This gives the single beam infrared spectrum. The typical transmittance or reflectance spectrum is the ratio spectrum of sample to reference.

3.2.2 Bruker IFS 113v Fourier transform infrared spectrometer

The majority of the far-infrared (21-700 cm^{-1}) and middle infrared (450-5000 cm^{-1}) reflectance and transmittance spectra in this work were obtained by using Bruker IFS 113v Fourier Transform Infrared (FTIR) spectrometer. Figure 3.11 displays a

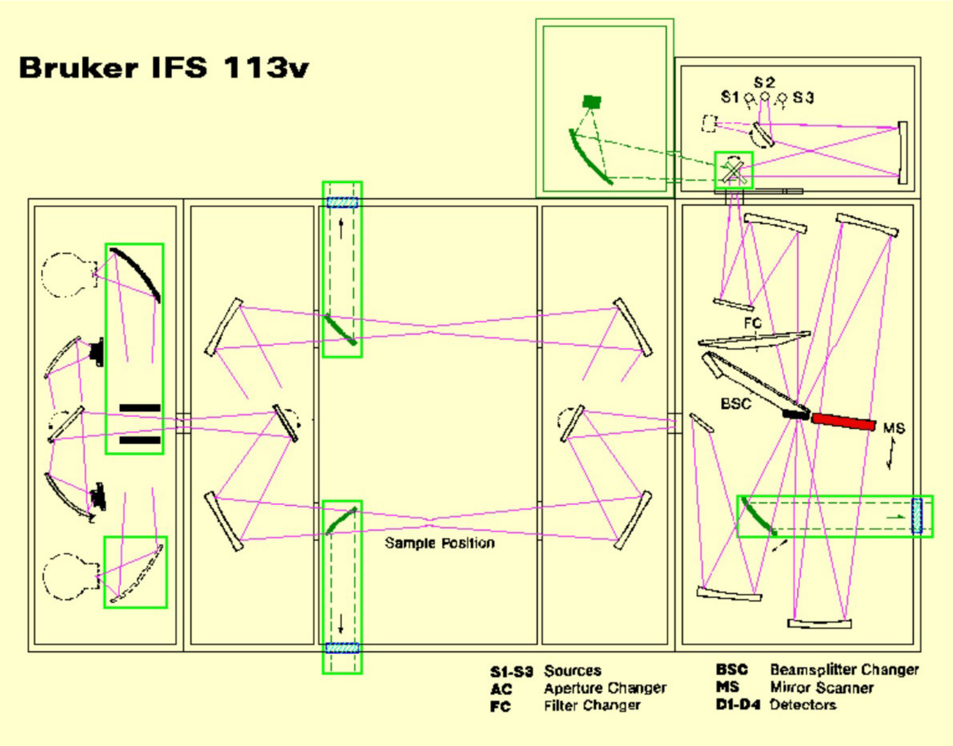

Figure 3.11: Schematic view of the Bruker IFS 113v FTIR spectrometer [168].

detailed design of the optical path inside the Bruker 113v spectrometer. The spectrometer contains four chambers – source, interferometer, sample, and detectors. The interferometer used here is Genzel-type, which is similar to the michelson interferometer described in the prior section. In the Bruker IFS 113v, a secondary laser/white light interferometer physically attached to the main Genzel-type interferometer provides an "optical marker" to initiate the start of spectrum data acquisition and also to precisely determine the optical path difference and speed of the main moving mirror. The sample chamber has the front and back channels, which are optimized for transmittance or reflectance measurements, respectively.

This system operates under vacuum to reduce the background noise. The Si or B-doped Si bolometer, which is cooled with liquid helium, provides extra sensitivity. A schematic view of the beam path and optics are provided in Fig. 3.11.

In order to capture different energy regions most efficiently, the instrument uses a series of sources, detectors, and beamsplitters for optimal resolution and signal. A list of these different parts are listed in Table 3.3.

3.2.3 Bruker Equinox 55 FTIR spectrometer with Bruker IR Scope II

Another important spectrometer in our lab is Bruker Equinox 55 FTIR spectrometer with Bruker IR Scope II. This instrument is a combination of a spectrometer with a microscope attachment. Compared to Bruker 113v, this instrument uses several different light sources, beam splitters, and detectors to provide a broader frequency range as well as the higher resolution and sensitivity for the measurements (600 - 17000 cm^{-1}). In this case, we have the overlapped energy regions to compare the spectra from this instrument with Bruker 113v, which allow us to double-check the accuracy and reliability of the shape and reflectance level of a spectrum.

Table 3.3: Bruker IFS 113v operating parameters

Range (cm^{-1})	Source	Beam splitter	Opt. Filter	Polarizer	Detector
10-50	Hg arc	Mylar 50 μ	Black PE	1	Si bolometer, DTGS
30-120	Hg arc	Mylar 23μ	Black PE	1	Si bolometer, DTGS
50-240	Hg arc	Mylar 12μ	Black PE	1	Si bolometer, DTGS
100-600	Hg arc	Mylar 3.5μ	Black PE	1	Si bolometer, DTGS
450-4000	Globar	KBr	open	2	B-doped Si bolometer, DTGS

PE = polyethylene. Polarizer 1 = wire grid on oriented PE, Polarizer 2 = wire grid on AgBr

Furthermore, the Bruker IR Scope II is designed for accurate measurement of micro samples, or small areas on larger samples. The different types of sources, beam splitters, and detectors are listed in Table 3.4.

The optical beam path of the spectrometer can be seen in Fig. 3.12.

3.2.4 Perkin Elmer λ-900 grating spectrometer

Besides the Bruker 113v and Bruker Equinox 55 FTIR spectrometers, we use a Perkin Elmer λ-900 grating spectrometer to measure spectra in the near-infrared, visible, and ultraviolet regions (3300 - 190nm, 3000 - 52000 cm^{-1}). The Perkin-Elmer λ-900 (or -1050) spectrometer features an all-reflecting, double-monochromator, double-beam optical system. The spectrometer is operated under nitrogen purging. The optical system is depicted schematically in Fig. 3.13.

Instead of using the interferometer, this instrument uses grating to get a specific energy/wavelength of light. An optical grating can split and diffract light into several beams travelling in the different directions. For the chromatic light, the diffraction angle is depend on the wavelength and the separation distance d between two successive grooves. This relation is known as the grating equation, given by

$$d \sin\theta = m\lambda \tag{3.79}$$

where m is an integer and the order of diffraction, d is the groove spacing, λ is the diffracted wavelength, and θ is diffraction angle. A series of sources, polarizers, gratings, and detectors are used in order to achieve the optical data. All of them change automatically when different energy windows are measured. The detailed information of those components are listed in Table 3.5.

Figure 3.13 displays the detailed optical path diagram for λ-900 (or -1050). Source change is controlled by flipping mirror M1. The radiation of source is reflected by

Table 3.4: Operating parameters of Bruker IRscope II

Range (cm^{-1})	Source	Beamsplitter	Detector
600-7500	Globar	KBr	MCT
4000-12000 with near-infrared polarizer	Tungsten	Quartz	InSb
9000 -17000 with visible polarizer	Tungsten	Quartz	Si diode

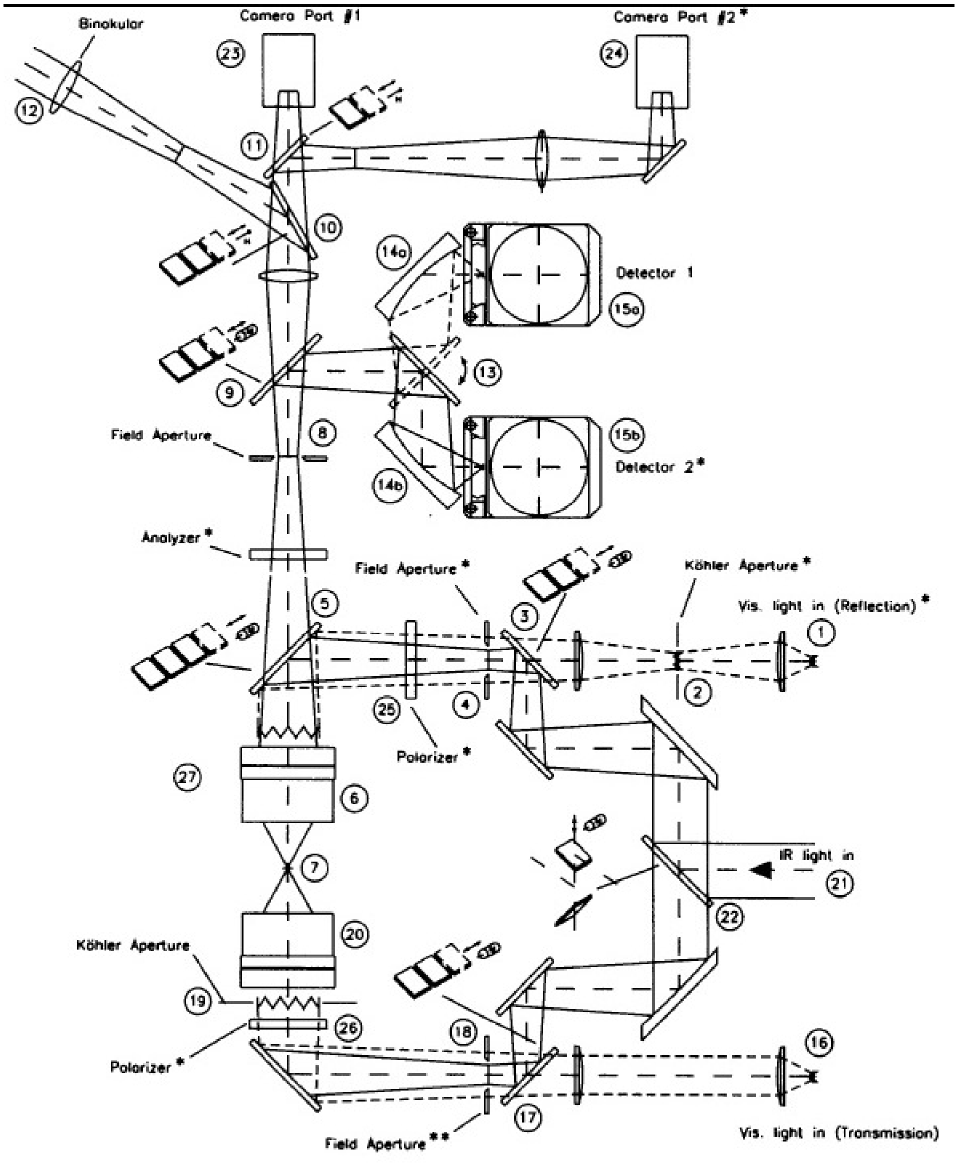

Figure 3.12: Optical path diagram of Bruker IRscope II. 1,16: visible light source; 2,19: visible light aperture; 3,22: motorized switch mirror; 4,18: optional iris or knife edge aperture; 5,9,10,17: beamsplitter changer; 6: objective lens; 7: Sample; 8: iris or knife edge aperture which defines the area of sample analyzed; 12: binocular eyepiece; 13: two position detector selection mirror; 14: mirror routing to detector; 15: detector; 20: condenser; 21: IR beam (from spectrometer); 23,24: camera port; 25,26,27: polarizers [168].

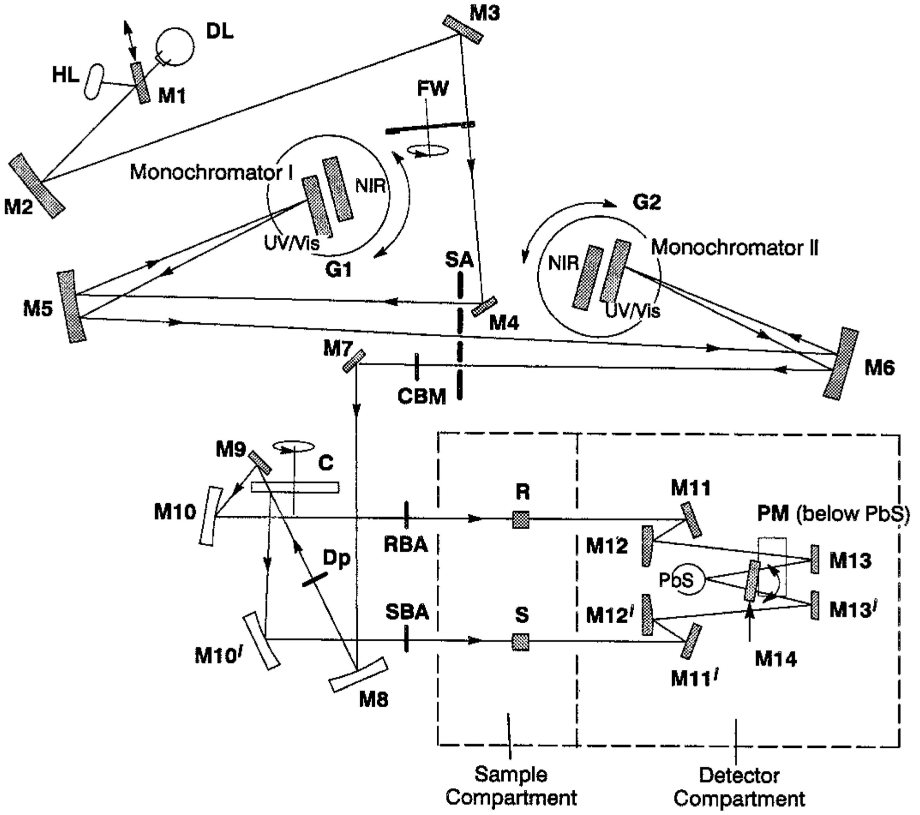

Figure 3.13: Optical layout of Perkin-Elmer λ-900 or -1050 [168].

Table 3.5: λ-900 or -1050 operating parameters

Range (cm^{-1})	Source	Grating	Polarizer	Detector
3100-14250	Halogen Lamp	1200 lines/mm	Glan-Thompson prism	PbS
11240-31330	Halogen Lamp	1200 lines/mm	Glan-Thompson prism	Photomultiplier
31330-52000	Deuterium Lamp	2400 lines/mm	Glan-Taylor prism	Photomultiplier

mirror M2, M3, and passes optical filter FW. Then, the beam is brought in monochromator I through M4, slit SA, and M5. Depending on the desired wavelength range, the collimated radiation beam strikes either the 2400 lines/mm grating or the 1200 lines/mm grating. The rotation position of the grating effectively selects a segment of the spectrum, reflecting this segment to mirror M5, to go through the exit slit, and enter Monochromator II. The advantage of the double-monochrometer is to maintain high spectral purity with an extremely low stray radiation content. The automatic grating change during monochromator slewing avoids the time-consuming re-alignment of the optics pathway due to the monochromator change.

The double beam is achieved via the chopper assembly C. As the chopper rotates, a mirror segment, a window segment and two dark segments are brought alternately into the radiation beam. When a window segment enters the beam, radiation passes through to mirror M9 and is then reflected via mirror M10 to create the reference beam (R). When a mirror segment enters the beam, the radiation is reflected via mirror M10' to form the sample beam (S). When a dark segment is in the beam path, no radiation reaches the detector, permitting the detector to create the dark signal (D). Then, the measured spectrum is expressed as:

$$spectrum = (S - D)/(R - D). \tag{3.80}$$

3.2.5 LabRAM HR Evolution Raman spectrometer

The LabRAM HR Evolution Raman microscopes are ideally suited for both micro and macro measurements. It contains the lasers with three different wavelength: 633 nm (red), 532 nm (green), and 473 nm (blue). This instrument is a triple Raman spectrometer and covers a wide frequency ranges from 25 - 3000 cm^{-1}. There are 10X, 50X, and 100X magnification microscopes, which give us a precise control of measuring different surface spots in a material. A CCD detector is used to collect signal.

Figure 3.14 displays a schematic view of a typical Raman spectrometer. There are four major parts in a conventional Raman spectrometer, which are: (i) The laser source, (ii) sample illumination and collection optics (set of mirrors and lenses), (iii) monochromator, and (iv) a detector. [157] The scattered beam from the sample is recollected to pass through a set of lenses and filters. Several mirrors then send the beam into a diffraction grading. The rotation of the diffraction grading selects different wavelength of the light and thus the spectrum is obtained. Finally, the spherical mirror focus the beam and direct it to the detector. Grating and width of the slit play the key role in obtaining the maximum spectral resolution. Grating resolution is given as:

$$R_s = \frac{\lambda_\omega}{\Delta\lambda_\omega} = N \cdot m, \tag{3.81}$$

where N is the number of illuminated slits and m is the order of the diffraction. We can see from Eqn 3.81 that the best way to improve the resolution is to increase the number of slits. In this case, a triple monochromater is used to better filter or reject of the stray light and thus can be used to measure Raman bands located very close to the Rayleigh line. Rayleigh filter (Fig. 3.14) is an essential part of the Raman instrumentation that allows selective elimination of the strong Rayleigh scattering and analysis of the weak Raman scattering. High detection sensitivity and signal-to-noise ratios are achieved by the use of array detectors, usually photodiode arrays or CCD's (charge-coupled devices). [157, 169]

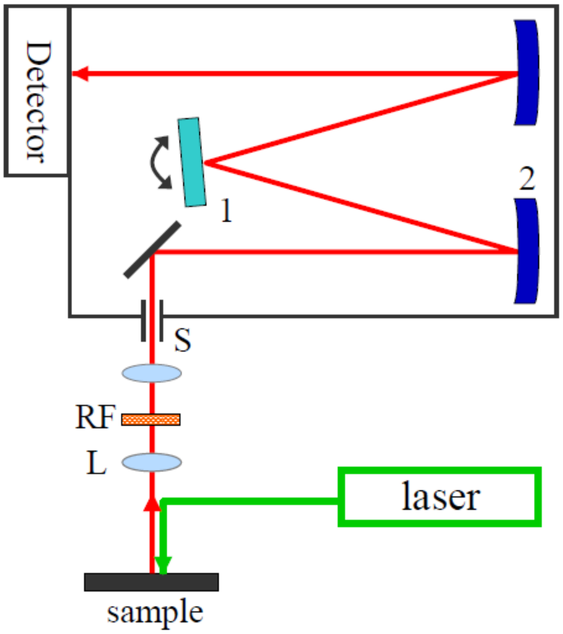

Figure 3.14: Schematic view of the Raman spectrometer. RF-Rayleigh filter, L-lens, S-entrance slit, 1-diffraction grating, 2-spherical mirror.

3.3 Spectroscopy under extreme conditions

Materials can display interesting properties under extreme conditions such as low temperature, high magnetic field, and high pressure. Spectroscopy under these extreme conditions provides a microscopic approach to detect how physical properties change through the phase transitions or due to the broken of symmetry, and how spin, charge, and lattice are coupled to each other. In this dissertation, we measure the reflectance or transmittance spectra of different materials to study the optical properties of materials under variable temperature and high magnetic field. Note that for reflectance measurements, we use the Aluminium mirror as the reference. The spectra signature of the Aluminium mirror is corrected by renormalization.

3.3.1 Variable temperature spectroscopy

We use an open-flow cryostat to perform the variable temperature spectroscopic measurements. The low-temperature experiments with the Bruker IFS 113v and Perkin-Elmer λ-900 are performed in combination with an APD LT-3-110 Heli-Tran cryostat system with dual temperature sensors and a Lakeshore Model 330 temperature controller. Measurements with the Bruker Equinox 55 are made with Oxford Instruments Microstat^{He}.

Figure 3.15 displays the complete setup of the system for variable temperature measurements. A series of components are needed to perform the spectroscopy measurements. These include a helium dewar, a helium gas tank, a transfer line, an open flow-cryostat, a temperature controller, a vacuum pump and a flowmeter. The helium dewar is connected to a He gas tank, which can build pressure inside the dewar in order to start the helium flow. A high efficiency transfer line is then connected so that helium can be transferred from the dewar to the cryostat. The sample is mounted at the sample holder at the tip end of the cryostat. Crycon grease is placed

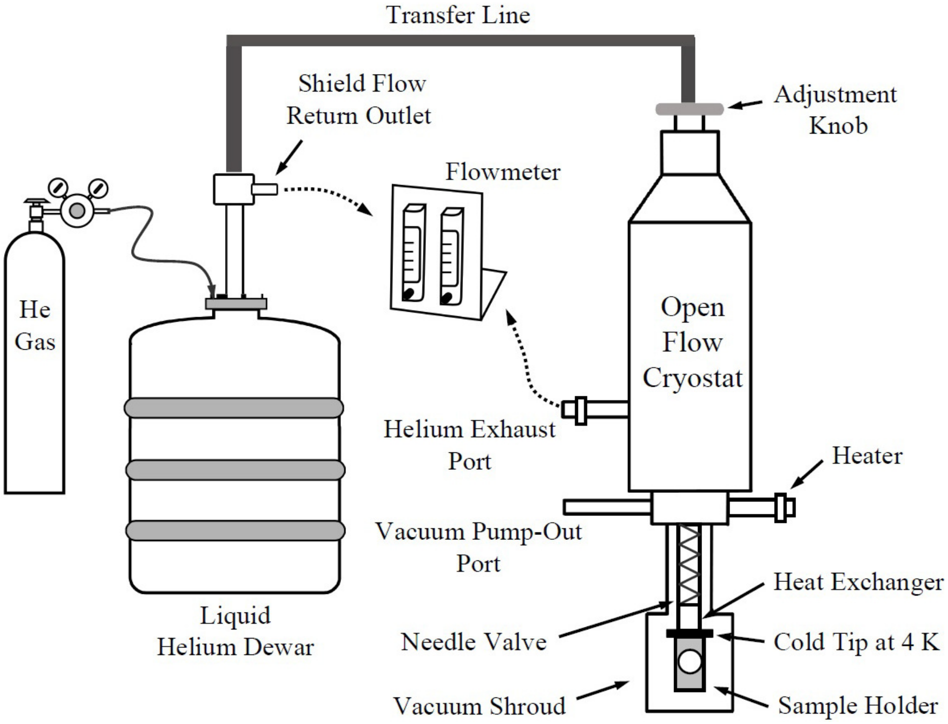

Figure 3.15: Set-up of LT-3-110 Heli-Tran liquid transfer line and cryostat [168].

between the cold stage of the cryostat and the sample holder to improve thermal contact. A heater is build in the cryostat to better control the temperature. The sample chamber has to be under vacuum when performing the measurements at low temperatures in order to avoid ice forming. A turbo pump station is thus connected to the vacuum pump-out port. The system must precool before helium flow will begin, which often takes 20-25 minutes. The lowest stable temperature is ∼5 K. After cooling the sample, the liquid helium evaporates and the gas is distributed in two ways: through the helium exhaust port on the side of the cryostat and back through the transfer line with exit at the shield outlet port. The additional shield/return flow helps to keep the transfer line cold. The base of the cryostat is also equipped with another heater to prevent ice buildup and vacuum seal freezing.

We control the cooling rate in several different ways: (i) changing and maintaining pressure in the supply dewar, (ii) adjusting the flowmeter (attached to the helium exhaust port and the shield gas outlet), and (iii) adjusting the knob that controls the position of the needle valve at the end of the transfer line. Samples are mounted with GE varnish, rubber cement, and silver paste. The sample is then mounted on the heat exchanger/sample holder, under vacuum, and optical access is achieved through appropriate windows (depending on the frequency/energy/wavelength of light that is being worked with). Two different thermal sensors are available. One is embedded in the tip of the cold stage and the other is mounted onto the sample holder. This gives a good measure of the real sample temperature.

3.3.2 Magnetic circular dichroism setup at National High Magnetic Field Laboratory

The magnetic circular dichroism experiments were performed at National High Magnetic Field Laboratory using the 25 T split helix magnet [170]. Figure 3.16 (a)

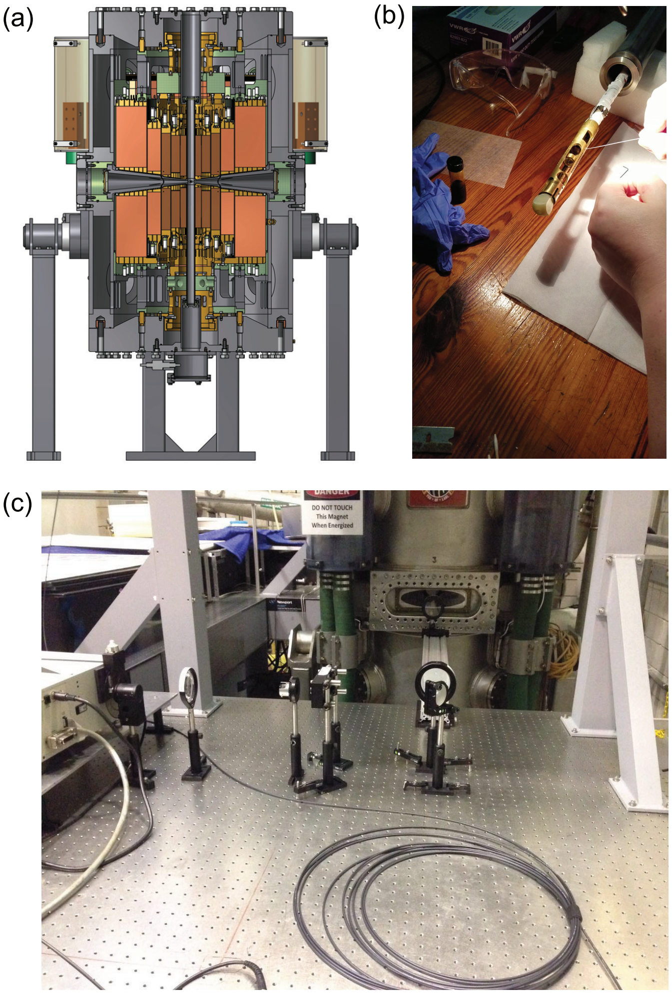

Figure 3.16: (a) Detailed structure of the 25 T split helix magnet in the NHMFL. Images are available at: https://nationalmaglab.org/about/around-the-lab/meet-the-magnets/meet-the-split-helix-magnet. (b) Sample mounting probe of the magnetic circular dichroism experiment. (c) MCD experimental setup in the NHMFL.

displays a cutaway design of the split helix magnet cryostat. This magnet consists of two resistive coils with four wide optical ports. These ports are used to shine light on the sample from the horizontal plane, giving access to more intricate and complicated measurements. High electric currents are applied in the resist coils to generate a magnetic field up to 25 T along the vertical direction. The direction of electric current can be switched in order to switch the magnetic field direction.

Figure 3.16 (b) shows the sample mounting probe for the transmission mode of the MCD experiment. The sample is mounted in a spherical sample holder by GE varnish. Since we use the Faraday geometry for the MCD experiment, the bottom part of the probe consists of a sliver mirror and a converging lens. The sliver mirror is used to reflect the light by 90 degree so that the light is propagating along the vertical direction, which is parallel or antiparallel to the direction of the magnetic field. Since the reflection will change the phase of the left and right circularly polarized light by an equal amount, using the sliver mirror will not affect the MCD signal. The sample holder is fixed at the back focal point of the converging lens to maximize the light power density.

Figure 3.16 (c) displays a complete setup for the magnetic circular dichroism experiment. A series of optical components are used to optimize the MCD signal. We use a 240 W Xe lamp as a light source and a 0.25 m monochromator. An optical chopper is employed to increase the signal to noise ratio at a constant frequency, followed by a linear polarizer that is set to 45 degree. A photoelastic modulator is placed after the linear polarizer to convert the linearly polarized light into left or right circular polarized light periodically at a constant time interval $\delta(\mathrm{t}) = \lambda/4$ $\sin(\omega \mathrm{t})$. Several lenses are used to increase the power density. We did not need to keep the phase information, so an optical fiber is used to collect the light and route it to the detector. The detector has the best sensitivity between 0.8 and 2.8 eV.

All signals were separated by lock-in amplifiers. The probe is in the liquid helium environment, a heater is built inside the probe to better control the temperature.

3.4 Project specific details: Sample growth, measurements and complementary calculations

3.4.1 $\mathbf{Fe}_x\mathbf{TaS}_2$ (x = 0, 1/4, 1/3) and $\mathbf{Cr}_x\mathbf{NbS}_2$ (x = 0 and 1/3)

3.4.1.1 Single crystals growth

High quality single crystals of Fe_xTaS_2 (x =1/4 and 1/3) were grown by chemical vapor transport methods. The Fe concentration was verified by magnetization and TEM [6,171]. $Cr_{1/3}NbS_2$ was grown by chemical vapor transport using iodine as the transport agent [11, 172]. Energy dispersive x-ray spectroscopy results along with a measurement of the magnetic transition temperature were used determine the Cr stoichiometry [11, 171, 173, 174]. For comparison with the intercalated materials, single crystals of 2H-TaS_2 and 2H-NbS_2 were grown by chemical vapor transport techniques and acquired from HQ graphene, Inc.

3.4.1.2 Spectroscopic measurements

We combined optical spectroscopy and inelastic Raman scattering measurements to reveal the electronic and vibrational properties of these crystals. For the optical spectroscopic method, we measured *ab*-plane reflectance using a series of spectrometers (4 meV-6.5 eV; 4.2-300 K) and employed a Kramers-Kronig analysis to extract the optical constants. Here, we are primarily interested in the optical conductivity ($\sigma_1(E)$) and the oscillator strength sum rule on $\sigma_1(E)$. For the data analysis, we employed traditional peak fitting techniques.

Raman scattering measurements (λ_{excit} = 476, 532 nm; $\leq$3.2 mW; averaged 45 s integrations; 4.2 - 300 K) were performed in the back-scattering geometry using a Labram HR Evolution spectrometer. An open flow cryostat provided temperature control.

3.4.1.3 Electronic structures calculations

Electronic structure calculations was performed using Density Functional Theory provided by Atomistix Toolkit [175,176]. Using a spin-polarized generalized gradient approach with an on-site potential (SGGA+U), the electronic structure, density of states (DOS), and electron density were determined [177]. The onsite potential localizes the Fe electrons that contribute to the overall magnetic moment; we find 3.8 μ_B for the Fe moment.

3.4.1.4 Lattice dynamics calculations

Phonon calculations were performed utilizing density functional theory (DFT) provided with QuantumATK [178–180]. Given the number of atoms in the intercalated unit cells, we employed a local density approximation (LDA) method to reduce computational time with an overall 3×3×3 k-point sampling on the same crystal structures used in Ref. 114. For the dynamical matrix calculations, we used 3×3×3 repetitions of the various unit cells, which produced supercells consisting of 27 unit cells with a total of 162 to 702 atoms depending on the system resulting in about 20,000 computational hours. In our analysis, we calculated the phonon density of states (DOS) and vibrational modes for comparison with and assignment of the experimental features.

Figure 3.17 shows the calculated phonon DOS for TaS_2, $Fe_{1/4}TaS_2$, and $Fe_{1/3}TaS_2$.

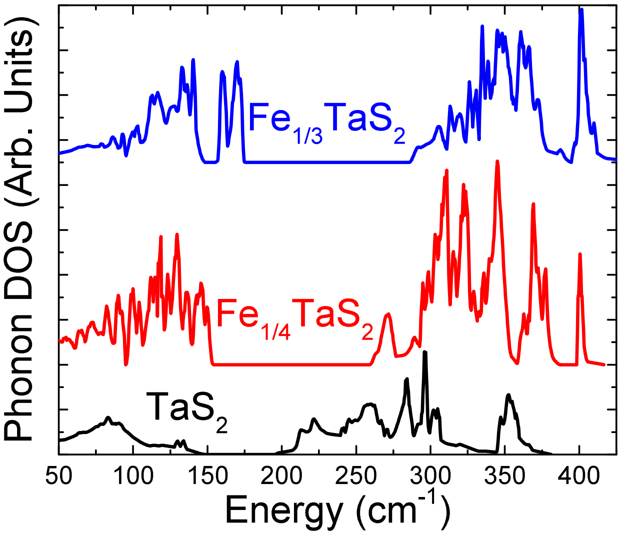

Figure 3.17: The calculated phonon DOS for TaS_2 (black), $Fe_{1/4}TaS_2$ (red), and $Fe_{1/3}TaS_2$ (blue). The curves have been offset for clarity.

The phonon calculations were performed with 5×5×2 k-point sampling. These calculations help provide a general understanding for the assignment of the lattice modes. The peaks between 100 and 175 cm^{-1} in the $x = 1/4$ and $1/3$ compounds attract our attention because they are related to the intercalated Fe monolayer excitations. This assignment is based on the fact that no modes are predicted in the parent compound at this frequency range. For a single unit cell of Fe_xTaS_2, the metal monolayers will have either in- or out-of-phase planar motion. The Raman-active out-of-phase excitations are (both in- and out-of-plane) of interest here because these motions provide an overall change in polarizability.

3.4.2 $(LuFeO_3)_m/(LuFe_2O_4)_1$ superlattices (m = 3, 7, 9) and two end members ($LuFeO_3$ and $LuFe_2O_4$)

3.4.2.1 Film growth and characterization of $(LuFeO_3)_m/(LuFe_2O_4)_1$

$(LuFeO_3)_m/(LuFe_2O_4)_1$ (m = 3, 7 and 9) superlattices thin films were grown using reactive-oxide molecular-beam epitaxy on (111) $(ZrO_2)_{0.905}(Y_2O_3)_{0.095}$ substrates [1]. Lutetium and iron were evaporated from elemental sources and oxidized by a mixture of ≈2% O_3 and O_2. The oxygen partial pressure was varied during the deposition to access the different iron valence states in $LuFe_2O_4$ ($Fe^{2.5+}$) and $LuFeO_3$ (Fe^{3+}). The $(LuFeO_3)_m/(LuFe_2O_4)_1$ (m = 3, 7 and 9) superlattices were grown as part of a full series of $(LuFeO_3)_m/(LuFe_2O_4)_n$ thin films to demonstrate consistent and reproducible trends in the ferroelectric and magnetic properties; characterization of the identical $(LuFeO_3)_3/(LuFe_2O_4)_1$ film presented here by x-ray diffraction and bulk SQUID magnetometry is presented in Ref. 1. The (3, 1), (7, 1) and (9, 1) superlattices as well as the two end member films of $LuFeO_3$ and $LuFe_2O_4$ were grown to a consistent number of iron layers to optimize the optical density and sensitivity for the transmission mode magnetic circular dichroism measurements.

Cross-sectional TEM specimens were prepared using an FEI Strata 400 Focused Ion Beam with a final milling step of 2 keV to reduce surface damage. High-resolution HAADF-STEM images were acquired on an aberration-corrected 300 keV FEI Titan Themis with a probe convergence semi-angle of 30 mrad.

3.4.2.2 Fe valence in the $(\mathrm{LuFeO_3})_3/(\mathrm{LuFe_2O_4})_1$ superlattices

The Fe valence states are the key to understand the electronic properties of the $(\mathrm{LuFeO_3})_m/(\mathrm{LuFe_2O_4})_1$ superlattices. In prior work, the Fe valence in the $\mathrm{LuFeO_3}$ and $\mathrm{LuFe_2O_4}$ parent compounds was studied. Single phase $\mathrm{LuFeO_3}$ films were grown by molecular-beam epitaxy and the effect of stoichiometry on the magnetic properties were investigated [16]. Using the phase-pure samples, $\mathrm{Fe^{3+}}$ in $\mathrm{LuFeO_3}$ samples is demonstrated by EELS. Annealing the samples in ozone post-synthesis did not change the observed valence or other properties, further suggesting that the synthesized samples in this dissertation were fully oxidized. In addition, excess Fe in these films tends to accumulate as $\mathrm{Fe_3O_4}$ precipitates ($\mathrm{Fe^{2.67+}}$) which are readily observed by magnetometry, AFM, and TEM imaging. The superlattice films used for magnetic circular dichroism spectroscopy, presented in this dissertation, are free of these $\mathrm{Fe_3O_4}$ inclusions as well.

The Fe valence in the $\mathrm{LuFe_2O_4}$ end member is also explored by EELS [181]. While an average $\mathrm{Fe^{+2.5}}$ valence is observed, discrete $\mathrm{Fe^{3+}}$ and $\mathrm{Fe^{2+}}$ states from a charge ordering pattern were unable to be identified. This could be due to instrumental limitations, for instance, performing a room temperature measurement during which the electron beam averages through a column of Fe atoms. This measurement was, however, in contrast to other prior work [34] which found discrete charge-ordering. Nevertheless, the samples in this dissertation are consistent with a bulk valence of $\mathrm{Fe^{2.5+}}$.

The Fe^{3+} valence in the $LuFeO_3$ layer in the $(LuFeO_3)_m/(LuFe_2O_4)_1$ superlattices is also confirmed by EELS. The iron valence in the $LuFe_2O_4$ layer is slightly different than the expected 2.5+. The origin of this effect is related to the different charge-ordering states. Prior DFT models suggest that there should be a small amount of Fe^{2+} present in the $LuFeO_3$ layers in the superlattices as a result of the ferroelectric domain walls [1, 7]. Those charged domain walls are due to the spontaneous charge transfer from the Fe^{2+} site in the $LuFe_2O_4$ layer to the Fe^{3+} site in the $LuFeO_3$ layer, which causes a symmetric/asymmetric Lu-layer distortion at the $LuFeO_3$ - $LuFe_2O_4$ interface and changes the polarization inside the Fe bilayers [1, 7]. This result in several nearly degenerate charge-ordered states in the superlattices. The charge transferred to the domain wall should be approximately 0.1 e-, yielding a net valence of 2.9+ if it were to be accumulated on a single Fe site.

We can place bounds on the likely fraction of Fe^{2+} in the $LuFeO_3$ layers by examining the candidate domain wall structure in the self-doped charge-ordering state reported in Ref. 1. Assuming that 0.1 e^- is transferred to only the middle Fe layer in $LuFeO_3$ - as prior theoretical model suggests - we find a maximum Fe^{2+} fraction of 3%.

Oxygen defects can also be present in films of this type, particularly in the $LuFe_2O_4$ layer that hosts the magnetism. There is not a good lattice match for $LuFeO_3$, so while the samples are phase pure and oriented, there are threading dislocations and similar types of structural defects. Similar dislocations are also present in the $LuFeO_3$ and $LuFe_2O_4$ parent compounds in approximately the same concentration. Prior works reported the magnetic moment from these defects is at least an order of magnitude smaller than that of the host compound [16, 22]. We therefore conclude that the magnetic circular dichroic signal from these defects is extremely weak.

3.4.2.3 Optical spectroscopy

We measured the *ab*-plane transmittance of the (3, 1), (7, 1) and (9, 1) superlattices, the $LuFeO_3$ and $LuFe_2O_4$ end members, as well as the blank substrate using a λ-900 grating spectrometer covering the energy range from 1 - 6 eV. The linear absorption spectrum is calculated from measured transmittance as $\alpha(E) = -\frac{1}{d}\ln(T(E))$, where $T(E)$ is the measured transmittance as a function of energy E and d is the sample thickness. The absolute absorption of (3, 1), (7, 1) and (9, 1) superlattices as well as the end members were determined by subtracting the response of the substrate. Because the optical density of the films was optimized for magnetic circular dichroism spectroscopy rather than linear absorption, the excitations are not as pronounced as in prior work [21, 182]. An open flow cryostat provided temperature control (4.2 - 300 K).

3.4.2.4 Magnetic circular dichroism spectroscopy

We measured the dichroic response of the superlattices ($m = 3$, 7 and 9), the $LuFeO_3$ and $LuFe_2O_4$ end members and the $(ZrO_2)_{0.905}(Y_2O_3)_{0.095}$ substrate between 0.8 and 2.8 eV. This is the energy window where our films transmit light. It is also the energy window where the most important excitations occur [21, 182]. These experiments were performed at the National High Magnetic Field Laboratory using the 25 T split helix magnet [170] in Faraday geometry along with a 240 W Xe lamp and a 0.25 m monochromator. We measured the difference in transmittance between left- and right-circularly polarized light at various magnetic fields and converted the result to absorbance difference as discussed in detail below. Thus, the dichroic spectrum is the difference in absorption between left- and right-circularly polarized light. A chopper was employed to increase the signal to noise ratio at a constant frequency, followed by a linear polarizer that was set to 45°. A photoelastic modulator was placed after the linear polarizer to convert the linearly polarized light into left or right circular polarized light periodically at a constant time interval $\delta(t) = \lambda/4 \sin(\omega t)$. We did not need to keep the phase information, so an optical fiber was used to collect the light and route it to the detector. All signals were separated by lock-in amplifiers. The field sequence was chosen based upon the needed resolution, always within the +25 T $\rightarrow$ 0^- T $\rightarrow$ -25 T $\rightarrow$ 0^+ T $\rightarrow$ +25 T run pattern. The positive or negative sign of the magnetic field corresponds to the magnetic field direction and is parallel or antiparallel to the light propagation direction, respectively. The 0^- and 0^+ are both zero field data; the sign denotes the sweep direction. Moreover, a training loop with this pattern was performed before each data collection run. The phase of the lock-in was set at full field. Magnetic circular dichroism spectra were taken at several different temperatures - from approximately 18 to 157 K for the (3, 1) and (7, 1) superlattices. For the (9, 1) superlattice, the temperature range was successfully increased to 218 K by adding an extra heater in the probe. Even so, we could not heat above this temperature.

3.4.2.5 Magnetic circular dichroism data treatment

In this dissertation, we report the magnetic circular dichroism spectra in two different ways: as an absolute $\Delta\alpha_{MCD}$ for each superlattice or one that is normalized by the number of repeat units (which is just $\Delta\alpha_{MCD}/N$). Here, N is the number of repeat units for the superlattices or end members. The latter rendering allows comparison of interface effects. Substrate correction to the magnetic circular dichroism spectrum is also important. As shown in the later chapters, the MCD spectrum of the $(ZrO_2)_{0.905}(Y_2O_3)_{0.095}$ substrate is not zero because of the weak ferromagnetism induced from the defects [183]. We therefore subtracted it from the dichroic response of the superlattices to obtain the true $\Delta\alpha_{MCD}$ (or $\Delta\alpha_{MCD}$ per repeat unit).

The magnetic circular dichroism spectra are obtained using the signal from the lockin referenced to the photoelastic modulator divided by the signal from the lockin referenced to the chopper. The chopper frequency is set to 217 Hz to improve the signal to noise ratio. There is, however, still some magnetic field dependent background signal in the raw data (including the natural circular dichroism and the signal due to the drift of the probe), which dramatically affects the data quality when the dichroic signal from the sample is low - for instance in a non-magnetic or antiferromagnetic material. To reveal the pure magnetic circular dichroism spectrum ($\Delta\alpha_{MCD}$), the field-induced background signal ($\Delta\alpha_{background}$) was subtracted from the total spectrum ($\Delta\alpha_{total}$) as: $\Delta\alpha_{MCD} = \Delta\alpha_{total}$ - $\Delta\alpha_{background}$. At a given field H, we isolate $\Delta\alpha_{background}$ by averaging the positive and negative signals of the same field magnitude. This is because the $\Delta\alpha_{background}$ for both the positive and negative fields is only dependent on the intensity (and not the sign). In contrast, $\Delta\alpha_{MCD}$ depends on both the sign and the intensity of the magnetic field - making it an odd function. As a result, at the field of interest, the following relations should apply:

$$\Delta\alpha_{MCD} = \frac{1}{2} \times (\Delta\alpha_{+H} - \Delta\alpha_{-H}) \tag{3.82}$$

$$\Delta\alpha_{background} = \frac{1}{2} \times (\Delta\alpha_{+H} + \Delta\alpha_{-H}), \tag{3.83}$$

where $\Delta\alpha_{\pm H}$ is the raw MCD signal from the measurement at a positive or negative magnetic field H, respectively. These equations indicate the pure MCD signal from the sample should be the average of the difference between the positive and negative fields. This method of analysis was applied to the (3, 1), (7, 1) and (9, 1) superlattices as well as to the spectra of the two end members.

3.4.2.6 Extracting the coercive field and interface response from the dichroic spectra

There are two aspects of the data treatment that deserve special mention. The first is the constant energy cuts of the MCD data. The second is the manner in which we extract the interface spectra. Constant energy cuts of $\Delta\alpha_{MCD}$ were used to reveal the behaviour of specific Fe centres and how the excitations of these centres contribute to the overall magnetic response. By taking fixed energy cuts of the dichroic spectra over the full +25 T → 0^- T → -25 T → 0^+ T → +25 T data set, we can generate optical hysteresis loops corresponding to the excitation of interest. For instance, cuts at 1.33 eV probe the $Fe^{2+} \rightarrow Fe^{3+}$ charge-transfer excitation in the spin-down channel and the hysteresis loop generated by these iron centres. We can extract a site-specific value of the coercive field from this type of optical hysteresis loop.

We also sought to isolate the interface response for each of the $(LuFeO_3)_m/(LuFe_2O_4)_1$ superlattices (m = 3, 7 and 9). This is important because high-temperature magnetism emanates from strain and rumpling at the interface. We could not, however, compare the measured MCD spectra directly because, even though each of the films were specifically designed to have a consistent number of Fe layers. This is because they have a different number of interfaces. To obviate this problem, we normalized the spectra by the number of repeat units. The MCD spectra per repeat unit is given by:

$$\Delta\alpha(E)_{per-repeat} = \frac{\Delta\alpha(E)_{MCD}}{N}, \tag{3.84}$$

where N is the number of repeat units. This quantity contains the information about the interface that we seek, but the response of the $LuFeO_3$ and $LuFe_2O_4$ layers has to be eliminated in order to uncover it. To estimate the effect of the different $LuFeO_3$ and $LuFe_2O_4$ layers in the absence of the interfaces, we created a composite spectrum and subtracted this quantity from the measured MCD spectrum per repeat unit. We construct the composite spectrum of a hypothetical superlattice as:

$$\Delta\alpha_{composite} = m \times \frac{\Delta\alpha_{LuFeO_3}}{N} + \frac{\Delta\alpha_{LuFe_2O_4}}{N}, \tag{3.85}$$

where $m = 3$, 7 and 9. As mentioned above, $\Delta\alpha_{Interface} = \Delta\alpha_{Measured} - \Delta\alpha_{Composite}$ on a "per repeat unit" basis. This process is discussed in detail in Chapter 6.

3.4.2.7 First-principles electronic structure theory

Density functional theory + U (DFT + U) calculations were performed using the plane augmented wave method (PAW) as implemented in the Vienna Ab-Initio Package (VASP), and selecting the Perdew-Burke-Ernzerhof form of exchange correlation functional (PBE). Lu $4f$ states were considered in the core and we set $U = 4.5$ eV and $J_H = 0.95$ eV for the Fe $3d$ states. Density of states calculations (DOS) were performed on the relaxed $(LuFeO_3)_3/(LuFe_2O_4)_1$ superlattice exhibiting a 2:1 ratio between Fe^{3+} and Fe^{2+} charges in each monolayer of the $LuFe_2O_4$ block. Specifically, in the Fe^{3+} - Fe^{3+} - Fe^{2+} layer of the $LuFe_2O_4$ block, the Fe^{3+} centers are anti-parallel to each other; one of the Fe^{3+} spins is up, and the other is down. The Fe^{2+}'s are in different layers and align ferromagnetically. The details of this structure which was found to be the lowest energy configuration among different charge orders were previously described in Ref 1. The DOS were calculated with a 4×4×2 k-point mesh and a kinetic energy cut-off of 500 eV. In order to probe the robustness of our results with respect to U, we also performed our calculations for a larger value, *e.g.*, U=5.5 eV. This introduces a global shift in the states above and below the Fermi level but leaves the main features of the DOS unaltered. This type of change in the value of U does not impact our transition assignments.

3.4.2.8 Absorption and magnetic circular dichroism spectra calculation based on different charge-ordering patterns

The dichroic response can be modeled using the calculated matrix elements of the optical conductivity tensor as [165, 166]:

$$\Delta\alpha_{MCD} \approx \frac{d\omega}{2c}\Im(\overleftrightarrow{n}_{+} - \overleftrightarrow{n}_{-}) \approx \frac{2\pi d}{c}\Im[\frac{\overleftrightarrow{\sigma}_{xy}}{(1+\imath\frac{4\pi}{\omega}\overleftrightarrow{\sigma}_{xx})^{1/2}}]. \tag{3.86}$$

Here, $\overleftrightarrow{n}_{\pm} = (\overleftrightarrow{\epsilon}_{xx} \pm \overleftrightarrow{\epsilon}_{xy})^{1/2}$ is the refractive index of right or left circularly polarized (RCP or LCP) light arising from the dielectric function ϵ, d is the film thickness, and c is the speed of light. The theoretical predictions for both the parent compounds and the (3, 1) superlattice were made based on this equation. The dielectric functions were calculated using exact diagonalization as implemented in VASP. The theoretically predicted magnetic circular dichroism spectra were calculated based on the predicted density of states of different charge-ordering patterns in $LuFe_2O_4$ layers. The spin configuration considered in each case corresponds to the ferrimagnetic collinear arrangement of spins obtained from direct calculation of the magnetic ground state. They are mostly characterized by a ferromagnetic alignment of the Fe^{2+} spins and an antiferromagnetic alignment of the Fe^{3+} ones. The magnetic dichroism spectrum of the $LuFeO_3$ was computed considering the non-collinear $A2$ magnetic phase, which has been determined to be the magnetic ground state for this system and corresponds to a 120° angle in-plane (with a small tilt in the z-direction) arrangement of the spins within the Fe-monolayers in $LuFeO_3$. [17] Because $LuFeO_3$ (where the spins form a 120° non-collinear structure) is expected to provide a smaller contribution to $\Delta\alpha(E)$ than the $LuFe_2O_4$ layer (chapter 6), $\Delta\alpha(E)_{MCD}$ of the two candidate charge-ordering models considering collinear spin structures in the $LuFeO_3$ layer are computed.

Chapter 4

Electronic chirality in the metallic ferromagnet $Fe_{1/3}TaS_2$

4.1 Layered free carrier response

Figure 4.1(a,b) displays the reflectance and optical conductivity of $Fe_{1/4}TaS_2$ and $Fe_{1/3}TaS_2$ compared with that of 2H-TaS_2 [79]. Intercalation dramatically changes the character of the optical conductivity. The trend is non-monotonic, with the Drude response in the x=1/3 system being more robust than for x=1/4. Although this family of transition metal dichalcogenides is metallic, there are several small structures between 10 and 40 meV in the x=1/3 compound that are not completely screened. They are present at 300 K but much more evident at low temperature [Fig. 4.1 (c,d)]. The energy scale of these features is consistent with assignment as either phonons or electronic excitations between spin split bands. Temperature effects are overall modest.

Figure 4.1 (e) displays a close-up view of the Drude-Lorenz fit to the optical conductivity of $Fe_{1/3}TaS_2$. Two Drude functions are needed to capture the response. The two-component nature of the free carrier behavior is due to the superposition

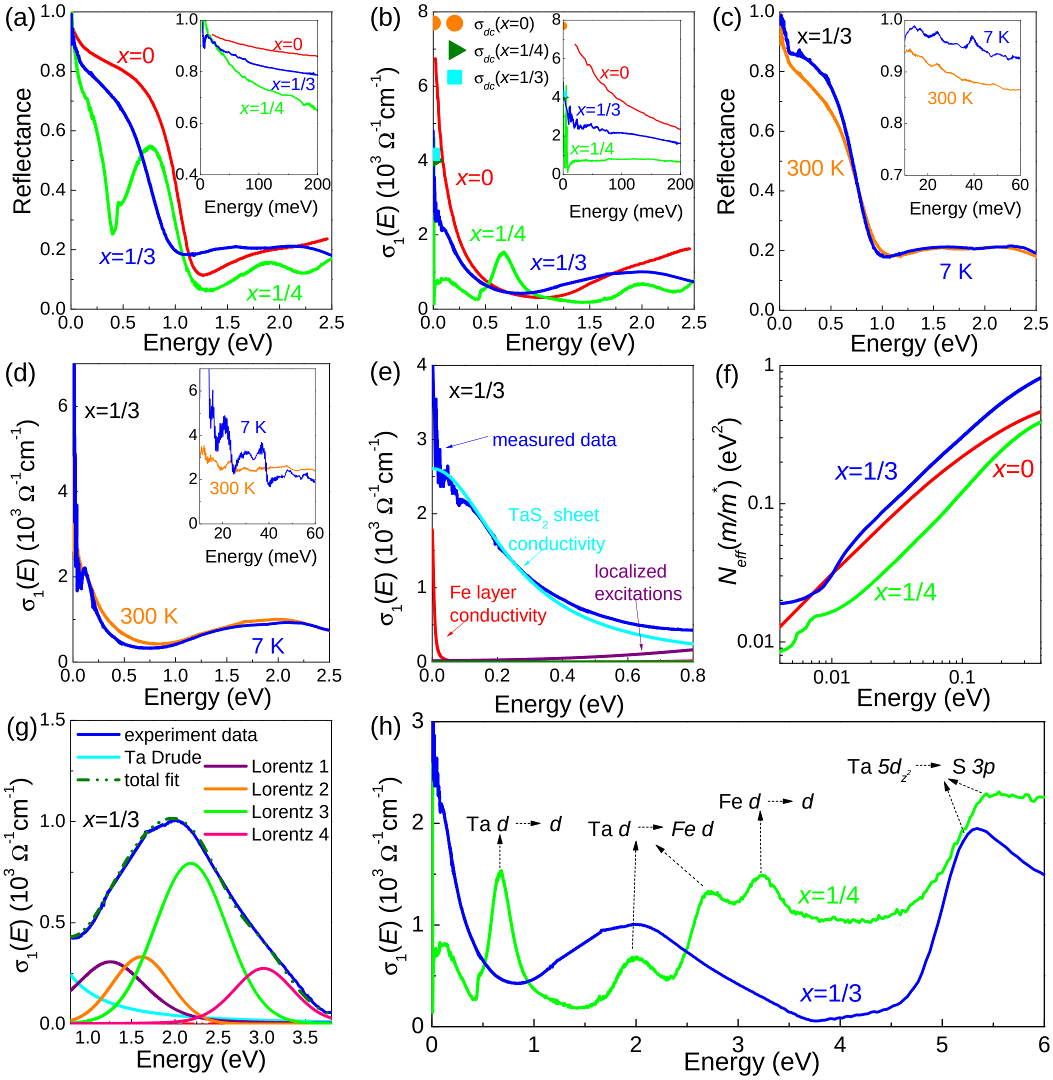

Figure 4.1: (a) Reflectance of $Fe_{1/4}TaS_2$, $Fe_{1/3}TaS_2$, and 2H-TaS_2. The 2H-TaS_2 data is reproduced from Ref. 79. Inset: close-up view of the low energy response. (b) Optical conductivity of these materials. Literature values of the *dc* conductivity [184–186] are also plotted; $\sigma_1(E)$ extrapolates to these values reasonably well. (c) Reflectance of $Fe_{1/3}TaS_2$ at 300 and 7 K. (d) Optical conductivity of the x=1/3 material at 300 and 7 K. Inset displays a close-up view of low energy response. (e) Close-up view of the two Drude oscillators needed to fit the response of $Fe_{1/3}TaS_2$. (f) Oscillator strength sum rule for the x=0, 1/4, and 1/3 compounds. (g) Drude-Lorentz fit of the localized excitations in $Fe_{1/3}TaS_2$. (h) Optical conductivity of $Fe_{1/4}TaS_2$ and $Fe_{1/3}TaS_2$ highlighting the difference in the localized excitations.

of Fe and TaS_2 layer conductivities. The former has only about 1% of the oscillator strength of the latter. Compared to 2H-TaS_2, intercalation at the x=1/3 level reduces the oscillator strength associated with the TaS_2 slab by approximately 40%, the plasma frequency by 15%, and the relaxation time by 35% [Table 4.1]. These trends quantify the fact that the TaS_2 layers are well isolated between Fe sheets. The Drude associated with the Fe layer is much narrower than that deriving from the Ta bands (which so prominently cross the Fermi surface).

A similar situation arises in $Fe_{1/4}TaS_2$ where fits to the optical response require two Drude oscillators. The metallic character is weaker than in the x=1/3 system due to a different degree of mixing of the hybridized Ta + Fe d bands crossing the Fermi level. The Fe Drude is extremely narrow because the distance between Fe centers is quite large (6.614 Å for x=1/4 vs. 5.737 Å for x=1/3), an effect that is evident in the charge density patterns. The lower density of atomic centers in the Fe sheet of the x=1/4 material reduces overlap and increases the relaxation time [Table 4.1]. An oscillator strength analysis [Fig. 4.1 (f)] provides additional evidence for a narrow Drude even though with phonons present in the vicinity.

Turning our attention to the higher energy portion of the spectra, the pattern of well-separated on-site and charge transfer excitations in the x=1/4 material and the superimposed set of features in the x=1/3 system seem dramatically different [Fig. 4.1 (h)]. Closer examination, however, reveals that the localized and charge transfer excitations reflect the trend in the Fe levels. In the x=1/4 system, we assign the band centered at 0.7 eV as a minority channel Ta $d \rightarrow$ Ta d excitation and those at 2.0, and 2.6 eV as Ta $d \rightarrow$ Fe d charge transfer excitations in the spin-down channel. The 3.2 eV peak is assigned to a minority channel Fe $d \rightarrow$ Fe d excitations. Four excitations also appear in the spectrum of the x=1/3 material, but they are clustered together at 1.2, 1.6, 2.2, and 3 eV [Fig. 4.1 (g)], and the assignment changes somewhat.

Table 4.1: Drude parameters of Fe_xTaS_2 (x=0, 1/4, 1/3) obtained from fits to the optical conductivity at 300 K. Error bars on the fit parameters are on the order of 1%, with the exception of the very narrow Fe Drude in the x=1/4 material, where the error bars are on the order of 5%.

Materials	Oscillator strength (eV^2)	Plasma freq (eV)	Relaxation time (s)
2H-TaS_2	0.18	1.19	2.5×10^{-14}
$Fe_{1/4}TaS_2$			
Fe Drude	0.37×10^{-3}	0.02	3.5×10^{-12}
TaS_2 Drude	0.038	0.66	1.3×10^{-14}
$Fe_{1/3}TaS_2$			
Fe Drude	1.78×10^{-3}	0.24	7.5×10^{-13}
TaS_2 Drude	0.11	1.02	1.6×10^{-14}

These excitations are superimposed at overall higher energy because the Fe bands have moved up in energy and are significantly more disperse compared to those in the x=1/4 system. This allows the Fe levels to hybridize with the Ta bands around 2 eV. There is also a band centered near 5.3 eV in both materials. In 2H-TaS$_2$, it is assigned as a Ta 5d_{z^2} conduction band to S 3p valence band excitation [187]. The characterization shifts to greater d-band contributions in the x=1/4 and 1/3 systems.

4.2 Electronic signatures of the chirality

Figure 4.2 displays the calculated electronic band structure and projected density of states for the three systems of interest. We used this band structure to assign all of the optical excitations in these materials. Where comparable, our findings are in good agreement with prior work [81, 188, 189]. In our analysis of 2H-TaS$_2$, there exist two distinct Ta-derived bands crossing the Fermi level [Fig. 4.2(a)] that are characteristic of Dirac lines [190]. These bands make the system metallic and produce excitations to the bands near 3.5 eV. These aspects of the electronic structure remain recognizable even with the addition of Fe and hybridization with Fe-related bands. Electron and hole pockets are predicted at the M- and K-points, respectively.

Introduction of an atomically thin layer of Fe into the van der Waals gap modifies the electronic structure profoundly. Our calculations employ a Hubbard U (similar to Ref. [189]) which acts to localize the Fe bands, leaving only a remnant of Fe density at the Fermi level. Localization is thus responsible for the weak metallicity of the Fe layer in the x=1/4 system (evidenced by small but distinct second Drude oscillator in the inset of Fig. 4.1 (b)). When Fe density increases (x=1/3), orbital overlap is improved, and the localized Fe bands are swept upward. This gives greater metallicity to the Fe layer because density at the Fermi surface is larger and, at the

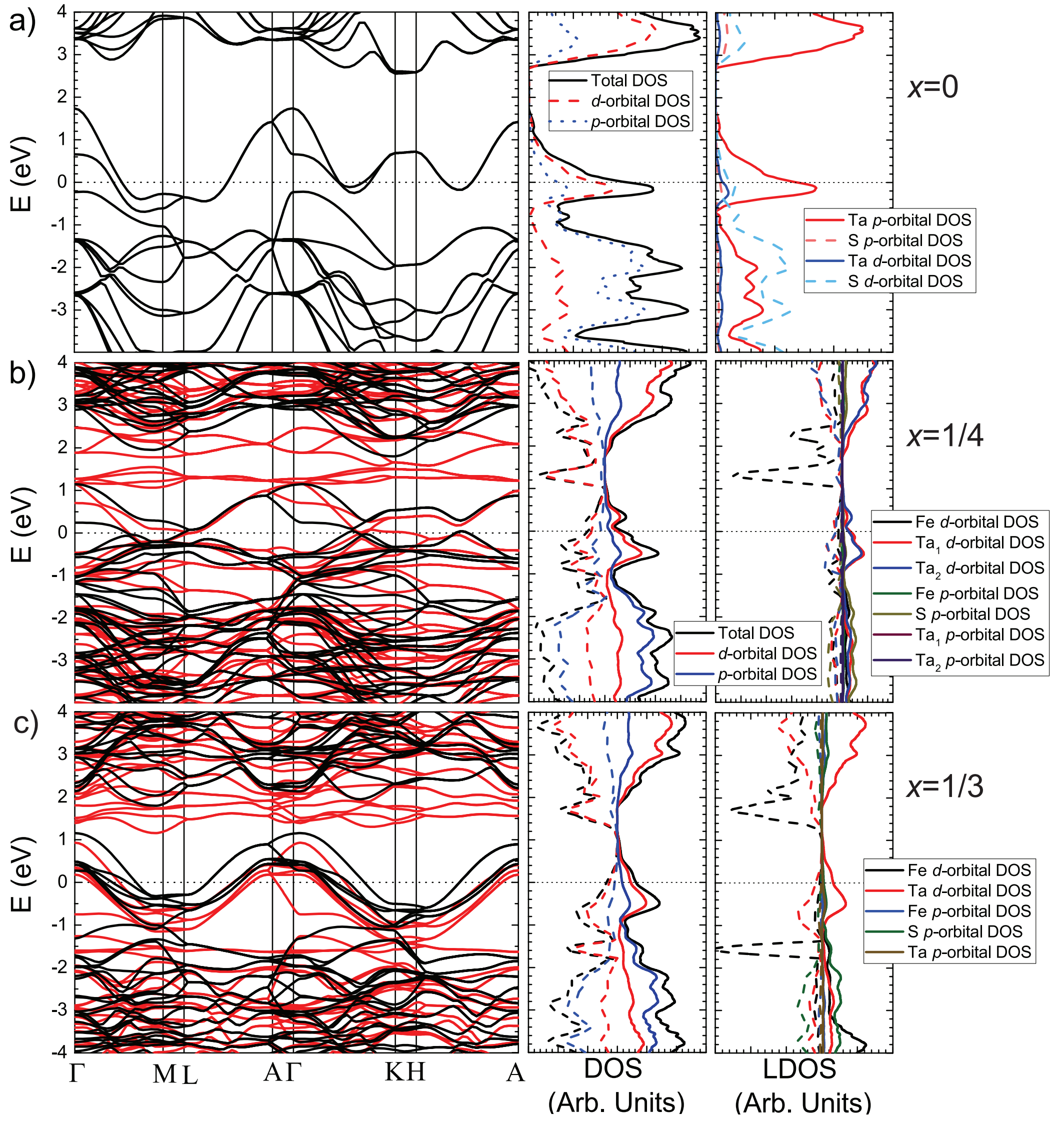

Figure 4.2: Calculated electronic band structure and DOS (total, partial, and local) for (a) 2H-TaS$_2$, (b) Fe$_{1/4}$TaS$_2$, and (c) Fe$_{1/3}$TaS$_2$. The black and red bands in the electronic structure and the solid and dashed lines in the DOS plots denote the spin-up and spin-down channels, respectively.

same time, raises the energy of the localized Fe bands which allows them to hybridize with the Ta-derived bands. This process strengthens the Fe-derived Drude and makes the localized excitations seem to disappear. The persistence of the Dirac lines produced by the TaS_2 slabs at high symmetry points demonstrates that these modifications are due to differences in overall electronic behavior rather than intercalation-induced structural changes.

To further examine the connection between symmetry and electronic structure, we projected the charge density onto the plane defined by the Fe centers [Fig. 2.23 (d-f)]. With these renderings, we see that as the Fe concentration increases, the overlap between Fe sites becomes stronger and more direct, and at the 1/3 level, the Fe centers even move out of the way of the S ions allowing for more direct orbital overlap. Thus, while the dominant Drude response is connected with free carriers in the Ta bands, the Fe ions introduce a second metallic signature - consistent with our spectroscopic findings. Remarkably, these contour plots also reveal a progression from a triangular (x=0) to Kagomé (x=1/4) to honeycomb (x=1/3) charge density pattern [Fig. 2.23 (d-f)]. The latter is (ironically) indicative of increased symmetry in the Fe plane - even though the overall crystal symmetry is reduced.

Another consequence of the evolving charge density pattern can be seen by comparing the electronic structure at the M and K symmetry points. In the centrosymmetric case [Fig. 4.2 (a, b)], the M-point sports an electron pocket whereas the K-point has a hole pocket. However, in the non-centrosymmetric case [Fig. 4.2 (c)], both locations host electron pockets. This hole to electron pocket crossover at the K-point, while certainly not simple, may be observable in a Hall measurement and could have important implications for the field of valleytronics [191]. We note that the crossover to electron pockets in $Fe_{1/3}TaS_2$ is not just due to increased carrier density from the Fe centers (although additional density does accumulate at the K-point) but rather due to the manner in which Fe breaks crystal symmetry. Therefore, a gating experiment that merely raises and lowers the Fermi energy against a rigid band structure should not show this effect.

Finally, we point out that broken inversion symmetry in the x=1/3 material is predicted to lift the spin degeneracy of the electronic bands near the Fermi surface [Fig. 4.3 (a)]. The energy scale of this splitting is on the order of tens of meV, consistent with the aforementioned features at 22 and 38 meV in the optical conductivity. Figure 4.3 (b) displays a close-up view of these structures. Although the excitation energies are in line with what might be expected for electronic band splitting, assignment is not straightforward because they are also consistent with phonon positions [192]. As shown in Fig. 4.3 (b, c), decreasing temperature red shifts the 22 and 38 meV structures and increases the oscillator strength. These trends are also apparent in the raw reflectance spectra (inset, Fig. 4.1 (c)). Both trends differ from what is expected for phonons on a conducting background [193]. Moreover, we do not anticipate significant differences in phonon effects between the x=1/4 and 1/3 materials, which again argues against a phonon interpretation. Returning to our picture of low energy spin split electronic excitations, there are several bands crossing the Fermi energy with vertical band-to-band transitions in the correct energy range [Fig. 4.3 (a)]. Recent models of Rashba splitting in BiTeI [194] suggest that thermal expansion and electron-phonon coupling effects combine to reduce the effective Rashba parameter and smear the gap(s) at elevated temperatures. Of course, while the 2H- structures technically lack inversion symmetry, they do have a vertical mirror plane, so we do not anticipate the same kind of strong inversion-breaking Rashba effects that are observed in BiTeI [195]. Additional evidence that the 22 and 38 meV excitations may be electronic in origin comes from the x=1/4 system where these features are not observed.

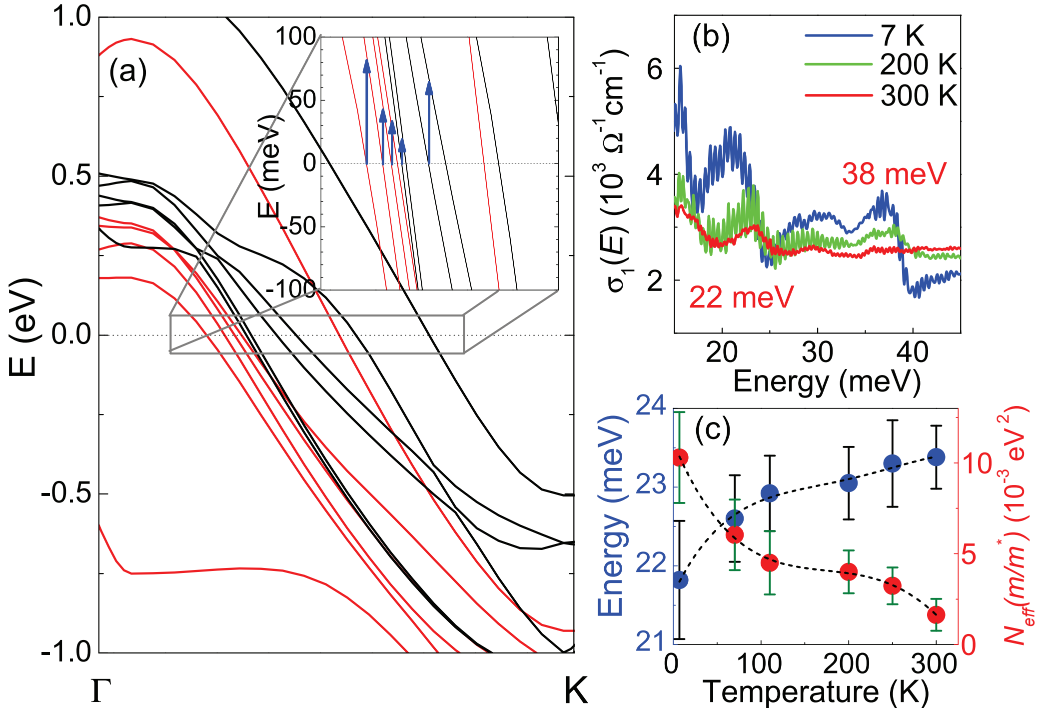

Figure 4.3: (a) Close up view of the band structure of $Fe_{1/3}TaS_2$ between the Γ and K-points. Inset: low energy excitations on the order of a few tens of meV due to the band splitting. (b) Temperature dependence of the optical conductivity of the x=1/3 materials in the vicinity of the 22 and 38 meV excitations. (c) Peak position and oscillator strength of the 22 meV feature as a function of temperature.

Chapter 5

Excitations of intercalated metal monolayers in transition metal dichalcogenides

Metal monolayers have a long and fascinating history [196]. Whether due to surface adsorption [197, 198] or intercalation [199], these structures display distinctive electronic and magnetic properties [118, 200] and play key roles in photovoltaic cells [201], semiconductor surfaces [202], and catalysts for batteries [203]. The importance of monolayer interactions has been demonstrated in metal intercalated graphite [204–206] and bilayer graphene [207, 208], both of which reveal superconductivity. Metal centers can also be intercalated into other van der Waals materials such as transition metal dichalcogenides [118, 209, 210], forming different patterns within the gap depending upon the concentration. When incorporated in this manner, metal monolayers support high temperature magnetic ordering [10,13,113], novel metallicity that is distinct from that of the parent compound [79, 114], and superconductivity [115, 211, 212]. Intercalated metal monolayers are also responsible for the development of different types of domain walls in layered chalcogenides [6]. The Fe_xTaS_2 family of materials [6] attracted our attention as a platform with which to reveal the fundamental excitations of the atomically-thin network of metal atoms embedded within the van der Waals gap.

2H-TaS_2 is well-known to display a $P6_3/mmc$ space group [125]. The crystal structure consists of TaS_2 slabs separated by a van der Waals gap and stacked together along the c-axes. Within a slab, each Ta center is surrounded by a trigonal prism of S anions. The structures of Fe_xTaS_2 ($x = 1/4$ and $1/3$) are shown in Fig. 5.1(a,b). It is well established that the transition metal dichalcogenide layers have strong covalent bonding, leaving the Fe atoms (which form a single metallic layer within the van der Waals gap) weakly bound. We refer to these ultra-thin well-ordered metal layers as “monolayers” or “atomically thin layers of metal atoms sandwiched between chalcogenide slabs” but of course, they are not isolated, free-standing monolayers in the sense of graphene or other exfoliated systems. They are embedded in the crystal itself - a consequence of the intercalation process. As shown in Fig. 5.1(a,b), the $x = 1/4$ system is centrosymmetric whereas the $x = 1/3$ material is non-centrosymmetric and chiral [6]. The embedded Fe monolayer layer brings a significant, distinct density of states to the Fermi level [81, 188, 189] and a narrow free-carrier response to the optical properties (in addition to the Drude that emanates from 2H-TaS_2 itself) [114]. Chirality in the $x = 1/3$ member manifests in (i) the nature of the hole/electron pockets, (ii) electron density patterns in the Fe plane, and (iii) the formation of $Z_2 \times Z_3$ structural domains with Z_6 vortices [6, 114].

The entire family of Fe_xTaS_2 materials is metallic. As demonstrated by prior optical properties work [114], metallic character precludes observation of odd-symmetry infrared-active phonons across the various magnetic transitions due to screening by the free carrier response. As a result, the local lattice distortions in this class of

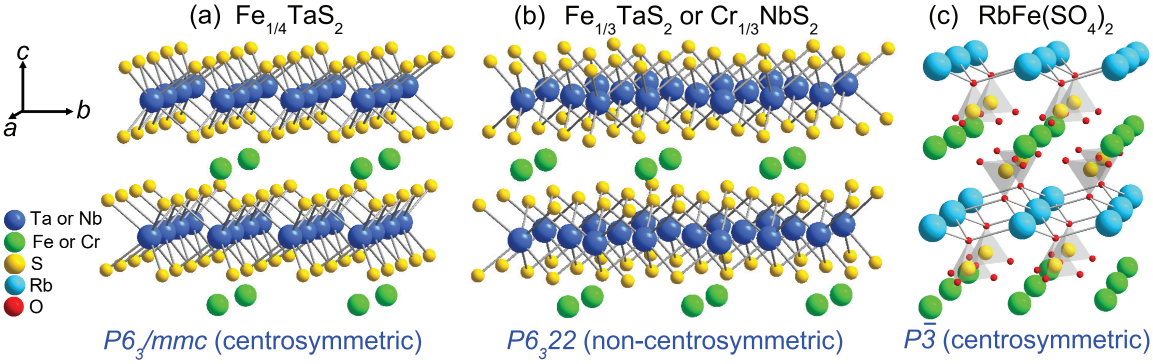

Figure 5.1: (a) $Fe_{1/4}TaS_2$ displays a centrosymmetric $P6_3/mmc$ space group [6]. The Fe layers have a $2a \times 2a$ superstructure in the plane and an AA-type stacking pattern along the c-axis. (b) Non-centrosymmetric, chiral structure of $Fe_{1/3}TaS_2$ and $Cr_{1/3}NbS_2$ (space group $P6_322$) [6,11]. The Fe layers have a $\sqrt{3}a \times \sqrt{3}a$ superstructure in the plane and an AB-type stacking pattern along c. (c) Crystal structure of $RbFe(SO_4)_2$ at room temperature (space group $P\bar{3}$) [213]. This system also has an Fe monolayer with AA-type stacking.

materials - particularly those that involve the metal monolayer - are highly underexplored. This is problematic because, as we shall discuss below, a number of properties and mechanisms depend upon phonons and their behavior [214]. We therefore turn to Raman scattering spectroscopy to reveal the even-symmetry vibrational modes and to search for evidence of monolayer excitations. As a reminder, the selection rules of infrared and Raman scattering spectroscopies determine whether odd or even symmetry vibrational modes are sampled. It is the site-specific nature of these techniques that allows us to extract the signature of the metal monolayer from the complex mode pattern in these materials.

In order to explore the vibrational properties of intercalated chalcogenides, we measured the Raman response of Fe_xTaS_2 ($x = 0$, 1/4, and 1/3) and compared our findings with complementary lattice dynamics calculations. For the first time, we identify a set of characteristic excitations of the embedded Fe monolayer that have both in- and out-of-plane components. These in- and out-of-plane vibrations of the intercalated Fe monolayer reveal frequency, linewidth, and intensity trends as well as spin-phonon coupling. In order to test whether similar excitations appear in other systems with weakly bound layers, we extended our work to include Cr_xNbS_2 ($x = 0$, 1/3) [10, 116, 215–218] and $\text{RbFe(SO}_4)_2$ [213, 219, 220] which have comparable metal ordering patterns inside the van der Waals gap [Fig. 5.1(b,c)]. In each case, we find that the metal monolayer is moving in a coherent fashion - not just filling space, adding/subtracting, or compensating charge. These results enable the development of structure-property relations and modeling of frequency vs. mass ratio effects. We discuss the consequences of in- and out-of-plane metal monolayer excitations on the properties of these materials as well.

5.1 Localized vibrational modes induced by Fe intercalation

Figure 5.2(a) displays the Raman spectra of the Fe_xTaS_2 family of materials at room temperature. We begin by assigning the modes of the parent compound - a process that also isolates excitations that emanate from the intercalated metal layer. In line with prior work on 2H-TaS_2, we assign peaks at 240, 308, and 380 cm^{-1} as E_{1g}, E_{2g}, and A_{1g} modes, respectively [Table. 5.1] [89,98,192,221,222]. We do not observe the 26 cm^{-1} E_{2g} mode due to the use of a cut-off filter. We assign the broad band centered near 180 cm^{-1} as a two-phonon mode [89, 98, 100]. It arises from the persistence of short-range charge density waves [89] and diminishes at low temperatures due to screening [Fig. 5.3(a)]. Several other features below 110 cm^{-1} are activated by remnant charge density wave effects as well [Fig. 5.3(a,b)] [89, 221]. One direct way to identify those charge density wave features is to compare the Raman spectra of 2H-TaS_2 with its structural analog. Figure 5.3(c) displays the Raman response of 2H-NbS_2 at 300 and 4 K for comparison. Prior literature reported that this system does not have a charge density wave transition [223–226]. The Raman behaviors at 4 and 300 K are nearly identical except that the phonon frequencies harden at low temperature. No new peaks emerge. This behavior confirms that symmetry breaking in 2H-TaS_2 is due to the charge density wave transition.

Next, we turn our attention to the intercalated materials [Fig. 5.2(a)]. A similar mode pattern emanates from the transition metal dichalcogenide slabs in the $x = 1/4$ and 1/3 compounds, although the exact symmetry designations reflect space group differences [Fig. 5.1]. The response below 200 cm^{-1} is more interesting. In the $x = 1/4$ compound, peaks emerge at 122 and 129 cm^{-1} whereas in the $x = 1/3$ material, new features appear at 139 and 156 cm^{-1} [Fig. 5.2(b)]. Based upon our lattice

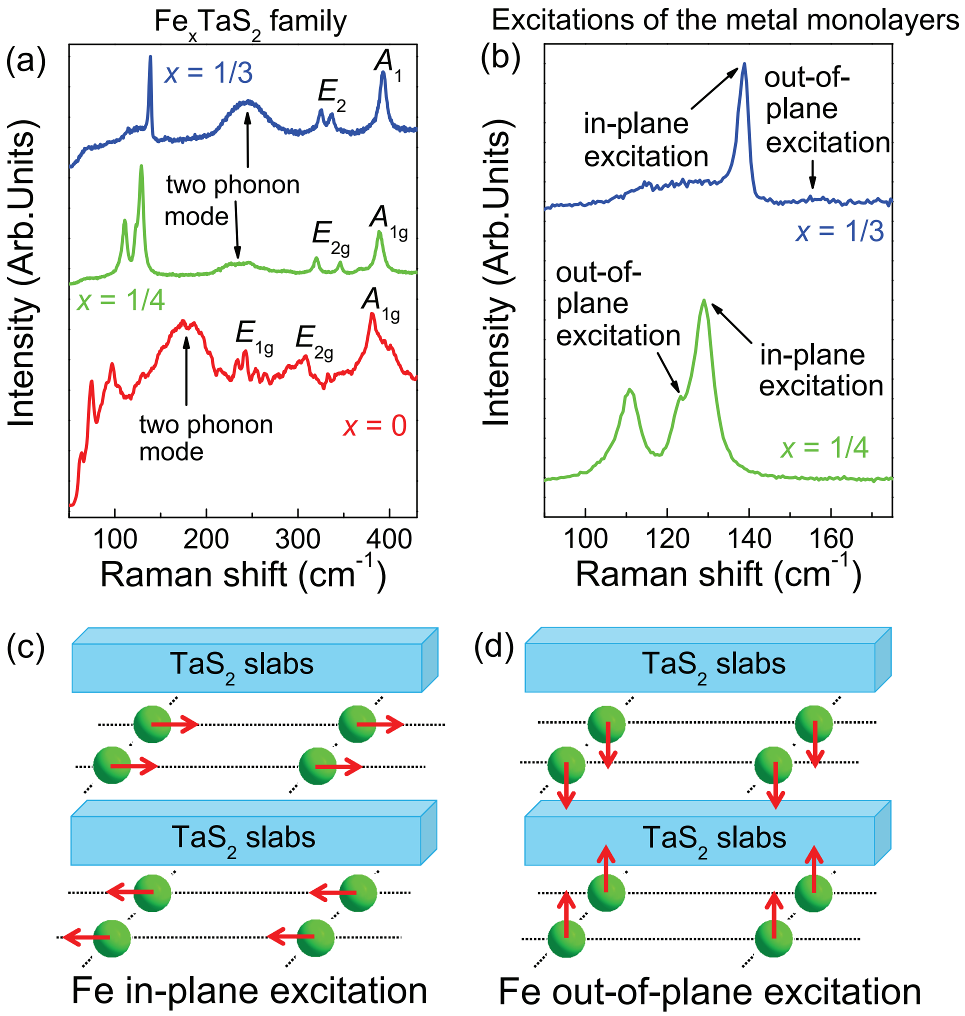

Figure 5.2: (a) Raman spectra of the Fe$_x$TaS$_2$ family of materials ($x = 0$, 1/4, and 1/3) at 300 K. (b) Close-up view of the in- and out-of-plane Fe monolayer excitaions in Fe$_{1/4}$TaS$_2$ and Fe$_{1/3}$TaS$_2$. (c,d) Schematic view of the in- and out-of-plane excitations of the Fe monolayer.

Table 5.1: Raman modes of Fe_xTaS_2, along with extracted symmetries, displacement patterns, and spin-phonon coupling constants.

material	**experimental (cm^{-1})**	**calculated (cm^{-1})**	**mode displacement pattern**	**symmetry**	**spin-phonon coupling constant (cm^{-1})**
2H-TaS_2	380	350-370	TaS_2 out-of-plane bending	A_{1g}	-
	308	255-310	TaS_2 in-plane bending	E_{2g}	-
	240	200 - 225	TaS_2 twisting mode	E_{1g}	-
	180	-	Two-phonon modes	-	-
	-	30 - 100	TaS_2 layer shifting mode	E_{2g}	-
$Fe_{1/4}TaS_2$	389	380 - 410	TaS_2 out-of-plane bending	A_{1g}	1.03
	320, 346	310 - 370	TaS_2 in-plane bending	E_{2g}	0.78, 0.83
	234	-	Two-phonon mode	-	-
	129	120 - 140	Fe in-plane monolayer excitation	E_{2g}	1.1
	122	125 - 145	Fe out-of-plane monolayer excitation	A_{1g}	0.3
	110	110 - 150	TaS_2 layer twisting mode	E_{1g}	-0.77
	43	30 - 100	TaS_2 layer shifting mode	E_{2g}	-
$Fe_{1/3}TaS_2$	393	400 - 420	TaS_2 out-of-plane bending	A_1	-
	325, 337	320 - 370	TaS_2 in-plane bending	E_2	-0.16, 0.07
	245	-	Two-phonon mode	-	-
	139	130 - 160	Fe in-plane monolayer excitation	E_2	-
	156	160 - 180	Fe out-of-plane monolayer excitation	A_1	-
	114	110 - 150	TaS_2 layer twisting mode	E_1	-
	46	30 - 100	TaS_2 layer shifting mode	E_2	-

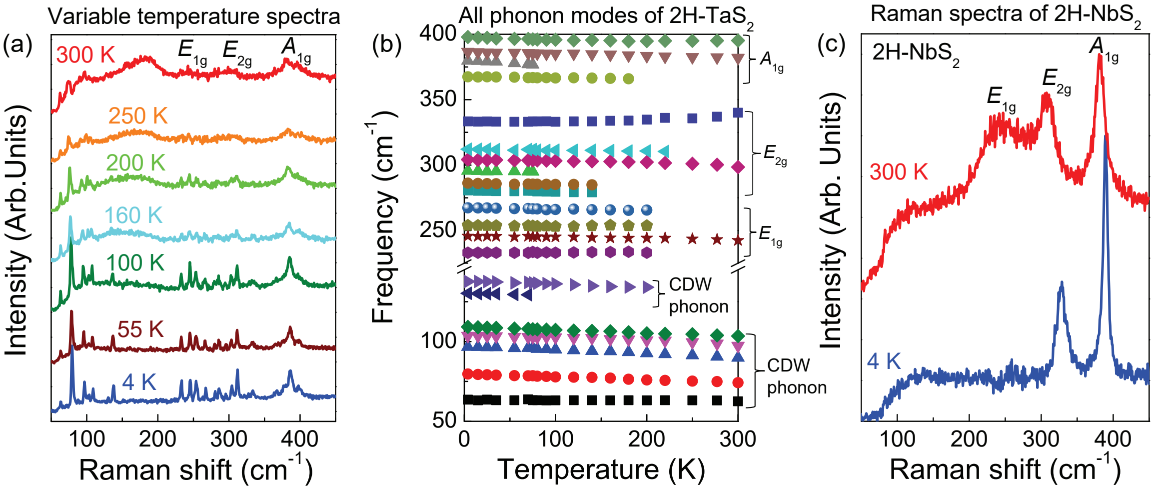

Figure 5.3: (a) Raman spectra of 2H-TaS$_2$ as a function of temperature. (b) Frequency vs. temperature trends for 2H-TaS$_2$, with the appropriate assignments. (c) Raman spectra of 2H-NbS$_2$ at 300 and 4 K along with peak assignments.

dynamics calculations, we assign these peaks as in- and out-of-plane excitations of the Fe monolayer [227]. We therefore find that an intercalated metal monolayer has a unique set of excitations and a fully-identifiable pattern even though it resides inside the van der Waals gap of a more complex material. The exact displacement pattern is challenging to visualize, but the motion is similar to that shown in the schematics [Fig. 5.2(c,d)].

One way to prove our assignments of the in- and out-of-plane Fe monolayer excitation is to compare the Raman spectra of intercalated ones with that of the parent compound. For the Raman spectra of the 2H-TaS_2 at 300 K, we did not observe any additional peaks between 100 and 200 cm^{-1} except for a two-phonon mode [Fig. 5.2(a)]. However, two new modes emerge between 110 and 150 cm^{-1} in 2H-TaS_2 at low temperatures. These features attracted our attention because they are very close to the proposed metal monolayer excitations at 122, 129, 139, and 156 cm^{-1} [Table 5.1]. However, the fact that these structures disappear above 200 K shows that they can be attributed to charge density wave-induced symmetry-breaking [Fig. 5.3(a,b)]. This finding is in good agreement with Ref. 221. It also reaffirms our assignment of in- and out-of-plane monolayer excitations at room temperature in the Fe intercalated compounds. Some lattice distortions associated with the charge density wave persist to higher temperature due to structural instabilities and short-range interactions [89].

Figure 5.2(b) displays a close-up view of the Fe monolayer excitations. A chalcogenide layer twisting mode involving weak interlayer interactions between the monolayer and TaS_2 slab is observed near 110 cm^{-1} as well. Although the in- and out-of-plane metal monolayer excitations have similar frequencies, they are best distinguished by relative intensities. The in-plane excitation is always the most intense. In order to understand why this is so, it is important to realize that the TaS_2 slabs are not rigid. As a result, they interact with (and dampen) the out-of-plane excitations of the metal monolayer. This effect is especially important in the $x = 1/4$ material and even causes the frequency of the out-of-plane excitation to shift below that of the in-plane mode. By contrast, in-plane Fe rattling is relatively unencumbered by the TaS_2 slabs. This leads to a higher intensity for the in-plane mode and a weaker intensity for the out-of-plane counterpart. The out-of-plane excitation is easy to identify in $Fe_{1/4}TaS_2$, but it is extremely weak in $Fe_{1/3}TaS_2$ [227]. We discuss frequency trends below.

5.2 Metal monolayer excitations in related materials

In order to develop structure-property relations involving intercalated metal monolayer excitations, we extended these Raman scattering measurements to include several related compounds. We begin with Cr_xNbS_2 ($x = 0$ and $1/3$) due to the similarity in the crystal structure and packing pattern of the Cr monolayer. Figure 5.4(a) displays the Raman spectra of the Cr_xNbS_2 family of materials ($x = 0$ and $1/3$). As expected, E_{1g}, E_{2g}, and A_{1g} modes are observed in the 2H- parent compound. The two-phonon mode is absent due to the lack of a density wave ground state. Turning to the $x = 1/3$ system, in- and out-of-plane vibrational modes of the Cr network are identified at 192 and 208 cm^{-1}, respectively. As before, the in-plane excitation is most intense. The out-of-plane excitation is significantly less intense compared to the in-plane mode, and it resonates at a higher frequency. This is because, although the out-of-plane excitation contains a small amount of slab motion, it is a less important part of the displacement pattern in the $x = 1/3$ system (compared to $x = 1/4$). We therefore see that metal monolayer excitations are an intrinsic part of the dynamics

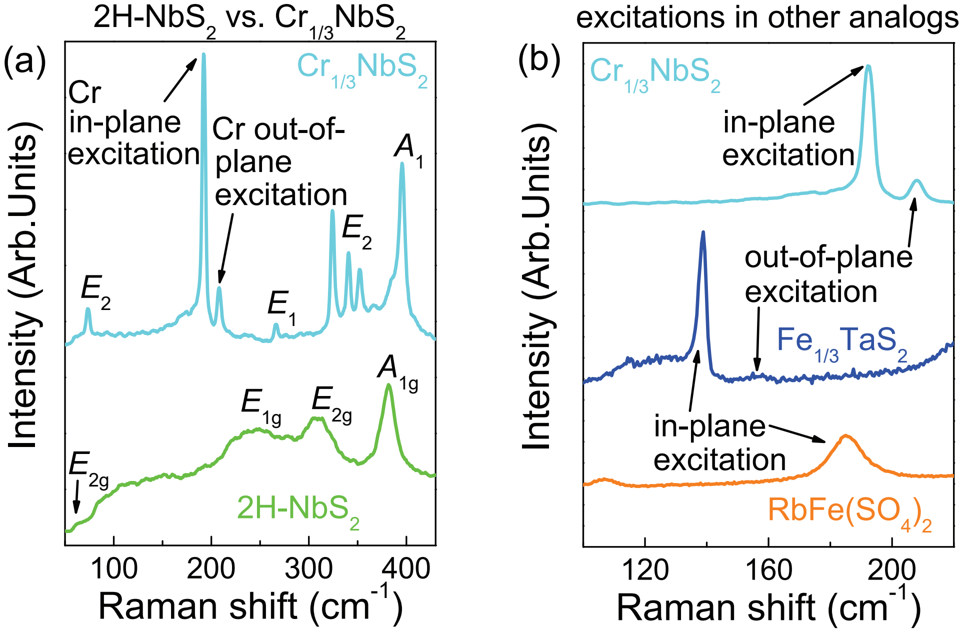

Figure 5.4: (a) Raman scattering spectra of the Cr$_x$NbS$_2$ family of materials ($x = 0$ and 1/3) at 300 K. (b) A close-up view of the in- and out-of-plane metal monolayer modes in Cr$_{1/3}$NbS$_2$, Fe$_{1/3}$TaS$_2$, and RbFe(SO$_4$)$_2$.

of intercalated transition metal dichalcogenides.

To further test our findings, we measured the Raman scattering response of $RbFe(SO_4)_2$. This system has Fe monolayers sandwiched between $Rb(SO_4)_2$ slabs with an AA-type stacking along the *c*-axis [Fig. 5.1(c)]. Figure 5.4(b) displays a close-up view of the Raman spectrum of $Cr_{1/3}NbS_2$, $Fe_{1/3}TaS_2$, and $RbFe(SO_4)_2$. Well-defined metal monolayer excitations emerge in all three compounds. The out-of-plane Fe monolayer mode is not present in $RbFe(SO_4)_2$ - even though the in-plane component is strong. We attribute its disappearance to the extremely narrow 2.31 Å van der Waals gap in this system [213] [Table 5.2], which quenches the out-of-plane motion of the embedded Fe monolayer.

Figure 5.5 summarizes how the monolayer excitations scale with characteristic distances and the metal-to-chalcogenide slab mass ratio. These parameters are summarized in Table 5.2. We find that the frequencies of the in- and out-of-plane metal monolayer excitations decrease with increasing metal-metal distance in the plane [Fig. 5.5(a,b)]. These trends emanate from softer potentials (and weaker force constants) in more weakly associated lower concentration networks. As we shall see below, an analysis of frequency trends in terms of the mass ratio provides an even more comprehensive framework for understanding these effects.

The in-plane metal-metal distance also impacts relative intensities of monolayer excitations [Fig. 5.5(c)]. The intensity of the out-of-plane excitation diminishes (and even falls to zero in $RbFe(SO_4)_2$) as the Fe network tightens and the narrower van der Waals gap confines motion to the *ab*-plane. In other words, when tightly packed, the out-of-plane motion of the metal monolayer is quenched, and the matrix element drops to zero.

Table 5.2: Summary of in-plane metal-metal distances, thicknesses of van der Waals gaps, and mass ratios for the materials of interest here. The metal-metal distances and van der Waals gap thicknesses are extracted from their structure files. [13, 188, 220] The mass ratio is defined as: $c \times M_{interc}/M_{host}$. Here, c is the concentration of intercalated element, M_{interc} is the atomic mass of the intercalated element, and M_{host} is the atomic mass of the host elements [228].

Materials	In-plane metal-metal distance (Å)	Thickness of van der Waals gap (Å)	Mass ratio
$Fe_{1/4}TaS_2$	6.61	2.93	0.06
$Fe_{1/3}TaS_2$	5.73	3.07	0.08
$Cr_{1/3}NbS_2$	5.75	2.89	0.11
$RbFe(SO_4)_2$	4.71	2.31	0.20

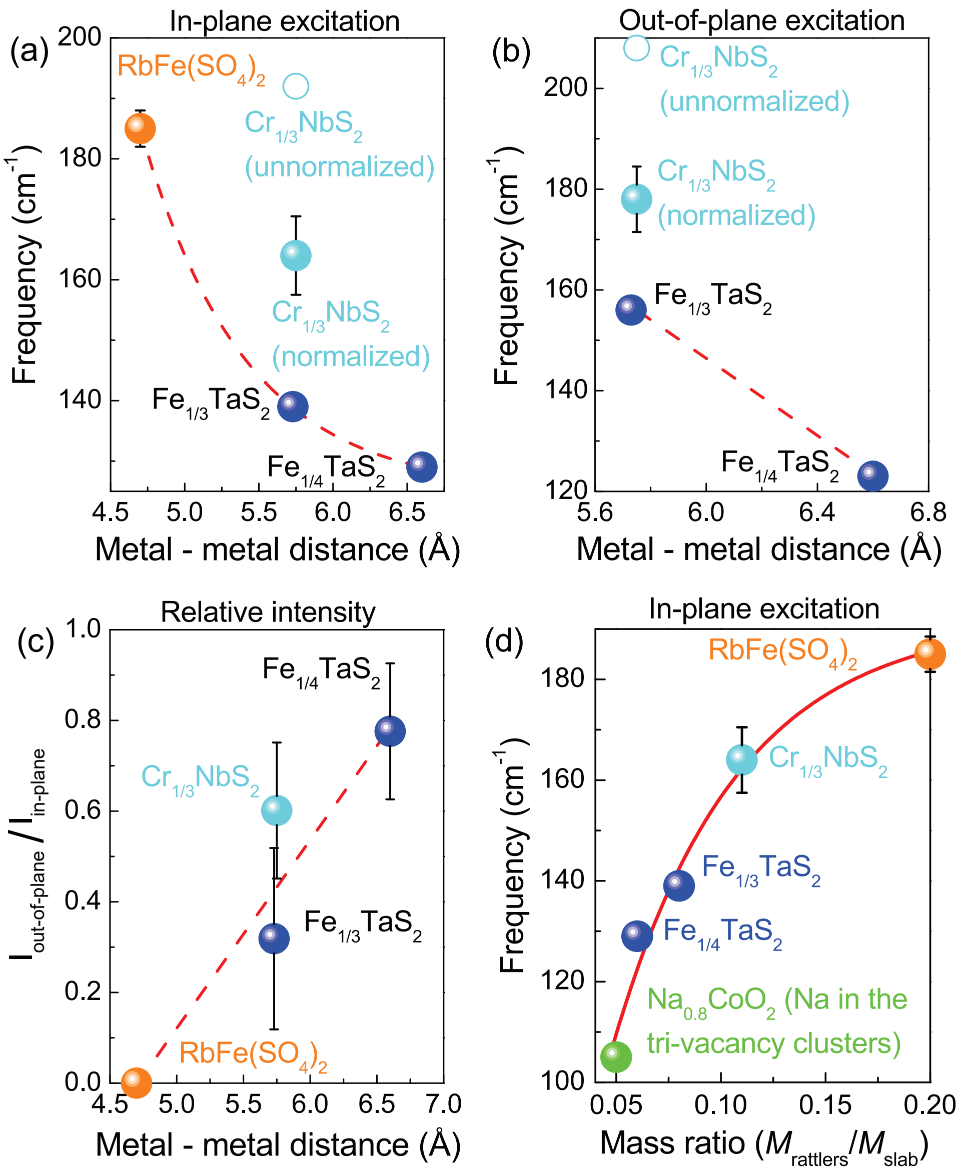

Figure 5.5: (a) Frequency of the in-plane metal monolayer excitation vs. in-plane metal-metal distance in Fe_xTaS_2 ($x = 1/4$ and $1/3$) and the analog materials. Results from $Cr_{1/3}NbS_2$ are normalized by the mass of the transition metal center as well as the slabs to better compare with the Fe-containing series. (b) Out-of-plane monolayer excitations as a function of in-plane metal-metal distance. (c) Relative intensity of the out-of-plane to in-plane rattling mode vs. in-plane metal-metal distance. (d) In-plane frequency vs. mass ratio between the intercalated metal monolayer and the chalcogenide slab. The red line is a fit to Eqn. 5.2. We find $\omega_{R,max} = 192$ cm^{-1} and $\kappa = 0.059$.

5.3 Modeling frequency vs. mass ratio effects

To examine the frequency vs. mass ratio relationship, we expanded the mode frequency ω_m about the mass ratio μ as:

$$\omega_m = \omega_{m,max} - \kappa(d\omega_m/d\mu). \tag{5.1}$$

Here, $\omega_{m,max}$ is the maximum mode frequency, and κ is an "effective" spring ratio between the monolayer and slab. The mass ratio is defined as the ratio of metal monolayer to the slab within the unit cell (M_m/M_s) [Table 5.2]. Assuming that κ is constant for the mode environment, frequency is given by:

$$\omega_m = \omega_{m,max}\Big(1 - e^{-\frac{\mu}{\kappa}}\Big). \tag{5.2}$$

This solution fits the data in Fig. 5.5(d) very well. We extract a maximum in-plane mode frequency of 192 cm^{-1} and an effective spring ratio of 0.059. Equation 5.2 also has a conceptually interesting limit impacting the growth process of these materials. Comparing the maximum mode frequency to the data in Fig. 5.5(a), we find that the minimum metal-metal distance is near 4.5 Å. The maximum possible mass ratio is therefore between 0.21 and 0.25, suggesting an intercalation threshold. Beyond this limit, interlayer interactions become comparable to intralayer interactions, blurring the distinction between weakly bound metal monolayers between chalcogenide slabs and a more standard multilayered material.

Initially, only the Fe and Cr systems were used for the fit, providing a prediction for other similar materials. To test our model further, we included data from Ref. 229. In sodium intercalated cobalt dioxide ($Na_{0.8}CoO_2$), only the Na atoms in the 2b Wyckoff site associated with clusters of three vacancies display in-plane excitations [229]. Strikingly, the mode frequency in $Na_{0.8}CoO_2$ is in excellent agreement with the overall frequency vs. mass ratio trend [Fig. 5.5(d)]. The agreement reveals that, for this specific type of chemical structure, the mass ratio effect is not dependent on the different chemical and interaction environments such that they do not modify the effective spring ratio for an intercalated metal monolayer. Although, the spring ratio is different for the in- and out-of-plane modes. This effect is also valid for the out-of-plane monolayer excitation where different $\omega_{m,max}$ and κ parameters are required to capture out-of-plane mode frequency vs. mass ratio effects.

5.4 Spin-phonon coupling in $Fe_{1/4}TaS_2$

In order to further explore metal monolayer excitations, we measured the Raman response of these materials as a function of temperature. $Fe_{1/4}TaS_2$ is unique in that it exhibits strong spin-phonon coupling across the magnetic ordering transition. This coupling may be due to the robust ferromagnetic ground state and sharp coercive field in the $x = 1/4$ compound. In contrast, the $x = 1/3$ member has frustration due to the triangular Fe lattice and a much softer coercive field. [6, 118] Figure 5.6(a) displays a close-up view of the Raman response of $Fe_{1/4}TaS_2$ at three characteristic temperatures. The rattling excitations become sharper and more well-separated with decreasing temperature due to standard mode hardening and line width effects. The in-plane excitation hardens most noticeably, at roughly twice the rate of the out-of-plane mode. We also observe a TaS_2 layer twisting mode nearby at 110 cm^{-1}, which softens at low temperatures. This effect is probably associated with a weak interlayer interaction between the Fe monolayer and TaS_2 slab.

Figure 5.6(b,c) displays frequency vs. temperature for the in- and out-of-plane modes of the intercalated Fe monolayer in $Fe_{1/4}TaS_2$. We use a Boltzmann sigmoid model to capture anharmonic and short-range interactions. [29, 230] The spectral data deviate from the fit below the 160 K ferromagnetic ordering temperature. The

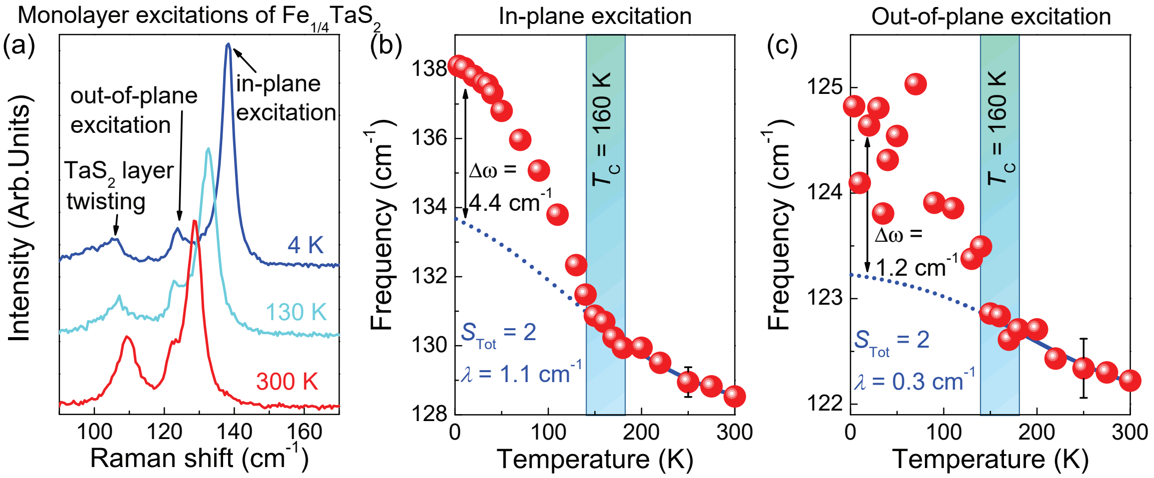

Figure 5.6: (a) Close-up view of the Raman response of $Fe_{1/4}TaS_2$ as a function of temperature. (b) In-plane mode frequency of the Fe monolayer vs. temperature. (c) Frequency of the out-of-plane mode of the Fe monolayer vs. temperature.

strong frequency shift across a magnetic ordering transition is clear evidence for spin-phonon coupling. [30,231,232] Assuming only nearest neighbor exchange interactions in the Fe monolayer (probably interacting through the S centers on the chalcogenide slabs), we extract the spin-phonon coupling constant as: [30,31]

$$\omega = \omega_0 + \lambda \langle S_i \cdot S_j \rangle. \tag{5.3}$$

Here, ω_0 denotes the unperturbed phonon frequency, ω is the renormalized frequency in the presence of spin-phonon coupling, $\langle S_i \cdot S_j \rangle$ is the spin-spin correlation function, and λ is the spin-phonon coupling constant. To extract the coupling constant, we assume a limiting low-temperature value of the spin-spin correlation function: $\langle S_i \cdot S_j \rangle = S^2 = (2)^2 = 4$. We find λ's for the in- and out-of-plane excitations to be 1.1 and 0.3 cm^{-1}, respectively. In-plane coupling is thus an order of magnitude larger than the out-of-plane effect. Spin-phonon coupling constants for other vibrational modes in $\mathrm{Fe}_{1/4}\mathrm{TaS}_2$ are summarized in Table 5.1.

5.5 How do metal monolayer excitations influence properties?

It is well known that rattlers in filled cavities and channels impact thermoelectricity and ionic conductivity [229, 233–235]. In this context, a rattler consists of a weakly bound atom with a large thermal elipsoid confined to a cavity or cage. Our situation is different because metal monolayer excitations are coherent, and as a result, they can change properties in completely different ways. In fact, any mechanism requiring a highly polarizable response or peak in the dielectric constant can benefit from these excitations. Since the collective excitations of intercalated metal monolayers act as highly sensitive terahertz resonators, this work may open opportunities for sensing and flash LiDAR detection. That the in-plane mode is more intense than the majority of chalcogenide slab-related phonons is useful for these applications.

Our structure-property relations suggest that external stimuli can tune metal monolayer excitations. One such example is electrical switching in $Fe_{1/3}NbS_2$, another magnetically intercalated transition metal dichalcogenide of interest as an antiferromagnetic spintronic device [118]. Here, the current draws the Fe centers back and forth, supported by the facile in-plane motion of the Fe network that we discuss in this work. Switching occurs as the field-induced motion of the ions changes both the low-temperature magnetism and transport properties. The ability to use a current pulse to rotate an in-plane component of the antiferromagnetic order [118] is also interesting and potentially related to the ability of the $x = 1/3$ materials to support chiral phonons [236].

Metal monolayer excitations may even influence crystal growth and microstructure. For instance, the structural Z_6 vortices in chiral $Co_{1/3}NbS_2$ and $Cr_{1/3}TaS_2$ are associated with antiphase domains with in-plane shift of intercalants, and the formation of Z_6 vortices [14] likely results from an order-disorder transition of intercalants far above room temperature. The in-plane monolayer excitation may act as a soft mode for this type of transition.

Chapter 6

Site-specific spectroscopic measurement of spin and charge in multiferroic superlattices $(\mathbf{LuFeO_3})_m/(\mathbf{LuFe_2O_4})_1$

Interface materials offer a means to achieve electrical control of ferrimagnetism at room temperature as was recently demonstrated in $(LuFeO_3)_m/(LuFe_2O_4)_1$ superlattices. A challenge to understanding the inner workings of these complex magnetoelectric multiferroics is the multitude of distinct Fe centres and their associated environments. This is because macroscopic techniques characterize average responses rather than the role of individual iron centres. Here, we combine optical absorption, magnetic circular dichroism and first-principles calculations to uncover the origin of high-temperature magnetism in these superlattices and the charge-ordering pattern in the $m = 3$ member. In a significant conceptual advance, interface spectra establish how Lu-layer distortion selectively enhances the $Fe^{2+} \rightarrow Fe^{3+}$ charge-transfer contribution in the spin-up channel, strengthens the exchange interactions and increases the Curie temperature. Comparison of predicted and measured spectra also identifies a non-polar charge ordering arrangement in the $LuFe_2O_4$ layer. This site-specific spectroscopic approach opens the door to understanding engineered materials with multiple metal centres and strong entanglement.

6.1 Crystal structures of the $LuFeO_3$ and $LuFe_2O_4$ end members

Figure 6.1a displays the crystal structure of h-$LuFeO_3$ viewed along the [100] direction. Fe is in a trigonal bipyramidal environment surrounded by five oxygen atoms, forming Fe^{3+} polyhedra that are corner shared by the oxygen atoms in the ab-plane. The space group is $P6_3cm$, which is polar. This space group results from distortion of the nonpolar $P6_3/mmc$ space group with the rotations of the FeO_5 polyhedra and Lu displacement along the c-direction [237]. This breaks inversion symmetry and allows for polarization to develop along the c-axis. $LuFeO_3$ is thus an improper ferroelectric [18, 237].

The other end member is $LuFe_2O_4$. The system contains Fe bilayers with both Fe^{2+} and Fe^{3+} sites. The Fe atoms are in trigonal bipyramidal environments. Prior studies reveal an antiferroelectric ground state [20, 23] due to charge-ordering in the Fe bilayer. Figure 6.1b displays the structure of the antiferroelectric state viewed along the [120] direction. Charge-ordering in the A and B bilayers are mirror images, which induces opposite electric polarizations along the c-axis. This leads to a centrosymmetric $C2/m$ space group with no net electric polarization. Lu-layer distortion is forbidden in this state.

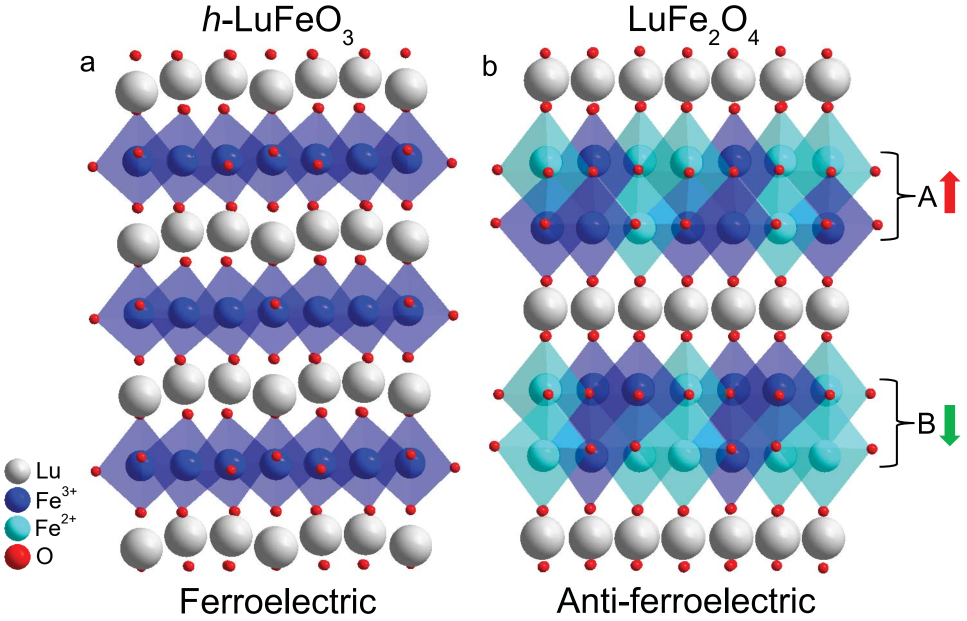

Figure 6.1: **Crystal structures of the end members.** **a** Crystal structure of h-LuFeO$_3$ with the $P6_3cm$ space group. **b** Crystal structure of LuFe$_2$O$_4$. The light and dark blue polyhedra represent the Fe^{2+} and Fe^{3+} site, respectively.

6.2 Uncovering the electronic excitations of different Fe centres in the (3,1) superlattice

We begin with the (3, 1) superlattice because it is the most theoretically tractable. Figure 6.2a,b displays the crystal structure highlighting the $(LuFeO_3)_3/(LuFe_2O_4)_1$ layer pattern along with a scanning transmission electron microscope (STEM) image of the film. Inversion symmetry in the $LuFe_2O_4$ layer is broken due to the rumpling imposed by the adjacent $LuFeO_3$ layers [1]. This is because the pattern of Lu-layer distortions around the Fe double layer is asymmetric with both down/up/up and down/up/down displacements along c. Here, d represents the size of the Lu-layer displacement. One way to separate the role of the different metal sites - at least in principle - is by projecting out the contribution of various layers and their Fe centres. Figure 6.2c displays the spin-projected density of states for the Fe double layer in $LuFe_2O_4$, the adjacent monolayer and the central monolayer in $LuFeO_3$. The six types of excitations (summarized in Table 6.1) provide for a site-specific analysis of magnetism in $(LuFeO_3)_3/(LuFe_2O_4)_1$. This is an unusual amount of complexity for dichroic analysis of an iron-containing material. Fortunately, of these six excitations, only three are important due to the relative size of the matrix elements. For instance, the two charge transfer excitations are quite strong in the linear absorption and magnetic circular dichroism because they involve Fe sites with different charges. The on-site Fe^{2+} d-to-d excitation is important in the dichroic response due to the large Fe^{2+} density of states in the spin-down channel [Fig. 1c]. This feature is also evident in the optical absorption of the $LuFe_2O_4$ end member [21]. That these structures occur in different energy regions allows us to separate closely-related Fe-containing excitations in both the optical absorption and magnetic circular dichroism.

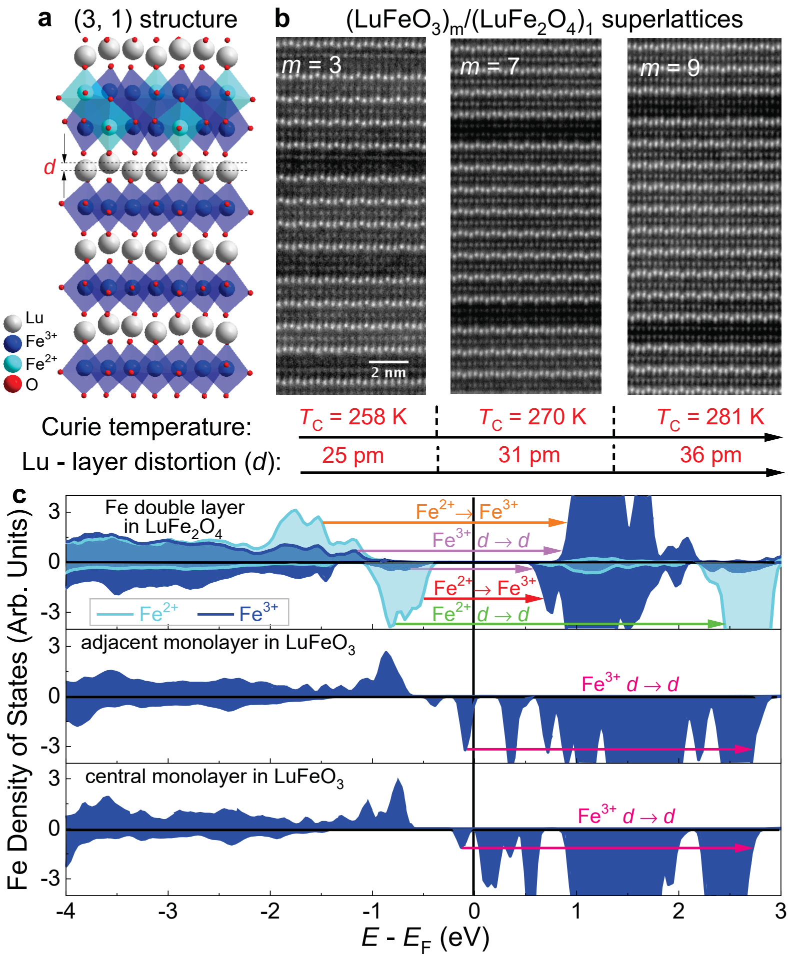

Figure 6.2: **Crystal structure, growth pattern, and spin-projected density of states. a** Crystal structure of the (3, 1) film showing how a $LuFe_2O_4$ slab (which has an iron oxide double layer with both Fe^{2+} and Fe^{3+} between two Lu layers) is sandwiched between three layers of $LuFeO_3$ [1]. d represents the Lu-layer displacement. **b** HAADF-STEM images of the $m = 3$, 7, 9 superlattices viewed along the $[1\bar{1}0]$ zone axis. Atomic number contrast shows the bright, heavy lutetium atomic rows layered with the less bright iron atomic rows. The scale bar is the same for all images. Trends in the ferrimagnetic T_C and Lu-layer distortion (which increases with the number of $LuFeO_3$ layers) are also shown. **c** Spin-projected density of states of the Fe double layer in $LuFe_2O_4$, an adjacent monolayer of $LuFeO_3$ and the central $LuFeO_3$ monolayer. These calculations were performed using the self-doped charge-ordering model as discussed in the text [Fig. 6.8b]. The Fe double-layer is non-polar, and the Lu-layer displacement is asymmetric with both down/up/up and down/up/down distortion patterns around the Fe bilayer. The Fe^{3+} and Fe^{2+} states are indicated with dark and light blue, respectively. The arrows denote different types of excitations.

Table 6.1: **Summary of different types of Fe excitations in the (3, 1) superlattice.** The first three rows indicate the most important excitations. The energy range for our measurement is from 0.8-2.8 eV.

Type of excitation	Excitation channel	Layer in the superlattice	Energy range (eV)	Intensity ($\Delta\alpha(E)$, $\alpha(E)$)
$Fe^{2+} \rightarrow Fe^{3+}$ charge transfer	spin-down	$LuFe_2O_4$	1 - 2.4	strong, strong
$Fe^{2+} \rightarrow Fe^{3+}$ charge transfer	spin-up	$LuFe_2O_4$	2 - 2.8	strong, strong
Fe^{2+} $d \rightarrow d$ on-site	spin-down	$LuFe_2O_4$	2.5 - 2.8	medium, medium
Fe^{3+} $d \rightarrow d$ on-site	spin-up	$LuFe_2O_4$	2 - 2.8	weak, weak
Fe^{3+} $d \rightarrow d$ on-site	spin-down	$LuFe_2O_4$	2 - 2.8	weak, weak
Fe^{3+} $d \rightarrow d$ on-site	spin-down	$LuFeO_3$	1 - 2.8	weak, weak

Figure 6.3a,b summarizes the spectroscopic response of $(LuFeO_3)_3/(LuFe_2O_4)_1$. The challenge that arises immediately - even upon cursory inspection of the dichroic spectra - is how to distinguish the different Fe contributions. One path forward is to employ the linear absorption spectrum, $\alpha(E)$, along with assignments from electronic structure calculations [1, 16, 17, 21, 182, 238] to determine characteristic excitation energies of each type of iron centre. Figure 6.3a displays the optical absorption spectrum of the (3, 1) superlattice. Based upon our spin-projected density of states calculations [Fig. 6.2c and Table 6.1], the Fe-related excitations take place over a broad energy range. We can address the various site-specific Fe-related excitations by dividing the spectra into different energy regions and performing subtractions where necessary. As a reminder, the most important are (i) the $Fe^{2+} \rightarrow Fe^{3+}$ charge-transfer excitations in the spin-up and spin-down channels of the $LuFe_2O_4$ double layer and (ii) the Fe^{2+} $d \rightarrow d$ on-site excitation in the spin-down channel of the $LuFe_2O_4$ double layer. These features are indicated in Fig. 6.3a.

Figure 6.3b displays the magnetic circular dichroism spectrum of the (3, 1) superlattice at full field. Access to the 25 T split helix magnet at the National High Magnetic Field Laboratory [170] was crucial to this work, providing both direct optical access and a field high enough to saturate the magnetic state of interest. Two zero-field spectra are also included. They are not the same because the measurement pathway is hysteretic (25 T $\rightarrow 0^-$ T $\rightarrow -$ 25 T $\rightarrow 0^+$ T $\rightarrow$ 25 T), and the ferrimagnetic film is not fully demagnetized when the field is removed. At full field, the dichroic spectra reveal a broad, asymmetric structure centered at 1.5 eV and a smaller lobe near 2.2 eV. Based upon Fig. 6.3a, we assign the 1.5 eV feature to the $Fe^{2+} \rightarrow Fe^{3+}$ charge-transfer excitation of the $LuFe_2O_4$ layer in the spin-down channel. The small 2.2 eV feature has a more complex origin because excitations are heavily mixed in this energy range. Our analysis shows that this structure emanates

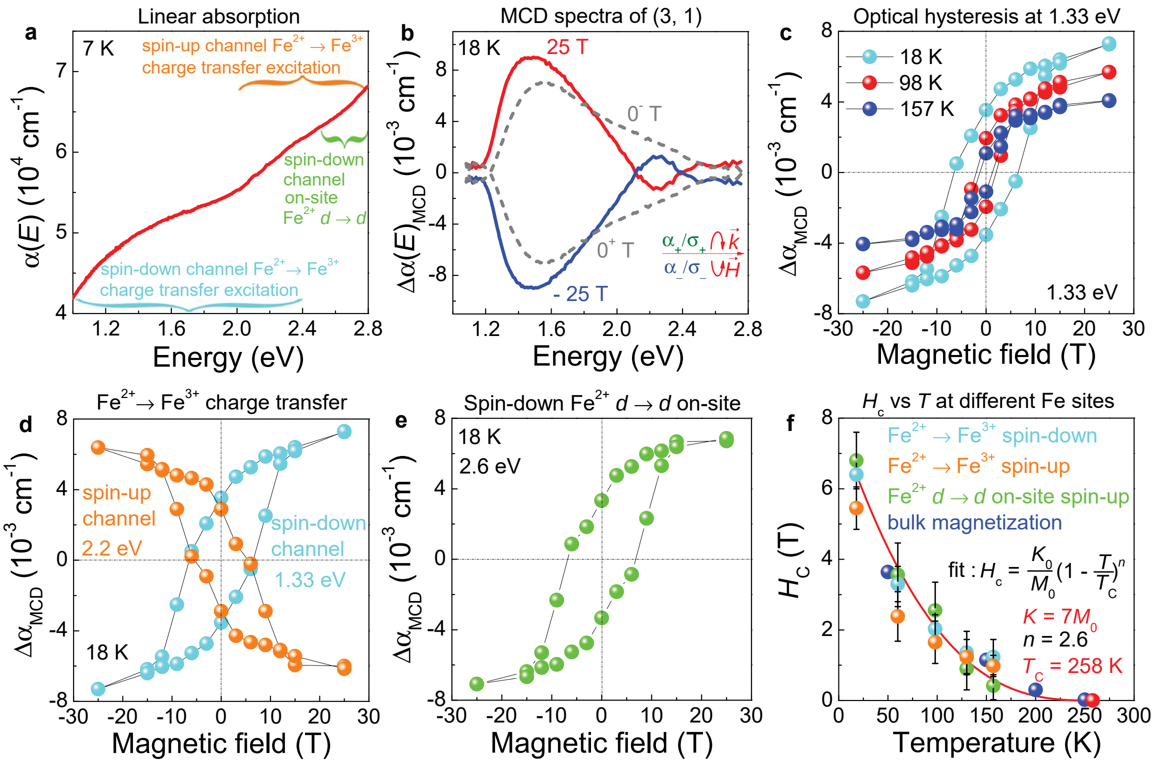

Figure 6.3: **Linear absorption spectrum, magnetic circular dichroism, and the magnetic behaviour of different Fe centres in $(\mathrm{LuFeO_3})_3/(\mathrm{LuFe_2O_4})_1$.** **a** Linear absorption spectrum of the (3, 1) superlattice. The three most important Fe-related excitations are indicated. **b** Magnetic circular dichroism spectra of the (3, 1) superlattice at ± 25 and ± 0 T after substrate correction. **c** Fixed energy cut of the magnetic circular dichroism spectrum at 1.33 eV as a function of magnetic field at various temperatures. **d** Optical hysteresis loop obtained from the analysis of the $\mathrm{Fe}^{2+} \rightarrow \mathrm{Fe}^{3+}$ charge-transfer excitation in the spin-up channel compared to that in the spin-down channel. **e** Hysteretic behaviour of the Fe^{2+} on-site *d*-to-*d* excitation in the spin-down channel. **f** Coercive fields extracted from the optical hysteresis loops for each type of excitation as a function of temperature. The model fit is described in the text. Bulk magnetization is included for comparison [16].

from a combination of charge-transfer excitations in both the spin-down and spin-up channels. The sign change at 2.1 eV is a reminder of how the spin-up channel density of states comes to dominate the response. There is another inflection point near 2.4 eV, above which $\Delta\alpha$ changes sign due to the way in which the spin-down channel Fe^{2+} $d \to d$ excitation dominates the dichroic response. The on-site d-to-d excitations of Fe^{3+} have much lower intensity [Table 6.1]. Importantly, features in the dichroic spectra $\Delta\alpha(E)_{MCD}$ are directly proportional to net magnetization, and since we can analyze this effect at different energies, the response can be correlated with specific iron centres. [32, 33, 165]

6.3 Revealing the role of each individual Fe centre

In order to uncover the role of each type of Fe centre, we take constant energy cuts of the dichroic spectra based upon the excitation of interest. For instance, constant energy cuts of the spectra at 1.33 eV reveal the behaviour of the $\mathrm{Fe}^{2+} \to \mathrm{Fe}^{3+}$ charge-transfer excitation in the spin-down channel. Remarkably, a plot of $\Delta\alpha_{MCD}$ at 1.33 eV vs. magnetic field unveils an optical hysteresis loop [Fig. 6.3c]. Because the charge-transfer excitation is located in the $\mathrm{LuFe_2O_4}$ layer, we can explicitly connect the behaviour of the Fe bilayer to the magnetic response. We also measure the dichroic spectra of the (3, 1) superlattice at different temperatures. Analysis again reveals optical hysteresis loops that close with increasing temperature [Fig. 6.3c].

We also consider how other Fe centres support high-temperature magnetism in the (3, 1) superlattice by taking cuts of $\Delta\alpha_{MCD}$ at several different energies [Fig. 6.3d,e]. While the optical hysteresis loop at 1.33 eV has a traditional shape, the loop becomes irregular at higher energies due to mixing [Fig. 6.4b,c]. The challenge is to extract the response of each individual Fe centre from the mixed state. We perform constant energy cuts at 1.8, 2.2 and 2.6 eV to address this issue [Fig. 6.4]. By

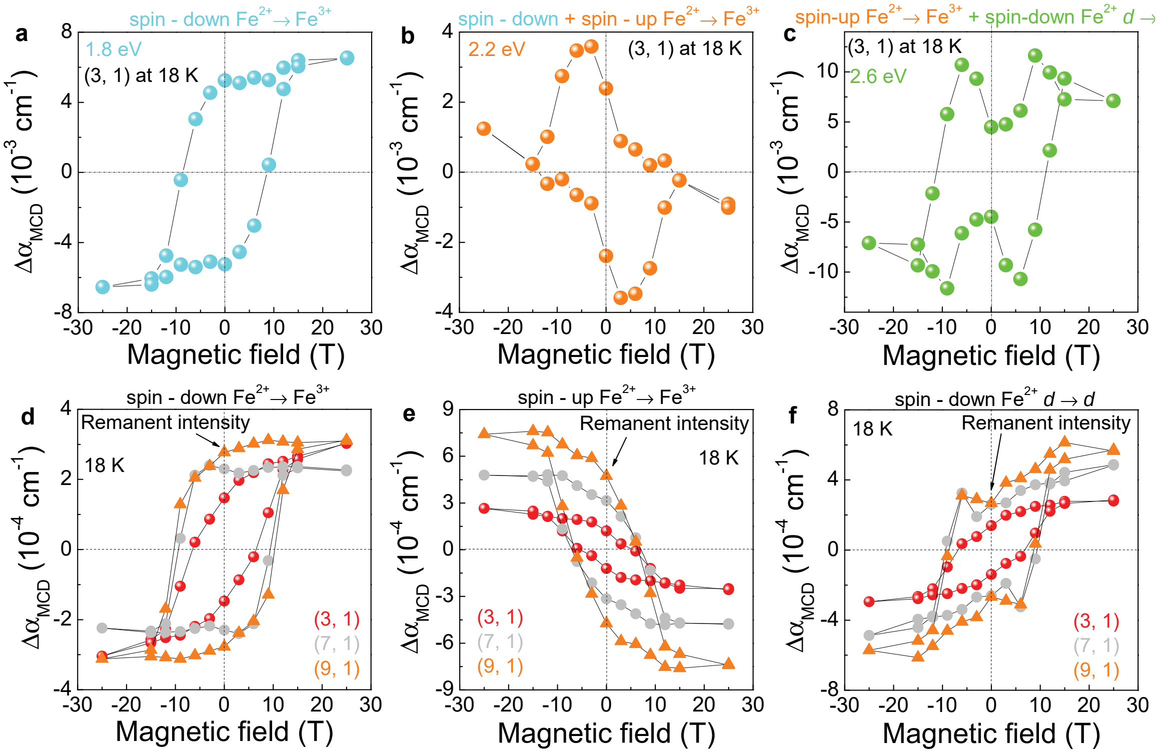

Figure 6.4: **Optical hysteresis at characterisic energies. a - c** Optical hysteresis at 1.8, 2.2 and 2.6 eV of the (3, 1) superlattice. The data points are directly obtained from the constant energy cuts of the raw spectra. **d** Optical hysteresis loops of (3, 1), (7, 1) and (9, 1) superlattices at 1.33 eV at 18 K. **e** Optical hysteresis of the spin-up channel $Fe^{2+} \rightarrow Fe^{3+}$ charge-transfer excitation at 18 K. **f** Optical hysteresis of the spin-down channel Fe^{2+} $d \rightarrow d$ on-site excitation at 18 K.

subtracting the dichroic response at 1.8 eV from that at 2.2 eV, we can obtain the pure signal of the charge-transfer excitation in the spin-up channel [Fig. 6.3d]. The direction of the hysteresis loop thus obtained is reversed because the spin state changes from down to up. A similar analysis is applied to the 2.6 eV energy cut of the spectral data. Here, spin-up charge transfer is strongly mixed with spin-down Fe^{2+} d-to-d on-site excitations. Subtraction yields the signature of the Fe^{2+} site [Fig. 6.3e]. Note that the shape of the hysteresis loop returns to "normal" because the spin state flips again.

In order to link the microscopic response of the spin in the Fe double layer with the bulk magnetic properties [1, 16], we extract the coercive fields from the optical hysteresis loops [Fig. 6.3c-e] and plot these spectroscopically-determined coercive fields (H_c) with those obtained from bulk magnetization as a function of temperature [Fig. 6.3f]. The trend in H_c is similar for all Fe centres, and the extracted coercive fields are in excellent agreement with bulk magnetization [1, 16]. This demonstrates that a significant portion of the magnetism in the (3, 1) superlattice originates from the $LuFe_2O_4$ layer. In other words, the global coercive field is approximately equal to the local coercive field in the $LuFe_2O_4$ layer. We fit the temperature dependence of the coercive field in the (3, 1) superlattice with the Néel relaxation and Bean-Livingston models [239, 240], which relate H_c to the single ion anisotropy (K), ferrimagnetic T_C and the power index n [Fig. 6.3f]. Overall, this model is in reasonable agreement with our data, although $n = 2.6$ may indicate a slightly non-classical response.

6.4 Interfacial responses in $(LuFeO_3)_m/(LuFe_2O_4)_1$

In order to unravel the mechanism of high-temperature magnetism and the consequences of Lu-layer distortion on the electronic structure of the interface, we measured the dichroic response of the (7, 1) and (9, 1) superlattices and compared the results to those of the (3, 1) material. As a reminder, higher order superlattices contain more $LuFeO_3$ layers, which increases the amplitude of the asymmetric Lu-layer distortion and raises the Curie temperature T_C [Fig. 6.2]. In order to make the most effective comparison, we need to isolate the spectroscopic response of the interface. We begin by normalizing the magnetic circular dichroism spectra on a "per repeat unit" basis by taking the raw dichroic signal and dividing by the number of repeat layers [Fig. 6.5b]. Next, we use the normalized spectra of two end members to construct a "composite spectrum" for each superlattice. The composite response is simply the dichroic signal generated from combining the per repeat unit end member spectra based upon the composition as given by m and n [Fig. 6.5c]. We extract the interface spectrum of each film by subtracting the composite response from the measured spectrum on a "per repeat unit" basis. A detailed discussion of this procedure is available in Chapter 3. We immediately see that the interface spectra, $\Delta\alpha_{MCD,\,Int.}$, is significant - at least at certain energies [Fig. 6.6a]. This indicates that additional magnetism arises from the $LuFe_2O_4$-$LuFeO_3$ layer interaction.

Figure 6.6a summarizes the interface response of our set of superlattices. Remarkably, the interface spectra are nearly identical below 2 eV, demonstrating that magnetism emanating from the $Fe^{2+} \rightarrow Fe^{3+}$ charge-transfer excitation in the spin-down channel is only minimally dependent upon the size of the Lu-layer distortion (or the number of $LuFeO_3$ layers in the superlattice). The situation is different above 2 eV where, despite mixing with the spin-down channel transitions, the charge-transfer excitation in the spin-up channel dominates the dichroic response [Fig. 6.2c]. This reveals that increased Lu-layer distortion selectively enhances the magnetic moment emanating from the spin-up channel $Fe^{2+} \rightarrow Fe^{3+}$ charge-transfer excitation, which amplifies the $LuFe_2O_4$ layer magnetization and therefore the dichroic signal. This analysis naturally raises the question of exactly how Lu-layer distortion impacts

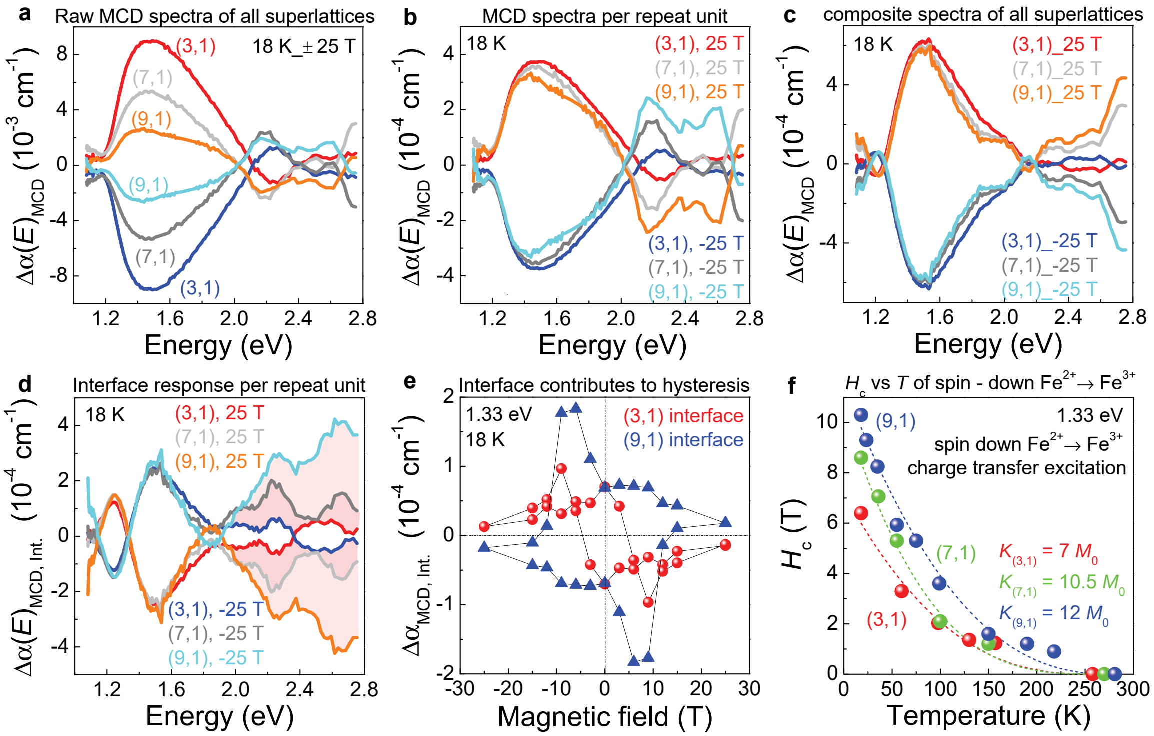

Figure 6.5: **Magnetic circular dichroism spectra of the $(\mathbf{LuFeO_3})_m/(\mathbf{LuFe_2O_4})_1$ (m = 3, 7, 9), along with the composite spectra and the coercivity trends. a** Raw magnetic circular dichroism spectra of the (3, 1), (7, 1) and (9, 1) superlattices at ± 25 T at 18 K, before the normalization to the number of repeat units. **b** Magnetic circular dichroism spectra after normalizing to the "per repeat unit basis." **c** Composite magnetic circular dichroism spectra of all superlattices. **d** The extracted interface spectra of all the superlattics. The pink area highlights differences. **e** $\Delta\alpha_{MCD,Int.}$ of (3, 1) and (9, 1) superlattices at 1.33 eV. **f** Coercive field obtained from analysis of the spin-down channel Fe^{2+} → Fe^{3+} charge transfer excitation in the (3, 1), (7, 1) and (9, 1) superlattices vs. temperature.

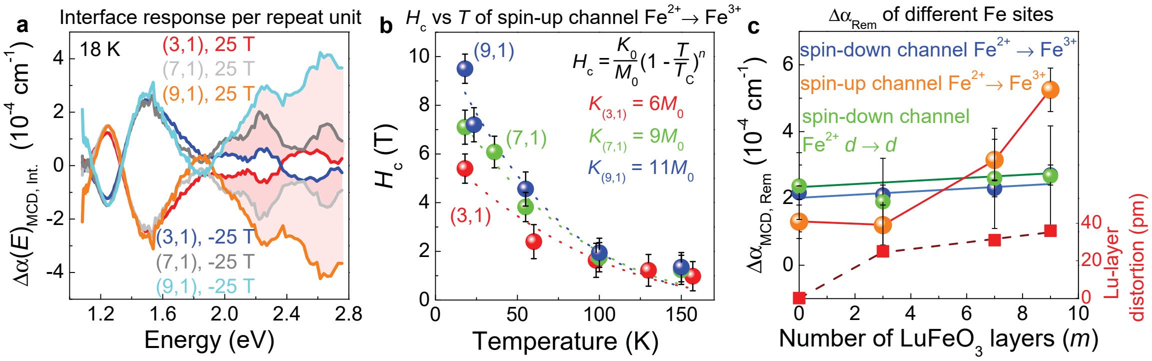

Figure 6.6: **Magnetic circular dichroism of the interfaces, coercive fields and remnant magnetization.** **a** Magnetic circular dichroism spectra of the interfaces on a "per repeat unit" basis. **b** Coercive fields obtained from analysis of the spin-up channel $Fe^{2+} \rightarrow Fe^{3+}$ charge transfer excitation in the (3, 1), (7, 1) and (9, 1) superlattices vs. temperature. **c** Remanent magnetic circular dichroism for different types of Fe-related excitations and Lu-layer distortion vs. the number of $LuFeO_3$ layers (m). The Lu-layer distortion is taken from Ref. 1, where total displacement d = $1.5 \times Q$ the distortion amplitude [241]. See Table 1 and associated text for exact energies.

individual Fe sites in the $LuFe_2O_4$ bilayer.

We unveil the interface behaviour of each Fe centre by taking constant energy cuts of $\Delta\alpha_{MCD,\,Int.}$ and plotting these values as a function of magnetic field. In addition to coercivity and related trends in the single ion anisotropy [Fig. 6.6b], the optical hysteresis loops that we extract from the magnetic circular dichroism spectra of the interface yield a remnant value of the dichroism ($\Delta\alpha_{MCD,\,rem.}$) that is proportional to remnant magnetization [Fig. 6.4 d-f]. We can therefore reveal how superlattice periodicity affects local Fe site magnetization. Figure 6.6c displays $\Delta\alpha_{MCD,\,rem.}$ for the different Fe-related excitations as a function of the number of $LuFeO_3$ layers. Because superlattice periodicity and the Lu-layer distortion are correlated, there is a relationship between $\Delta\alpha_{MCD,\,rem.}$ and the Lu-layer distortion as well. Above m = 3, the remnant signal from the charge-transfer excitation in the spin-up channel increases sharply - consistent with the theoretically predicted saturation moment in the $LuFe_2O_4$ layer [1]. By contrast, spin-down charge transfer and the Fe^{2+} $d \rightarrow d$ excitation are relatively insensitive to the number of $LuFeO_3$ layers (and the Lu-layer distortion). This behaviour demonstrates that increasing magnetic moment in the $LuFe_2O_4$ layer emanates from rising Fe^{2+} and Fe^{3+} density of states in the spin-up channel of the higher order superlattices. This conclusion emanates from the corresponding changes in the dichroic spectra. At the same time, it provides a microscopic explanation for how high-temperature magnetism in these superlattices derives from Lu-layer distortion as well as the more growth-oriented parameter of superlattice periodicity. We can understand in part why the enhanced magnetic moment emanates from the spin-up channel excitations by considering the charge-ordered state in greater detail.

6.5 Determining the charge ordering pattern in $(LuFeO_3)_3/(LuFe_2O_4)_1$

Because charge ordering is one of the highest energy scales in the system [1,20,21,23], magnetism in the $(LuFeO_3)_m/(LuFe_2O_4)_1$ superlattices depends intimately upon the charge ordering pattern in the Fe double layer. In order to reveal the relative importance of these states and distinguish between them, we calculated magnetic circular dichroism of several different candidate charge ordering patterns using first-principles methods and compared the results to the experimental dichroic spectra. The (3, 1) material has a large supercell containing 132 atoms, so we began by testing our predictions against the end members. Importantly, we tested two different states for the $LuFe_2O_4$ parent compound: CO-I and CO-II. The COII state is higher than the COI by about 4 meV per formula unit. Here, CO-I is an antiferroelectric state in which Lu trimer distortion is forbidden by symmetry [Fig. 6.7a] [20,242]. CO-II, on the other hand, allows Lu trimer distortion and has alternate Fe^{2+}- and Fe^{3+}-rich layers, the stacking of which breaks inversion and introduces ferroelectricity [Fig. 6.7b] [243]. The computed spectra of both $LuFe_2O_4$ and $LuFeO_3$ are in good agreement with our measurements [Fig .6.8a, b], and a CO-I pattern is identified in the $LuFe_2O_4$ end member [20,242]. We therefore extended this approach to the (3, 1) superlattice.

The charge ordered state in $(LuFeO_3)_3/(LuFe_2O_4)_1$ is more complicated than that in the $LuFe_2O_4$ end member due to Lu-layer distortion at the interface which is induced by the $LuFeO_3$ layer. As a result, the CO-II type state is more stable than CO-I for $m \geqslant 3$ superlattices even though it has higher energy scale in the bulk $LuFe_2O_4$. Based on a CO-II arrangement in the $LuFe_2O_4$ bilayer, theory predicts two possible charge-ordering patterns for the (3, 1) superlattice [1]. These candidates,

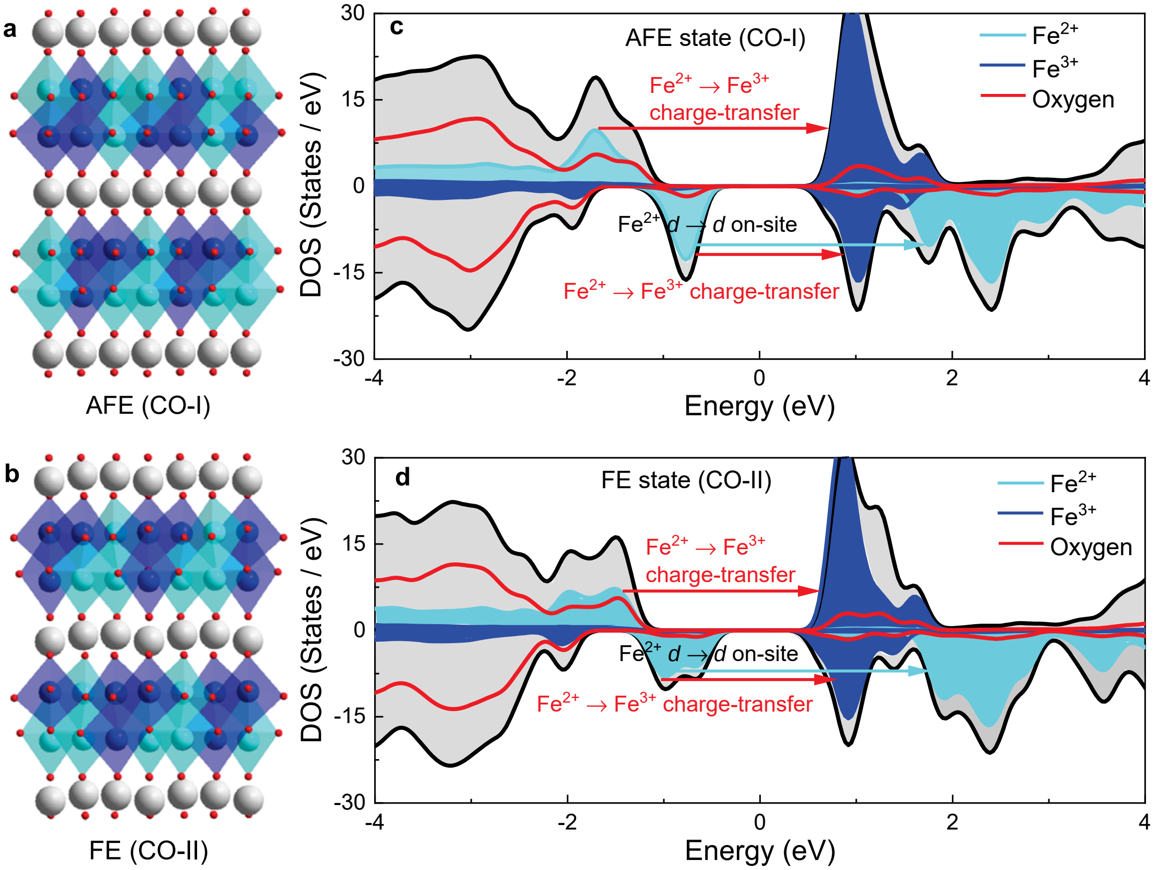

Figure 6.7: **Computed density of states of $LuFe_2O_4$ system. a, b** Optimized crystal structures of the CO-I and CO-II charge-ordering states, respectively. The light and dark blue polyhedra indicate the crystal environment of Fe^{2+} and Fe^{3+} centers, respectively. **c, d** Calculated partial density of states corresponding to the CO-I and CO-II charge-ordering patterns, respectively.

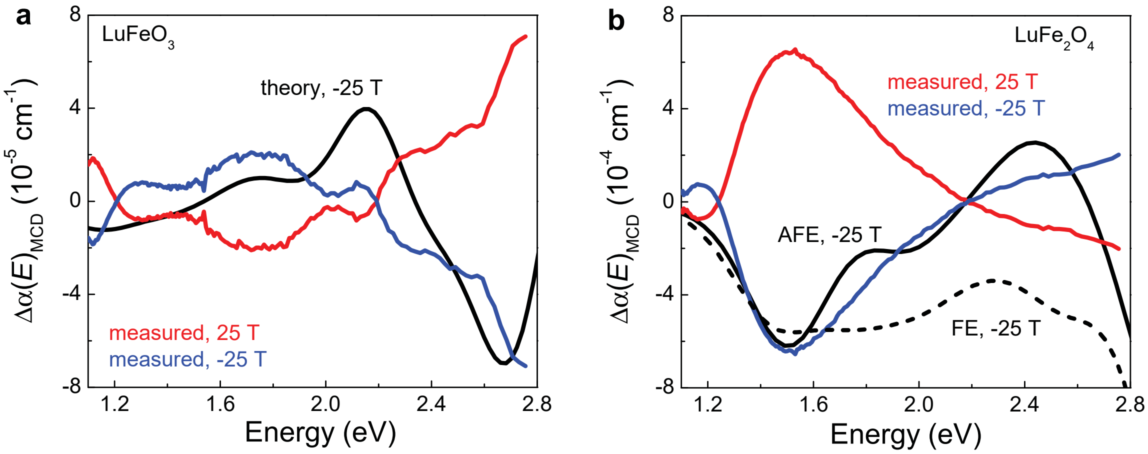

Figure 6.8: **The calculated vs. measured dichroic spectra of the end members. a, b** Computed and measured magnetic circular dichroism (MCD) spectra for the $LuFeO_3$ and $LuFe_2O_4$ end members, respectively. The calculated MCD spectra for the CO-I (AFE) and CO-II (FE) states are indicated by solid and dashed lines, respectively. AFE and FE refer to antiferroelectric and ferroelectric, respectively.

termed CO-FE and CO-DOPED for reasons that will become clear below, are slight variations (subsets) of the aforementioned CO-II pattern. What differentiates these candidates is (i) polar vs. non-polar character of the Fe double layer and (ii) symmetric vs. asymmetric Lu-layer displacement. The latter is closely associated with the phase shift across the ferroelectric domain wall in the superlattices [7]. We find that the single-domain type charge ordering state (CO-FE) is ferroelectric [Fig. 6.9a]. This is because the Lu-layer distorts in the same direction along c and with the same down/up/up pattern throughout the material. On the other hand, the Lu-layer displacement is asymmetric in the doped-type state (CO-DOPED). Here, our calculations predict a spontaneous electron transfer from Fe^{2+} sites in the bilayer to Fe^{3+} sites in the $LuFeO_3$ layer [Fig. 6.9b]. This leads to an Fe^{3+}-rich bilayer, which increases magnetization in the $LuFe_2O_4$ slab - consistent with a larger coercive field and higher moment. It is the electron transfer that periodically reverses the Lu-layer distortion to create the asymmetric down/up/up and down/up/down pattern across the Fe bilayer. This changes the direction of electric polarization across each domain wall which acts to create a non-polar Fe double-layer and overall antiferroelectric state. As we shall see below, this is the state that corresponds most closely with experiment.

Figure 6.9c compares the dichroic spectra for the (3, 1) superlattice with our calculations. As discussed above, two different CO-II type charge-ordering patterns were imposed in the simulations with the goal of distinguishing between them. These include CO-FE and CO-DOPED [Fig. 6.9a,b]. Overall, the experimental spectrum is in agreement with the CO-DOPED model. This means that the Fe double layer is non-polar, and the Lu-layer displacement is asymmetric. Comparison reveals very similar results below ≈1.5 eV for both states. The model predictions separate above this energy - similar to what we find for the case of bulk $LuFe_2O_4$ [Fig. 6.8b]. Spectral

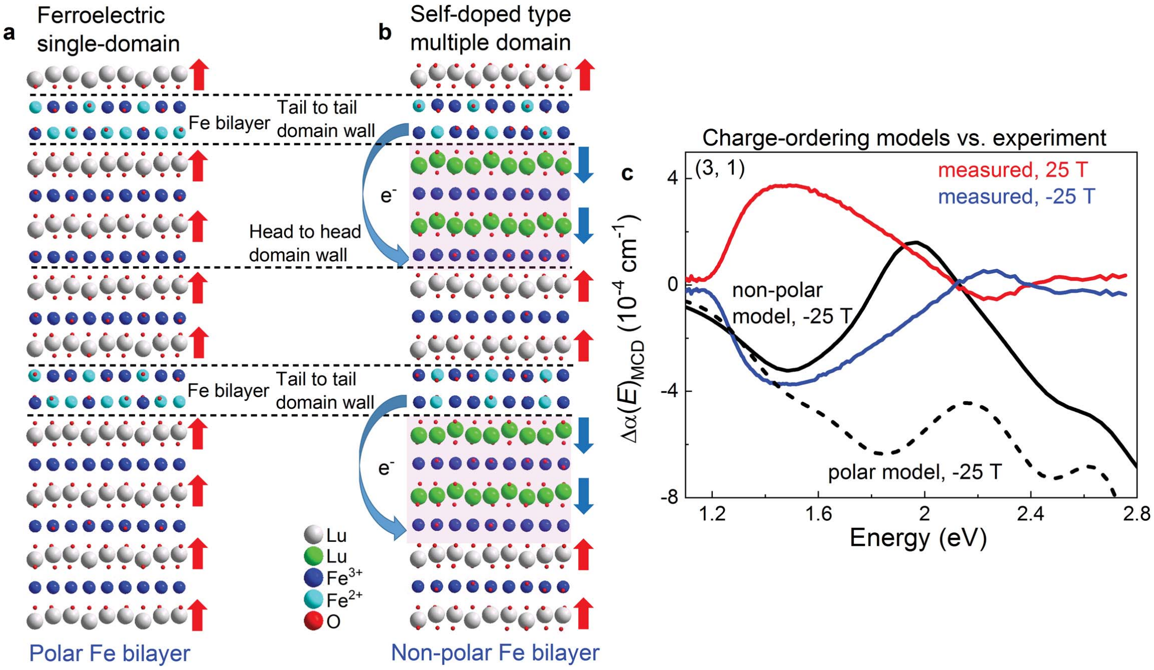

Figure 6.9: **Candidate charge-ordering patterns for $(\mathbf{LuFeO_3})_3/(\mathbf{LuFe_2O_4})_1$ and comparison of calculated vs. measured dichroic spectra.** **a** Ferroelectric single-domain type (CO-FE) charge-ordered state with a polar Fe bilayer. The Lu-layer displacement is symmetric, and red arrows indicate the polarization direction. **b** Self-doped type (CO-DOPED) multi-domain charge-ordered state with a non-polar Fe bilayer, unveiling spontaneous electron transfer from the Fe bilayers to the $LuFeO_3$ layers. The polarization changes direction across the domain boundaries (dashed lines) as shown by the red and blue net dipole arrows, and the Lu-layer displacement is asymmetric with both down/up/up and down/up/down Lu distortion patterns surrounding the Fe double layer. **c** Experimental dichroic spectra $\Delta\alpha(E)_{MCD}$ along with calculated $\Delta\alpha(E)_{MCD}$ of the CO-FE (polar Fe bilayer) and CO-DOPED (non-polar Fe bilayer) charge-ordering states in the (3, 1) superlattice.

signatures that distinguish the CO-DOPED model include the minimum near 1.5 eV and sign change near 2 eV. The overall agreement becomes less quantitative at higher

energies - possibly due to additional complexity in the charge ordering pattern due to charged ferroelectric domain walls or reduced measurement sensitivity as the absorption coefficient rises [Fig. 6.3a]. In any case, all of our calculations in Figs. 6.2c and 6.9c implement this particular charge ordering pattern and are internally consistent. The CO-DOPED model is likely to apply to the higher-order superlattices (m = 7, 9) due to the stronger Lu-layer distortion, although calculations cannot be performed at this time due to the extraordinary size of the unit cells. Our finding for the non-polar CO-DOPED model is consistent with real space HAADF-STEM images as well [Fig. 6.2b] [1].

6.6 Developing interface design rules for increasing T_C and enhancing magnetoelectric coupling

In order to develop a heuristic argument for why the spin-up channel charge transfer excitation is so important in the $(LuFeO_3)_m/(LuFe_2O_4)_n$ superlattices, we sought to identify which orbitals are active in the Fe double-layer. To do so, we consider a slab of $LuFe_2O_4$ surrounded by $LuFeO_3$. Each Fe center - regardless of charge - is in a trigonal bipyramidal geometry. Given this local structure, the $d_{x^2-y^2}$ and d_{xy} orbitals are in-plane [Fig. 6.10a]. They are also degenerate and orthogonal. We hypothesize that the in-plane orbital arrangement in the spin-up channel is responsible for the increasingly robust magnetism [Fig. 6.6b] and higher T_C in the (3, 1) → (7, 1) → (9, 1) series. How the overlap and hybridization change in response to distortion of the Lu layer is likely to impact magnetoelectric coupling as well.

Figure 6.10b,c displays the in-plane orbitals in a hypothetical $LuFe_2O_4$ slab. The top-down view emphasizes the honeycomb arrangement of the Fe^{2+} and Fe^{3+} centres, the $d_{x^2-y^2}$ and d_{xy} orbitals, and their overlap with the O p_x and p_y orbitals. The side-on schematic - with its simplified linear arrangement of polyhedra and lack of O p_x and p_y orbitals - allows us to clearly see the structural distortions that take place in the bilayer. Examination reveals that Lu rumpling has an important effect on the overlap of the in-plane orbitals. This is due to the tendency of the Fe^{3+}-containing trigonal bipyramids to rotate and elongate in response to the Lu-layer distortion. The Goodenough-Kanamori rules govern how local structure distortions modify orbital overlap and exchange interactions [244]. Based upon the modification of orbital overlap and hybridization, these rules qualitatively explain trends in the (3, 1), (7, 1), and (9, 1) series.

We already know from STEM and first principles calculations that larger m yields greater Lu-layer distortion and higher T_C [Fig. 6.2] [1]. Our analysis suggests that the Lu-layer distortion causes the Fe^{3+} polyhedra in the $LuFe_2O_4$ double layer to elongate and rotate, changing the in-plane orbital overlap in such a way as to make the spin-up charge transfer more important. Therefore, by controlling the atomistic details of the rotation, one can influence hybridization. The structurally-induced orbital reconstruction modifies the net magnetic moment on the Fe^{3+} sites such that bilayer magnetism becomes more robust. This raises the coercive field [Fig. 6.6b] and the magnetic Curie temperature.

One consequence of an elongated polyhedron is a possible off-mirror plane distortion of the Fe^{3+} centers. Such a distortion was recently observed in the ferrimagnetic quantum paraelectric $BaFe_{12}O_{19}$ [245]. Our STEM images provide an upper bound of $\leq$ 10 - 20 pm to any Fe^{3+} off-centering in the $(LuFeO_3)_m/(LuFe_2O_4)_1$ superlattices. This level of off-centering is negligible and does not contribute to the properties

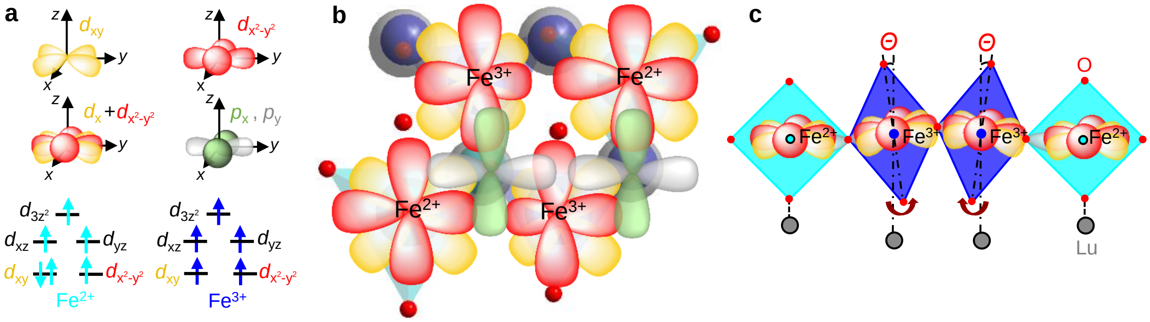

Figure 6.10: **Schematic view of the in-plane orbital overlap and the consequences of Lu-layer distortion.** **a** Schematic view of the Fe d_{xy} and $d_{x^2-y^2}$ orbitals + the O p_x and p_y orbitals. The ground state energy diagrams for the Fe^{2+} and Fe^{3+} sites are shown as well. **b** Top view of the $LuFe_2O_4$ double layer in the self-doped structure showing how tilting of the FeO_5 trigonal bipyramids modifies hybridization. This changes the overlap of the in-plane orbitals. **c** Schematic side-on view of a hypothetical linear array of FeO_5 trigonal bipyramids and the rotation and elongation that result from Lu-layer distortion. The tilting and elongation is highly exaggerated in this rendering, and the O p_x and p_y orbitals are omitted for simplicity.

of these materials.

Chapter 7

Summary and Outlook

In this dissertation, I present a spectroscopic investigation of natural occuring and engineered superlattices, revealing how symmetry-breaking and interface characters lead to interesting and exotic properties. While probing the fundamental excitations in these materials under external stimuli such as low temperature, high magnetic field, and chemical substitution, I reveal the microscopic mechanism of coupling between spin, charge, and lattice degrees of freedom in a site-specific manner. These findings advance the understanding of the interfacial problem in low-dimensional multilayered systems.

The first project focuses on investigating the spectroscopic signatures of chirality in the natural occuring superlattices Fe_xTaS_2 ($x = 1/4$ and $1/3$). We bring together optical spectroscopy and first-principles calculations to reveal how electronic properties change with the Fe intercalation concentration. The Fe intercalation dramatically modifies metallic characters such as plasma frequency and relaxiation time of the parent compound 2H-TaS_2, which also induces a second free carrier response in the Fe monolayer. When crystal structures change from centrosymmetric to non-centrosymmetric, signatures of chirality for the $Fe_{1/3}TaS_2$ are deeply embedded in the electronic structures. These include a transition of the electron density patterns from triangular to Kagomé to honeycomb, a hole → electron crossover at the K-point, and low energy electronic excitations between spin split bands at the Fermi level. These findings advance the understanding of intercalation and symmetry breaking on the fundamental excitations in metallic chalcogenides.

The second project is closely related to the first. Here, we extend the work on Fe_xTaS_2 by combining Raman scattering spectroscopy, correlation group analysis, and lattice dynamics calculations to reveal the vibrational properties. The results uncover coherent in- and out-of-plane excitations in the Fe monolayer. Extending the measurements to other chalcogenides including $Cr_{1/3}NbS_2$ and $RbFe(SO_4)_2$ reveals that the intercalated monolayer excitations are intrinsic and general. In addition, the frequency and linewidth of the monolayer excitations are strongly associated with the in-plane metal-metal distance, size of the van der Waals gap, and metal-to-chalcogenide slab mass ratio. We developed a mass ratio model to fit the experimental data, which reveals that different chemical and interaction environments can modify the effective spring ratio for an intercalated metal monolayer. We also find the monolayer excitations couple to the magnetism in $Fe_{1/4}TaS_2$. These findings advance the understanding of how intercalation affects the interactions between metal monolayers and its surroundings in different chemical environments. This work also provides a possible explanation of electrical switching in antiferromagnetism and chiral phonons in the $M_{1/3}TX_2$ systems.

The third project focuses on investigating the origin of high temperature magnetism in multiferroic superlattices $(LuFeO_3)_m/(LuFe_2O_4)_n$. Here, we combine optical spectroscopy, magnetic circular dichroism, and first-principles calculations to uncover the interface induced magnetism and charge-ordering in a site-specific manner. Analysis of the magnetic dichroic spectra reveals optical hysteresis for different Fe sites. We extract the coercivity vs. temperature trends for different types of

Fe-related excitations and compare them with the trend from bulk magnetization measurement. The result indicates that bulk magnetism principally comes from the $LuFe_2O_4$ layer. We successfully extract the interface dichoic spectra by subtracting the composite response from the experimental spectra. Analysis of interface spectra reveals that the enhanced magnetism in the higher order superlattices comes from increasing spin-up channel Fe^{2+} and Fe^{3+} density of states in the $LuFe_2O_4$ layer. Comparison of the theoretically predicted magnetic circular dichroism with the experimental spectrum also establishes the non-polar self-doped structure as the precise charge-ordering arrangement within the $LuFe_2O_4$ layer of the (3,1) film, thus resolving controversy regarding the many different isoenergetic charge states. These findings provide direct, microscopic, and site-specific information about interface magnetism in a two-dimensional material with multiple magnetic centres. In addition, this work provides a pathway to link bulk and interface properties in other engineered materials.

Looking forward, this work provides several opportunities for future research. One direction is to perform the Raman scattering measurements under variable pressure in the intercalated transition metal dichalcogenides. The metal monolayer excitations are highly sensitive to volume and different chemical environments of the crystal. We expect to observe dramatic changes of frequencies, lineshapes, and amplitudes of the monolayer excitations. Studying the controlling and switching behaviors of these monolayer excitations are important because they have huge potential for designing new types of resonators in the terahertz range. Another direction is to detect chiral phonons using Raman spectroscopy. Circular polarizors need to be used to reveal the phonon chirality. Revealing the chiral phonons are important for understanding electron-phonon coupling in solids, phonon-driven topological states, and energy-efficient information processing [236]. For $(LuFeO_3)_m/(LuFe_2O_4)_1$

superlattices, our interface extraction technique can be applied to analyze other heteroepitaxial superlattices with higher magnetic transition temperature such as $(LuFeO_3)_m/(CoFe_2O_4)_n$. Moreover, magnetic linear dichroism can be performed to $(LuFeO_3)_m/(LuFe_2O_4)_n$ superlattices to reveal the magnetoelectric coupling constant in a site-specific manner. Combining our interface extraction technique, we should be able to study how site-specific magnetoelectric coupling changes with the interfacial lattice distortion. Revealing the microscopic origin of magnetoelectric coupling is very important because it can open the door of designing new multiferroics with coexistence of large magnetoelectric coupling and room-temperature magnetic transition temperature.

Bibliography

[1] J. A. Mundy, et. al., Nature **537**, 523 (2016).

[2] M. P. Singh, CH. Simon, B. Raveau and W. Prellier. Growth of multiferroic superlattices. Phase Transitions. **79**, 973 (2006).

[3] M. Herman, W. Richter, and H. Sitter, Heteroepitaxy; Growth Phenomena, Epitaxy. Springer Series in MATERIALS SCIENCE, **62**. Springer, Berlin, Heidelberg (2004).

[4] H. Guo et. al. Interface-induced multiferroism by design in complex oxide superlattices. PNAS. **114**, E5062 (2017).

[5] H. Wang, F. Tang, P. H. Dhuvad and X. Wu, Interface enhanced functionalities in oxide superlattices under mechanical and electric boundary conditions, npj Computational Materials, **6**, 52 (2020).

[6] Y. Horibe, J. Yang, Y. H. Cho, X. Luo, S. B. Kim, Y. S. Oh, F. T. Huang, T. Asada, M. Tanimura, D. Jeong, and S. W. Cheong, J. Am. Chem. Soc. **136**, 8368 (2014).

[7] Holtz, M. E. *et al.*, Dimensionality-induced change in topological order in multiferroic oxide superlattices, arXiv:2007.03872 [cond-mat.mtrl-sci].

[8] K.A. Smith, et. al., Infrared nano-spectroscopy of ferroelastic domain walls in hybrid improper ferroelectric $Ca_3Ti_2O_7$. Nat. Comm. **10**, 5235 (2019).

[9] D. J. Kim, J. G. Connell, S. S. A. Seo and A Gruverman, Domain wall conductivity in semiconducting hexagonal ferroelectric $TbMnO_3$ thin films. Nanotechnology, **27**, 155705 (2016).

[10] Y. Togawa, T. Koyama, K. Takayanagi, S. Mori, Y. Kousaka, J. Akimitsu, S. Nishihara, K. Inoue, A. S. Ovchinnikov, and J. Kishine, Chiral magnetic soliton lattice on a chiral helimagnet, Phys. Rev. Lett. **108**, 107202 (2012).

[11] N. J. Ghimire, M. A. McGuire, D. S. Parker, B. Sipos, S. Tang, J. -Q. Yan, B. C. Sales, and D. Mandrus, Phys. Rev. B **87**, 104403 (2013).

[12] C. -W. Chen, S. Chikara, V. S. Zapf, and E. Morosan, Correlations of crystallographic defects and anisotropy with magnetotransport properties in Fe_xTaS_2 single crystals ($0.23 \leq x \leq 0.35$), Phys. Rev. B, **94**, 054406 (2016).

[13] Morosan, E.; Zandbergen, H. W.; Li, L.; Lee, M.; Checkelsky, J. G.; Heinrich, M.; Siegrist, T.; Ong, N. P.; Cava, R. J., Sharp switching of the magnetization in $Fe_{1/4}TaS_2$, *Phys. Rev. B* **2007**, *75*, 104401.

[14] Chae, S. C.; Horibe, Y.; Jeong, D. Y.; Rodana, S.; Lee, N.; Cheong, S. -W., Self-organization, condensation, and annihilation of topological vortices and antivortices in a multiferroic, *PNAS* **2010**, *107*, 21366-21370.

[15] R. Ramesh and D. G. Schlom, Creating emergent phenomena in oxide superlattices, Nat. Rev. Mater, **4**, 257–268 (2019).

[16] Moyer, J. A. *et al.* Intrinsic magnetic properties of hexagonal $LuFeO_3$ and the effects of nonstoichiometry. *APL Mater.* **2**, 012106 (2014).

[17] Das, H., Wysocki, A. L., Geng, Y., Wu, W., and Fennie, C. J. Bulk magnetoelectricity in the hexagonal manganites and ferrites. *Nat. Commun.* **5**, 2998 (2014).

[18] Disseler, S. N., *et al.* Magnetic structure and ordering of multiferroic hexagonal $LuFeO_3$. *Phys. Rev. Lett.* **114**, 217602 (2015).

[19] Cao, S., et al. The stability and surface termination of hexagonal $LuFeO_3$. J. Phys.: Condens. Matter. **27**, 175004 (2015).

[20] Angst, M. *et al.* Charge order in $LuFe_2O_4$: antiferroelectric ground state and coupling to magnetism. *Phys. Rev. Lett.* **101**, 227601 (2008).

[21] Xu, X. S. *et al.* Charge order, dynamics, and magnetostructural transition in multiferroic $LuFe_2O_4$. *Phys. Rev. Lett.* **101**, 227602 (2008).

[22] Brooks, C. M. *et al.* The adsorption-controlled growth of $LuFe_2O_4$ by molecular-beam epitaxy. *Appl. Phys. Lett.* **101**, 132907 (2012).

[23] Xu. X. S. *et al.* Lattice dynamical probe of charge order and antipolar bilayer stacking in $LuFe_2O_4$. *Phys. Rev. B.* **82** 014304 (2010).

[24] Wu, W. et al. Formation of pancakelike Ising domains and giant magnetic coercivity in ferrimagnetic $LuFe_2O_4$. Phys. Rev. Lett. **101** 137203 (2008).

[25] N. W. Ashcroft and N. D. Mermin. Solid State Physics, Saunders College, (1976).

[26] D. B. Tanner. Optical effects in solids, University of Florida, lecture notes.

[27] T. V. Brinzari, P. Chen, Q. Sun, J. Liu, L. Tung, Y. Wang, J. A. Schlueter, J. Singleton, J. L. Manson, M. Whangbo, A. P. Litvinchuk, and J. L. Musfeldt. Phys. Rev. Lett. **1**, 237202, (2013).

[28] K. D. Hughey, A. J. Clune, M. O. Yokosuk, K. R. O. Neal, S. Fan, N. Abhyankar, H. Xiang, Z. Li, J. Singleton, N. S. Dalal, and J. L. Musfeldt. Phys. Rev. B, **96**, 1 (2017).

[29] M. O. Yokosuk, S. Artyukhin, X. Wang, J. Yang, Z. Li, S.-w. Cheong, D. Van- derbilt, and J. L. Musfeldt. Phys. Rev. B, **92**, 1 (2015).

[30] Rudolf, T.; Kant, C.; Mayr, F.; Hemberger, J.; Tsurkan, V.; Loidl, A., Polar phonons and spin-phonon coupling in $HgCr_2S_4$ and $CdCr_2S_4$, studied with far-infrared spectroscopy, Phys. Rev. B, **76**, 174307 (2007).

[31] Fennie C. J.; Rabe, K. M., Magnetically induced phonon anisotropy in $ZnCr_2O_4$ from first principles, Phys. Rev. Lett. **96**, 205505 (2006).

[32] Dobrowolska, M., et al. Controlling the Curie temperature in (Ga,Mn)As through location of the Fermi level within the impurity band. Nat. Mater. **11**, 444-449 (2012).

[33] Rice, W. D., et al. Persistent optically induced magnetism in oxygen-deficient strontium titanate. Nat. Mater. **13**, 481 (2014).

[34] N. Ikeda, Ferroelectricity from iron valence ordering in the charge-frustrated system $LuFe_2O_4$. Nature **436**, 1136–1138 (2005).

[35] K. Aizu, Possible species of ferromagnetic, ferroelectric, and ferroelastic crystals. Phys. Rev. B **2**, 754–772 (1970).

[36] D. B. Litvin, Ferroic classifications extended to ferrotoroidic crystals. Acta Crystallogr. Sect. A **64**, 316–320 (2008).

[37] M. Fiebig, T. Lottermoser, D. Meier and M. Trassin, The evolution of multiferroics. Nat. Rev. Mats. **1**, 16046 (2016).

[38] A. S. Zimmermann, D. Meier, and M. Fiebig, Ferroic nature of magnetic toroidal order. Nat. Comm. **5**, 4796 (2014).

[39] N. A. Spaldin and M. Fiebig, The Renaissance of Magnetoelectric Multiferroics. Science, **309**, 391-392 (2005).

[40] J. M. Rondinelli, A. S. Eidelson, and N. A. Spaldin. Phys. Rev. B, **79**, 1 (2009).

[41] I. B. Bersuker. Journal of Physics: Conference Series, **428**, 0 (2013).

[42] N. A. Hill. Journal of Physical Chemistry B, **104**, 6694 (2000).

[43] F. Kubel and H. Schmid. Acta crystallographica, B **46**, 698 (1990).

[44] J. Wang, J. B. Neaton, H. Zheng, V. Nagarajan, S. B. Ogale, B. Liu, D. Viehland, V. Vaithyanathan, D. G. Schlom, U. V.Waghmare, N. A. Spaldin, K. M. Rabe, M. Wuttig, and R. Ramesh. Science, **299**, 1719 (2003).

[45] T. Kimura, T. Goto, H. Shintani, K. Ishizaka, T. Arima, and Y. Tokura. Nature, **426**, 55 (2003).

[46] N. A. Spaldin and R. Ramesh, Advances in magnetoelectric multiferroics. Nat. Mater., **18**, 203 (2019).

[47] S. A. Fedulov, Determination of Curie temperature for $BiFeO_3$ ferroelectric. Dokl. Akad. Nauk SSSR **139**, 1345 (in russian) (1961); English translation available in Sov. Phys. -Dokl. **6**, 729 (1962).

[48] S. V. Kiselev, R. P. Ozerov, and G. S. Zhdanov, Detection of magnetic order in ferroelectric $BiFeO_3$ by neutron diffraction. Dokl. Akad. Nauk SSSR **145**, 1255 (in russian) (1962); English translation available in Sov. Phys. -Dokl. **7**, 742 (1963).

[49] Y. Tokura, S. Seki and N. Nagaosa, Multiferroics of spin origin, Rep. Prog. Phys. **77** 076501 (2014).

[50] C. Ederer and N. A. Spaldin, Origin of ferroelectricity in the multiferroic barium fluorides BaMF4: A first principles study. Phys. Rev. B, **74**, 024102 (2006).

[51] C. J. Fennie and K. M. Rabe, Ferroelectric transition in YMnO3 from first principles. Phys. Rev. B, **72**, 100103(R) (2005).

[52] M. S. Senn, J. P. Wright, and J. P. Attfield, Charge order and three-site distortions in the Verwey structure of magnetite. Nature **481**, 173–176 (2012).

[53] I. E. Dzyaloshinskii, A thermodynamic theory of "weak" ferromagnetism of antiferromagnetics. J. Phys. Chem. Solids, **4**, 241–255 (1958).

[54] R. E. Newnham, J. J. Kramer, W. A. Schulze, and L. E. Cross, Magnetoferroelectricity in Cr_2BeO_4. J. Appl. Phys. **49**, 6088–6091 (1978).

[55] I. A. Sergienko and E. Dagotto, Role of the Dzyaloshinskii–Moriya interaction in multiferroic perovskites. Phys. Rev. B **73**, 094434 (2006).

[56] T. Aoyama et al. Giant spin-driven ferroelectric polarization in $TbMnO_3$ under high pressure. Nat. Commun. **5**, 4927 (2014).

[57] H. Murakawa, Y. Onose, S. Miyahara, N. Furukawa, and Y. Tokura, Ferroelectricity Induced by Spin-Dependent Metal-Ligand Hybridization in $Ba_2CoGe_2O_7$. Phys. Rev. Lett. **105**, 137202 (2010).

[58] T. ARIMA, Ferroelectricity Induced by Proper-Screw Type Magnetic Order. J. Phys. Soc. Jpn. **76**, 073702 (2007).

[59] D. Sando et al. Crafting the magnonic and spintronic response of $BiFeO_3$ films by epitaxial strain. Nat. Mater. **12**, 641–646 (2013).

[60] J. H. Haeni et al. Room-temperature ferroelectricity in strained $SrTiO_3$. Nature **430**, 758–761 (2004).

[61] J. S. White et al. Strain-induced ferromagnetism in antiferromagnetic $LuMnO_3$ thin films. Phys. Rev. Lett. **111**, 037201 (2013).

[62] C. -G. Duan, S. S. Jaswal, and E. Y. Tsymbal, Predicted magnetoelectric effect in Fe/$BaTiO_3$ multilayers: ferroelectric control of magnetism. Phys. Rev. Lett. **97**, 047201 (2006).

[63] H. J. A. Molegraaf et al. Magnetoelectric effects in complex oxides with competing ground states. Adv. Mater. **21**, 3470–3474 (2009).

[64] T. H. E. Lahtinen, K. K. A. Franke, and S. van Dijken. Electric-field control of magnetic domain wall motion and local magnetization reversal. Sci. Rep. **2**, 258 (2012).

[65] S. Valencia et al. Interface-induced room-temperature multiferroicity in $BaTiO_3$. Nat. Mater. **10**, 753–758 (2011).

[66] J. Seidel et al. Conduction at domain walls in oxide multiferroics. Nat. Mater. **8**, 229–235 (2009).

[67] S. Farokhipoor and B. Noheda. Conduction through 71° domain walls in $BiFeO_3$ thin films. Phys. Rev. Lett. **107**, 127601 (2011).

[68] P. Maksymovych et al. Dynamic conductivity of ferroelectric domain walls in $BiFeO_3$. Nano Lett. **11**, 1906–1912 (2011).

[69] G. Catalan, J. Seidel, R. Ramesh, and J. F. Scott. Domain wall nanoelectronics. Rev. Mod. Phys. **84**, 119–156 (2012).

[70] E. A. Eliseev, A. N. Morozovska, G. S. Svechnikov, V. Gopalan, and V. Y. Shur. Static conductivity of charged domain walls in uniaxial ferroelectric semiconductors. Phys. Rev. B **83**, 235313 (2011).

[71] K. S. Novoselov, A. K. Geim, S. V. Morozov, D. Jiang, Y. Zhang, S. V. Dubonos, I. V. Grigorieva, and A. A. Firsov. Electric Field Effect in Atomically Thin Carbon Films. Science. **306**, (5696): 666–669 (2004).

[72] E. Cappelluti, R. Roldán, J. A. Silva-Guillén, P. Ordejón, and F. Guinea, Phys. Rev. B **88**, 075409 (2013).

[73] K. F. Mak, C. Lee, J. Hone, J. Shan, and T. F. Heinz, Phys. Rev. Lett. **105**, 136805 (2010).

[74] W. Zhao, R. M. Ribeiro, M. Toh, A. Carvalho, C. Kloc, A. H. Castro Neto, and G. Eda, Nano Lett. **13**, 5627 (2013).

[75] W. Jin, P.-C. Yeh, N. Zaki, D. Zhang, J. T. Sadowski, A. Al-Mahboob, A. M. van der Zande, D. A. Chenet, J. I. Dadap, I. P. Herman, et al., Phys. Rev. Lett. **111**, 106801 (2013).

[76] Y. Zhang, T.-R. Chang, B. Zhou, Y.-T. Cui, H. Yan, Z. Liu, F. Schmitt, J. Lee, R. Moore, Y. Chen, et al., Nat. Nano. **9**, 111 (2014).

[77] M. Dragoman and D. Dragoman, 2D Nanoelectronics: Physics and Devices of Atomically Thin Materials. NanoScience and Technology, DOI 10.1007/978-3-319-48437-2.

[78] A. W. Tsen, R. Hovden, D. Wang, Y. Kim, J. Okamoto, K. A. Spoth, Y. Liu, W. Lu, Y. Sun, J. C. Hone, L. F. Kourkoutis, P. Kim, and A. N. Pasupathy, Structure and control of charge density waves in two-dimensional 1T-TaS$_2$, PNAS, **112**(49), 15054-15059 (2015).

[79] W. Z. Hu, G. Li, J. Yan, H. H. Wen, G. Wu, X. H. Chen, and N. L. Wang, Phys. Rev. B **76**, 045103 (2007).

[80] S. N. Shirodkar and U. V. Waghmare, Phys. Rev. Lett., **112**, 157601 (2014).

[81] L. F. Mattheiss, Phys. Rev. B **8**, 3719 (1973).

[82] Zhang, X.; Qiao, X.; Shi, W.; Wu, J.; Jiang D.; Tan, P., Phonon and Raman scattering of two-dimensional transition metal dichalcogenides from monolayer, multilayer to bulk material, *Chem. Soc. Rev.* **2015**, *44*, 2757.

[83] Q. H. Wang, K. Kalantar-Zadeh, A. Kis, J. N. Coleman and M. S. Strano, Nat. Nanotechnol. **7**, 699–712, (2012).

[84] P. Avouris, et. al. 2D Materials Properties and Devices, Cambridge University Press, ISBN: 9781107163713, **14**, 262 (2017).

[85] A. H. Castro Neto, Charge Density Wave, Superconductivity, and Anomalous Metallic Behavior in 2D Transition Metal Dichalcogenides, Phys. Rev. Lett. **86**, 4382-4385 (2001).

[86] R. Roldán, A. Castellanos-Gomez, E. Cappelluti, and F. Guinea, Strain engineering in semiconducting two-dimensional crystals, Journal of Physics: Condensed Matter **27**, 313201 (2015).

[87] K. S. Novoselov, A. Mishchenko, A. Carvalho, and A. H. Castro Neto, 2D materials and van der Waals heterostructures, Science, **353**, 6298 (2016).

[88] M. Yoshida, R. Suzuki, Y. Zhang, M. Nakano, Y. Iwasa, Memristive phase switching in two-dimensional 1T-TaS$_2$ crystals, Sci. Adv. **1**, e1500606 (2015).

[89] Joshi, J.; Hill, H. M.; Chowdhury, S.; Malliakas, C. D.; Tavazza, F.; Chatterjee, U.; Walker, A. R. H.; Vora, P. M., Short-range charge density wave order in 2H-TaS$_2$, *Phys. Rev. B* **2019**, *99*, 245144.

[90] B. Sipos, et al. From Mott state to superconductivity in 1T-TaS$_2$. Nat. Mater. **7**, 960–965, (2008).

[91] R. Zhao, et. al. Tuning phase transitions in 1T-TaS$_2$ via the substrate. Nano Lett. **17**, 3471–3477, (2017).

[92] N. Z. Wang, et al. Tunable superconductivity by electrochemical intercalation in TaS$_2$. New Journal of Physics **20**, 023014, (2018).

[93] M. Yoshida, T. Gokuden, R. Suzuki, M. Nakano, and Y. Iwasa, Current switching of electronic structures in two-dimensional 1T-TaS$_2$ crystals. Phys. Rev. B **95**, 121405 (2017).

[94] J. Pan, et al. Enhanced superconductivity in restacked TaS$_2$ Nanosheets. J. Am. Chem. Soc. **139**, 4623–4626, (2017).

[95] N. E. Moratalla, et al. Enhanced superconductivity in atomically thin TaS$_2$. Nat. Communs. , 11043, (2016).

[96] L. -Y. Gan, et al. Strain tuning of the charge density wave in monolayer and bilayer 1T-TaS$_2$. Physical Chemistry Chemical Physics , 3080–3085, (2016).

[97] W. Wang, D. Dietzel, and A. Schirmeisen, Lattice discontinuities of 1T-TaS$_2$ across first order charge density wave phase transitions, Scientific reports, **9**, 7066 (2019).

[98] Sugai, S.; Murase, K.; Uchida, S.; Tanaka, S., Studies of lattice dynamics in 2H-TaS_2 by Raman scattering, *Solid State Comm.* **1981**, *40*, 399.

[99] R. Grasset, Y. Gallais, A. Sacuto, M. Cazayous, S. MañasValero, E. Coronado, and M.-A. Méasson, Pressure-induced collapse of the charge density wave and Higgs mode visibility in 2HTaS_2, Phys. Rev. Lett. **122**, 127001 (2019).

[100] Hajiyev, P.; Cong, C.; Qiu, C.; Yu, T., Contrast and Raman spectroscopy study of single- and few-layered charge density wave material: 2H-$TaSe_2$, *Sci. Rep.* **2013**, *3*, 2593.

[101] H. M. Hill, S. Chowdhury, J. R. Simpson, A. F. Rigosi, D. B. Newell, H. Berger, F. Tavazza, and A. R. Hight Walker, Phonon origin and lattice evolution in charge density wave states, Phys. Rev. B **99**, 174110 (2019).

[102] X. Xi, L. Zhao, Z.Wang, H. Berger, L. Forró, J. Shan, and K. F. Mak, Strongly enhanced charge-density-wave order in monolayer $NbSe_2$, Nat. Nanotechnol. **10**, 765 (2015).

[103] M. V. Klein, Theory of two-phonon Raman scattering in transition metals and compounds, Phys. Rev. B **24**, 4208 (1981).

[104] J. C. Tsang, J. E. Smith, and M. W. Shafer, Raman spectroscopy of soft modes at the charge-density-wave phase Transition in 2H$NbSe_2$, Phys. Rev. Lett. **37**, 1407 (1976).

[105] R. Roldán, J. A. Silva-Guillén, M. P. López-Sancho, F. Guinea, E. Cappelluti, and P. Ordejón, Annalen der Physik **526**, 347 (2014).

[106] C. -H. Chang, X. Fan, S. -H. Lin and J. -L. Kuo, Orbital analysis of electronic structure and phonon dispersion in MoS_2, $MoSe_2$, WS_2, and WSe_2 monolayers under strain, Phys. Rev. B, **88**, 195420 (2013).

[107] A.P. Nayak, T. Pandey, D. Voiry, J. Liu, S.T. Moran, A. Sharma, C. Tan, C.H. Chen, L.J. Lee, M. Chhowalla et al., Pressure-dependent optical and vibrational properties of monolayer molybdenum disulfide, Nano Lett. **15**, 346 (2015).

[108] A. Ramasubramaniam, D. Naveh, and E. Towe, Tunable band gaps in bilayer transition-metal dichalcogenides. Phys. Rev. B **84**, 205325 (2011).

[109] A. V. Kolobov and J. Tominaga, Two-Dimensional Transition-Metal Dichalcogenides, SSMATERIALS, **239**, DOI 10.1007/978-3-319-31450-1, (2016).

[110] B. Radisavljevic, A. Radenovic, J. Brivio, V. Giacometti, A. Kis, Single-layer MoS_2 transistors. Nat. Nanotech. **6**, 147 (2011).

[111] B.W. Baugher, H.O. Churchill, Y. Yang, P. Jarillo-Herrero, Intrinsic electronic transport properties of high-quality monolayer and bilayer MoS_2. Nano Lett. **13**, 4212 (2013).

[112] B. Radisavljevic, A. Kis, Mobility engineering and a metal-insulator transition in monolayer MoS_2. Nat. Mater. **12**, 815 (2013).

[113] Kumar, P.; Skomski, R.; Pushpa, R., Magnetically ordered transition-metal-intercalated WSe_2, *ACS Omega.* **2017**, *2*, 7985.

[114] Fan, S.; Manuel, I.; al-Wahish, A.; O'Neal, K. R.; Smith, K. A.; Won, C. J.; Kim, J. W.; Cheong, S. -W.; Haraldsen, J. T.; Musfeldt, J. L., Elec-

tronic chirality in the metallic ferromagnet $Fe_{1/3}TaS_2$, *Phys. Rev. B* **2017**, *96*, 205119.

[115] Morosan, E.; Zandbergen, H. W.; Dennis, B. S.; Bos, J. W. G.; Onose, Y.; Klimczuk, T.; Ramirez, A. P.; Ong, N. P.; Cava, R. J., Superconductivity in Cu_xTiSe_2, *Nature Physics* **2006**, *2*, 544.

[116] Tang, S.; Fishman, R. S.; Okamoto, S.; Yi, J.; Zou, Q.; Fu, M.; Li, A.; Mandrus, D.; Gai, Z., Tuning magnetic soliton phase via dimensional confinement in exfoliated 2D $Cr_{1/3}NbS_2$ thin flakes, *Nano Lett.* **2018**, *18*, 4023.

[117] Aczel, A. A.; DeBeer-Schmitt, L. M.; Williams, T. J.; McGuire, M. A.; Ghimire, N. J.; Li, L.; and Mandrus, D., Extended exchange interactions stabilize long-period magnetic structures in $Cr_{1/3}NbS_2$. *Appl. Phys. Lett.* **113**, 032404 (2018).

[118] Nair, N. L.; Maniv, E.; John, C.; Doyle, S.; Orenstein, J.; Analytis, J. G., Electrical switching in a magnetically intercalated transition metal dichalcogenide, *Nature Mater.* **2020**, *19*, 153.

[119] H. Y. Hwang, Y. Iwasa, M. Kawasaki, B. Keimer, N. Nagaosa, and Y. Tokura, Nat. Mater. **11**, 103 (2012).

[120] S. Singh, J. T. Haraldsen, J. Xiong, E. M. Choi, P. Lu, D. Yi, X. -D. Wen, J. Liu, H. Wang, Z. Bi, P. Yu, M. R. Fitzsimmons, J. L. MacManus-Driscoll, R. Ramesh, A. V. Balatsky, J. -X. Zhu, and Q. X. Jia, Phys. Rev. Lett. **113**, 047204 (2014).

[121] B. -W. Li, M. Osada, Y. Ebina, S. Ueda, and T. Sasaki, J. Am. Chem. Soc. **138**, 7621 (2016).

[122] Y. Sun, T. Xiong, F. Dong, H. Huang, and W. Cen, Chem. Commun. **52**, 8243 (2016).

[123] J. J. Yang, Y. J. Choi, Y. S. Oh, A. Hogan, Y. Horibe, K. Kim, B. I. Min, and S. -W. Cheong, Phys. Rev. Lett. **108**, 116402 (2012).

[124] L. Fang, J. Im, W. DeGottardi, Y. Jia, A. Glatz, K. A. Matveev, W.-K. Kwok, G. W. Crabtree, and M. G. Kanatzidis, Sci. Reports **6**, 35313 (2016).

[125] A. Meetsma, G. A. Wiegers, R. J. Haange, and J. L. de Boer, Acta Cryst. C **46**, 1598 (1990).

[126] Th. Danz, Q. Liu, X. D. Zhu, L. H. Wang, S. W. Cheong, I. Radu, C. Ropers, and R. I. Tobey, J. Phys.: Condens. Matter, **28**, 356002 (2016).

[127] Q. Liu, X. D. Zhu, L. H. Wang, S. W. Cheong, and R. I. Tobey, J. Phys.: Condens. Matter, **28**, 194002 (2016).

[128] S. S. P. Parkin and R. H. Friend, Phil. Mag. B, **41**, 65 (1980).

[129] Choi, Y. J.; Kim, S. B.; Asada, T.; Park, S.; Wu, Weida; Horibe, Y.; Cheong, S.-W, Giant magnetic coercivity and ionic superlattice nano-domains in $Fe_{0.25}TaS_2$, Euro. Phys. Lett. **86**, 37012 (2009).

[130] Ohtomo, A., and Hwang, H. Y., A high-mobility electron gas at the $LaAlO_3/SrTiO_3$ heterointerface. Nature. **427**, 423 (2004).

[131] Bousquet, E., et al. Improper ferroelectricity in perovskite oxide artificial superlattices. Nature. **452**, 732 (2008).

[132] Wu, X., Stengel, M., Rabe, K. M., and Vanderbilt, D. Predicting polarization and nonlinear dielectric response of arbitrary perovskite superlattice sequences. Phys. Rev. Lett. **101**, 087601 (2008).

[133] May, S. J., et al. Enhanced ordering temperatures in antiferromagnetic manganite superlattices. Nat. Mater. **8**, 892 (2009).

[134] Birol, T., Benedek, N. A., and Fennie, C. J. Interface control of emergent ferroic order in ruddlesden-popper $Sr_{n+1}Ti_nO_{3n+1}$. Phys. Rev. Lett. **107**, 257602 (2011).

[135] Bennett, C. J. C., et al. Compositional tuning of the strain-induced structural phase transition and of ferromagnetism in $Bi_{1-x}Ba_xFeO_{3-\delta}$. J. Mater. Res. **26**, 1326 (2011).

[136] Lee, J. H., and Rabe, K. M. Coupled magnetic-ferroelectric metal-insulator transition in epitaxially strained $SrCoO_3$ from first principles. Phys. Rev. Lett. **107** 067601 (2011).

[137] Lee, S., et al. Artificially engineered superlattices of pnictide superconductors. Nat. Mater. **12**, 392 (2013).

[138] Zhao, H. J., et al. Near room-temperature multiferroic materials with tunable ferromagnetic and electrical properties. Nat. Commun. **5**, 4021 (2014).

[139] Ravichandran, J., et al. Crossover from incoherent to coherent phonon scattering in epitaxial oxide superlattices. Nat. Mater. **13**, 168 (2014).

[140] Chakhalian, J., Freeland, J. W., Millis, A. J., Panagopoulos, C., and Rondinelli, J. M. Colloquium : emergent properties in plane view: strong correlations at oxide interfaces. Mod. Phys. **86**, 1189 (2014).

[141] Schick, J. T., Jiang, L., Saldana-Greco, D., and Rappe, A. M. Coupling between octahedral rotations and local polar displacements in WO_3/ReO_3 superlattices. Phys. Rev. B, **89**, 195304 (2014).

[142] Xu, R. J., et al. Ferroelectric polarization reversal via successive ferroelastic transitions. Nat. Mater. **14**, 79-96 (2015).

[143] Yadav, A. K. et al. Observation of polar vortices in oxide superlattices. Nature. **530**, 198–201 (2016).

[144] Zhang, C. et al. Ubiquitous strong electron-phonon coupling at the interface of FeSe/$SrTiO_3$. Nat. Commun. **8**, 14468 (2017).

[145] Frenkel, Y. et al. Imaging and tuning polarity at $SrTiO_3$ domain walls. Nat. Mater. **16**, 1203 (2017).

[146] Hellman, F., et al. Interface-induced phenomena in magnetism. Invited review article, Rev. Mod. Phys. **89**, 025006 (2017).

[147] Yadav, A. K. et al. Spatially resolved steady-state negative capacitance. Nature **565**, 468–471 (2019).

[148] Das, S. et al. Observation of room-temperature polar skyrmions. Nature **568**, 368–372 (2019).

[149] Phan. M. H. et al. Complex magnetic phases in $LuFe_2O_4$. Solid State Commun. **150** 341 (2010).

[150] Zhang, Q. H. et al. Direct observation of interlocked domain walls in hexagonal $RMnO_3$ (R =Tm, Lu). Phys. Rev. B **85**, 020102 (2012).

[151] V. Barone. Computational strategies for spectroscopy: from small molecules to nano systems. Wiley **78**, **79** (2011).

[152] S. Gasiorowicz. Wiley: Quantum physics, 3rd edition - Stephen Gasiorowicz. Wiley, New York, 3 ed. **79**, 371 (2003).

[153] D. Andrews. Molecular photophysics and spectroscopy. Morgan Claypool Publishers **79**, (2014).

[154] D. Bhattacharya, N. Vaval, and S. Pal. J. Chem. Phys., **138**, 094108 (2013).

[155] C. Kittel, Introduction to solid state physics, Wiley, New York, (2005).

[156] F. Wooten, Optical Properties of Solids. Academic Press, New York, NY (1972). **80**, **81**, **99**, **100**, **168**

[157] J. R. Ferraro, K. Nakamoto, and C. W. Brown, Introductory Raman Spectroscopy, 2nd ed., Academic Press, San Diego, (2003).

[158] K. D. Mielenz. Journal of Research of the National Bureau of Standards, **76A**, 455 (1972).

[159] K. D. Mielenz and R. Mavrodineanu. Journal of Research of the National Bureau of Standards, **77A**, 699 (1973).

[160] M. Tinkham, Far infrared properties of solids. Plenum Publishing, Plenum, NY (1970). **80**, **97**, **148**, **164**, **168**

[161] T. W. Cronin. A different view: Sensory Drive in the polarized-light realm, Current Zoology, **64**, 513–523 (2018).

[162] W. R. Mason. A Practical Guide to Magnetic Circular Dichroism Spectroscopy, ISBN:9780470069783 (2006).

[163] K. Ando. Science, **312**, 1883 (2006).

[164] B. S. Holinsworth, N. C. Harms, S. Fan, D. Mazumdar, Arun Gupta, S. A. McGill, and J. L. Musfeldt, Magnetic field control of charge excitations in $CoFe_2O_4$. APL Mater. **6**, 066110 (2018).

[165] Holinsworth, B. S., *et al.* Magnetic field tunability of spin-polarized excitations in a high-temperature magnet. *Phys. Rev. B*, **96**, 094427 (2017).

[166] Amft, M., Burkert, T., Sanyal, B., and Oppeneer, P. First-principles calculations of optical and magneto-optical properties of $Ga_{1-x}Mn_xAs$ and MnAs. *Physica B.* **404**, 3782 (2009).

[167] P. R. Griffiths and J. A. de Haseth. Fourier transform infrared spectrometry. Jon Wiley and Sons Inc., Hoboken, 2nd ed. (2007).

[168] M. Yokosuk, Magnetically-driven phase transitions in multiferroics, dissertation, Univerisity of Tennessee, 2019.

[169] B. C. Smith, Fundamentals of Fourier Transform Infrared Spectroscopy, 2nd ed., CRC Press, Taylor and Francis Group, LLC., Boca Raton, (2011).

[170] Toth, J., and Bird, M. D. FEA-aided design for a working model of a split Florida-helix. *Applied Superconductivity IEEE Transactions* **18**, 1051-8233 (2008).

[171] D. E. Newbury and N. W. M. Ritchie, Is scanning electron microscopy/energy dispersive X-ray spectrometry (SEM/EDS) quantitative? *Scanning* **2013**, *35*, 141-168.

[172] T. Miyadai, K. Kikuchi, H. Kondo, S. Sakka, K. Arai, and Y. Ishikawa, J. Phys. Soc. Jpn. **52**, 1394 (1983).

[173] S. S. P. Parkin and R. H. Friend, Philos. Mag. B **41**, 95 (1980).

[174] S. S. P. Parkin and R. H. Friend, Physica B + C **99**, 219 (1980).

[175] Atomistix ToolKit version 13.8, QuantumWise A/S (www.quantumwise.com)

[176] J. M. Soler, E. Artacho, J. D. Gale, A. Garcia, J. Junquera, P. Ordejon, and D. Sanchez-Portal, J. Phys.: Condens. Matter **14**, 2745 (2002).

[177] Energy minimization tolerance of $<10^{-5}$ Hartree with a k-point sampling of 10x10x10 were used along with potentials of $U_{Ta} = 2.5$ eV and $U_{Fe} = 4.0$ eV.

[178] QuantumATK version 2018.06, synopsys quantumATK (https://www.synopsys.com/silicon/quantumatk.html)

[179] Smidstrup, S.; Stradi, D.; Wellendorff, J.; Khomyakov, P. A.; Vej-Hansen, U. G.; Lee, M. -E.; Ghosh, T.; Jónsson, E.; Jónsson, H.; Stokbro, K., First-principles Green's-function method for surface calculations: a pseudopotential localized basis set approach, *Phys. Rev. B* **2017**, *96*, 195309.

[180] Smidstrup, S.; Markussen, T.; Vancraeyveld, P.; Wellendorff, J.; Schneider, J.; Gunst, T.; Verstichel, B.; Stradi, D.; Khomyakov, P. A.; Vej-Hansen, U. G. *et al.*, QuantumATK: an integrated platform of electronic and atomic-scale modelling tools, *J. Phys.: Condens. Matter.* **2020**, *32*, 015901.

[181] Mundy, J. A. *et. al.* Atomic-resolution chemical imaging of oxygen local bonding environments by electron energy loss spectroscopy. *Appl. Phys. Lett.* **101**, 042907 (2012).

[182] Holinsworth, B. S., *et al.* Direct band gaps in multiferroic h-LuFeO_3. *Appl. Phys. Lett.* **106**, 082902 (2015).

[183] Bayati, R., *et al.* Modification of properties of yttria stabilized zirconia epitaxial thin films by excimer laser annealing. *Appl. Mater. Interfaces.* **6**, 22316 (2014).

[184] S. S. P. Parkin and R. H. Friend, Physica **99b**, 219 (1980).

[185] J. G. Checkelsky, M. Lee, E. Morosan, R. J. Cava, and N. P. Ong, Phys. Rev. B **77**, 014433 (2008).

[186] M. Naito and S. Tanaka, J. Phys. Soc. Jpn. **51**, 219 (1982).

[187] S. S. P. Parkin and S. C. Bayliss, J.Phys. C: Solid State Phys. **15**, 6851 (1982).

[188] J. Dijkstra, P. J. Zijlema, C. F. van Bruggen, C. Haas, and R. A. de Groot, J. Phys.: Condens. Matter **1**, 6363 (1989).

[189] S. Mankovsky, K. Chadova, D. Kodderitzsch, J. Minar, H. Ebert, and W. Bensch, Phys. Rev. B **92**, 144413 (2015).

[190] R. M. Geilhufe, A. Bouhon, S. S. Borysov, and A. V. Balatsky, Phys. Rev. B **95**, 041103 (2017).

[191] J. R. Schaibley, H. Yu, G. Clark, P. Rivera, J. S. Ross, K. L. Seyler, W. Yao, and X. Xu, Nature Rev. Mater. **1**, 16055 (2016).

[192] W. G. McMullan and J. C. Irwin, Can. J. Phys. **62**, 789 (1984).

[193] J. Choi, J. L. Musfeldt, J. He, R. Jin, J. R. Thompson, D. Mandrus, X. N. Lin, V. A. Bondarenko, and J. W. Brill, Phys. Rev. B **69**, 085120 (2004).

[194] B. Monseratt and D. H. Vanderbilt, arXiv:1706.07809 [cond-mat.mtrl-sci] (2017).

[195] C. Martin, E. D. Mun, H. Berger, V. S. Zapf, and D. B. Tanner, Phys. Rev. B **87**, 041104 (2013).

[196] Rhead, G. E., Metal monolayers, *Contemporary Physics* **1983**, *24*, 535.

[197] Chen, W.; Santos, E. J. G.; Zhu, W.; Kaxiras, E.; Zhang, Z., Tuning the electronic and chemical properties of monolayer MoS_2 adsorbed on transition metal substrates, *Nano Lett.* **2013**, *13*, 509.

[198] Bogicevic, A.; Jennison, D. R., Variations in the nature of metal adsorption on ultrathin Al_2O_3 films, *Phys. Rev. Lett.* **1999**, *82*, 4050.

[199] Luo, L.; Zhao, B.; Xiang, B.; Wang, C. -M., Size-controlled intercalation-to-conversion transition in lithiation of transition-metal chalcogenides-$NbSe_3$, *ACS Nano*, **2016**, *10*, 1249.

[200] Nakamura, K.; Shimabukuro, R.; Fujiwara, Y.; Akiyama, T.; Ito, T., Giant modification of the magnetocrystalline anisotropy in transition-metal monolayers by an external electric field, *Phys. Rev. Lett.* **2009**, *102*, 187201.

[201] Zheng, S.; So, J. -K.; Liu, F.; Liu, Z.; Zheludev, N.; Fan, H. J., Giant enhancement of cathodoluminescence of monolayer transitional metal dichalcogenides semiconductors, *Nano Lett.* **2017**, *17*, 6475.

[202] Wang, Y.; Li, L.; Yao, W.; Song, S.; Sun, J. T.; Pan, J.; Ren, X.; Li, C.; Okunishi, E.; Wang, Y. -Q.; Wang, E.; Shao, Y.; Zhang, Y. Y.; Yang, H. -T.; Schwier, E. F.; Iwasawa, H.; Shimada, K.; Taniguchi, M.; Cheng, Z.; Zhou, S.; Du, S.; Pennycook, S. J.; Pantelides, S. T.; Gao, H. -J., Monolayer $PtSe_2$, a new semiconducting transition-metal-dichalcogenide, epitaxially grown by direct selenization of Pt, *Nano Lett.* **2015**, *15*, 4013.

[203] Yu, Y.; Li, G.; Huang, L.; Barrette, A.; Cai, Y. -Q.; Yu, Y. L.; Gundogdu, K.; Zhang, Y. -W.; Cao, L., Enhancing multifunctionalities of transition-metal dichalcogenide monolayers via cation intercalation, *ACS Nano.* **2017**, *11*, 9390.

[204] Dresselhaus M. S.; Dresselhaus, G., Intercalation compounds of graphite, *Adv. Phys.* **1981**, *30*, 139.

[205] Weller, T. E.; Ellerby, M.; Saxena, S. S.; Smith, R. P.; Skipper, N. T., Superconductivity in the intercalated graphite compounds C_6Yb and C_6Ca, *Nature Physics* **2005**, *1*, 39-41.

[206] Tiwari, A. P.; Shin, S.; Hwang, E.; Jung, S. -G.; Park, T.; Lee, H., Superconductivity at 7.4 K in few layer graphene by Li-intercalation, *Journal of Physics: Condensed Matter* **2017**, *29*, 445701.

[207] Ichinokura, S.; Sugawara, K.; Takayama, A.; Takahashi, T.; Hasegawa, S., Superconducting calcium-intercalated bilayer graphene, *ACS Nano* **2016**, *10*, 2761.

[208] Margine, E. R.; Lambert, H.; Giustino, F., Electron-phonon interaction and pairing mechanism in superconducting Ca-intercalated bilayer graphene, *Sci Rep.* **2016**, *6*, 21414.

[209] Eames C.; Islam, M. S., Ion intercalation into two-dimensional transition-metal carbides: global screening for new high-capacity battery materials, *J. Am. Chem. Soc.* **2014**, *136*, 16270.

[210] Wang, X.; Shen, X.; Wang, Z.; Yu, R.; Chen, L., Atomic-scale clarification of structural transition of MoS_2 upon sodium intercalation, *ASC Nano.* **2014**, *8*, 11394.

[211] Heguri, S.; Kawade, N.; Fujisawa, T.; Yamaguchi, A.; Sumiyama, A.; Tanigaki, K.; Kobayashi, M., Superconductivity in the graphite intercalation compound BaC_6, *Phys. Rev. Lett.* **2015**, *114*, 247201.

[212] Li, L. J.; Lu, W. J.; Zhu, X. D.; Ling, L. S.; Qu, Z.; Sun, Y. P., Fe-doping–induced superconductivity in the charge-density-wave system 1T-TaS_2, *EPL* **2012**, *97*, 67005.

[213] Serrano-González, H.; Bramwell, S. T.; Harris, K. D. M.; Kariuki, B. M.; Nixon, L.; Parkin, I. P.; Ritter, C., Magnetic structures of the triangular lattice magnets $AFe(SO_4)_2$ (A=K, Rb, Cs), *Journal of Applied Physics* **1998**, *83*, 6314.

[214] Barath, H.; Kim, M.; Karpus, J. F.; Cooper, S. L.; Abbamonte, P.; Fradkin, E.; Morosan, E.; Cava, R. J.; Quantum and classical mode softening near the charge density wave-superconductor transition in Cu_xTiSe_2, *Phys. Rev. Lett.* **2008**, *100*, 106402.

[215] Togawa, Y.; Kishine, J.; Nosov, P. A.; Koyama, T.; Paterson, G. W.; McVitie, S.; Kousaka, Y.; Akimitsu, J.; Ogata, M.; Ovchinnikov, A. S., Anomalous temperature behavior of the chiral spin helix in $CrNb_3S_6$ thin lamellae, *Phys. Rev. Lett.* **2019**, *122*, 017204.

[216] Aoki, R.; Kousaka, Y.; Togawa, Y., Anomalous nonreciprocal electrical transport on chiral magnetic order, *Phys. Rev. Lett.* **2019**, *122*, 057206.

[217] Wang, L.; Chepiga, N.; Ki, D. -K.; Li, L.; Li, F.; Zhu, W.; Kato, Y.; Ovchinnikova, O. S.; Mila, F.; Martin, I.; Mandrus, D.; Morpurgo, A. F., Controlling the topological sector of magnetic solitons in exfoliated $Cr_{1/3}NbS_2$ Crystals, *Phys. Rev. Lett.* **2017**, *118*, 257203.

[218] Clements, E. M.; Manh-Huong Phan, R. D.; Li, L.; Keppens, V.; Mandrus, D.; Osofsky, M.; Srikanth, H., Magnetic field dependence of nonlinear

magnetic response and tricritical point in the monoaxial chiral helimagnet $Cr_{1/3}NbS_2$, *Phys. Rev. B* **2018**, *97*, 214438.

[219] Klimin, S. A.; Popova, M. N.; Mavrin, B. N.; van Loosdrecht, P. H. M.; Svistov, L. E.; Smirnov, A. I.; Prozorova, L. A.; Krog von Nidda, H. -A.; Seidov, Z.; Loidl, A.; Shapiro, A. Ya.; Demianets, L. N., Structural phase transition in the two-dimensional triangular lattice antiferromagnet $RbFe(MoO_4)_2$, *Phys. Rev. B* **2003**, *68*, 174408.

[220] J. Yang *et. al.*, in preparation (2020).

[221] Shi, J.; Wang, X.; Zhang, S.; Xiao, L.; Huan, Y.; Gong, Y.; Zhang, Z.; Li, Y.; Zhou, X.; Hong, M.; Fang, Q.; Zhang, Q.; Liu, X.; Gu, L.; Liu, Z.; Zhang, Y., Two-dimensional metallic tantalum disulfide as a hydrogen evolution catalyst, *Nature Comm.* **2017**, *8*, 958.

[222] Zhang, X.; Qiao, X.; Shi, W.; Wu, J.; Jiang D.; Tan, P., Phonon and Raman scattering of two-dimensional transition metal dichalcogenides from monolayer, multilayer to bulk material, *Chem. Soc. Rev.* **2015**, *44*, 2757.

[223] Guillamón, I.; Suderow, H.; Vieira, S.; Cario, L.; Diener, P.; Rodière, P., Superconducting density of states and vortex cores of 2H-NbS_2, *Phys. Rev. Lett.* **2008**, *101*, 166407.

[224] Kačmarčik, J.; Pribulová, Z.; Marcenat, C.; Klein, T.; Rodière, P.; and Samuely, L. C. P., Specific heat measurements of a superconducting NbS_2 single crystal in an external magnetic field: energy gap structure, *Phys. Rev. B* **2010**, *82*, 014518.

[225] Moncton, D. E.; Axe, J. D.; DiSalvo, F. J., Study of superlattice formation in 2H-NbSe$_2$ and 2H-TaSe$_2$ by neutron scattering, *Phys. Rev. Lett.* **1975**, *34*, 734.

[226] Tissen, V. G.; Osorio, M. R.; Brison, J. P.; Nemes, N. M.; García-Hernández, M.; Cario, L.; Rodière, P.; Vieira, S.; Suderow, H., Pressure dependence of superconducting critical temperature and upper critical field of 2H-NbS$_2$, *Phys. Rev. B* **2013**, *87*, 134502.

[227] The 156 cm^{-1} out-of-plane excitation in the $x = 1/3$ material is weak - consistent with predictions for a small matrix element - although it is easier to see at low temperature [Fig. S6(a)]. The frequency separation between the in- and out-of-plane modes of the intercalated metal monolayer is nicely predicted by our first principles calculations as well [Fig. S7].

[228] The metal to chalcogenide slab mass ratio for Fe$_{1/4}$TaS$_2$ is calculated as: Mass ratio = $\frac{1}{4}$M$_{Fe}$ / [M$_{Ta}$ + 2M$_S$] = 0.25*56 / [181 + 2×32] = 0.06.

[229] Voneshen, D. J.; Refson, K.; Borissenko, E.; Krisch, M.; Bosak, A.; Piovano, A.; Cemal, E.; Enderle, M.; Gutmann, M. J.; Hoesch, M.; Roger, M.; Gannon, L.; Boothroyd, A. T.; Uthayakumar, S.; Porter D. G.; Goff, J. P., Suppression of thermal conductivity by rattling modes in thermoelectric sodium cobaltate, *Nature Mater.* **2013**, *12*, 1028.

[230] Casto, L. D.; Clune, A. J.; Yokosuk, M. O.; Musfeldt, J. L.; Williams, T. J.; Zhuang, H. L.; Lin, M. -W.; Xiao, K.; Hennig, R. G.; Sales, B. C.; Yan, J. -Q.; Mandrus, D., Strong spin-lattice coupling in CrSiTe$_3$, *APL Mater.* **2015**, *3*, 041515.

[231] Wysocki A. L.; Birol, T., Magnetically induced phonon splitting in ACr_2O_4 spinels from first principles, *Phys. Rev. B* **2016**, *93*, 134425.

[232] Sushkov, A. B.; Tchernyshyov, O.; Ratcliff, W.; Cheong, S. -W.; Drew, H. D., Probing spin correlations with phonons in the strongly frustrated magnet $ZnCr_2O_4$, *Phys. Rev. Lett.* **2005**, *94*, 137202.

[233] Mandrus, D.; Sales, B. C.; Jin, R., Localized vibrational mode analysis of the resistivity and specific heat of LaB_6, *Phys. Rev. B* **2001**, *64*, 012302.

[234] Sales, B. C.; Mandrus, D.; Williams, R. K., Filled skutterudite antimonides: a new class of thermoelectric materials, *Science* **1996**, *272*, 1325.

[235] Choi, J.; Musfeldt, J. L.; Yang, Y. J.; Koo, H. -J.; Whangbo, M. -H.; Galy, J.; Millet, P., Optical investigation of $Na_2V_3O_7$ nanotubes, *Chemistry of Materials* **2002**, *14*, 924.

[236] Zhu, H.; Yi, J.; Li, M. -Y.; Xiao, J.; Zhang, L.; Yang, C. -W.; Kaindl, R. A.; Li, L. -J.; Wang, Y.; Zhang, X., Observation of chiral phonons, *Science.* **2018**, *359*, 579-582.

[237] W. Wang., et al. Room-temperature multiferroic hexagonal $LuFeO_3$ films. Phys. Rev. Lett. **110**, 237601 (2013).

[238] Xiang, H. J., and Whangbo, M. -H. Charge order and the origin of giant magnetocapacitance in $LuFe_2O_4$. *Phys. Rev. Lett.* **98**, 246403 (2007).

[239] Mendonca, E. C., *et al.* Temperature dependence of coercive field of $ZnFe_2O_4$ nanoparticles. *J. Appl. Phys.* **111**, 053917 (2012).

[240] Wang, J., Zhao, F., Wu, W., and Zhao, G. M. Unusual temperature dependence of the magnetic anisotropy constant in barium ferrite $BaFe_{12}O_{19}$. *J. Appl. Phys.* **110**, 096107 (2011).

[241] Artyukhin, S., Delaney, K. T., Spaldin, N. A., and Mostovoy, M. Landau theory of topological defects in multiferroic hexagonal manganites. *Nat. Mater.* **13**, 42-49 (2014).

[242] Groot, J., *et al.* Charge order in $LuFe_2O_4$: an unlikely route to ferroelectricity. *Phys. Rev. Lett.* **108**, 187601 (2012).

[243] Nagano, A., Naka, M., Nasu, J., and Ishihara, S. Electric polarization, magnetoelectric effect, and orbital state of a layered iron oxide with frustrated geometry. *Phys. Rev. Lett.* **99**, 217202 (2007).

[244] Goodenough, J. B. Magnetism and the chemical bond. *Interscience-Wiley, New York.* (1963).

[245] Cao, H. B., *et al.* High pressure floating zone growth and structural properties of ferrimagnetic quantum paraelectric $BaFe_{12}O_{19}$. *APL Mater.* **3**, 062512 (2015).

Vita

Shiyu Fan was born in the city of Taiyuan, Shanxi province, China. He attended Nanjing University of Information Science and Technology between 2008 and 2012, where he received his B.S. degrees majoring in Applid Physics. Shiyu joined the physics department of the University of Tennessee in the fall of 2013, and then he joined the nuclear physics research group of Dr. Galindo-Uribarri, Alfredo in the Spring of 2014, pursuing his Master degree. In the August of 2014, he passed his physics qualify exam, and switched from the Masters program to pursue his Ph.D. degree. He switched to the group of Dr Janice L. Musfeldt in the spring of 2015. His research focuses on the spectroscopic investigation of ferroic superlattices and the complex coupling between charge, spin, orbital and the lattice inside the materials. Shiyu Fan received a Doctor of Philosophy Degree in Physics from the University of Tennessee in the Spring of 2021.